Brain Magnetic Resonance Elastography based on Rayleigh damping material model

Andrii Petrov

A thesis submitted in partial fulfilment
of the requirements for the degree of
Doctor of Philosophy
in
Mechanical Engineering
at the
University of Canterbury,
Christchurch, New Zealand.

2 July 2013

Abstract

Magnetic Resonance Elastography (MRE) is an emerging medical imaging modality that allows quantification of the mechanical properties of biological tissues *in vivo*. MRE typically involves time-harmonic tissue excitation followed by the displacement measurements within the tissue obtained by phase-contrast Magnetic Resonance Imaging (MRI) techniques. MRE is believed to have great potential in the detection of wide variety of pathologies, diseases and cancer formations, especially tumors.

This thesis concentrates on a thorough assessment and full rheological evaluation of the *Rayleigh damping* (RD) material model applied to MRE. The feasibility of the RD model to accurately reconstruct viscoelastic and damping properties was assessed. The goal is to obtain accurate quantitative estimates of the mechanical properties for the *in vivo* healthy brain via the subzone optimization based non-linear image reconstruction algorithm.

The RD model allows reconstruction of not only stiffness distribution of the tissue, but also energy attenuation mechanisms proportionally related to both elastic and inertial effects. The latter allows calculation of the concomitant damping properties of the material. The initial hypothesis behind this research is that accurate reconstruction of the Rayleigh damping parameters may bring additional diagnostic potential with regards to differentiation of various tissue types and more accurate characterisation of certain pathological diseases based on different energy absorbing mechanisms. Therefore, the RD model offers reconstruction of three additional material properties that might be of clinical diagnostic merit and can enhance characterisation of cancer tumors within the brain.

A pneumatic-based actuator was specifically developed for *in vivo* human brain MRE experiments. Performance of the actuator was investigated and the results showed that the actuator produces average displacement in the range of 300 μm and is well suited for generation of shear waves if applied to the human head. Unique features of the the actuator are patient comfort and safety, MRI compatibility, flexible design and good displacement characteristics.

In this research, a 3D finite element (FE) subzone-based non-linear reconstruction algorithm using the RD material model has been applied and rigorously assessed

to investigate the performance of elastographic based reconstruction to accurately recover mechanical properties and a concomitant damping behaviour of the material. A number of experiments were performed on a variety of homogenous and heterogeneous tissue-simulating damping phantoms comprising a set of materials that mimic range of mechanical properties expected in the brain. The result showed consistent effect of a poor reconstruction accuracy of the RD parameters, ρ_I and μ_I, which suggested the nonidentifiable nature of the RD model.

A structural model identifiability analysis further supported the nonidentifiabilty of the RD parameters μ_I and ρ_I at a single frequency. Therefore, two approaches were developed to overcome the fundamental identifiability issue. The first one involved application of multiple frequencies over a broad range. The second one was based on parametrisation techniques, where one of the damping parameters was globally defined throughout the reconstruction domain allowing reconstruction of the two remaining parameters.

Based on the findings of this research, multi-frequency (MF) elastography was performed on the tissue-simulating phantoms to investigate improvement of the elastographic reconstruction accuracy. Dispersion characteristics of the materials as well as RD changes across different frequencies in various materials were also studied. Simultaneous multi-frequency inversion was undertaken where two models were evaluated: a zero-order model and a power-law model. Furthermore, parametric-based RD reconstruction was carried out to evaluate enhancement of accurate identification of the reconstructed parameters. The results showed that parametric-based RD reconstruction, compared to MF-based RD results, allowed better material characterisation on the reconstructed shear modulus image. Also, significant improvement in material differentiation on the remaining damping parameter image was also observed if the fixed damping parameter was adjusted appropriately.

In application to *in vivo* brain imaging, six repetitive MRE examinations of the *in vivo* healthy brain demonstrated promising ability of the RD MRE to resolve local variations in mechanical properties of different brain tissue types. Preliminary results to date show that reconstructed real shear modulus and overall damping levels correlate well with the brain anatomical features. Quantified shear stiffness estimates for white and gray matter were found to be 3 ± 0.11 kPa and 2.1 ± 0.11 kPa, respectively. Due to the non-identifiability of the model at a single frequency, reconstructed RD based parameters μ_I and ρ_I limit any physical meaning. There-

fore, MF-based and parametric-based cerebral RD elastography was also performed.

Foreword

Material properties of brain tissue have been investigated under different experimental protocols, such as compression, shear, tension, and oscillatory loading. However, reported mechanical estimates from *in vivo* and *in vitro* brain specimens have been generally inconsistent and vary between studies by a large degree. These large variations in the obtained results might be due to different experimental conditions, constitutive models used, and the highly anisotropic and inhomogeneous nature of the intracranial tissue.

Furthermore, the majority of biomechanical models applied to MRE have been unsuccessful in procuring accurate and reproducible measurements of brain mechanical properties *in vivo*. This thesis contributes to the field of brain elastography by exploring an alternative Rayleigh damping (RD) model which is able to capture variations of not only elastic modulus distribution, but can also estimate damping behaviour deduced from two different energy attenuation mechanisms. Furthermore, the research conducted in this thesis presents a series of mathematical analyses, technical improvements of the MRE methodologies in application to in vivo brain imaging and validation investigation of the RD model as a diagnostic imaging modality in a clinical setting. In particular:

Chapter 1 gives a a brief overview of the current methods for elasticity imaging, brain tumors and state of the art imaging modalities used for brain tumor visualisation. Background information on brain tissue mechanical properties as well as introduction to MRE as an elasticity imaging modality is also given.

Chapter 2 deals with constitutive modelling of the brain tissue. First, brief introduction to the brain anatomical structures and their relevant physiology is described. Second, an overview of constitutive models used to estimate brain tissue mechanics followed by a summary of important aspects relevant to modelling the brain is provided. Lastly, an overview of brain elastography methods and results is given.

Chapter 3 provides a general description of the MRE technical aspects, such as MRE image acquisition, motion encoding, data conversion and processing of the results. It also includes detailed description of the development of acoustic brain

actuation system.

Chapter 4 defines mathematical formulation of the RD model applied to a time-harmonic MRE. It also presents a mathematical analysis on rheological interpretation of the constitutive model parameters.

Chapter 5 provides detailed description of the fully 3D subzone-based nonlinear image reconstruction algorithm used for inversion processing of the mechanical properties.

Chapter 6 reports on phantom construction, initial MRE imaging experiments and actuation methods used.

Chapter 7 shows selected results and various analyses of the simultaneous three parameter-based RD reconstructions from tissue-simulating damping phantoms. Thorough evaluation of the RD model to accurately map mechanical properties is also contained in this chapter.

Chapter 8 presents a structural mathematical identifiability analysis of the RD model applied to time-harmonic MRE. More specifically, the identifiability of the RD model is assessed.

Chapter 9 describes multi-frequency MR elastography experiments with tissue-mimicking phantoms. It also contains parametric-based RD MRE study results. Comparison between elastographic reconstruction accuracy of constitutive parameters from both methods is also presented.

Chapter 10 shows clinical evaluation of the RD MRE in application to *in vivo* brain imaging. Parametric-based RD reconstruction are compared with full three parameter-based RD reconstructions.

Chapter 11 summarises and concludes the outcomes of this thesis. The suggestions for future work and possibilities from the outcomes of the thesis are also presented.

Acknowledgement

I would like express the deepest appreciation to my supervisory UC team: Prof. Geoffrey J Chase, Dr. Mathieu Sellier and Dr. Paul Docherty for providing tremendous support and always supplying valuable advice no matter what the question was. I owe a great deal of gratitude to you and truly appreciated all your input. Thank you guys for taking me under your wing.

I also would like to thank Prof. David Wall for helping in understanding complex mathematical concepts of elastography problems and anything mathematic related that was beyond my comprehension. Special thanks goes to Assoc. Prof. Elijah Van Houten for initiating this fascinating research project and providing this unrivalled opportunity. Also, thanks to Dr Stefanie Gutschmidt for being extremely helpful and willing to share your expertise with me.

I also would like to greatly acknowledge Dr Peter Latta and Dr Marco Gruwell from National Research Council of Canada and PhD students Curtis Johnson from University of Illinois at Urbana-Champaign and Matthew McGarry from Dartmouth College of Engineering for their contribution into the project with MRE human studies.Many thanks goes to Dr Vladimir Mencl and Tony Dale from the *Blue Fern* high performance computing services for providing technical support and helping in resolving constantly arising issues with running computations and code debugging.

Of course, to all the PhD students in BioEngineering, Mechanical Engineering and Physics Department for your support, patience and encouragement when I was going through rough times.

To my parents for teaching me the virtues of life and providing unconditional love and support throughout the years I have been away from home. And yes, Dad, one day I will get a job.....I promise!

Finally, this project would not be possible without financial support provided by Premier Scholarship from the Department of Mechanical Engineering and HPC Supercomputing Scholarship that allowed me to undertake project related courses. Also, genuine thanks you goes to Maurice & Paykel travel grant for providing partial financial support to attend IEEE EMBC12 conference in San Diego which was an absolutely amazing experience and definitely one of highlights of this PhD projects.

Contents

List of Figures

List of Tables

Nomenclature

Normal type indicates scalars, bold uppercase indicates a Matrix, bold lowercase indicates a vector.

Roman Symbols

$\mathbf{A}(\mu, \lambda, \rho)$:	Forward FEM matrix with elements $\mu(x, y, z)$, $\lambda(x, y, z)$ and $\rho(x, y, z)$
$\mathbf{A}(\mathbf{x})$:	Real valued amplitude of MR-detected motions.
B_0:	Static magnetic field of the MRI.
$\mathbf{C}$:	Damping matrix in discretised form of Navier's equation.
$\mathbf{D}(\mathbf{x})$:	Displacement, $\mathbf{D}(\mathbf{x}) = \mathbf{A}(\mathbf{x})\cos(P(\mathbf{x}))$.
E:	Elastic, or *Young's* modulus.
E^*:	Complex modulus developed from a spring-dashpot configuration.
$F(k)$:	Fourier transform.
F_{res}:	Elastic restoring force acting on a mass-spring-damper system.
F_{tot}:	Total force of a mass-spring-damper system.
F_d:	Damping restoring force acting on a mass-spring-damper system .
$\mathbf{G}_r$:	Time dependent function of the magnetic gradients.
^{H}:	Complex conjugate transpose operator.
$\boldsymbol{I}$:	Second-order identity tensor.
$\|J\|_g$:	Global Jacobian size.
K:	Bulk Modulus, related to E and ν by $K = \frac{E}{3(1-2\nu)}$.
$\mathbf{K}$:	Elastic stiffness matrix in discretised form of Navier's equation.
$\hat{\mathbf{K}}$:	Normalised $\mathbf{K}$ after taking out a common factor of μ.
$\mathbf{L}$:	Momentum of the system, defined as $\mathbf{L} = m\dot{\mathbf{u}}$
$\mathbf{M}$:	Mass matrix in discretised form of Navier's equation.
$\hat{\mathbf{M}}$:	Normalised $\mathbf{M}$ after taking out a common factor of ρ.
NO:	Number of observations.
NP:	Number of reconstructed parameters.
N_z:	Number of subzones.
$P(\mathbf{x})$:	Phase of MR-detected motions.
P_{tot}:	Total pressure of a poroelastic medium.
P_s:	Pressure level accosted with the solid compartment in a poroelastic medium.
P_f:	Pressure level accosted with the fluid compartment in a poroelastic medium.

V:	Magnitude of the phase velocity of the wave.
V_s:	Volume of the solid compartment in a poroelastic medium.
V_f:	Volume of the fluid compartment in a poroelastic medium.
Y:	Complex module formulated from viscoelastic theory ($Y = Y_R + iY_I$) .
$\mathbf{b}$:	Internal body force.
$\mathbf{c}$:	Unknown elemental basis constants for linear least squares.
c:	Damping coefficient of a dashpot of a mass-spring-damper system .
d:	Inside diameter of a straight cylindrical waveguide.
f:	Frequency (Hz).
$f(j)$:	Vector of phase values over effective delay times for a particular voxel.
$f(\phi)$:	Phase offset of oscillating arbitrary voxel within tissue.
$\mathbf{f}$:	Discretised description of external and body forces.
$\mathbf{f}(\mathbf{x}, t)$:	Time-harmonic force, $\mathbf{f}(\mathbf{x}, t) = \hat{\mathbf{f}} e^{iwt}$
$\mathbf{g}$:	Gradient, a vector of the first derivative of the error, Φ w.r.t each of the reconstruction variables.
i:	The imaginary unit, $\sqrt{-1}$.
$\mathbf{i}, \mathbf{j}, \mathbf{k}$:	Unit vectors in x, y and z directions respectively.
k:	Stiffness of the spring of a mass-spring-damper system.
m:	Mass of a mass-spring-damper system .
$\mathbf{p_k}$:	Search direction.
$\mathbf{p_{k-1}}$:	Previous search direction.
$\mathbf{p}_{sd}$:	Steepest descent search direction.
$\mathbf{p}_t$:	Unscaled conjugate-gradient search direction.
$\mathbf{p}_t^s$:	Scaled conjugate-gradient search direction.
t:	Time.
$\mathbf{r}(t)$:	Position of the nuclear spins as a function of time.
$\mathbf{u}(\mathbf{x}, t)$:	Real-valued measurable displacement occurring at a point $\mathbf{x}$ at time t.
$\hat{\mathbf{u}}$:	Time-harmonic motion.
$\hat{\mathbf{u}}_c$:	Complex motion phasor
$\mathbf{u}, \dot{\mathbf{u}}, \ddot{\mathbf{u}}$:	The discretised description of the displacement, velocity and acceleration.
$\mathbf{u}^c$:	Displacements simulated using the current $\boldsymbol{\theta}$ estimate.
$\mathbf{u}^m$:	Displacements measured by phase-contrast MRI techniques.
$\mathbf{u}_R$:	Real part of the displacements.
$\mathbf{u}_I$:	Imaginary part of the displacements.
u_x, u_y, u_z:	Displacement components in the x, y and z direction.
$\hat{u}_x, \hat{u}_y, \hat{u}_z$:	Approximate FE displacement solutions onto the set of FE basis functions (ϕ_j)

w_{sf}: Weighting applied to spatial filtering.
$\mathbf{x}$: Vector of position.
x: Coordinate direction.
y: Coordinate direction.
z: Coordinate direction.

Greek Symbols

Γ: Boundary of Ω.
Γ_z: Boundary of Ω_z.
Δ_θ: Integral of a basis function over all connected elements.
$\mathbf{\Phi}$: Objective error function (residual between measured and simulated displacement)
$\mathbf{\Phi}_{tk}$: Error function with Tikhonov regularisation.
$\mathbf{\Phi}_{tv}$: Error function with total variation minimisation.
Ω: Whole problem domain.
Ω_z: Subzone of problem domain.
α_k: Conjugate-gradient scalar.
α_{tk}: Tikhonov regularisation weight.
α_{tv}: Total variation minimisation weight.
$\bar{\alpha}$: Proportionality constant relating damping force to velocity.
α: Proportionality constant of the mass matrix in a proportional damping assumption.
β: Proportionality constant of the stiffness matrix in a proportional damping assumption.
γ: Gyromagnetic ratio of the specific material.
δ: A given change in material property value.
δ_s: The step size used for the finite difference approximation of the second derivative in the secant method.
$\boldsymbol{\epsilon}$: Volumetric strain tensor.
$\mathrm{tr}(\boldsymbol{\epsilon})$: Trace function of $\boldsymbol{\epsilon}$
ζ: Local FE coordinate corresponding to the z direction.
η: Local FE coordinate corresponding to the y direction.
$\boldsymbol{\theta}$: A general reconstructed variable.
λ: First Lamé parameter, $\lambda = \frac{\nu E}{(1+\nu)(1-2\nu)}$.
λ_s: Approximate shear wavelength.
μ: Shear Modulus, or second Lamé parameter, $\mu = \frac{E}{2(1-\nu)}$.

μ_R: Real part of μ.
μ_I: Imaginary part of μ.
ν: Poisson's ratio.
ξ: Local FE coordinate corresponding to the x direction.
ξ_d: Damping ratio.
ρ: Density.
ρ_R: Real part of ρ.
ρ_I: Imaginary part of ρ.
ϕ: Relative phase offset between the externally induced motion and MEGs.
$\boldsymbol{\sigma}$: Stress tensor.
$\phi(\tau)$: Phase shift of the NMR signal.
ϕ_j: Set of FE basis functions used to facilitation approximate FE displacement solutions.
$\phi_k(x, y, z)$: Continuous FE basis functions used to facilitate material property solutions.
$\phi^T\ \phi$: Normalised eingenvector of the system.
μ^*: Complex valued shear modulus from viscoelastic theory.
λ^*: Complex valued first Lamé's parameter from viscoelastic theory
ω: Angular frequency of time-harmonic motion ($rad\ s^{-1}$).
∇: Gradient operator, $\nabla = \hat{\mathbf{x}}\frac{\partial}{\partial x} + \hat{\mathbf{y}}\frac{\partial}{\partial y} + \hat{\mathbf{z}}\frac{\partial}{\partial z}$
$\nabla\cdot$: Divergence operator, $\nabla\cdot = \frac{\partial U}{\partial x} + \frac{\partial V}{\partial y} + \frac{\partial W}{\partial z}$

Acronyms

CNRC: National Research Council Canada.
CSF: Cerebrospinal fluid.
CT: Computed tomography.
CV: Coefficient of variation.
CG: Conjugate-gradient.
DOF: Degree of freedom.
EPI: Echo-planar imaging
FE: Finite element.
FEA: Finite element analysis.
FEM: Finite element method.
FFT: Fast Fourier transform.
FOV: Field of view.
GN: Gauss-Newton.
GRE: Gradient Recall Echo.

LHS: Left hand side.
MCG: Motion sensitising gradients.
MEG: Motion encoding gradients.
MR: Magnetic resonance.
MRE: Magnetic resonance elastography.
MRI: Magnetic resonance imaging.
NMR: Nuclear magnetic resonance.
NPH: Normal pressure hydrocephalus.
PDE: Partial differential equation.
PAD: Pneumatically actuated driver.
OSS: Octahedral-shear strain.
RBM: Rigid body motion.
RD: Rayleigh damping.
RF: Radio frequency.
RHS: Right hand side.
ROI: Region of interest.
SE: Spin-echo.
SNR: Signal to noise.
STD: Standart deviation.
TE: Time to repetition.
TR: Time to echo.
TV: Total variation minimisation.
US: Ultrasonograohy

Chapter 1

Introduction

1.1 Methods for imaging elastic properties of biological tissue

Over the centuries, a wide range of examination tools have been developed to assess the mechanical properties of biological tissues. In fact, in clinical medicine the palpation of soft tissue remains a standard diagnostic procedure used to detect pathological tissue change (Di Ieva et al., 2010). It is based on the mechanical resistance of tissue to compression and shear deformations. Indeed, many tumors are still first detected by touch (Manduca et al., 2001). For example, it is common to first encounter a breast cancer by means of palpation during clinical breast examination (Rimsten et al., 1975). However, the sensitivity of this method is limited to soft tissues located in the vicinity of the body surface. There are many organs, such as the brain, liver or heart that are not accessible to palpation and thus do not naturally present a simple means of diagnosis by stiffness contrast.

The stiffness of biological tissues can vary up to four orders of magnitude (Duck, 2012). Existing research has shown that tissues display different stiffness characteristics in response to variances in physiological state (Sarvazyan, 1993). For example, engagement and relaxation of the muscles, changes of the muscle state due to external or internal stress conditions, involuntary constriction or damage as a result of injuries can also effect the consistency of biological tissues (Duck, 2012; Gennisson et al., 2005). In addition to muscle state, abnormalities in tissue cells can also cause changes in mechanical properties of biological tissues. Although, there is a paucity of information available, some studies have shown that breast cancer can differ from

the surrounding healthy tissues by a factor of 2 to 20 fold (Samani et al., 2007). As a result of stiffness contrast associated with the previously mentioned factors, current research is now focussed on advancing the assessment of elastic properties of the tissues in a non-invasive manner (Lewa and Certaines, 1995; Ophir et al., 1999; Peters et al., 2004; Scholz et al., 2005). In this context, accurate quantitate estimates of tissue's mechanical properties that can enable diagnosis remains the ultimate goal.

It is important to consider which mechanical property is the most indicative of palpation. *Young's modulus* (E) describes deformation in response to normal stress, while the *shear modulus* (μ) relates the transverse strain in response to transverse stress and associated shear wave propagation. The *bulk modulus* (K) is associated with the volume change of a material in response to a uniform compression. Finally, *Poisson's ratio* is a ratio of transverse contraction to longitudinal extension. Due to the high water content, most biological tissues are highly saturated and, therefore, have Poisson's ratio between 0.49 and 0.4999 (Oliphant et al., 2001). As such, a high Poisson's ratio is associated with a nearly incompressible material behaviour. Although the shear modulus of tissue can differ significantly, the bulk modulus of most soft tissues are within 15 % of that of water. Therefore, based on the broadest quantitative range, Young's and shear moduli are the first potential candidates to be imaged and are the closest representative of what is felt by palpation.

All elasticity imaging methods involve a tissue excitation followed by method of measuring tissue response and associated displacement pattern (Greenleaf et al., 2003). Tissue excitation can be categorised into static and dynamic methods. In the static approach, the tissue is typically subjected to a slow compression followed by a measurement of the resulting deformation. In contrast, dynamic methods involve tissue excitation in a steady state manner by application of the external actuation device coupled to the tissue of interest. The advantage of dynamic approach over the static approach is mainly based on constitutive relations between stress and resulting strain. More specifically, in dynamic methods the resulting strain or displacements are described by the 3D equation of motion compared to the static methods, where the stiffness is commonly assumed to be inversely proportional to the resulting strain, such that low strain would correspond to higher stiffness and vice versa.

Another way to categorise excitation methods is based on spatial characteristics of the excitation, segregating external and internal aspects. External methods

include application of a compression force directly onto the skin to deform the tissue beneath. For instance, a plate is pressed and held steady against the skin in the static approach, or vibrated with some sort of actuation device in the dynamic approach. Alternatively, internal excitation methods excite the tissue of interest internally by direct application of the excitation force onto the tissue. For example, an ultrasound beam that produces concentrated acoustic force within the tissue and thus able to probe the tissue simultaneously at multiple points can be considered an internal method. Natural biological processes, such as respiration or cardiovascular pulsation, can also be attributed to the internal excitation of tissue.

Depending on the physical phenomena used to capture displacements, detection methods can also be categorised into several groups. Ultrasound (US), nuclear magnetic resonance (NMR) and acoustic detection are the main techniques used for measurement of tissue response. The displacement measurement within the ultrasound is based on either Doppler effect or pulse-echo methods (Skovoroda et al., 1995). The acoustic approach of detecting tissue response is based on measuring sound levels exhibited by a tissue vibration. Lastly, measurement of tissue displacement with NMR is performed by utilising a phase contrast magnetic resonance imaging (MRI) technique with added motion encoding gradients (MEGs) (Lewa, 1991). Equally, digital imaging (DIET) has also begun to be used (Peters et al., 2004).

1.2 Brain tumors

A brain tumor is an uncontrolled abnormal cell devision forming a solid neoplasm within the cranium or spinal cord system. Brain tumors can occur in any outer part of the brain, such as blood vessels, nerves, lymphatic tissue, meninges, pituitary gland and even the solid skull. Tumors can also appear within the brain itself in the cells composing the intracranial matter. The cells are mainly neurons or glial cell which include ependymal cells, astrocytes and oligodendrocytes. The cancers from other organs of the body can also trigger the appearance of brain tumors.

Importantly, brain tumors are located where palpation is not possible. In fact, many are not detected with computed tomography (CT) or MRI after the onset of serious symptoms. Thus, a simple means of diagnosis using mechanical properties

would be of a significant value.

Whether the brain tumor is benign or malignant, it equally represents a threat, as it occurs within the non expandable intracranial cavity. Its threat to life is dependant on the tumor type, where it is located, the size and its development phase (Ali-Osman, 2005). However, not all brain tumors are fatal.

Brain tumors are categorized into two types: primary (70%) and secondary (or metastatic) (30%) (Drevelegas, 2011). Primary tumors initially start in the brain. Gliomas, meningiomas, pituitary adenomas and nerve sheath tumors make up the bulk of primary tumors and constitute 50.4%, 20.8%, 15% and 8%, respectively (Lee, 2008). Secondary tumors spread from other parts of the body to the brain. The spread process involves cancerous cells from other affected organs leak into the lymphatic or blood stream systems and travel to the brain, where they multiply and grow, once deposited. The most common source of the secondary brain tumors are breast cancer, kidney cancer, lung cancer and colon cancer.

Primary intracranial tumors, such as gliomas in men and meningiomas in woman comprise 60% and 20% of all brain tumors respectively (Drevelegas, 2011). Tumors, originating from glial cells are the most frequent cancer in adults (Aronen et al., 1994). Middle aged individuals are commonly found with anoplastic astrocytomas. In contrast, young adults are more prone to low-grade gliomas (Maia et al., 2005). Generally, malignancy level corresponds to increase in age (Law et al., 2006).

Some tumors are detected after symptoms and some can appear on unrelated CT or MRI scans. An early detection of brain tumors is only possible when diagnostic imaging tools are directly applied to cranial cavity. Therefore, unfortunately tumors are generally detected at later stages upon follow up investigation from recurring symptoms.

Intracranial tumors can also be differentiated according to their origin. Some of them originate from brain tissue and cells and are called intraxial tumors. Others originate from meninges, cranial bones, glandular cells of the pituitary or from cranial nerves and are called extraxial tumors. The latter have the common characteristic to grow in a rather rigid skull, thus compressing the healthy brain tissue. Gliomas are the most common intraxial tumors and can be subdivided into the following types.

- Atrocytomas,
- Oligodendrogliomas,
- Ependymomas,
- Glioblastomas.

1.2.1 Astrocytomas

The most common glioma is the *astrocytoma* which originates from the *astrocites* cells found in the cerebrum. Astrocytoma can appear in any part of the brain and occasionally in the spinal cord (Drevelegas, 2011). Astrocytomas are usually found in adults, however do appear in elderly individuals as well.

Astrocytomas can be divided into four grades, depending on the severity. Grade I type astrocytomas can be removed surgically allowing radiation therapy treatment of any remaining cancer cells. Grade II type are characterised by deeper penetration into the brain tissue and thus complicating the surgical procedure. Reoccurrence rate of the grade II astrocytomas is more probable due to the infiltration of the cancer cells into the healthy brain tissues. The treatments, such as radiotherapy or chemotherapy are available to post surgery patients to minimise the risk of reoccurrence. Survivability and ability to return to a normal lifestyle are age dependant. Grade III astrocytomas, also called *anaplastic astrocytoma*, results in headaches, neurological deficit and seizures. A standard clinical treatment includes removal of tumor by surgery followed radiation therapy to eliminate remaining cells. Two to three years is the usual expected survival rate after having the tumor removed (Ohgaki and Kleihues, 2005). Lastly, grade IV astrocytoma is called *glioblastoma multiforme*. It is the most malignant and life-threatening tumor due to the rapid spreading to other parts of the brain. Surgical removal in this case is only considered if no damage is incurred in other brain regions. In cases where surgery is not an option, radiotherapy can prolong life of the patient without having to cure the glioblastoma. Fig. 1.1 shows an example of glioma astrocytoma grade IV in a 55 year old male.

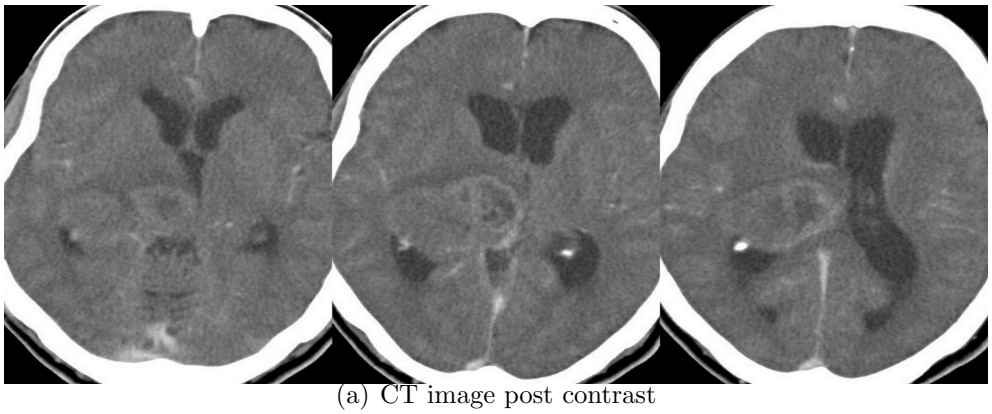

(a) CT image post contrast

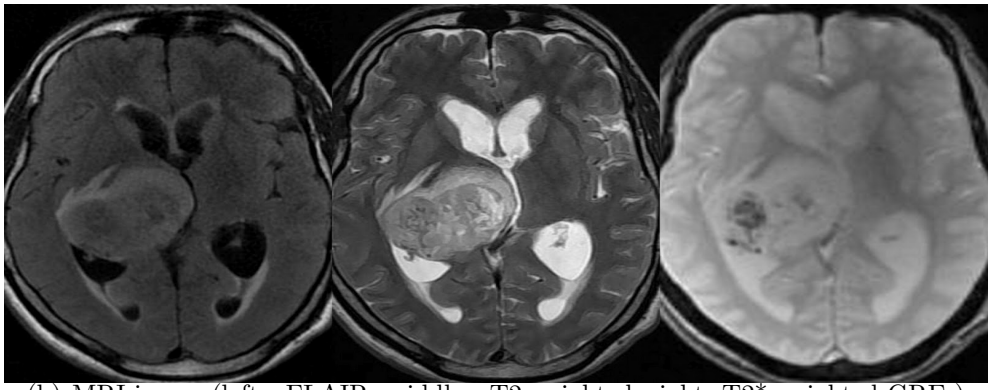

(b) MRI image (left - FLAIR, middle - T2-weighted, right -T2*-weighted GRE)

Figure 1.1 MRI image of the thalamic glioma-astrocytoma (Grade IV). A heterogeneously enhancing neoplastic soft tissue density space occupying lesion centred to right thalamus. Third ventricle compressed with mild trapping of lateral ventricles. (a) Contrast enhanced CT Image; (b) MRI image (left - MRI FLAIR, middle - T2-weighted, right - T2*-weighted GRE). Image courtesy of Dr Balaji Anvekar's Neuroradiology Cases (Anvekar, 2012). Reprinted with permission.

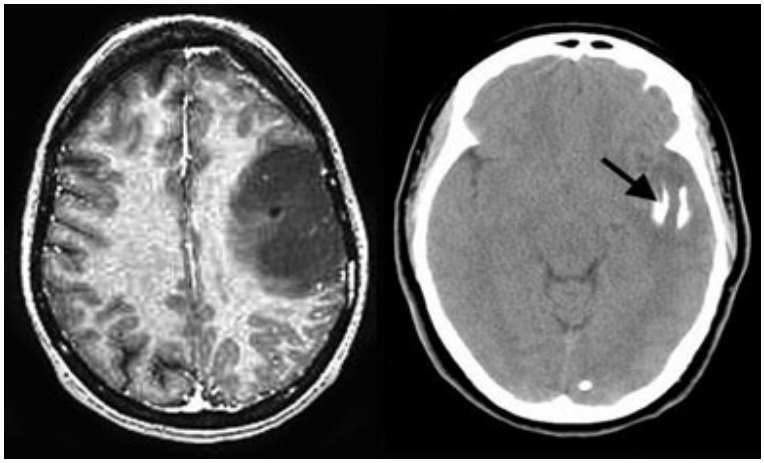

Figure 1.2 The MRI image (left) of a large oligodendroglioma in a left frontal lobe. Corresponding CT scan (right) indicates partial calcification of the tumor (arrow). Image courtesy of Department of Radiation Oncology UCLA (UCLA, 2013).

1.2.2 Oligodendrogliomas

Oligodendrogliomas originate from brain tissue cells *oligodendrocytes* that support transmission of nerve impulses within the brain. Oligodendrogliomas are primary brain tumors which occur more often in adult men compared to women. Generally, these tumors are rare and account for only 10% of primary intracranial neoplasms (Ohgaki and Kleihues, 2005).

The survival rate of patients with oligodendrogliomas is approximately 10 years. Strong headaches and reoccurring seizures are common features. Depending on the geometry and location of the tumor, several neurological deficits, such as disruption of motor function, partial or complete loss of vision and cognitive decline, can be triggered (Engelhard et al., 2003).

Contrast-enhanced CT (CCT) or MRI scans are usually required for assessment purposes. Standard treatment strategies include surgery followed by a choice between radiation therapy or chemotherapy. Fig. 1.2 shows an MRI and corresponding CT images of the oligodendroglioma in the left frontal lobe.

1.2.3 Ependymomas

An *Ependymoma* is a type of glioma that has originated from the cells within the ependyma tissue. Ependymoma is found in a fluid filled passages and hollow cavities of the brain. Ependymomas are commonly found in the forth ventricle where they obstruct the flow of cerebrospinal fluid (CSF), thus causing appearance of severe headaches, nausea, vomiting and vision loss (Pollack et al., 1995).

Although 85 % of all ependymomas are benign, these tumors represent potential threat because of the possibility of a spread from the brain to the spinal cord due to the movement of fluids. Low grade ependymomas can be surgically removed and further suppressed by radiation therapy. Response to a chemotherapy treatment is usually very low. Overall, these tumors are very rare and constitute only 5% of all intracranial gliomas in adults and up to 10% of childhood tumors.

Extraxial tumors can be subdivided into the following types:

- Meningiomas,
- Pituitary adenomas,
- Neurinomas,
- Angiomas,

1.2.4 Meningiomas

Meningiomas initially originate from endothelial cells found in meninges of the brain. These tumors are the most common primary brain tumors, accounting for 20% of all intracranial tumors in adults (Goldsmith et al., 1994). Most of the meningiomas are benign in nature (grade I - 90%), although some tumors appear to have malignant presentations (grade III - 2%) (Lee, 2008). Fig. 1.3 shows an example of a falcine maligannt meningioma on the right side of the flax cerebri.

Many meningiomas are silent, producing no symptoms throughout the life. In this case, no specific treatment is required other than periodic monitoring of tumor

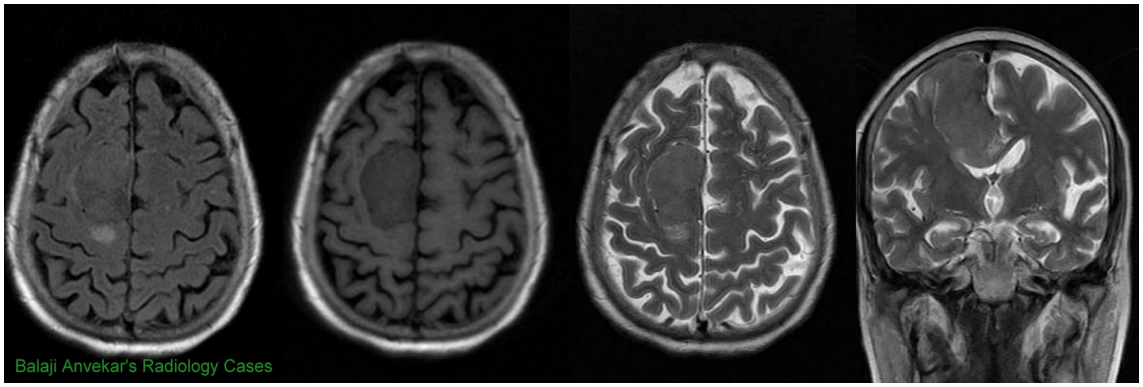

Figure 1.3 Falcine meningioma in the right side of the falx cerebri. Image courtesy of Dr Balaji Anvekar's Neuroradiology Cases (Anvekar, 2011). Reprinted with permission.

progression and overall behaviour. However, symptomatic meningiomas are usually treated by conventional neurosurgery or, alternatively, with radio surgery.

Meningiomas are highly vascularised tumors, therefore CCT or gadolinium DTPA based contrast-enhanced MRI are the preferred imaging modalities (Engelhard, 2001). Cerebral angiography can be also used to visualise vascular encasement of meningiomas (Raksin, 2003). Positron emission tomography (PET) imaging studies have shown potential in differentiation of meningiomas.

1.2.5 Pituitary adenoma

Pituitary adenomas are benign slow-growing neoplasms that originate from cells in the pituitary gland. These tumors constitute 10 % of all intracranial neoplasms and more commonly found in women (Drevelegas, 2011). Pituitary adenomas are characterised according to their size, aggressiveness and hormone secretion.

Depending on the size, pituitary adenomas are generally classified into microadenomas which are less than one centimetre, and macroadenomas which are more than one centimetre. Regarding the aggressiveness, pituitary adenomas are subdivided into benign adenoma, invasive adenoma and carcinoma. Lastly, based on hormone secretion functions, pituitary adenomas are classified into hormonally active or functional adenomas and non-functional adenomas which do not display hormonal and proliferative activity. Tumors in the pituitary gland may present symptoms such as

visual loss, severe headaches and diplopia. Pituitary adenomas are usually discovered on unrelated conventional CT to MRI follow up investigations of nonspecific symptoms, such as dizziness or headaches.

1.2.6 Neurionomas

Neurionomas, also called *schwannomas*, are relatively slow-growing, homogeneous in consistency tumors that originate in the *schwann cells* (White et al., 2006). Neurionomas are located on the periphery of the nerve fibers and used for transmission of electrical impulses along axons. Tumors of the cranial nerve sheath constitute 5% to 10% of all intracranial neoplasms (Drevelegas, 2011). 99% of these tumors are benign in nature and only 1% constitute to malignancy (Sordillo et al., 2006). Malignant neurionamas are also called *neurofibrosarcoma*.

Shwannomas can arise in any nerves within the body. However, the most common appearance of the tumor is seen in the nerves of the neck and head, particularly in the acoustic nerve (Matthies and Samii, 1997). Tumor cells do not normally penetrate throughout the nerves and tend to stay on the periphery. However, enlargement of the tumor might push the nerves against the bone which can cause damage or rupture. Also, during development stage shwannoma might cause compression the brainstem and the cerebellum which can lead to a *hydrocephalus*.

Treatments for malignant schwannomas include resection by means of neurosergery followed by radiotherapy (Unger et al., 2002). Response to a chemotherapy is usually low. However, chemotherapy can still be applied in an attempt to reduce the size of the tumor, but unlikely with a purpose of cure.

1.3 Current diagnostic methods for brain tumors

Accurate assessment of intracranial tumors is a complicated task. In fact, imaging plays a crucial role in overall evaluation of brain tumors. Over the years, medical imaging modalities have progressed from visualising purely anatomy-based features, such as geometry, location and consistency of the neoplasms, to quantitative mapping of functional, metabolic, diffusion and perfusion alterations within the tumors.

Today, state of the art neuroimaging combines a set of advanced diagnostic tools that allow comprehensive evaluation of anatomical, biological and morphological variations to establish accurate diagnosis and characterisation of intracranial neoplasms. Imaging is also commonly utilized to assess treatment response and patient prognosis.

The standard imaging modalities of brain tumors are conventional CT and MRI. Generally, MRI is superior compared to CCT, providing better soft tissue contrast and thus allowing detection of smaller tumors (Schellinger et al., 1999). Other advantages of MRI over CT include better spatial resolution, higher SNR, absence of bone artifacts and less partial volume effects. However, some patients with implanted medical devices, such as pacemakers, cannot safely have an MRI examination. CT automatically becomes an acceptable alternative in such cases.

Advancement in the technical aspects of MRI has resulted in new evolving imaging techniques that quantitatively evaluate tissue blood flow (perfusion imaging), water motion (diffusion imaging) (Kono et al., 2001), and metabolism (Proton MR spectroscopy) (Majós et al., 2004), which has significantly improved the detection and the evaluation of brain neoplasms (Weber et al., 2006). These modalities thus offer added diagnostic data that conventional CT or MRI alone cannot.

In particular, neoplasms will often show as added regions of differing material properties in CT or MRI scans. Generally, with MRI the contrast between brain metastases and primary intracranial neoplasms is well differentiated. Benign tumors usually appear in darker intensities than healthy brain tissues (hypodense) on CT scans. With MRI, depending on consistency of the tumor, they are represented either in darker or similar intensities (isodense) as brain tissues on T1-weighted images, and usually in brighter intensity (hyperdense) on T2-weighted images. Contrast enhancement is commonly administrated in both CT and MRI to allow better visualization and spatial delineation of tumor boundaries as well as improved differentiation between benign and malignant tumors (Claussen et al., 1985).

Once the symptoms indicate the presence of the tumor, imaging becomes a first definite diagnostic tool to determine anatomical-based features as well as non-invasive measurement of the consistency and composition of the tumor infrastructure. The data obtained from imaging diagnosis is crucial in the selection of an appropriate follow up treatment procedure, such as neurosurgery, radiation or chemother-

apy. However, a definite diagnosis of the tumor is established through a thorough examination of histological properties of the tumor sample removed by means of biopsy or neurosurgery (Vaquero et al., 2000). A standard histological examination includes assessment of the fresh tissue followed by microscopic investigation of the stained tissue and comprehensive genetic analysis. The end results should thus be a definite diagnosis.

1.3.1 Computed Tomography (CT)

CT is an important radiological diagnostic imaging tool and a second alternative imaging modality to MRI. CT uses a set of X-rays that in combination produce tomographic images (slices) of specific area of the body. It is cheap and fast, and superior in detection of tissue calcifications, investigating bones and haemorrhage. CT can also be used for assessment of bone changes related to intracranial tumors (Sze et al., 1990). Due to the relatively fast image acquisition, CT is also commonly used as a first imaging response in intensive care and emergency units as well as in traumotology.

Introduction of CT to clinical use in 1972 initiated a number of cerebral studies, such as traumatic brain injury, stroke, etc. Gradual technical advancements in image acquisition, processing time, reduction of scanning time has resulted in expansion of CT applications and triggered new research initiatives (Roberts et al., 2002). CT can be also used for diagnosis of lungs, heart, abdomen and liver. Administration of contrast medium is usually required for assessment of brain tumors. Contrast agents improve contrast characteristics between abnormal and surrounding healthy tissues.

1.3.2 Magnetic Resonance Imaging (MRI)

MRI plays a central role in the imaging of intracranial neoplasms and tumors. After its introduction to clinical practice in the 1980s as a diagnostic imaging tool, MRI has became the best available neuroimaging modality. MRI allows high resolution imaging of the fine anatomical details in relatively short acquisition times. Compared to conventional X-ray and CT based techniques, MRI allows more accurate

delineation of tumors and better spatial resolution (Schellinger et al., 1999). In addition, MRI is based on non-invasive application of a magnetic field accompanied by a radio frequency excitation contrary to ionising radiation induced by X-ray or CT. Similar to CT, introduction of contrast agents can help to distinguish some tumors within the normal tissues (Claussen et al., 1985). The most common agent used for the central nervous system is gadolinium DTPA. DTPA accumulates in the tumor intracellular space thus making it appear brighter in the MR images.

MRI has emerged from a purely anatomical-based imaging modality to being able to offer mapping of functional properties of the entire brain. For example, functional MRI (fMRI) is capable of assessing the functional activity of the brain during performance of a particular task. More specifically, fMRI is able to capture brain areas characterized by higher oxygen consumption associated with increase of blood flow to the active regions of the brain (Moonen and Bandettini, 2000).

Another extension of conventional MRI is spectroscopic MRI which allows spectroscopy based identification of various protein components within the healthy / pathological tissue. The ability of the spectroscopic MRI to differentiate amino acids contained in proteins may help in tissue characterisation and better diagnosis of pathological tissue states, such as brain edema, cancer and radionecrosis (Majós et al., 2004).

Echo-planar MRI (EP-MRI) is a functional MRI modality that is able to quantitatively map blood flow dynamics and, therefore, may complement better differentiation of highly vascularised tumor versus abnormal accumulation of fluid within the intracranial tissue (Noguchi et al., 1999). Furthermore, imaging of the functional activity of the brain in response to appropriate stimuli may also provide additional information on tumor differentiation (Okamoto et al., 2000). Due to utilisation of ultrafast image acquisition techniques, EP-MRI allows suppression of motion related arifacts commonly seen due to the rigid body movement.

1.3.3 Positron Emission Tomography (PET)

Positron emission tomography (PET) allows imaging of multiple metabolic features of brain tumors, such as blood flow, oxygen consumption, glucose intake and amino acid metabolism (Wong et al., 2002). Malignant brain tumors commonly display

increased levels of glucose metabolism, which can be detected by 18 Fluorodeoxyglucose (FDG) tracer. In PET, the image acquisition is performed after administration of radioactive glucose. Image quality is directly related on glucose uptake by the investigated area of the brain. FDG-PET images are often co-registered with MRI or CT scans for improving diagnostic accuracy, evaluation of tumor grade, and prognosis of tumor development. FDG-PET imaging can help in reducing the number of biopsy samples. FDG-PET is also used for evaluating residual or recurrent tumors.

1.3.4 Single Photon Emission Tomography (SPECT)

Preoperative thallium-201 single-photon emission computed tomography (SPECT 201-Tl) is useful for distinguishing benign from malignant brain lesions, predicting the histologic grade of brain tumors, and localising areas of maximum 201-Tl uptake for biopsy. There appears to be a correlation between early and delayed tumor uptake of 201-Tl and the subsequent grade of the surgically resected tumor, allowing a distinction between low and high grade astrocytomas. SPECT 201-Tl has not been as helpful as fluorodexoyglucose (FDG)-PET in distinguishing radiation necrosis from recurrent tumor (Biersack et al., 1991).

1.3.5 Summary

Palpation has been used for centuries by medical practitioners in routine clinical examinations. The fundamental idea behind palpation is that pathology would often be associated with change in tissue mechanical properties that can be detected by touch. In fact, many tumors and lesions are first detected during surgeries even after performing modern imaging examinations.

It has been shown, that pathological tissues, such as malignant lesions, have unambiguously different elastic properties compared to surrounding healthy tissue. Therefore, a method of non-invasive assessment of tissue mechanical properties would be of use and might add an additional valuable information to current diagnostic methods.

Although, advancements in conventional imaging techniques, such as CT, MRI,

and SPECT, make it possible to detect brain tumors, they are not capable of directly assessing their mechanical properties. This information about tumor composition would be extremely useful when planning neurosurgical procedures, as many tumors cannot be removed completely due to the lack of prior knowledge about their consistency. *In vivo* measurement of brain viscoelasticity is also crucial to the understanding of certain physiological and pathological cerebral processes.

1.4 Measuring mechanical properties of the brain

Because of the diagnostic potential of the brain stiffness information, assessment of the mechanical properties of brain tissue is an area of significant research and clinical interest (Braun et al., 2002; Fallenstein et al., 1969; Galford and McElhaney, 1970; Green et al., 2006; Hirakawa et al., 1981; Kruse et al., 2006, 1999; Lewa, 1991; Lewa and Certaines, 1995; McCracken et al., 2005, 2004; Miller and Chinzei, 2002; Muthupillai et al., 1995; Uffmann et al., 2005, 2004; Walsh and Schettini, 1976). However, the difficulties involved in working with an organ like the brain have so far prevented its mechanical properties from being adequately investigated. Assessment of brain stiffness requires an application of defined mechanical stress, which is naturally hampered by the shielding of the brain through the skull, cerebrospinal fluid (CSF), and meninges. Therefore, most of the measurements were obtained *in vitro* on dissected postmortem brain specimens (Arbogast and Margulies, 1998; Donnelly and Medige, 1997; Fallenstein et al., 1969; Miller, 2005; Miller and Chinzei, 2002; Shuck and Advani, 1972; Vappou et al., 2007) and there is no certainty whether they reflect the intact physiological environment of the brain.

The *in vivo* brain is a highly heterogeneous vascularised tissue, and there is a paucity of information regarding the effect of perfusion on brain mechanical properties. In fact, the mechanical properties of the brain *in vivo* may be also affected by the following components:

- The tissue component, determined by the corresponding properties of the cells, nerve fibers and vessel walls;
- The blood component, which affects changes in the volume of blood in the cerebral vessels and in the intravascular pressure level;

- The extracellular fluid component and the associated pressure level acting throughout the soft tissue matrix;
- The CSF component and associated ventricular pressure in the ventricles of the brain and the subarachnoid spaces.

These different effects might explain the inconsistent estimates of the shear modulus of brain tissue in the literature as shown Fig. 1.4 (Kruse et al., 2007).

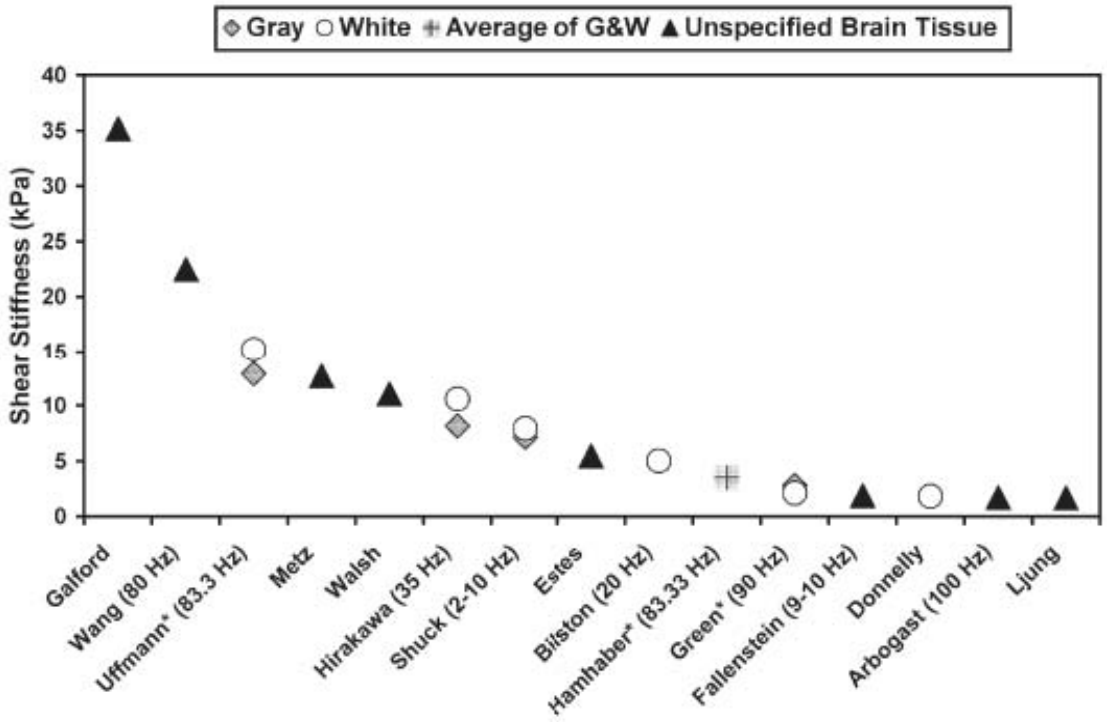

Figure 1.4 Summary of reported quantitative elasticity estimates of the brain *in vitro*, *ex vivo* and *in vivo* (denoted by *) obtained using different experimental protocols (Arbogast and Margulies, 1998; Bilston et al., 1997; Donnelly and Medige, 1997; Estes and McElhaney, 1970; Fallenstein et al., 1969; Galford and McElhaney, 1970; Green et al., 2006; Hamhaber et al., 2006; Hirakawa et al., 1981; Ljung, 1975; Metz et al., 1970; Uffmann et al., 2004; Walsh and Schettini, 1976; Wang and Wineman, 1972). Image courtesy of (Kruse et al., 2007)

Accurate quantitative estimates of brain mechanical properties may have useful applications for characterising various brain diseases. For example, Alzheimer's disease pathology is characterized by the development of senile plagues and neurofibrillary tangles (dysfunctional connections between neurones) over healthy brain cells throughout the intracranial tissue. Such processes might affect the mechanical

properties of cerebral tissue (Kruse et al., 2007). It has also been hypothesised that certain diseases, such as Normal Pressure Hydrocephalus (NPH), may be detected in the early stages by changes in the mechanical properties of the brain (Bradley Jr et al., 1991). Sack et al. (2007) proposed a hypothesis that widespread symptomatic changes in global brain viscoelasticity may be attributable to diffuse effects of neurodegenerative diseases such as Multiple Sclerosis (MS).

It has been demonstrated that Magnetic Resonance Elastography (MRE) can directly visualise and measure tissue elasticity (Kruse et al., 1999; Lewa and Certaines, 1995; Manduca et al., 2001; Muthupillai et al., 1995; Van Houten et al., 1999). MRE is a relatively novel imaging modality that allows noninvasive determination of the shear modulus of tissue *in vivo*. The MRE technique requires an application of acoustic or mechanical waves to tissue, conventional MRI system, and a sophisticated model inversion methodology to generate an elastic modulus map of the tissue of interest. Shear waves in the range of $50 - 200$ Hz are commonly used because their wavelength in tissue-like material is in the useful range of millimeters to tens of millimeters.

Utilising MRI for measuring the displacement field caused by acoustic waves and assessment of viscoelastic properties of tissue was first proposed by Lewa and Certaines (1995). This idea was further developed by Muthupillai et al. (1995) and continued by MR community (Jurgen et al., 2001; Manduca et al., 2001; Van Houten et al., 2001; Weaver et al., 2001). *In vivo* MRE has been successfully applied to reveal the stiffness of a variety human tissues and organs, such as muscle (Bensamoun et al., 2005; Gennisson et al., 2005; Papazoglou et al., 2006; Uffmann et al., 2004), breast (Lorenzen et al., 2002; McKnight et al., 2002; Plewes et al., 2000; Sinkus et al., 2005; Van Houten et al., 2002), liver (Asbach et al., 2008; Rouvière et al., 2006; Venkatesh et al., 2008) and the brain (Green et al., 2006, 2008; Klatt et al., 2007; Kruse et al., 2006, 2007; Sack et al., 2007, 2009; Wuerfel et al., 2010; Xu et al., 2007). Despite a number of attempts to characterise mechanical properties of the *in vivo* brain with MRE, an overall discrepancy in the obtained results indicates limitations of existing mechanical models to perform accurate reproducible measurements of brain viscoelastic properties.

MRE has also been used to study the mechanical properties of lungs (Goss et al., 2006a; McGee et al., 2007), kidneys (Manduca et al., 2001; Shah et al., 2004), heart (Elgeti et al., 2008; Sack et al., 2008), connective tissue (Chen et al., 2008; Lopez

et al., 2008), blood vessels (Zheng et al., 2007) and high-resolution microscopic studies for assessments of the mechanical properties of developing tissues (Othman et al., 2005).

Most MRE work to date has been performed upon breast lesions. In breast cancer imaging, MRE was able to capture the macroscopic alterations associated with abnormal and uncontrolled cell division in the tumors and may, therefore, overcome some of the limitations of conventional palpation (Sinha and Sinha, 2009). In fact, palpation is a subjective technique and can only identify surface lesions that are at least 8-10 mm in diameter (McKnight et al., 2002). In contrast, MRE is able to non-invasively delineate tumors throughout the healthy breast tissue .

Various MRE studies have also been performed to quantitatively assess viscoelastic (VE) properties of the liver (Asbach et al., 2008; Rouvière et al., 2006; Venkatesh et al., 2008). In fact, the first well-established clinical application of MRE was evaluation of liver diseases, such as *hepatic fibrosis*. It has been suggested that hepatic MRE should be included among the morphological and perfusion imaging procedures used to detect liver cancer and steatosis and assess liver function (Venkatesh et al., 2008). However, do date, MRE is still not an established clinical modality.

MRE applications for prostate pathology are also rapidly evolving. Recent MRE studies (Chopra et al., 2009; Kemper et al., 2004) attempting to investigate the mechanical behavior of prostate tissue and to define elastographic features of the prostate have shown this technique to be a promising imaging tool.

In vivo measurements of the elastic properties of muscle could help evaluate muscle diseases early as well as during follow-up. Ultrasound elastography has been used to measure muscle elasticity but only within a limited range (Uffmann et al., 2004), whereas MRE enables the entire muscle to be studied and has no limitations in terms of penetration depth or the maximum resolvable field of view (Papazoglou et al., 2006). Although MRE is not yet used clinically, it does offer a unique means of measuring muscle tissue elasticity and there are already reports demonstrating significant differences in patients with paraplegia and a history of poliomyelitis.

MRE of the brain may be effective in diagnosing conditions, such as meningitis, traumatic head injury, Alzheimer's disease, NPH, and intraventricular hemorrhage. Valid VE moduli of the brain are also necessary prerequisites for finite element

analysis (FEA) studies of brain trauma (Bayly et al., 2006; Brands et al., 2004; Pena et al., 2005) and in the development of neurosurgery simulation techniques. Hence, there are several potential uses of MRE for the brain beyond tumor or cancer diagnosis.

Once healthy physiological material property ranges are known, MRE could be used to detect anomalies in tissue stiffness that may indicate the presence of tumors or other diseases (Srinivasan et al., 2004). Furthermore, MRE seems to be capable of pre-operative evaluation of the consistency of a brain tumor (Uffmann et al., 2005; Xu et al., 2006). Knowledge of the consistency of a meningioma, in addition to its vascular and histopathological characteristics, could help in planning a surgical strategy, particularly in patients with a tumor at the base of the skull-base or encasing cranial nerves and major blood vessels. An imaging method capable of reproducing these different elastic properties would provide useful detailed information concerning the composition of the lesion and the boundary between it and normal tissue (Scholz et al., 2005).

1.5 Summary

Pathological tissues have long been recognised to display markedly deferent mechanical properties compared to the surrounding healthy tissues. None of the conventional imaging modalities, such as MRI, CT or PET / SPECT are able to directly assess tissue elasticity which would be extremely useful when, for example, planning surgical procedures. For instance, lack of initial knowledge about consistency of the intracranial tumors can complicate neurosurgical procedure and obstruct accurate tumor resection. Therefore, a method able to quantitatively map tissue elasticity might bring valuable diagnostic potential in evaluation of a number of diseases, pathologies, tumors and neurological illnesses.

Recently, a number of methods has been developed to assess tissue elasticity. The basic principle of all elasticity imaging methods is based on tissue excitation followed by measurement of a concomitant tissue response. Depending on the type of excitation used, elasticity methods can be categorised into dynamic and static as well as internal and external. On the other hand, based on physical phenomenon used to capture resulting tissue response, the detection methods are classified into

US, NMR and acoustic.

MRE is an evolving elasticity imagining modality that utilises phase-contrast MRI techniques extended with the motion encoding gradients (MEGs) to visualise propagating acoustic waves and measure global displacements within the tissue subjected to a time-harmonic actuation. MRE allows non-invasive quantitative assessment of tissue elasticity and have been applied to image mechanical properties of the liver, muscle, lungs, heart and even the brain.

However, large variations in the obtained values measured by MRE indicated that it has been unsuccessful in accurate and reproducible non-invasive measurement of brain tissue mechanical properties. The variation of the results might also be affected by the following factors: difficulties in efficiently generating acoustic waves inside the cranium due its natural shielding by the skull, CSF and meninges; different inversion methodologies used, different actuation frequencies, complex intracranial boundary conditions and fundamental limitations of the biomechanical models to account for such a complex, heterogeneous and orthotropic media like the brain.

Measurement of mechanical properties of the brain could provide significant clinical merit and complement existing imaging modalities to enhance diagnosis of the brain in a pathological state. Accurate quantification of brain elastic properties requires a biomechanical model that is able to accurately match the observed response. The consistency of the brain has been evaluated using a number of constitutive models, however most of them were unsuccessful in accurately reflecting brain's rheology. An overview of the constitutive models used for approximation of brain structural mechanics is given in Chapter 2.

This thesis thoroughly investigates an alternative biomechanical model, known as *Rayleigh damping* (RD) material model, able to quantitatively map both elastic and damping properties of the material based on two different attenuation mechanisms. Since mechanical properties of the biological tissues are dramatically affected by the presence of the pathological changes, the ability of the RD model to quantitatively assess damping behaviour might bring additional diagnostic potential and help in early detection as well as more accurate characterisation of the brain tumors.

Chapter 2

Anatomy and constitutive models of the brain

2.1 Anatomy of the human head

The human head is a very complex structure. It is made of solid components, such as skull, meninges, brain, blood vessels, and fluidic components, such as cerebrospinal fluid (CSF), blood and microstructural fluids underlying soft tissue matrix. Fig. 2.1 illustrates MRI images of the human head.

The outermost layer of the head is known as the *scalp*. It is comprised from multiple layers of skin, connective tissue, and pericranium. The thickness of the scalp normally ranges from 3 to 6 mm. The scalp is firmly adhered to a rigid anatomical structure, known as the *skull*. The skull encapsulates the brain throughout and provides protection from external mechanical influence. The only place where the skull does not enclose the brain is in the junction between spinal cord and the brain. *Meninges* are the next inward structure that separate the skull from the brain. The gap between layers of meninges is called *subarachnoid space* and it is filled with the CSF. CSF is also present in multiple intracranial cavities and channels within the brain and circulates through the ventricular system. The rigid component of the human head (skull) does not influence mechanical properties of the intracranial matter. Therefore, a more detailed description of the anatomy and physiology of the brain, meninges and the ventricular system is given in this chapter.

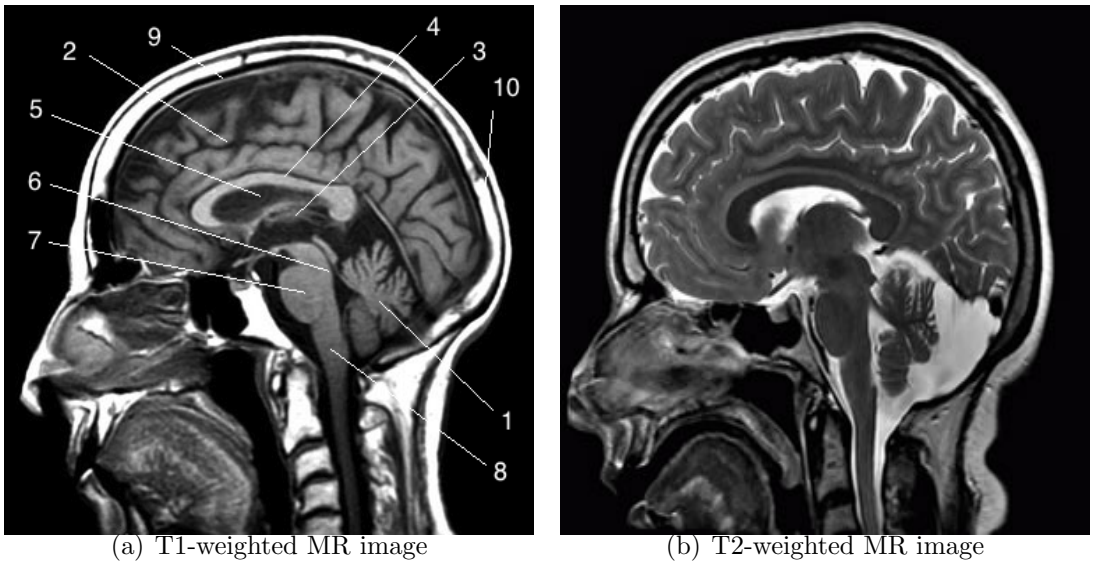

(a) T1-weighted MR image (b) T2-weighted MR image

Figure 2.1 MR images of the human head depicting anatomical atlas. (a) T1-weighted image of the human head illustrating its main structures: 1 - Cerebellum, 2 - Cerebrum, 3 - Thalamus, 4 - Corpus Callosum, 5 - Lateral Ventricle, 6 - Mid Brain, 7 - Pons, 8 - Brain stem, 9 - Meninges, 10 - Skull. (b) Corresponding T2-weighted image of the human head. Image courtesy of the Oxford Centre for Functional MRI of the Brain (OXCFMRI, 2013).

2.1.1 Anatomy and physiology of the human brain

The human brain is highly heterogeneous orthotropic complex organ that consist of multiple components. It is made of four major structures: the *cerebrum*, the *cerebellum*, the *brain stem* and the *basal ganglia*. The cerebrum is made of two cerebral hemispheres. Cerebral hemispheres can be divided into four major parts: temporal lobe, frontal lobe, parietal lobe and occipital lobe. Cerebral hemispheres are connected through the *corpus callosum*. The surface of the cerebral hemispheres contains cortical folds, also knows as *sulcus*, and smooth transitions between the folds, *gyrus*. Other anatomical structures of the brain include a network of interconnected fluid-filled ventricles, hypothalamus, thalamus, pituitary gland, and many others. These structures are shown in Fig. 2.2.

Human brain is the centre of the nervous system and is made up of large number of cells. There are two types of cells in the brain: nerve cells (*neurons*) and a variety of supporting cells (*glial cells*) (Nolte, 2009). *Neurons* are the cells excited by electrical impulses. Billions of neurons create an interconnected network through

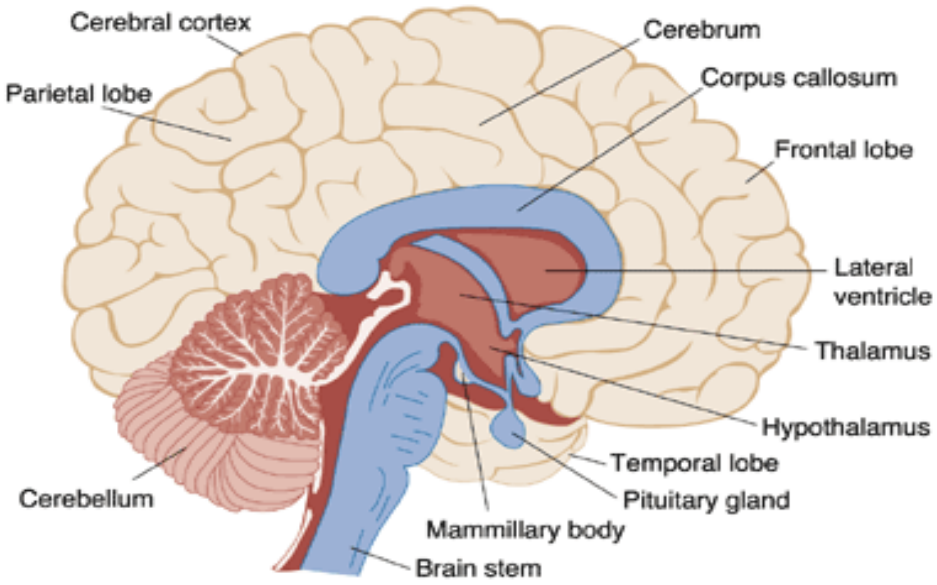

Figure 2.2 Schematic representation of the anatomy of the human brain. Source: (Welsh, 1997)

which information is transmitted and processed within the brain.

A typical neuron cell consists of three major components: *dendrites*, the *cell body*, and *axons*, as shown in Fig. 2.3. The central part of the neuron is a cell body, also known as the *soma*. It contains the nuclei of the neuron and is responsible for metabolic processes within the cell. Dendrites are cytoplasmic extensions with multiple branches. They arise from the cell body, forming a so called dendritic tree which serves as a communication input for a particular neuron. Lastly, axons are a communication output of the neurons. They support transmission of the electrical signals away from the soma and passing them to surrounding neurons, thus enabling communication with other cells. On the other hand, *glial cells* serve various supporting roles, such as holding neurons together and providing supply of various nutrients and oxygen (Purves, 2012).

With regards to mechanical properties of the brain, it has long been recognised as a soft, highly non-linear viscoelastic solid characterised by high strain-rate sensitivity (Bilston et al., 1997; Fallenstein et al., 1969; Galford and McElhaney, 1970; Hirakawa et al., 1981; Pamidi and Advani, 1978; Shuck and Advani, 1972). Generally, stiffness of the brain increases with increase of strain rate. Furthermore, regional variation

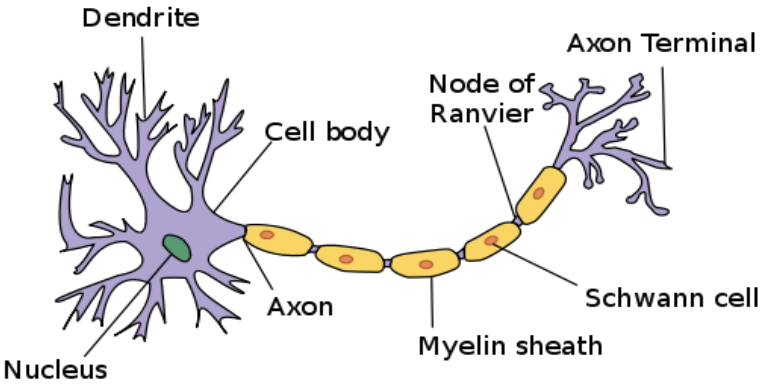

Figure 2.3 Structure of a typical neuron. Each neuron consists of three basic parts: a cell body (soma) that contains the nucleus; one or more dendrites, which are short branches off the body that receive incoming impulses; and a single, long axon that carries impulses away from the body and to the next neuron. Image courtesy of the New World Encyclopedia (Encyclopedia, 2013)

in mechanical properties of the intracranial matter has been also suggested by a number of studies (Kyriacou et al., 2002; Margulies and Prange, 2002; Miller and Chinzei, 1997; Prange et al., 2000).

Depending on the structural alignment and composition of the cells, intracranial matter can be categorised into *gray matter* and *white matter*, as shown in Fig. 2.4. Gray matter occupies outer surface of the cerebral cortex and is mainly comprised of cell bodies, dendrites and unmyelinated axons, and supporting capillary network. Alternatively, white matter consists of directionally-depended myelinated axons and supporting glial cells. Amount of myelin determines the color characteristics of the matter.

The brain may exhibit regional anisotropic behaviour due to the underlying microstructure. White matter was found to be anisotropic due to the structural composition of axonal fiber bundles (Prange et al., 2000). Some studies showed that white matter has twice as high a stiffness along the axonal fibre direction compared to perpendicular direction under shear deformation and in tension. However, other studies have not confirmed varying stiffness distribution in white matter under compression (Bilston et al., 1997).

Previously reported results are generally consistent with the fact that cerebral white matter is stiffer than gray matter *in vivo* (Kruse et al., 2007; McCracken et al., 2005; Uffmann et al., 2004; Xu et al., 2007). However, Nagashima et al. (1990)

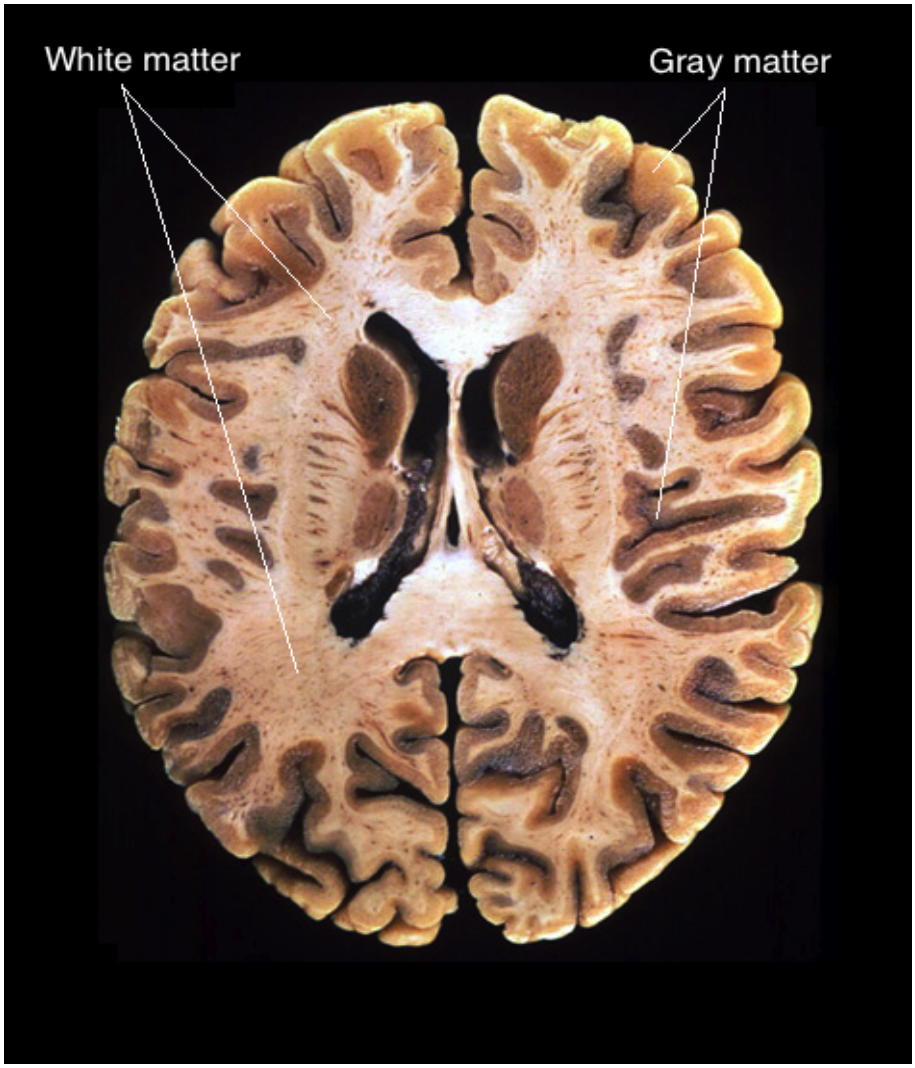

Figure 2.4 Human brain in transverse plane, illustrating white and gray matter of the cerebral hemispheres surrounding the internal structures and ventral surface. Photo by Ralph Hutchings. Source: (Hutchings, 2013)

assumed gray matter to be stiffer than white matter for an FE of brain oedema, and Green et al. (2008) found even more contrast in stiffness with MRE. This affirms that while there is not currently a definite way to confirm brain's stiffness estimates *in vivo*, there is distinct difference in the elasticity of gray and white matter. Rapid attenuation of wave propagation towards the centre of the brain was studied by Kruse et al. (2007) in 25 healthy adult volunteers and the trend observed was that of increasing wavelength. This is indicative of the shear wave travelling through increasingly stiffer media. Anisotropy of brain tissue might be one of the reasons in varying results across a wide range of mechanical tests.

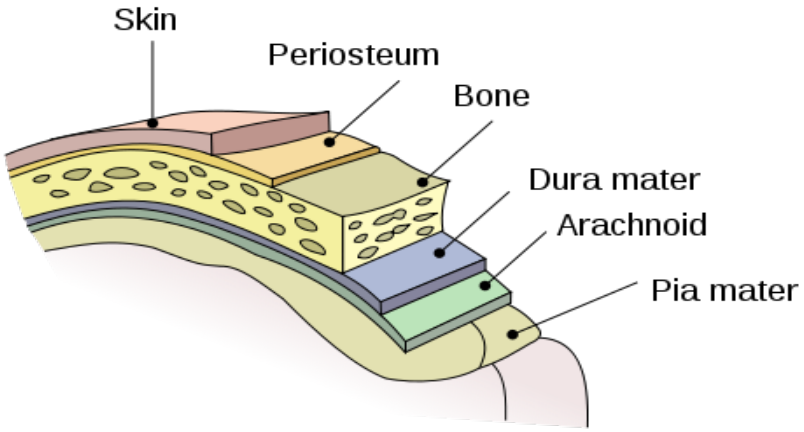

Figure 2.5 Diagrammatic representation of meninges. Image courtesy of the US National Cancer Institute (Institute, 2013)

2.1.2 Meninges

The brain is surrounded by a system of membranes called *meninges*. The latter is comprised of three layers: the outermost *dura mater*, the intermediate *arachnoid mater*, and the innermost *pia mater*, as seen Fig. 2.5. The meninges stabilise the shape and the position of the brain, and protect it from external impact. The brain is anchored to the skull via the layers of meninges that constrain the movement of the brain. Moreover, the space between arachnoid and pia mater is filled with CSF which suspends the brain (Nolte, 2009).

The *dura mater* is the outermost layer which is adjacent to the inner surface of the skull. It forms a tough collagenous membrane comprised from a fibrous connective tissue (Weller, 2008). The thickness of dura mater ranges from 0.3 to 1 mm (Vandenabeele et al., 1996). Dura mater infolds itself in multiple areas, creating a number of dural reflections. Dural reflections include: *falx cerebri*, which separates the cerebral hemispheres; *tentorium cerebelli*, which separates the occipital lobes from cerebellum; and *falx cerebelli*, which separates the cerebellar hemispheres. The structures of the falx cerebri and tentorium cerebelli are shown in Fig. 2.6. The dura mater also contains some large blood vessels that diverge into multiple branches creating large capillary trees in the pia mater.

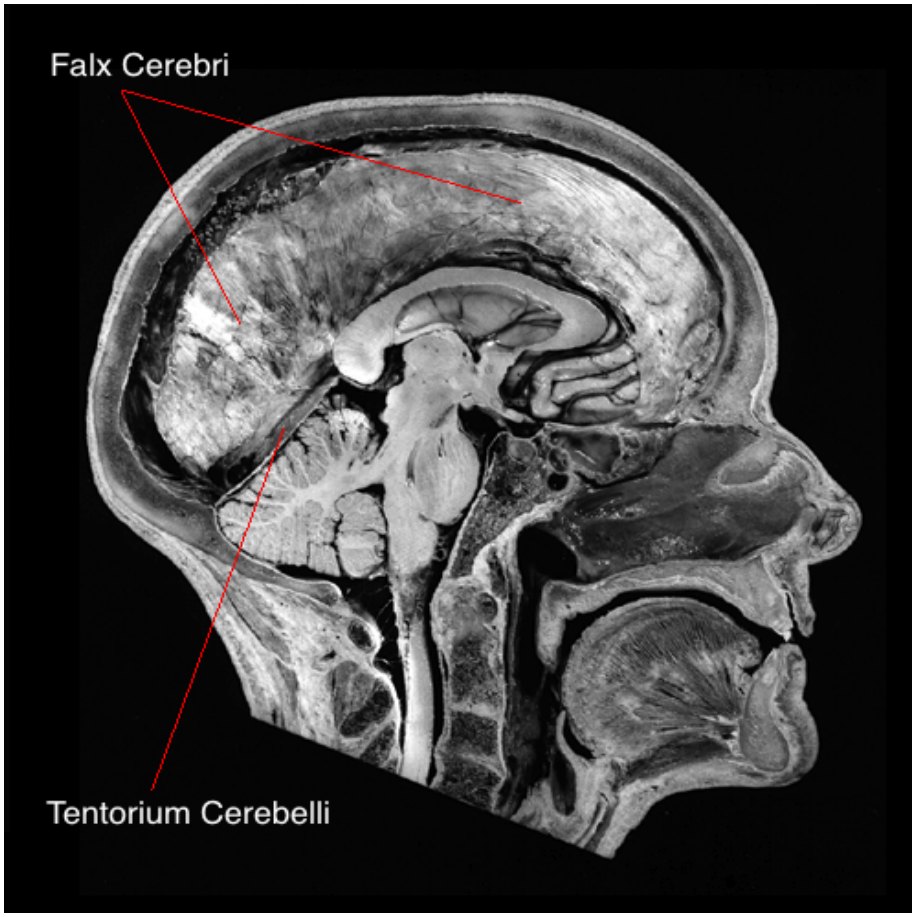

Figure 2.6 T1-weighted MR image of the human brain illustrating infolding of dura matter in the areas of falx cerebri and tentorium cerebelli. Image courtesy of University of Iowa Hospitals & Clinics. Photo by Paul Reimann, receipt of BPA Medical Education Award (Reimann, 2013).

Several studies have attempted to investigate the mechanical properties of the dura mater. Biomechanically, the dura mater may be classified as a viscoelastic material due to the underlying microsturctural composition (Galford and McElhaney, 1969). Wilcox et al. (2003) studied time-dependant viscoelastic properties of the dura mater in the longitudinal and circumferential direction. Patin et al. (1993) observed relaxation in the dura mater which was attributed to the viscoelastic behaviour. Significant differences were also observed between human and canine dural properties.

The *arachnoid mater* is a middle membrane, comprised from a few layers of cells which give it a semitransparent appearance. The consistency of the arachnoid mater also gives its impermeability to fluid. The outer surface of the arachnoid mater is attached to the inner surface of the dura mater. Unlike the pia mater, the arachnoid layer does not fully follow convoluted surface of the cortex, however it generally covers the shape of the brain, providing a cushioning effect. The gap between the arachnoid mater and the pia mater is called the *subarachnoid space* and filled with the CSF.

Lastly, the *pia mater* is an extremely thing layer that follows the main topographical features of the brain's surface. Generally, pia is only one cell thick. It also contains large amount of capillary trees branching out from larger blood vessels located in the dura mater. This capillary network descends further into the brain and spinal cord providing necessary transport of nutrients and oxygen.

2.1.3 Ventricular system

The cerebral ventricular system is a set of interconnected fluid-filled cavities, chambers and spaces within the brain. The main purposes of the ventricular system are protection of the brain from trauma and transport of CSF. The ventricular system includes four ventricles: the right and left *lateral ventricles*, the *third ventricle* and the *fourth ventricle*. The lateral ventricles are located in the cerebral hemispheres and connected to the third ventricle through the *interventricular foramina* at the midline of the brain. The third ventricle communicates with the fourth ventricle via the narrow *cerebral aqueduct* in the brain stem. From the fourth ventricle, the CSF flows into the the central canal of the spinal cord where it is further transmit-

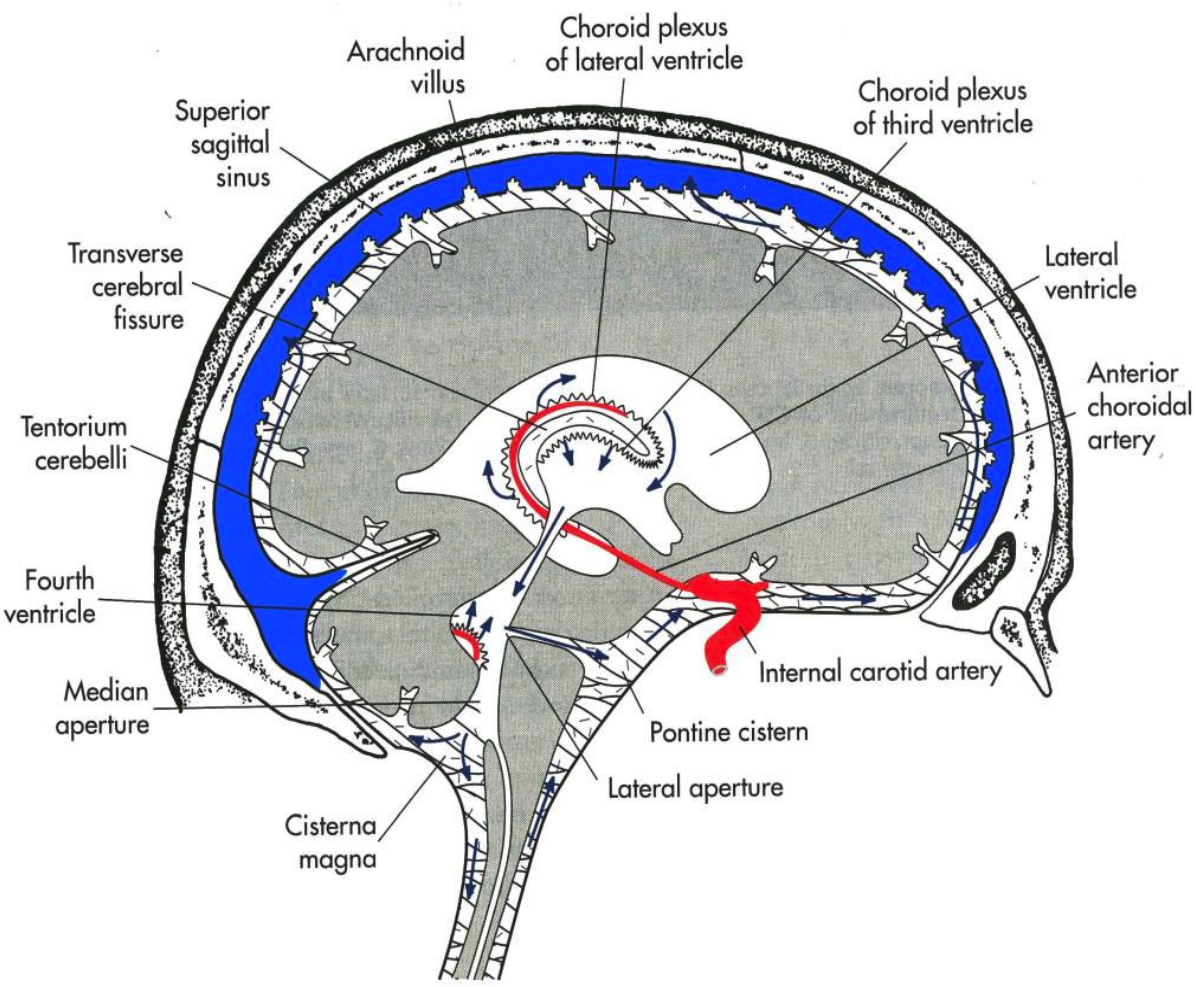

Figure 2.7 Path of circulation of CSF in the ventricular system of the brain. Source: (Ozan, 2008).

ted to the subarachnoid space by the pressure gradient. Circulation of CSF in the ventricular system is illustrated in Fig. 2.7 (Nolte, 2009).

CSF is a clear and colorless fluid produced by specialized tissue in the *choroid plexus* of the brain. Bloomfield et al. (1998) performed studies on viscosity measurements of CSF over a range of the shear strain rates. It was found that total protein and blood cell content did not significantly affect the viscosity of the CSF. Thus, CSF was concluded to be a clearly Newtonian viscous fluid, with its viscosity at 37 degrees of 0.7 - 1 mPa.s. This leads to a nearly zero elasticity and a loss modulus $\mu_I = \omega\nu = 0.5\ kPa$ (Green et al., 2008).

2.2 Constitutive models for brain tissue mechanics

Modelling brain tissue mechanical behaviour is an extremely complicated and demanding task. Existing constitutive brain tissue models have been unsuccessful in characterising the exact brain rheology (Dommelen et al., 2009). These models are intended for the quantification of material behavior under various loading scenarios. Often the selection of a suitable model is determined by combining the observed response and known key material properties such as its histology, composition and structure.

For brain tissues, mechanical behaviours are modelled according to the required conditions, with emphasis on the strain rate magnitude. Depending on the required application and specification, varying constitutive settings would be necessary for the same material. Hence, the time scale characteristic plays a vital role in the selection of the material model.

An ideal constitutive model would be able to give a reasonable approximation of the brain tissue behaviour in tension, compression and shear deformation. A number of constitutive equations have been applied to investigate brain mechanical response. However, there is no accepted gold-standard constitutive model that is able to incorporate a full spectrum of a non-linear, strain-rate dependant, viscoelastic behaviour observed in the brain tissue.

Here, we mainly consider elastic, viscoelastic, and poroelastic (or mixture theory) constitutive relations. An elastic behavior may be defined as one in which the stress state depends only on strain; a viscoelastic behavior may be defined as one that the stress state depends both on strain and strain history. A poroelastic behavior may be defined as one that results from two or more phases, with a porous elastic solid immersed in a viscous fluid. The overall deformation is dependant on resistance of a fluid-flow due to a pressure gradient through a network of interconnected pores.

There are very few existing FE brain tissue models with each designated for very specific loading conditions only. In the 1970s, there was a demand to better understand brain's mechanical behaviour during a physical trauma and the consequent adverse effects. For simulation purposes, the cranium was subjected to high accel-

eration ending with a sudden deceleration ("impact"). The brain model by Engin (1969), which modelled the brain as an inviscid compressible fluid, was suitable for the analysis of compressive wave damages.

However, Fallenstein et al. (1969), stated that the brain was viscoelastic, quoting previous experimental work on various species of brain tissue. Studies by Galford and McElhaney (1969) found out of phase force and displacement in the brain tissue implying damping was present. The viscoelasticity of brain was further confirmed by the in-phase association in an elastic solid and the 90 degrees out-of-phase association of viscosity. Viscoelastic characteristics were also observed in brain during creep and relaxation.

For head trauma modelling, experimental data were collected by Estes and McElhaney (1970) to establish the brain tissue constitutive relations. Using these data on human brain tissue, Wang and Wineman (1972) proposed a linear viscoelastic model, but Pamidi and Advani (1978) applied non-linear constitutive relations. Apart from the viscoelasticity assumption (Sahay et al., 1992; Walsh and Schettini, 1984), other studies have assumed the brain to be a linear, isotropic and homogeneous material. In addition, linear viscoelastic (Bandak et al., 1995), or nonlinear viscoelastic (Bilston et al., 1997; Donnelly and Medige, 1997) models were applied to study falls or vehicular accident brain trauma in 1990's.

A single-phase non-linear viscoelastic continuum model was used by Miller and Chinzei (1997) in both quasi-static and fast processes for an approximation of brain tissue behaviour. Further studies by Miller's group (Miller and Chinzei, 2002; Miller et al., 2000) attempted to prove that the hyper-viscoelastic model based on the strain energy function in polynomial form with time-dependent coefficients, was suitable for description of brain tissue deformation behaviour *in vivo* at low strain rates which is typical for surgical procedures. It was also concluded that to obtain near perfect reproduction of the experimental curve *in vivo*, only slight adjustment to the stiffness parameter was necessary without altering the structure of the model.

Investigation of the loading conditions applied to quasi-static processes, such as found in neurosurgical retraction or brain removal during surgery; and neuropathological processes, such as hematomas, hydrocephalus and hemorrhage, required a second line of inquiry in brain tissue modelling. This inquiry involved more sophisticated and detailed representations of the brain. Depending on the application,

mainly poroelastic (Basser, 1992; Kaczmarek et al., 1997; Miga et al., 2000, 1998a; Paulsen et al., 1999; Pena et al., 1999), viscoelastic (Bilston et al., 1997; Donnelly and Medige, 1997; Green et al., 2006, 2008; Kruse et al., 2007; Miller et al., 2000; Nagashima et al., 1990; Pamidi and Advani, 1978; Sack et al., 2007) or linear elastic (Ferrant et al., 2000; Škrinjar et al., 2001; Walsh and Schettini, 1984) and even nonlinearly elastic models (Sahay et al., 1992) were used to simulate the quasi-static processes.

An FE based poroelastic computational model was suggested by Paulsens group (Miga et al., 2000, 1998a; Paulsen et al., 1999) to estimate intracranial tissue motion in computer-assisted stereotactic surgery. Based on multi-phase consolidation theory, this model considers the brain to be a sponge-like material in which tissue motion is characterised by an instantaneous deformation of the contact area plus pressure gradient induced deformation resulting from exiting pore fluid. For similar application, Ferrant et al. (2000) had used a linear elastic material and linear strain; and Škrinjar et al. (2001) had instead used both a linear mass spring (discrete) model and a linear (both material and strain linearity) elastic continuum model.

Nagashima et al. (1990) used a linear material and linear strain with a poroelastic 2D FEM theory which allowed the modelling of edema and hydrocephalus. The biomechanics of hydrocephalus and other structural neurologic diseases was studied numerically by Neff *et al.* Kaczmarek et al. (1997) using similar model but with a nonlinear strain definition and a linear material. Additionally, using material properties, boundary conditions and image intensities, brain biomechanics has been used in successfully matching / registering brain volumes of two different individuals.

Valid estimation of mechanical properties of the brain requires a biomechanical model that can provide an accurate description of the mechanical behaviour of brain tissue. To date, reconstruction approaches generally assume tissue to be purely elastic, although some groups have employed more advanced models such as viscoelasticity (Green et al., 2008; Kruse et al., 2007; Sack et al., 2007) and even poroelasticity (Perriez et al., 2010). However, none of the constitutive models have been able to accurately characterise brain tissue behaviour (Dommelen et al., 2009). Inconsistent and contradictory results reported in the literature suggest the use of a more sophisticated biomechanical models.

Viscoelasticity (VE) is typically used to model impact (Hirakawa et al., 1981).

Poroelacticity and combined theory for interstitial fluidity are used to model hydrocephalus and similar long term processes (Miga et al., 2000, 1998a; Paulsen et al., 1999). While VE models are believed to give a reasonable approximation of damping characteristics for viscous solids, poroelasticity is assumed to be a better model for fluid-saturated porous biological tissues due to direct de-coupling of the mechanical properties of solid tissue structure matrix from those related to fluid component and associated fluid pressure (Perriez et al., 2010). Thus, although the VE model contributes to the observed deformation behavior, it does not explicitly account the fluid-phase present *in vivo*. Lastly, an elastic based model would be just as adequate for image registration purposes (Ferrant et al., 2000).

Appropriate implementation of the damping effects can improve model accuracy (McGarry et al., 2007). In biological tissue, these effects arise from a complex interaction between microstructural elements of the tissue. However, most constitutive models have a continuum based formulation and therefore treat complex micro-heteregenous tissue structure as a continuum. Development of the appropriate model for a reasonable approximation of the attenuation behaviour within the tissue requires a proportional scaled combination of damping aspects that contribute to an overall damping profile.

Rayleigh Damping (RD) or *proportional* damping is an alternative model for soft tissue attenuation for elastic materials which incorporates attenuation behavior proportionally related to both elastic and inertial forces. In contrast, the majority of viscoelastic damping models commonly used in elastography consist of only a complex shear modulus and thus only a single damping parameter. The inertial damping effects are modelled through the use of complex density where the imaginary term represents the attenuation coefficients. Equally, viscoelastic damping effects are approximated via the complex valued shear modulus with real and imaginary terms representing storage and loss modulus respectively. The RD model is believed to provide a more accurate description of elastic energy attenuation in the tissue (McGarry and Van Houten, 2008).

The motivation that supports this research arises from a current lack of available MRE methodologies for performing accurate and reproducible measurements of mechanical properties of the *in-vivo* brain. This issue is driven by attenuation of shear waves inside the skull due to strong viscosity of the brain tissue, and the limitations of the existing inverse problem techniques to account for the heteroge-

neous, orthotropic, viscoelastic media like brain tissue. Therefore, the aim of this project is the establishment of the MRE using a RD material model for the human brain. A number of experiments must be performed to obtain accurate information on viscoelastic brain tissue behavior in relation to the RD material model.

In addition, current brain actuation methods are not patient-comfort friendly and generally not well suited to clinical application due to technology complexity and device non-portability. Most mechanical drivers are mounted to bite bars with individual denture molds (Green et al., 2006; McCracken et al., 2003; Uffmann et al., 2005; Xu et al., 2006, 2007). The mouse-piece is then vibrated at a specific frequency via some form of mechanical actuator. Well trained subjects can tolerate this procedure for a moderate duration up to 20-30 minutes. Another design is a head rocker actuator containing carbon fiber rod of variable length (2-3 meters) that couples the centre of the loudspeaker membrane on one end and a head rocker on the other end (Klatt et al., 2006, 2007; Sack et al., 2007). For this purpose, a new pneumatic actuator design, as an alternative to an electromechanical actuator used in previous MRE brain studies, has been developed.

MRE based on the RD material model is believed to have potential for the noninvasive *in vivo* determination of mechanical properties of the intracranial tissue. Each year, doctors in the New Zealand diagnose approximately 250 new primary brain tumors, and 1500 new secondary brain tumors. As tumor tissue commonly displays a shear modulus up to 100 times that of a normal tissue, the MRE method is believed to provide important information for effective brain tumor recognition. Also, an ability of the RD model to measure viscous tissue behavior can be used for differentiating benign and malignant intracranial tumors. The current identification process in clinical practice requires removal a small piece of the tumor for biopsy. Frequently this can be done with a needle through a small hole in the skull, a procedure known as stereotactic biopsy. Obviously, the noninvasive MRE approach would be a significant improvement over the current clinical diagnostic procedure.

2.3 Important considerations in development of *in vivo* constitutive models for the brain

When modelling the brain tissue, some important aspects must be considered, such as:

- Compressible vs. incompressible material behavior;
- Fluid vs. solid approach;
- Differentiating between gray and white matter properties;
- Effect of tissue weight, fluid filled cavities (ventricles, subarachnoid space) and falx/tentorium, and the issue of mesh generation.

2.3.1 Compressible vs incompressible model

Like most soft highly saturated biological tissues, brain tissue is typically assumed to be incompressible or nearly incompressible due to the high water content. The brain tissue also mainly exhibits incompressible behaviour in impact situations, yet exhibits compressible behaviour in long duration processes, such as hydrocephalus or mass lesions, involving interstitial fluid flow throughout brain parenchyma (Kaczmarek et al., 1997). Although fluid movement and subsequent local volume changes are apparent in fluid brain cavities, such as the ventricles, subarachnoid space and their interconnections (Sarron et al., 2000), the ventricular and subarachnoid cavities are not included in many existing brain models. Thus, it is conservative to use a compressible material behaviour.

In retrospect, volume change was not observed in the 1-D compression experiments by Miller and Chinzei (1997). However, due to the technical constraints rigorous measurement of the volume change was not possible. Using swine brain tissue, the Miller et al. (2000) model invokes incompressibility to simulate the deformation for quasi-static surgical manipulations.

By definition, the poroelastic model is compressible in an aggregate sense even if its constituents are incompressible and thus allows movement of fluid. Where fluid

movement is irrelevant, a relatively simpler viscoelastic model is more effective, compared to a poroelastic model, for the estimation of an appropriate viscoelastic compressibility term through simple simulations of the poroelastic model.

Various research teams have worked on compressibility constants. Tenti et al. (1999) had used a linear poroelastic material properties to calculate a dry Poissons ratio ν=0.4 partly based on the reevaluation of the data by Metz et al. (1970). Using an approximate value of ν=0.45 from a range that minimised errors in their experiments, Miga et al. (1998b) used an inflated balloon inside a swine brain and measured the displacement of the inserted beads.

Alternatively, a linear elastic material with the possibility of viscous component was used by Guillaume et al. (1997). The findings were that a ν=0.35 gave the best agreement with bovine brain based hypergravity experiments. To minimize errors between intraoperative data and calculated data, Škrinjar et al. (2001) used varying ν values and concluded that ν=0.4 gave the optimal results. Nevertheless, there is still a lack of rigorous experimental work in estimating either *in vitro*, or even more importantly, *in vivo* brain tissue compressibility.

2.3.2 Fluid vs solid model

Since brain tissue has no long term elastic modulus, Bilston et al. (1997) referred to it as a fluid. This was supported by Shuck and Advani (1972) who concluded that viscoelastic fluid behaviour better represents the brain material behaviour compared to that of viscoelastic solid. However, this conclusion was refuted by Donnelly and Medige (1997) who discovered that deformed brain tissue is able to return to a defined shape when immersed in the saline solution, thus requiring a solid model. However, this characteristic was not applicable when the tissue was removed from the saline solution.

Since fluid models are not yield associated, the yield properties of brain tissue further strengthens the solid model theory Shuck and Advani (1972). These apparent disagreements could be due to the fact that data in Bilstons experimental range had a modulus of approximately 800 Pa. Meanwhile, Millers's data had a much smaller strain long term modulus of approximately 500 Pa.

The other possibility is the elastoplastic material constitutive model. This model supports the contradiction that brain tissue behaviour is that of an elastic solid when immersed in saline and that of fluid when not immersed in saline. When not in saline, the tissue experiences gravitational forces that could be larger than the elastoplastic yield point. Therefore, the tissue behaviour is fluid under such conditions.

2.3.3 Gray vs white matter elastic properties

The white matter mainly consists of axonal fiber bundles suggesting structural anisotropy. Bilston et al. (1997) stated that some studies found similarities between the elastic properties of the white and gray brain matter. However, some other studies found differences. Nagashima et al. (1990) had assumed a conservatively stiffer (10-fold) gray matter with no justification. Kaczmarek et al. (1997) had used the lowest strain tests results performed by Metz et al. (1970) as elastic behaviour for both the white and gray matter. Nevertheless, a sensitivity analysis simulation with the gray matter was also attempted with increasing stiffness values ranging from that of the white matter and ending with a stiffness four times larger, on the expectation that the gray matter is indeed stiffer than the white matter. While investigating the effect of regional, directional, and species effects on brain mechanical properties using fresh swine brain tissue, Prange et al. (2000) found that the gray matter (thalamus) is about 30 % stiffer than the white matter (corona radiata and corpus callosum).

Directional dependence of stiffness was also observed in the white matter which was approximately 70% stiffer in the second direction. This outcome held to a much lesser extent in gray matter, which was approximately 10% stiffer in the second direction. In view of this anisotropy, the white matter stiffest direction may be relatively stiffer than the gray matter stiffest direction. Margulies and Prange (2002) studied the anisotropy of the gray and white matter at large strains and found that white matter exhibited higher anisotropy (31 - 48% difference) compared to gray matter (10% difference) which was found nearly isotropic. Studies performed by Arbogast and Margulies (1998) on anisotropic properties in three orthogonal directions of the brainstem in 2.5% dynamic sweep experiments confirmed difference of up to 30%.

Manduca et al. (2001) concluded that MRE indicated a relatively stiffer white matter (average shear stiffness of 14.2 kPa) compared to gray matter (average shear stiffness of 5.3 kPa). In place of dynamic, time-harmonic MRE, McCracken et al. (2005) applied transient-based MRE to measure *in vivo* brain mechanical properties. The feasibility of measuring brain stiffness *in vivo* using a transient mechanical excitation was demonstrated. A white and gray matter shear stiffness of 12 kPa and 8 kPa were observed respectively. Though the Prange et al. (2000) work seems most convincing, there is still significant scope for further investigation.

2.3.4 Effect of gravity and CSF submersion

Due to the very low stiffness of the brain tissue, the gravitational force is a key factor in modelling mechanics. The brain is submerged in CSF in physiological conditions and thus its weight is neutralised by the buoyant fluid pressures (buoyant force). This aspect is vital for neurosurgical navigation during open skull surgery, and the loss of CSF is a dominant factor in inducing a deformation average of 10 mm namely along the direction of gravity. This clearly indicates the importance of the brain weight for modelling and for compression experiments for determining material properties, especially when full sized brain are analysed.

2.4 Mechanical parameter estimation in MRE

There are many approaches applicable for inversion of the MRI captured motion data to obtain mechanical properties. Each approach has limitations based on the simplification assumptions that underlie fundamental physical concepts of the method. Yet regardless of the extensive nature of the data and many inversion methodologies, the extraction of high resolution accurate results from naturally noisy data for complex and heterogeneous organs, such as the brain, is still a challenging uphill task.

Quantified mechanical properties, such as the shear modulus, can be calculated using information about propagation of the shear strain waves within the imaged volume. Generally, equations of motion based mathematical inversion algorithms are simplified with assumptions of local isotropy, homogeneity, and incompressibility.

For homogeneous, anisotropic and viscoelastic materials, the constitutive equation of motion factors an applied stress to the resultant strain and can be expressed as a rank 4 tensor with 21 independent complex quantities. Assuming isotropy reduces the number of independent quantities to the two typical Lame's constants λ and μ, which are responsible for longitudinal and shear strains, respectively. A VE model can be justified by assuming both Lame's constants to be complex valued, where the imaginary components represent attenuation due to the viscosity.

Most biological soft tissues are nearly incompressible, thus the first Lame's parameter λ is normally much larger than the shear modulus μ (typically 10^4 or more). This difference in magnitude makes it impractical to simultaneously calculate both λ and μ. In fact, the longitudinal wavelength in the tissue is very long (tens of meters) which brings additional challenges for accurate estimation of λ. Alternatively, in some cases if the excitation is primarily shear, the effect of λ can be simply neglected or removed by filtering out longitudinal wave motion using curl filtering techniques (Manduca et al., 2001).

If μ is assumed to be complex valued, it may be written as $\mu_R + i\mu_I$, where μ_R represents the storage modulus and μ_I is the loss modulus representing the attenuation in a viscoelastic medium. Using this complex shear modulus, the shear wave speed at a specific frequency can be calculated. The effective shear modulus, also known as the shear stiffness, can then be calculated from this simple relation: $\mu = \rho V_s^2$, where ρ is the material density (typically assumed at 1000 kg/m^3 for tissue in MRE) and V_s is the speed of the shear wave. The shear wave speed is derived as a product of the operating frequency and the spatial wavelength, and hence early MRE methods focused on measuring the shear wave wavelengths which was done manually. Over time, automatic algorithms that calculated the wavelength (local frequency estimation, (LFE); phase gradient (PG)) were applied Manduca et al. (2001). As this science progressed, algorithms were developed to directly calculate both μ_R and μ_I (direct inversion (DI). Despite these advancements, for convention and convenience, stiffness is still often reported as a product of density and wave speed squared. (Manduca et al., 2001) provides details of these methods.

Elastograms are the images of the mechanical properties of tissue calculated in MRE at a particular frequency of operation. Based on the technique used to derive the elastograms, they can have half the resolution of the native MR images which could range anything from 50 m to 10 mm depending on the application. Often,

they are typically one-third to one-fifth of the MRI resolution. Artifacts in the stiffness calculations using the aforementioned methods can result from shear wave interference. Directional filtering is a preprocessing technique developed to reduce these artifacts.

2.5 Overview of the MRE applied to *in-vivo* brain imaging

Brain MR elastography was first mentioned by Kruse et al. (1999), where it showed promising results to visualise propagating strain waves in the brain tissue. Since then, the method has been significantly improved. However, the *in vivo* values for the dynamic modulus still differ significantly with stiffness estimates for white matter ranging from 2.5 to 15.2 kPa and for gray matter from 2.8 to 12.9 kPa (Green et al., 2008; Kruse et al., 2007; McCracken et al., 2005; Sack et al., 2007; Uffmann et al., 2005, 2004; Xu et al., 2007).

In a recent study investigating the mechanical properties of the brain using MRE, Kruse et al. (2007) summarised the considerable variability of *in vivo* and *ex vivo* measurements of brain tissue properties reported in the literature. The lack of agreement suggests that more sophisticated mechanical models may be required to describe the deformation behavior of brain and other tissues. The variations of the results may also be due to several factors, such as a mismatch between the data generated by the MR displacement imaging gradients and the model used for inversion; the dispersion of the shear wave speed at different excitation frequencies; varying wave aptitudes, and complex or mis-modelled boundary conditions.

Manduca et al. (2001) elaborated on the various techniques of the MRE method for the imaging of elasticity. He also discussed limitations and assumptions of the different reconstruction processing algorithms, such as Local Frequency Estimation (LFE), Phase Gradient (PG) and Algebraic inversion of the differential equation. New methods were introduced by Jurgen et al. (2001) for the simulating and analysing of MRE wave images. For the agar gel phantom, good correlation was noted between the simulated wave patterns and reconstruction results, computed by LFE algorithm. Also, the brain image calculations using elasticity estimates for the gray and white matters showed that even small distributions of pathologically changed brain tissue are detectable by MRE even for the limit of relatively low shear

wave excitation frequency.

Braun et al. (2002) described the ultrafast Echo Planar acquisition techniques for the MRE of human brain. This technique improved the signal-to-noise ratio (SNR) and the complete 3D wave propagation visualisation in the human brain. The MR imaging of brain's transverse acoustic waves was performed by Moore et al. (2003) and the acoustic coupling was observed to be better at a 125Hz excitation frequency with an electromechanical actuator at the left temporal window.

Mechanical transient-based MRE was applied by McCracken et al. (2003) (McCracken et al., 2003, 2005) to study the biomechanics of traumatic brain injury. Using an electromechanical driver coupled to a bite-bar, low amplitude mechanical shear transients were directed to the heads of volunteers; the axial and coronal plane shear displacements were duly measured. Two methods of processing for the calculation of shear stiffness from transient data were developed. When tested in phantom studies, the transient results were found to be in good agreement with time-harmonic MRE results and the white matter (12 kPa) was found to be stiffer than the gray matter (8 kPa).

The results of a FE study of the hydrocephalus biomechanics was presented by Taylor and Miller (2004) with emphasis on the parenchyma's elastic modulus reassessment. The Young's modulus used in previous studies for the brain's parenchyma corresponded well to strain rates much higher than those presented in hydrocephalic brains. Uffmann et al. (2004) used MRE in an attempt to determine gray and white matter elasticities. Mean shear modulus observed were 13 kPa and 15 kPa for the gray matter and white matters, respectively.

A 2D multiple slice Spin Echo-Echo Planar Imaging (SE-EPI) for fast MRE of the brain was introduced by Kruse et al. (2006). This technique allowed complete field capture within the clinically conservative duration of 10 minutes or less. A high resolution 3D brain MRE was developed by Green et al. (2006) to enable the optimization of several parameters yet still maintaining good SNR. This technique allowed MRE image acquisition of a healthy brain in high resolution. About the ventricles, a much lower elasticity (1.1 kPa) central brain region was found surrounded by the higher elasticity white (2.1 kPa) and gray (2.8 kPa) matter regions.

Hamhaber et al. (2006) used 3D MRE *in vivo* human brain experiments to

observe the direction of wave propagation and subsequently infer in-plane elastic properties. A recent algorithm was used to determine the direction of wave propagation; it identified the minimal wave velocities of rays from surface into the brain. An acoustic approach was used by Rossman et al. (2006); this novel approach introduced the use of shear waves in brain MRE. A pneumatically actuated driver (PAD) dual channel system was developed to increase the mechanical vibration tolerance level of the head and brain.

A non-invasive assessment of the brain rheology was conducted by Klatt et al. (2007) using multifrequency MRE. The ability to recreate the observed dispersion curves were tested on five existing standard rheological models, such as the Maxwell, Voigt, Zener, Jeffreys and fractional Zener models. To suppress the noise and compression wave components, a 2D Butterworth filter was used. The model that yielded the most consistent results was the three parameter Zener model.

Sack et al. (2007) used MRE at different driving frequencies in a non-invasive measurement attempt of brain viscoelasticity. This method was based on a phase-sensitive EPI acquisition. The inter-individual mean shear moduli and shear viscosities were recorded at 1.17 kPa and 3.1 Pas for 25 Hz and 1.56 kPa and 3.4 Pas for 50 Hz, respectively. By comparing the rotational rheometry of *in vitro* brain tissue viscoelasticity measurements, Vappou et al. (2007) discovered that the dynamic behavior of loss (G") moduli and shear storage (G') from both rheometry and MRE at varying frequency ranges was equal to the linear viscoelastic properties of brain tissue found in other researches.

Preliminary observation on the application of MRE on the human brain was carried out by Xu et al. (2007). This research indicated that the shear wave lengths in the gray matter was relatively shorter than in the white matter and that both varied with the varying excitation frequency. Difference in tissue elasticity between the gray and white matters was noted in the elasticity images; the white matter had a higher elastic modulus compared to the gray matter. Using a full 3D reconstruction, Green et al. (2008) had applied the MRE technique at 3T to extract the complex shear modulus for in vivo brain tissue by applying a curl operator to remove dilatational wave effects. The results showed a significantly stiffer gray matter (3.1 kPa) compared to the white matter (2.7 kPa).

With regards to the stiffness quantification of brain tumors, Uffmann et al.

(2005) highlighted the use of LFE based MRE. It involved a patient with a left hemisphere glioma. Individual elasticity measures were taken for each the gray matter, the white matter and the tumor. The stiffest elasticity of 28.4 kPa and 24.2 kPa were noted for the tumor and the neighbouring white matter in the left hemisphere respectively while the white matter in the right hemisphere had a 18.7 kPa elasticity. The conclusion was that MRE may be applicable in areas where MRI has its limitation in the characterisation of brain tumors.

Six patients with known solid brain tumors (four meningiomas, one schwannoma and one hemangiopericytoma) were studies by Xu et al. (2006) using LFE based MRE. A radiologist had evaluated each patient tumor before the MRE based surgery. The propagation of shear waves in the brain was imaged and the change in the wavelength when propagation through the tumor was identified. The wave images were assessed and the tumor elasticity was classified relative to the elasticity of the white matter as less than, more than or similar to. The tumors were subsequently evaluated surgically by a neurosurgeon who had no knowledge of the MRE results; the consistency of the tumors were classified as soft, hard or intermediate which respectively meant softer than white matter, stiffer than white matter or similar to white matter. The MRE based tumor elasticity corresponded well with the neurosurgeons consistency assessment for all the patients Xu et al. (2006). However, due to the elasticity image's limited resolution, accurate evaluation of small tumours was not possible. This limitation also applies to infratentorial tumors as well as tumors with cystic changes where shear waves cannot propagate through the cystic components Xu et al. (2006).

Sack et al. (2009) used multifrequency MRE with a range from 25 to 62.5 Hz to investigate the *in vivo* viscoelasticity of healthy human brain in 55 volunteers (23 females) ranging in age from 18 to 88 years. By means of MRE, the authors revealed for the first time how physiological ageing changes the global viscosity and elasticity of the brain, showing that the healthy adult brain undergoes steady parenchymal liquefaction. Moreover, a significant difference between female and male brain elasticity was also found.

2.6 Summary

The human head is a very complex structure. It is made of solid components, such as the skull, meninges, brain, blood vessels, and fluidic components such as, CSF and blood. The skull encapsulates the brain and protects it from external impact. Meninges are located beneath the skull and stabilise the brain. The brain is a highly heterogeneous media which consists of a large variety of components.

Accurate description of the 3D mechanical response of the brain over a broad range of loading conditions is a very challenging task. This entails that the model should incorporate appropriate constitutive relations to account for the shear, compressive and tensile response of the brain tissue corresponding to a particular loading scenario. Due to the complex, non-linear, anisotropic and viscoelastic properties of the brain tissue, no acceptable models have been proposed to equally represent brain tissue response over a broad range of loading conditions.

A number of sophisticated rheological models, such as linear / non-linear elastic, linear / non-linear VE as well as poroelastic model have been developed in attempt to accurately characterise mechanical properties of the brain tissue. Depending on the application, different constitutive equations are better suited. For example, neurosurgical simulations usually require a large-deformation framework and lack sensitivity to any constitutive model. In case that distribution of a fluid is not required, single-phase based models might be appropriate to model the brain in the pathological state, such as hydrocephalus. However, more sophisticated models, such as poroviscoelasticity might be used to account for a fluid flow within the brain. Due to high computational intensity and despite implied limitations, simplified constitutive models are often used to model head trauma or injury. These models include linear VE as well as hyper elastic models that do or do not incorporate viscous components.

Model accuracy can be improved by appropriate addressing of the damping effects. In the VE formulation, damping is implemented through a complex shear modulus where the damping level is directly proportional to the elastic forces. The Rayleigh damping (RD) model is an extension of the VE model which incorporates attenuation modulus proportional to both elastic and inertial effects. If the RD model provides a better approximation of attenuation behaviour than the VE model,

reconstruction accuracy of other parameters, such as real shear modulus, my also be improved due to decreased data-model discrepancy. This would imply, that the RD material model would be superior over traditional VE model allowing better accuracy of elastographic based reconstruction.

MRE was first applied to *in vivo* brain imaging by Kruse et al. (1999) where non-invasive palpation of the brain tissue was demonstrated. Since then, the method has been significantly improved. Technical advancements in brain MRE resulted in the development of faster pulse sequences allowing MRE image acquisition in the clinically acceptable examination time. New actuation methodologies as well as a number of inverse reconstruction techniques have been proposed to improve accuracy of elastographic based reconstruction. Brain cancer diagnosis using MRE still remains a challenging scientific field with a number of difficulties, such as efficient generation of the mechanical waves inside the brain, complex interior reflections of the waves within the cranium, dispersion of the stain waves at different frequencies and limitations of the existing inverse problem techniques to account for a highly complex, anisotropic, heterogeneous organ like the brain.

Chapter 3

MRI data measurement, conversion and processing of the results

Magnetic Resonance Elastography (MRE) is an emerging imaging modality that allows quantitative assessment of the mechanical properties of tissue *in vivo*. The results produced by MRE can be considered as a 3D imaging based counterpart to palpation, commonly used by physicians to detect pathological tissue change. Stiffness estimates are deduced from the displacements fields caused by propagation of mechanical waves which are encoded by phase-contrast MRI techniques. The technique essentially involves the steps illustrated in Fig. 3.1.

- Generating shear waves in the tissue.
- Motion encoding via phase-contrast MRI techniques.
- Processing the images of the shear waves to generate quantitative maps of tissue stiffness, called elastograms.

A constitutive model is required to produce quantitative estimates of the material properties. The model that provides good approximation of the observed behaviour of the tissue will lead to accurate recovery of the material property distribution that are close to true tissue properties.

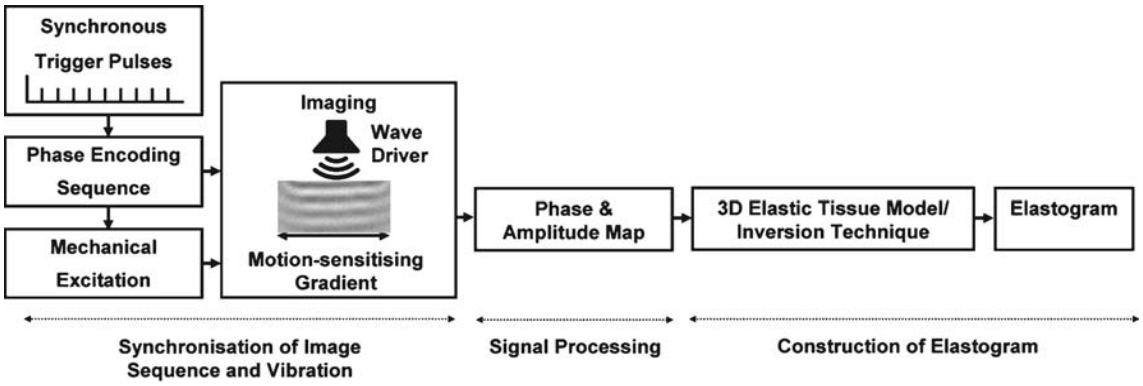

Figure 3.1 Schematic representation of the MRE examination. Mechanical excitation is performed by means of electromagnetic, acoustic or other type of the actuator. Trigger pulses are used synchronised MRI image acquisition with the induced mechanical vibrations. 3D motion encoding is performed via a phase-contrast MRI image sequence extended with motion encoding gradients (MEGs). As a results, information about amplitude and phase of the propagating waves can be obtained at every point within imaging volume. This information is used by the biomechanical constitutive model to recover elasticity distribution across reconstruction domain. The resulting image is called elastogram. Image courtesy of Di Ieva et al. (2010).

3.1 Mechanical actuation

To generate harmonic oscillations within the brain, a special actuator was designed. According to the performance requirements defined, the brain actuator must:

- Provide a steady state harmonic displacement of at least 100 μm to the head,
- Have non-magnetic properties to minimize possible interference with the MR imaging process,
- Provide maximum comfort and safety for the patient,
- Enable easy and fast setup of the MRE examination in order to fit within the time restrictions available,
- Possess a flexible design allowing reconfiguration of the actuator setup for experiments with the phantoms

Considering these criteria, an acoustic actuator concept was chosen based on prior attempts (Goss et al., 2006b; Latta et al., 2010; Rossman et al., 2006). To compensate for the shear wave attenuation in a large organ like brain, the approach

was a double driver principle (Zheng et al., 2007). A pair of modified dual-voice passive subwoofers were used as remote pressure sources. To achieve maximum output of 300 W RMS, dual voice coils of 4 Ohm were wired in series for 8 Ohms and then both speakers were connected to an individual amplifier channel. Acoustic pressure waves, generated by the speaker cone excursion, were used to engage the passive drivers connected via stiff walled flexible tubes of various length.

Acoustic waveguide principles were considered prior to choosing the long tubing. The basic principle is that in a straight cylindrical waveguide there is just one propagating acoustic mode, as long as the free space wavelength is greater than 1.71 times the inside diameter $\lambda > 1.71d$ (Neville H. Fletcher, 1991).

The wavelength λ of a sinusoidal waveform traveling at a constant speed V is defined:

$$\lambda = \frac{V}{f} \tag{3.1}$$

where V is the phase speed (magnitude of the phase velocity) of the wave and f is the wave's frequency. For sound waves in the air, the speed of a sound is $V = 344$ m/s at $20°C$. Based on Eq. 3.1, the wavelength of the sound waves at 100 Hz is $\lambda = 3.44$ m. To achieve only one propagating mode in the waveguide the following condition has to be satisfied:

$$d < \frac{\lambda}{1.71} \tag{3.2}$$

Considering that the highest possible actuation frequency for the brain is 200 Hz, the diameter of the flexible tubing had to be no more than 2 meters.

A pair of passive subwoofers "Atomic Manhattan MA 15D" were modified with the 25 mm airtight acrylic lids mounted over the speaker membrane and used as a source of the air pressure (refer to Fig. 3.2 (a)). Mutual phase shift of 180° between the subwoofers was achieved by reversing the wires on the input leads of the subwoofers. A special hose connector was mounted at the centre of the lids to attach flexible tubes for the transmission of acoustic waves into the passive drivers (see Fig. 3.2 (b).

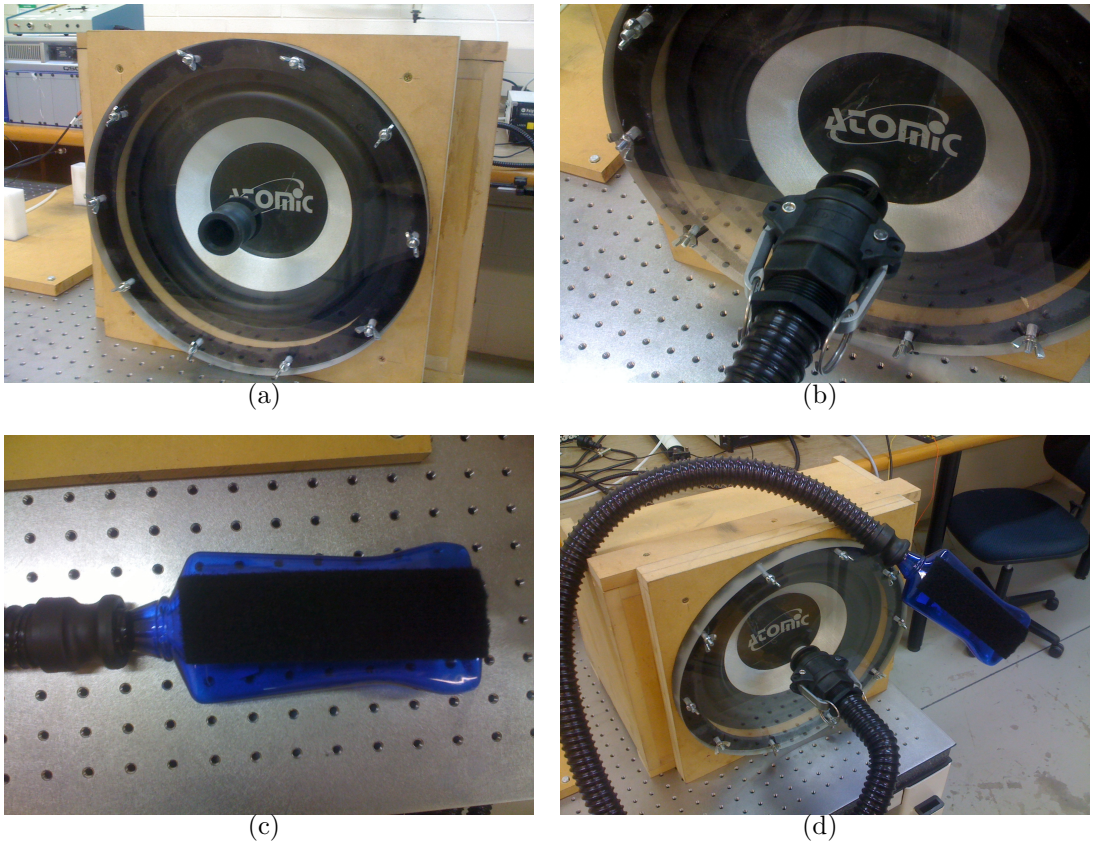

Figure 3.2 Pneumatic based acoustic actuator for brain MRE. (a) Modified subwoofer for delivering the air pressure; (b) Hose connection between the subwoofer and long flexible tubing; (c) Pneumatically actuated driver (PAD); (d) Full actuator configuration

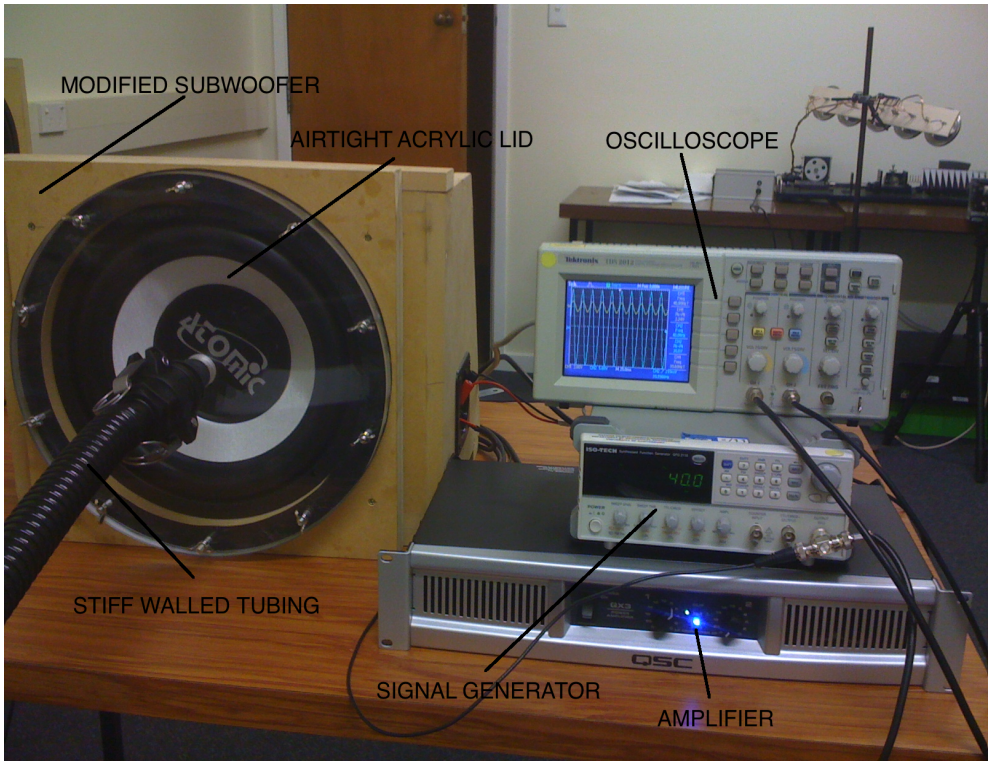

Figure 3.3 Experimental set up of the acoustic brain actuator. A signal generator is connected to an amplifier through a two channel oscilloscope. One channel is connected to a passive subwoofer used to generate acoustic pressure waves and drive pneumatically actuated drivers (PADs). Another channelled is to be connected to an MRI scanner via an RS422 converter to allow synchronisation of induced mechanical motion with MRI image acquisition to allow motion encoding.

The experimental setup used an ISO-TECH GFG 2110 signal generator connected to a QSC QX3 amplifier through Tektronix TDS2012 two channel oscilloscope, as depicted in Fig. 3.3. The sinusoidal signal from the waveform generator was set to 1 V amplitude and a frequency range of 10 to 200 Hz, stepped in 10 Hz increments. The second channel was to be connected to the MRI scanner via the RS422 converter to trigger the actuation signal with the MRI signal acquisition. The custom made RS422 converter consists of a voltage regulator and the LTC490 IC that converts two voltage levels between standards in both direction.

Standard plastic bottles, commonly used for cosmetic products, were utilized as pneumatically actuated drivers (PADs). It was found that polyethylene containers from commercial hand sanitizer were well suited for this application. The containers had a flat rectangular shape with the flexible walls and could be easily placed in between the patients head and the bottom of the MR head coil. The PADs were

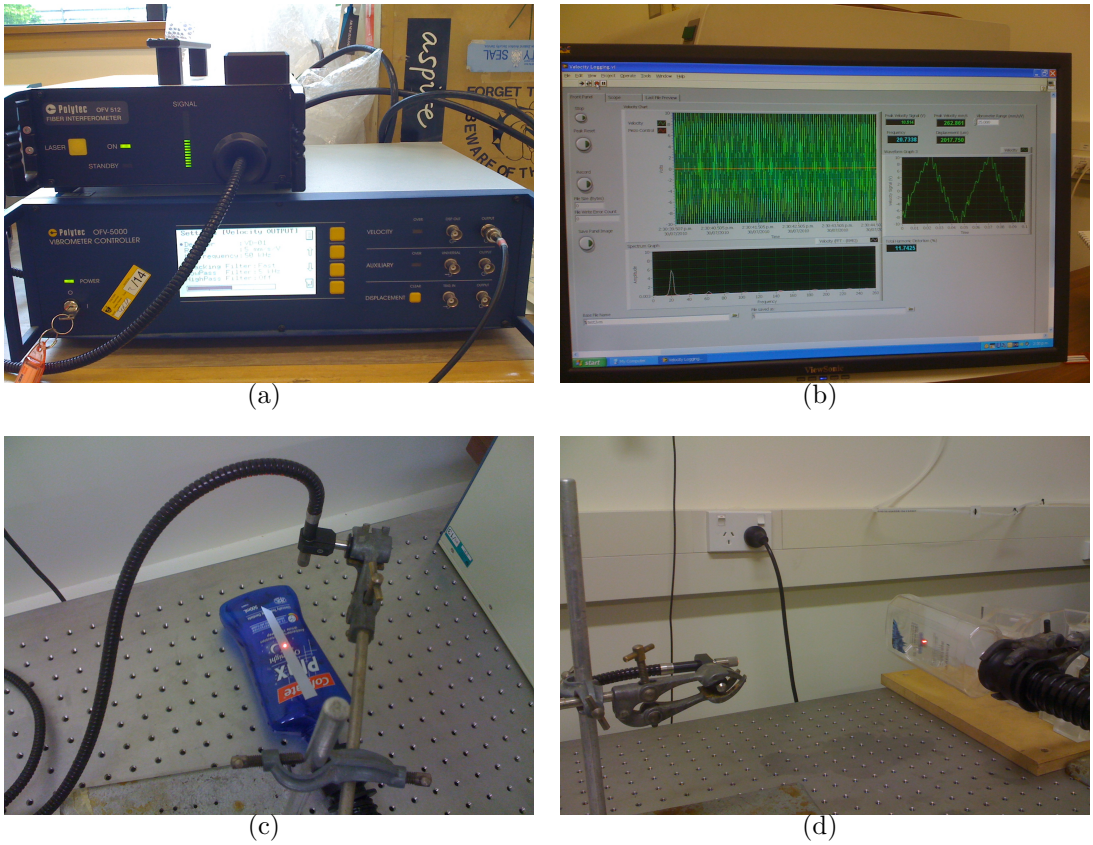

Figure 3.4 Experimental setup used for investigating frequency characteristics of the different configurations of the pneumatically actuated drivers with the laser interferometer. (a) The laser interferometer device; (b) LabVIEW software program interface specifically designed to operate the laser interferometer; (c) The PAD is attached to the surface; (d) The PAD is in pendant position.

intended to be used as cushions on which the patient would rest his head. A purpose-made fitting was used to connect the container to the hard-walled flexible tubes (see Fig. 3.2 (c)). Various container configurations were investigated to achieve maximum displacement output of the PADs. The full pneumatic actuator is shown in Fig. 3.2 (d). Initially, the actuator was designed to operate with the standard MR head coil. However, it could be also utilized for performing experiments with various phantoms as well.

To investigate the frequency and motion characteristics of different PADs, a laser interferometer (OFV-5000, Polytec GmbH, Waldbronn, Germany) was used to measure actuated motion, as shown in Fig. 3.4 (a). LabVIEW software (National Instruments Corp., Austin, TX, USA) was used for data acquisition. The user

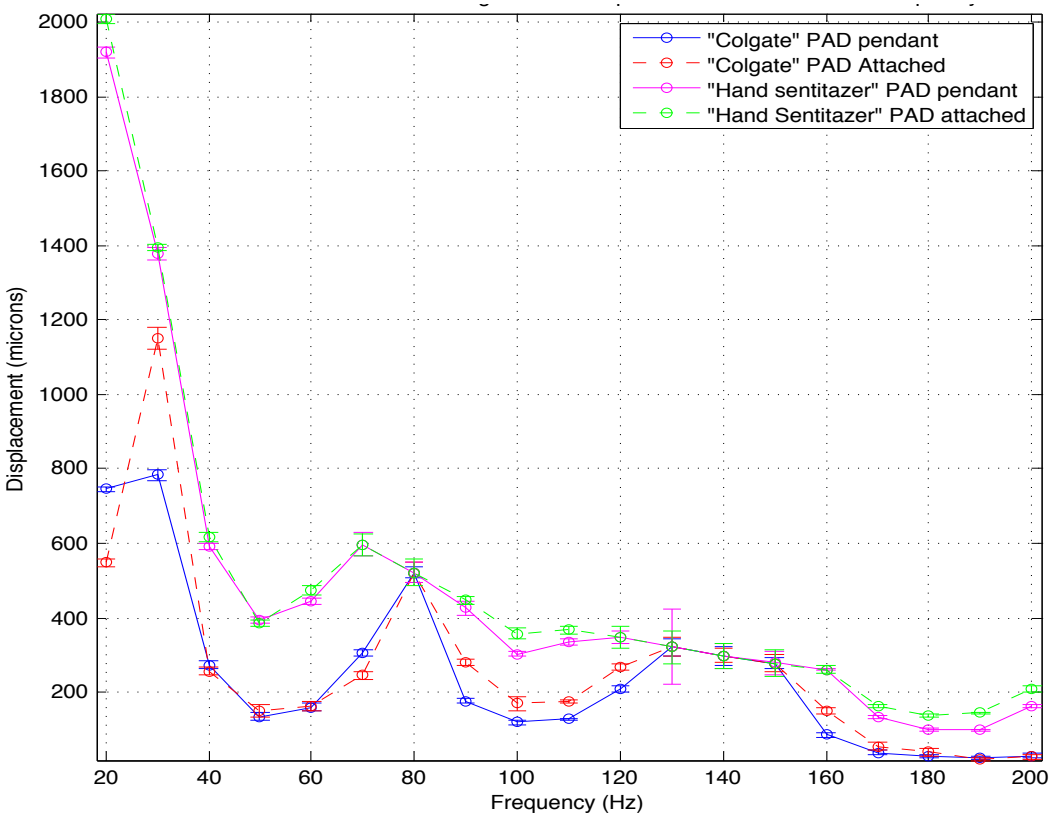

Figure 3.5 Actuator displacements as a function of frequency for two different PAD configurations. The data was measured using a laser interferometer. Signal distortions are depicted as the error bar indicators. It can be seen that most effective frequency range, producing displacement values of more then 200 microns, is between $60 - 80$ Hz. The PAD made of the commercial hand sanitizer generally showed better displacement characteristics then the PAD made of a "Colgate" mouth wash container.

interface of the software program is shown in Fig. 3.4 (b).

Two different PAD configurations were examined. One was a bottle from the commercial hand sanitizer and another was a container from the Colgate mouth wash. The displacements of the PADs were examined at two different configurations: attached to the surface mimicking placing two PADs in the MRI head coil (see Fig. 3.4 c) and pendant configuration (see Fig. 3.4 d). The displacement plots for the two PAD configurations are shown in Fig. 3.5. The plot reveals that the actuator is operating most efficiently for frequencies up to $60 - 80$ Hz, where the motion amplitudes are above 200 microns.

3.2 Motion encoding

Motion measurement and encoding is performed with an MRI scanner. External oscillations, applied to the sample being imaged result in harmonic motions propagating throughout the imaging volume and can be then detected using phase contrast MRI techniques. The latter combines conventional MR imaging methods and additional motion encoding gradients (MEGs) that allow quantitative motion measurement by measuring accumulated phase shift of the nuclear spins.

Motion detection via Nuclear Magnetic Resonance (NMR) was first described by Muthupillai et al. (1995). The phase shift $\phi(\tau)$ in the NMR signal resulting from the motion of nuclear spins in the presence of a magnetic field gradient is given by:

$$\phi(\tau) = \gamma \int_0^\tau \mathbf{G}_r(t)\mathbf{r}(t)dt \tag{3.3}$$

where γ is the gyromagnetic ratio of the specific material, τ is the time duration of the applied MEGs after excitation, $\mathbf{G}_r(t)$ is a time dependent function of the magnetic gradients, superimposed on the static magnetic field B_0 and $\mathbf{r}(t)$ describes the position of the nuclear spins as a function of time. Eq. 3.3 holds true for the direct relation between accumulated phase shift and voxel displacement, allowing the imaging of the motion fields in the object by application of the special MEGs.

MEGs are sinusoidal (or trapezoidal) gradients applied in one of the three spatial directions during the pulse sequence. A complete MRE acquisition entails measuring motion in all three directions, thus leading to a full 3D description of the motion at every point in space within the imaged volume. This technique produces complex displacement values at internal grid points together with the MR signal strengths. The frequency of the applied MEG is the same as the frequency of the induced vibration. If a sample is subjected to sinusoidal actuation along with a sinusoidal MEGs to decipher resulted motions, the observed phase shift in the MR signal produces an amplitude and phase that uniquely determines the amplitude and phase of the harmonic vibration response (Muthupillai et al., 1995).

To accurately sample the resulting waveform, multiple phase-offsets between the MEGs and the applied vibration are required. Commonly, eight relative phases

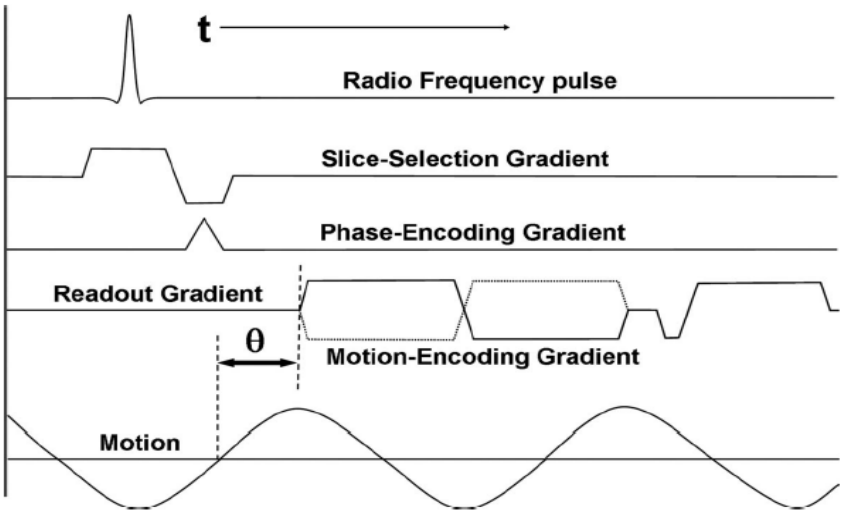

Figure 3.6 Example of a gradient-recall echo MRE pulse sequence. A typical bipolar motion-encoding gradient used for phase-contrast imaging is depicted in solid and dotted lines.The MEG (frequency-encoding direction) is placed directly after the RF excitation and before the measurement of the induced signal. Temporal relationship between induced continuous sinusoidal motion of the tissue and MEG is controlled with the phase-offset θ. Source: (Mariappan et al., 2010).

are used to acquire snapshots of the propagating waves. To ensure a zero average phase at sampling, the phase harmonics are evenly distributed across a single cosine motion cycle. Fig. 3.6 shows a schematic representation of the MRE pulse sequence using a gradient-recalled echo (GRE) with conventional radio frequency (RF) pulse, slice-selection gradient, phase-encoding gradient and frequency-encoding gradients.

This technique is a highly sensitive with the ability to detect motion on the order of hundreds of nanometers (Muthupillai et al., 1996). Fig. 3.7 shows an initial displacement data of *in vivo* brain obtained from an MR phase contrast displacement imaging sequence. The sequence only generates the phase $P(\mathbf{x})$ (refer to Figs. 3.7 (c) and 3.7 (d)) and amplitude $\mathbf{A}(\mathbf{x})$ (refer to Figs. 3.7 (e) and 3.7 (f)) information. The initial displacements values (refer to Figs. 3.7 (g) and 3.7 (h)) were calculated from amplitudes $\mathbf{A}(\mathbf{x})$ and phases $P(\mathbf{x})$ through the relation $\mathbf{D}(\mathbf{x}) = \mathbf{A}(\mathbf{x})\cos(P(\mathbf{x}))$ where $\mathbf{D}(\mathbf{x})$ is the displacement.

The resulting MR image contains information about the propagating wave and is called a wave image. Typically, two such wave images are collected with opposite polarity of the MEG and a phase-difference image is then calculated to remove

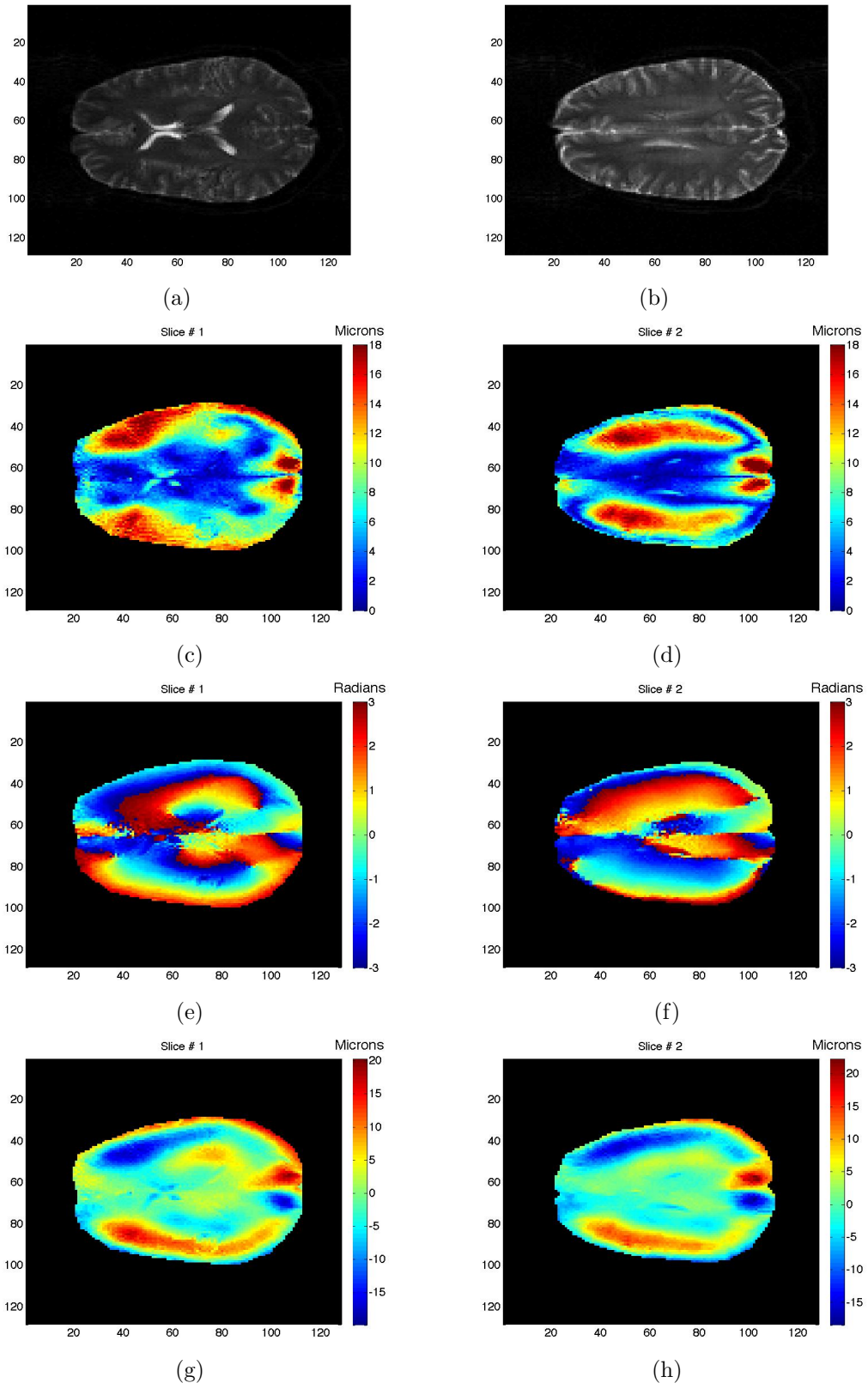

Figure 3.7 Initial *in vivo* raw data of the normal human brain from the MR motion encoding gradient in the y direction (from left to right) actuated with the pneumatic brain actuator located underneath the head. (a) and (b): 2 slices of fast spin-echo T2*-weighetd MR magnitude gray scale image visualising brain anatomy; (c) and (d): magnitude of the displacement in [μm]; (e) and (f): phase of the displacement in [*rad*]; (g) and (h): reconstructed real displacement in [μm] from magnitude and phase.

non motion-related phase information. The solid and the dotted lines in Fig. 3.6 indicate the MEG waveforms with opposed polarities used sequentially to produce these phase-difference wave images.

3.3 Raw data conversion

The motion data, captured during the MRI process, is stored in the phase of the NMR signal and further converted into computational file formats that allows later analysis. Irrespective of the data format, for example, PAR/REC images from Philips MRI scanners or DICOM images from Siemens MRI machines, the same basic information is stored as a volume image with a steady state vector displacement field. To reconstruct mechanical properties within the imaged volume, all three motion directions are required. In this analysis, the raw data is converted into 3D arrays in Matlab format and represents information about the phase and amplitude of the voxel displacement. It is important that the amplitude and phase information is converted into a form that is consistent with the complex displacement aptitudes used in the inversion code.

Thus, the imaged motion can be represented as a vector:

$$\mathbf{u}(\mathbf{x},t) = u_x(\mathbf{x},t)\mathbf{i} + u_y(\mathbf{x},t)\mathbf{j} + u_z(\mathbf{x},t)\mathbf{k}, \tag{3.4}$$

where $\mathbf{u}(\mathbf{x},t)$ is the displacement field as a function of time and position, where $u_x(\mathbf{x},t)$ is the displacement component in the x direction, $u_y(\mathbf{x},t)$ is the displacement component in the y direction and $u_z(\mathbf{x},t)$ is the displacement component in the z direction component of the motion. Alternatively, since it is the steady state of the wave that is being imaged, the Eq. 3.4 can be re-written as the real part of a product of two complex numbers

$$\mathbf{u}(\mathbf{x},t) = \Re\Big\{\hat{\mathbf{u}}_c(\mathbf{x})e^{i\omega t}\Big\}. \tag{3.5}$$

Here, $\mathbf{u}(\mathbf{x},t)$ is the real-valued measurable displacement occurring at a point $\mathbf{x}$ at time t; and $\hat{\mathbf{u}}_c$ is a complex phasor which defines the amplitude of a harmonic

displacement with frequency ω. The real and imaginary components of $\hat{\mathbf{u}}_c$ can be defined:

$$\mathbf{u}_c = \mathbf{u}_R + i\mathbf{u}_I. \tag{3.6}$$

Eq. 3.5 can be expanded using Euler's formula, $e^{i\theta} = \cos\theta + i\sin\theta$, to give:

$$\begin{aligned}
\mathbf{u}(\mathbf{x},t) &= \Re\Big\{\hat{\mathbf{u}}_c(\mathbf{x})e^{i\omega t}\Big\} \\
&= \Re\Big\{(\mathbf{u}_R + i\mathbf{u}_I)(\cos(\omega t) + i\sin(\omega t))\Big\} \\
&= \Re\Big\{\mathbf{u}_R\cos(\omega t) + i\mathbf{u}_R\sin(\omega t) + i\mathbf{u}_I\cos(\omega t) - \mathbf{u}_I\sin(\omega t)\Big\} \\
&= \mathbf{u}_R\cos(\omega t) - \mathbf{u}_I\sin(\omega t).
\end{aligned} \tag{3.7}$$

Eq. 3.7 describes the form of the real harmonic motions. It is important that measured MR motions are represented in the same form. Since motion is always a real number, the imaginary part only appears due to material damping.

The MR-detected motions are given as real-valued amplitude, $\boldsymbol{A}(\mathbf{x})$, and phase, $P(\mathbf{x})$, for each point, so that the displacement at a point $\mathbf{x}$ and time t is given:

$$\mathbf{u}(\mathbf{x},t) = \boldsymbol{A}(\mathbf{x})\cos(\omega t + P(\mathbf{x})) \tag{3.8}$$

Euler's formula allows Eq. 3.8 to be re-written:

$$\begin{aligned}
\mathbf{u}(\mathbf{x},t) &= \Re\Big\{\boldsymbol{A}(\mathbf{x})e^{i(\omega t+P(\mathbf{x}))}\Big\} \\
&= \Re\Big\{\boldsymbol{A}(\mathbf{x})e^{iP(\mathbf{x})}e^{i(\omega t)}\Big\} \\
&= \Re\Big\{\boldsymbol{A}(\mathbf{x})(\cos(P(\mathbf{x}))+i\sin(P(\mathbf{x})))(\cos(\omega t)+i\sin(\omega t))\Big\} \\
&= \boldsymbol{A}(\mathbf{x})\cos(P(\mathbf{x}))\cos(\omega t)-\boldsymbol{A}(\mathbf{x})\sin(P(\mathbf{x}))\sin(\omega t). \qquad (3.9)
\end{aligned}$$

Eq. 3.9 is in the same form as Eq. 3.7, and the real and imaginary components of the equivalent complex displacement amplitude are defined:

$$\begin{aligned}
\mathbf{u}_R(\mathbf{x}) &= \boldsymbol{A}(\mathbf{x})\cos(P(\mathbf{x})) \\
\mathbf{u}_I(\mathbf{x}) &= \boldsymbol{A}(\mathbf{x})\sin(P(\mathbf{x}))
\end{aligned} \qquad (3.10)$$

The motion is expected to undergo sinusoidal displacement in response to the steady state harmonic actuation conditions. Therefore, a Fast Fourier Transform (FFT) is applied to the motion data in all three directions, decomposing the signal into a set of sine waves. More specifically, the motion data in a particular direction is rearranged such that an FFT is taken for every voxel across the number of relative phase offsets between the actuation signal and MR signal. The FFT is defined:

$$F(k)=\sum_{j=1}^{N} f(j)e^{\frac{-2\pi i}{N}(j-1)(k-1)} \qquad (3.11)$$

where $f(j)$ is the vector of phase values over effective delay times for a particular voxel; $F(k)$ is its Fourier transform. j and k are elements in their respective vectors; N is the number of delay times.

Then, a discrete inverse FFT is performed to generate a Fourier fitting of the

measured data:

$$f(j) = \frac{1}{N} \sum_{k=1}^{N} F(k) e^{\frac{-2\pi i}{N}[-(j-1)(k-1)]} \tag{3.12}$$

The inverse FFT returns a complex value at each frequency. Complex magnitude and phase, returned by inverse Fourier transform, is then recorded at each voxel for all three motion directions within the imaged volume and stored in 4D arrays. The first three dimensions of this array contain the spatial coordinates of the imaged volume; the fourth dimension contains the magnitude and phase data. This complex data is then incorporated into the finite element mesh for further processing.

3.4 Phase wrapping

In MRE, the motion is captured by means of phase-contrast MR technique that is able to decipher accumulated phase shifts of every voxel in the tissue subjected to time harmonic oscillations. Relative phase offsets are applied between an induced mechanical signal and MEGs to acquire snapshots of the propagating waves. After two acquisitions of MRE images with opposite polarity of MEGs, phase subtraction is made between those two images to produce a relative phase image. In the phase image, the intensity of each pixel represents the direction and the amount of motion velocity. The phase offset of oscillating arbitrary voxel within tissue can be expressed as a function of the relative phase offset ϕ between the externally induced motion and MEGs (Wang et al., 2011):

$$f(\phi) = A\cos(\phi + \Theta) \tag{3.13}$$

where $\phi = 2\pi\phi/N$ and N is the number of evenly spaced phase offsets within one cycle. The amplitude A and phase Θ characterize the harmonic motion and are estimated from the sampled $f(\phi)$ values. When the accumulated phases, $f(\phi)$, are out of the (-π, π) range, the true phase values will be wrapped back to this range, creating discontinuities in the phase maps and subsequently in the estimated motion (Wang et al., 2011). Thus the phase needs to be unwrapped before the motion can

be estimated accurately.

The initial reason for the phase wrapping is the large amplitude of the induced mechanical motion. Since shear waves attenuate quickly in certain tissues, large amplitudes near the surface may be required to achieve sufficient amplitude in a deep region of interest. Excessive amplitude can cause phase wrapping; i.e. large enough displacements can cause accumulated phase shifts outside the range π, which are ambiguous. This sets an upper limit to the amplitude at which the tissue should be driven. However, the three-dimensional quality-guided phase unwrapping method can be applied to MRE data with good success (Wang et al., 2011). The upper limit on amplitude can then be increased as long as the phases can be reliably unwrapped.

The other challenging phase wrapping problem we have experienced was due to a linear phase shift caused by the translation component of the rigid body motion, e.g head movement of the subject. Such a rotation gave a constant phase shift across the entire field of view (FOV). To resolve this problem the zero and first order phase correction in the k-space domain was applied prior to FFT in order to further suppress phase errors and minimise wrap around problems. Figs. 3.8, 3.9 and 3.10 show how eliminating linear phase shift significantly improved quality of the motion data in the x, y and z directions correspondingly. Images located in the left column on each figure (a, c and e) represent the raw MR motion data with linear shift present and images in the right column (b, d and f) show corrected data with suppressed linear phase shift. Significant improvement of the data quality is clearly evident with smooth transition of the motion pattern throughout the brain.

3.5 Finite element mesh

The finite element method (FEM) is a method for finding approximate solutions of partial differential equations (PDE) over discretized space. The quality of PDE solutions is directly related to resolution of the FEM. The two most common FE representation for this type of 3D volume analysis are tetrahedral or cubic elements.

Every FE description of 3D geometry consists of a certain number of nodes

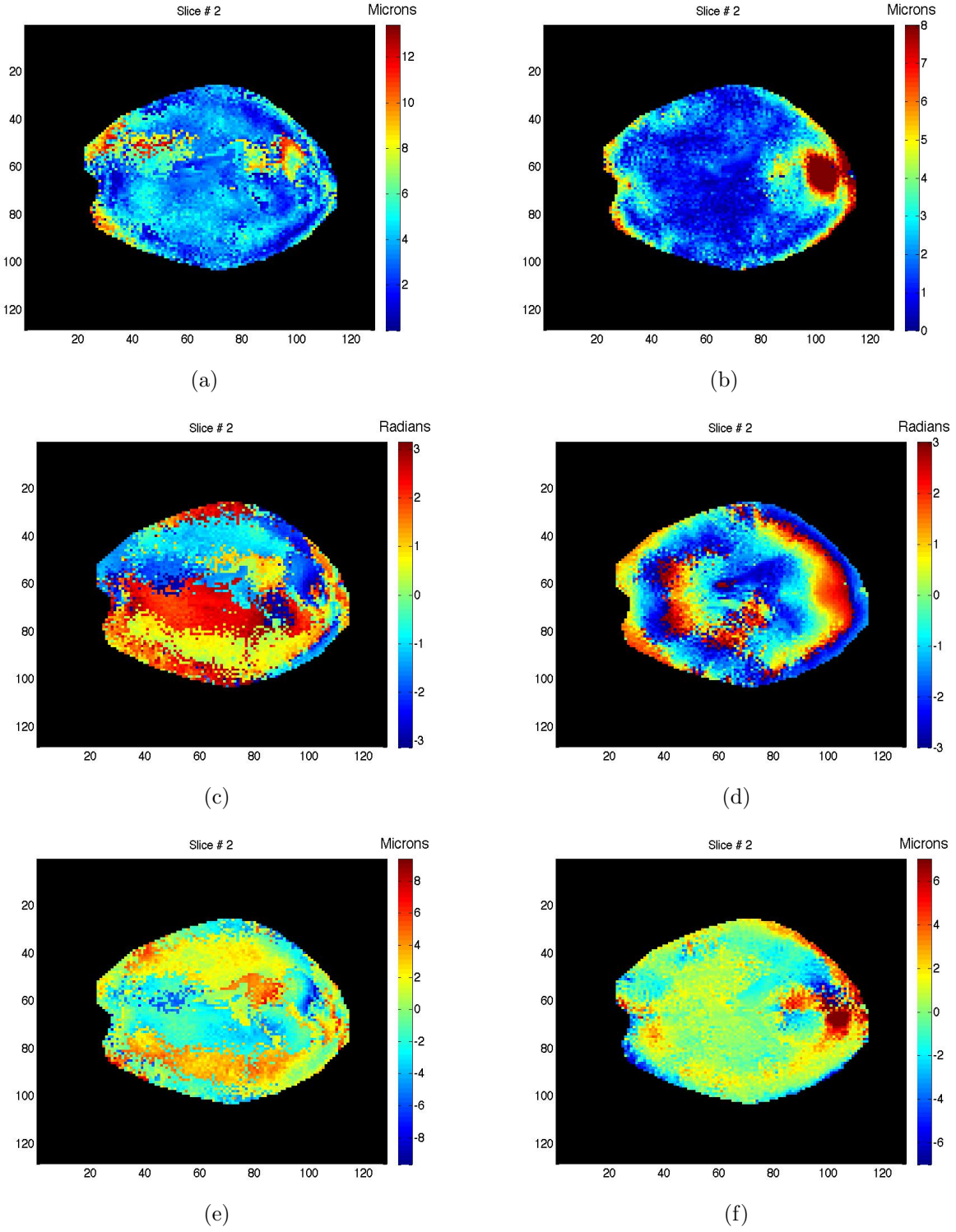

Figure 3.8 Initial *in vivo* raw data of the normal human brain from the MEG applied in the x direction. Images (a), (c) and (e) represent magnitude of the displacement [μm], phase of the displacement [rad] and reconstructed real displacement with the linear shift error present correspondently. Images (b), (d) and (f) images represent corrected data with linear shift removed

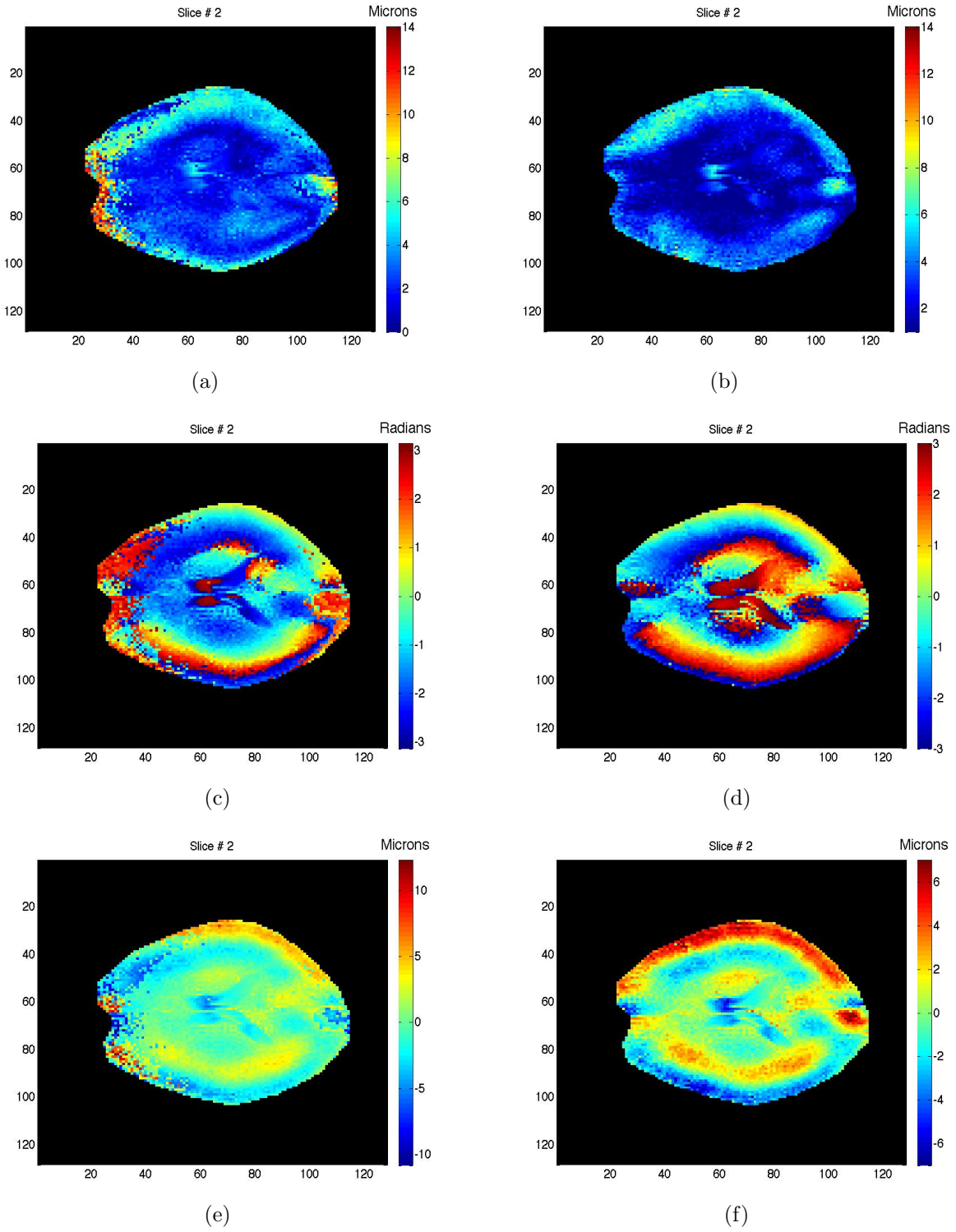

Figure 3.9 Initial *in vivo* raw data of the normal human brain from the MEG applied in the y direction. Amplitude of the motion is high near the brain-skull boundary and decreasing as waves propagate in the inner brain. Images (a), (c) and (e) represent magnitude of the displacement [μm], phase of the displacement [rad] and reconstructed real displacement with the linear shift error present correspondently. Images (b), (d) and (f) represent corrected data with linear shift removed.

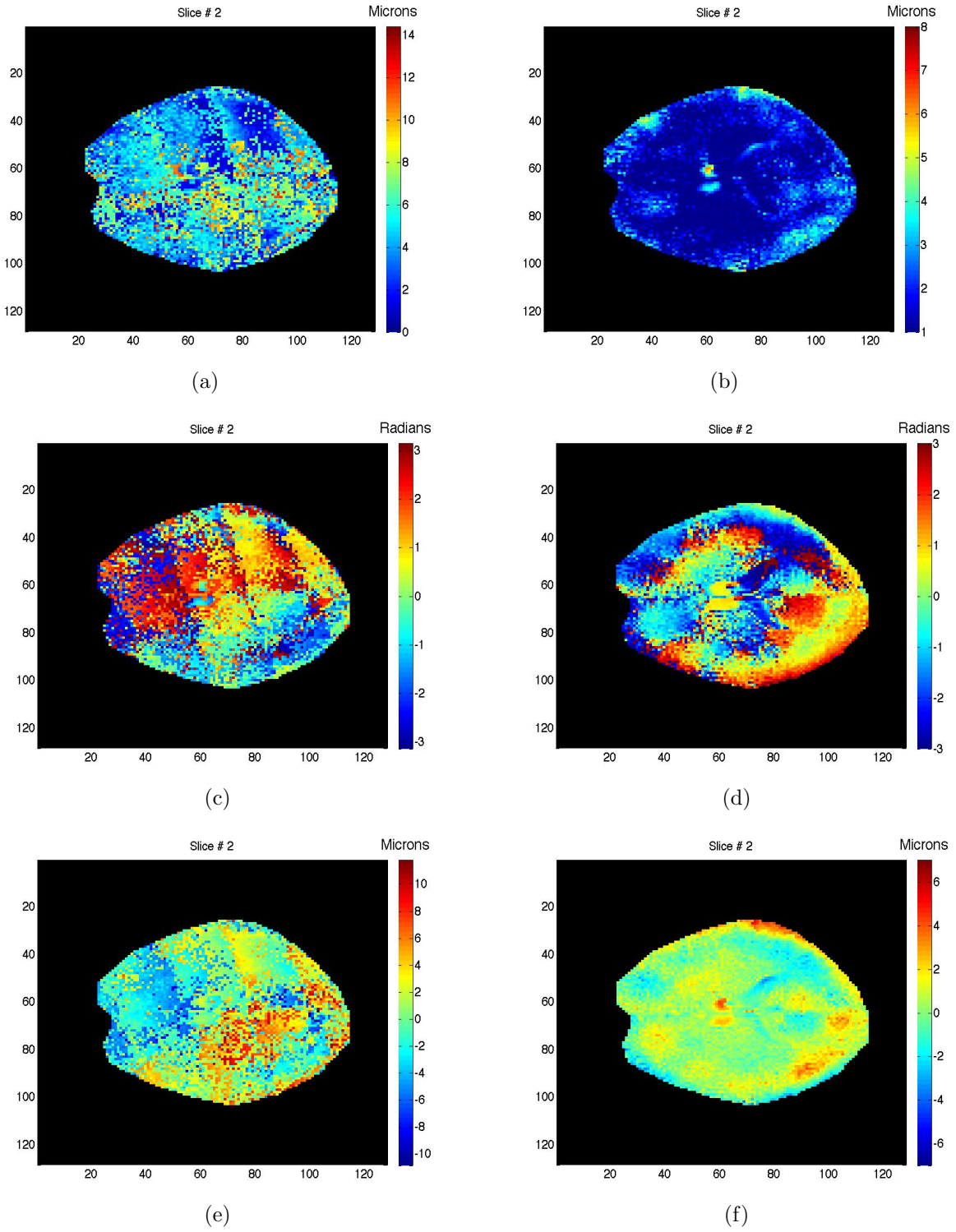

Figure 3.10 Initial in vivo raw data of the normal human brain from the MEG applied in the z direction. Due to actuation method, displacement is quite small as z axis is the axis of the head rotation. (a), (c) and (e) represent magnitude of the displacement [μm], phase of the displacement [rad] and reconstructed real displacement with the linear shift error present correspondently. (b), (d) and (f) represent corrected data with linear shift removed

that are interconnected to define a finite model of volumes. The node describes a particular location in space, in x, y and z coordinates. The combination of all elements and all nodes is called a *mesh*. The more nodes present in the mesh, the higher the resolution of the motion pattern across the volume that can be described.

In this work, 27 node quadratic hexahedral elements (six sided 3D object) are used to create a mesh as shown in Fig. 3.11. Since there are three nodes along each element axes, the values between the nodes are interpolated by a second order polynomial. In the conversion process, every node is surrounded by a voxel and the displacement data of this particular voxel is assigned to a particular node.

The motion data from MRI comes in voxels that are indexed as $\mathbf{u}_R\,(i, j, k)$. It is noted here that in the physical space x, y and z coordinates are applied. However, in the voxel space it is i, j, k. As it is rather challenging to segment the raw motion data into triangular elements, each voxel is directly applied to a node in an appropriately scaled hexahedral FE mesh such that the node is located at the centre of a voxel. This technique leads to a MR pixel resolution in the reconstructed material properties and avoids any errors in interpolation.

To overcome the difficulty of creating a 27 node hexahedral element list from a grid of points, the commercial meshing program GAMBIT is used to generate a template. By running a specifically designed mesh converter in MATLAB, the raw MR motion data can be converted into the FE mesh by assigning each MRI voxel to a corresponding mesh node. This approach provides an initial template mesh of a FE model to be used in MRE.

A region of interest (ROI) is selected by applying a mask using an image processing toolbox in Matlab. The final outputs are the FE node, element and displacement files. The MRI magnitude image output is in the same format as the material input file. This format allows comparison with the reconstructed property distributions. If any node for a particular element is outside of the ROI, the entire element is discarded.

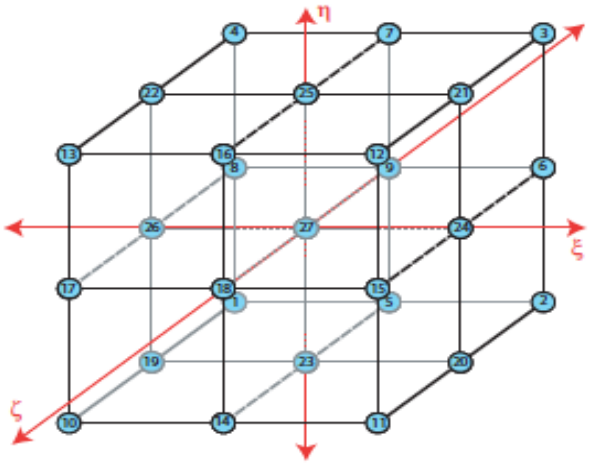

Figure 3.11 27 node Hexahedral element with node numbering scheme and local coordinate (ξ, η, ζ) system shown (McGarry, 2008)

3.6 Summary

A convertible pneumatic actuator was constructed to generate vibration for the *in vivo* brain MRE experiments. The actuator allows an easy and convenient experimental set up and can be used for both phantoms and *in vivo* brain MRE experiments. The actuator does not have any metal parts that can interfere with the MR magnet. The experimental results with a laser interferometer showed that the actuator produced sufficient displacement to generate propagation of the shear waves in the brain. The actuator operated most efficiently within the 60-80 Hz frequency range and produced motion of more than 200 μm. The frequency range is suitable for performing brain MRE examinations.

The subject head is positioned on the PADs in a natural way allowing comfort and a good tolerance of induced vibrations. Different PAD configurations of varying size and shape can be used to fit available head coils of the MRI scanner. Due to the limited access to the MRI scanners in Canterbury, this particular actuator is to be tested in a clinical setting. However, a similar actuator based on this design was applied for phantom and *in vivo* brain MRE examinations by a collaborating institute CNRC. Data obtained from that actuator was used in this research.

Motion encoding is performed by a phase-contrast MRI technique that allows

extraction of the magnitude and phase of the propagating shear strain waves. MEGs are applied during a pulse sequence in three orthogonal directions to allow a full 3D capture of the motion pattern. The frequency of the MEGs is the same as the frequency of mechanical vibration. Typically multiple phase offsets between induced motion and MEG are are required to accurately describe induced vibration.

MRE data acquisition allows capture of the complex valued displacement fields described as a real valued magnitude $\boldsymbol{A}(\mathbf{x})$ and phase $P(\mathbf{x})$ at each point, so that the complex displacement amplitude is defined :

$$\begin{aligned} \mathbf{u}_R(\mathbf{x}) &= \boldsymbol{A}(\mathbf{x}) \cos(P(\mathbf{x})) \\ \mathbf{u}_I(\mathbf{x}) &= \boldsymbol{A}(\mathbf{x}) \sin(P(\mathbf{x})) \end{aligned} \tag{3.14}$$

Solution of PDEs that describe the mechanical motion is required by the mathematic model to compute FE formulation of the displacement pattern. Therefore, the captured motion data is descritized by the FEM where the centre of each MR voxel corresponds to a single node within the mesh. This technique allows MRI voxel revolution of the reconstructed material properties and avoids any errors in interpolation to FEM. The conversion process yields the FE node location, element configurations and displacements files.

The following chapters describe the constitutive RD model applied to time-harmonic MRE as well as a subzone-based image reconstruction algorithm used for inversion processing of mechanical properties.

Chapter 4

Rayleigh damping model in Magnetic Resonance Elastography

The most common constitutive model applied to MRE is the viscoelastic (VE) model that assumes stiffness, μ to be a complex valued quantity. Here, the damping is expressed by an imaginary component of the complex shear modulus, μ_I, representing attenuation due to the elastic forces. Therefore, VE only accounts for a single damping effect (Oliphant et al., 2001).

To date, qualitative shear stiffness maps have proven to be the most successful imaging candidates in clinical diagnosis and showed promising potential for pathological tissue indication in liver (Asbach et al., 2008; Klatt et al., 2007; Venkatesh et al., 2008), breast (Sinkus et al., 2005) and the brain (Murphy et al., 2011; Xu et al., 2006). However, depending on the model formulation, identification of other parameters can also be of value. For example, estimated distribution of the loss modulus showed potential for improving diagnostic accuracy of the breast cancer (Siegmann et al., 2010; Sinkus et al., 2007) as well as indicated distinct decrease of the loss modulus corresponding to the tissue degradation associated with NPH (Streitberger et al., 2011).

However, imaging of the loss modulus failed in augmenting a diagnostic potential in other applications (Green et al., 2008; Sack et al., 2007; Sinkus et al., 2005). Alternatively, other parameters such as ratio of transverse anisotropy (Sinkus et al., 2005) or poroelastic hydraulic conductivity (Pattison et al., 2011), have also been proposed as a potential imaging candidates. Accurate estimation of these alternative mechanical properties requires data of very high quality, high SNR and full structural identifiably of the model.

The Rayleigh damping (RD) model is an extension of a VE model that treats both shear modulus and density as complex valued. This choice assumes that attenuation forces are proportional to both elastic and inertial forces in the material. Thus, the RD material model, when applied to MRE, allows these two damping parameters to be extracted from an MRE motion dataset and provides a more complete description of the energy attenuation occurring in the tissue under time-harmonic actuation.

The primary purpose of this research is to perform a thorough investigation of the RD model, applied to time-harmonic MRE, to accurately reconstruct viscoelastic properties and damping behaviour of the tissue simulating phantoms and *in vivo* healthy brain in different experimental settings. Details on the initial implementation of the model followed by a number of simulation studies can be found in (McGarry and Van Houten, 2008). The theory on RD is briefly outlined in this chapter.

4.1 Introduction to Rayleigh damping

Damping is a physical phenomenon that dissipates kinetic energy in an oscillatory system. The dynamic response of a system to an applied external oscillation force is dependant in part on the damping properties of the system. Therefore, damping must be considered for any type of dynamic analysis. For a single-degree-of-freedom system there are multiple damping models available, most commonly viscous damping, Coulomb damping and structural damping.

In mechanics, a dashpot is frequently used to represent a viscous damping element in which the damping force is assumed to be proportional to the relative velocity between two particles. The viscous damping model assumes that damping is linearly proportional to the velocity. Similarly, Coulomb damping uses the relative motion of surfaces, whilst structural damping assumes energy dissipation of continuous elements.

An alternative damping model, known as *Rayleigh damping*, introduces damping in the form of a damping matrix $\mathbf{C}$. This concept expresses the energy dissipation mechanism responsible for damping as a symmetric matrix of coefficients. A further

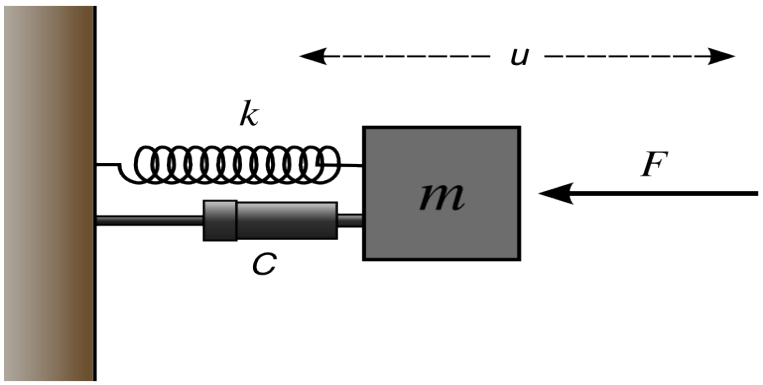

Figure 4.1 A mass-spring-damper system consisting of mass m, spring of stiffness k and a damper with damping coefficient c. F is an external force acting on the system causing displacement u. Image courtesy of Wikipedia. Image by IImari Karonen (llmari Karonen, 2005).

idealisation was that the symmetric damping matrix $\mathbf{C}$ is a linear combination of two terms. One is proportional to the mass matrix $\mathbf{M}$ (inertial damping) and the other to stiffness matrix $\mathbf{K}$ (elastic damping). It is commonly used in a range of structural dynamics fields, including civil structures and automative structures.

The RD model can be derived through the use of a mass-spring damped system. A mass - spring damped system (Fig. 4.1) is idealised with mass (m), spring constant (k) and viscous damping coefficient (c) subjected to an elastic restoring force (F_{res}):

$$F_{res} = -ku, \tag{4.1}$$

and a damping restoring force:

$$F_d = -cv = c\frac{du}{dt} = -c\dot{u}. \tag{4.2}$$

Assuming that the mass is a free body, based on Newton's second law, the total force F_{tot} on the body is defined:

$$F_{tot} = ma = m\frac{d^2u}{dt^2} = -m\ddot{u}. \tag{4.3}$$

Since $F_{tot} = F_{res} + F_d$,

$$m\ddot{u} = -ku - c\dot{u}. \tag{4.4}$$

Eq. 4.4 is a general form of the equation of motion and can be rearranged:

$$m\ddot{u} + c\dot{u} + ku = 0 \tag{4.5}$$

The equation of motion for a system with multi-degrees of freedom under time-harmonic force is given:

$$\mathbf{M\ddot{u}} + \mathbf{C\dot{u}} + \mathbf{Ku} = \mathbf{f_t} \tag{4.6}$$

where $\mathbf{M}$, $\mathbf{C}$ and $\mathbf{K}$ are mass, damping and stiffness matrices, respectively, and $\mathbf{u}$ is the displacement vector, with $\dot{\mathbf{u}}$ and $\ddot{\mathbf{u}}$ corresponding to the first and second order time derivatives, and $\mathbf{f_t}$ is an applied force vector, which is a function of time.

By orthogonal transformation, Eq. 4.6 expends (Humar, 2012):

$$\phi^T\mathbf{M}\phi\ddot{\mathbf{u}} + \phi^T\mathbf{C}\phi\dot{\mathbf{u}} + \phi^T\mathbf{K}\phi\mathbf{u} = \phi^T\mathbf{f_t}. \tag{4.7}$$

where ϕ is the normalised eigenvector of the system. Eq. 4.7 shows a diagonalised damping matrix using the eigenvalues and eigenvectors of its associated undamped mass and stiffness matrices. Thus, indicating, on this occasion, that the damping matrix $\mathbf{C}$ shares the same eigenvectors with $\mathbf{M}$ and $\mathbf{K}$. Normalised mass and stiffness matrices, $\hat{\mathbf{M}} = \phi^T\mathbf{M}\phi = 1$ and $\hat{\mathbf{K}} = \phi^T\mathbf{K}\phi = \omega_n^2$, take the form:

$$\hat{\mathbf{M}} = \begin{pmatrix} 1 & 0 & \cdots & 0 \\ 0 & 1 & \cdots & 0 \\ \vdots & \vdots & \ddots & \vdots \\ 0 & 0 & \cdots & 1 \end{pmatrix} \qquad \hat{\mathbf{K}} = \begin{pmatrix} \omega_1^2 & 0 & \cdots & 0 \\ 0 & \omega_2^2 & \cdots & 0 \\ \vdots & \vdots & \ddots & \vdots \\ 0 & 0 & \cdots & \omega_n^2 \end{pmatrix} \tag{4.8}$$

The resulting governing equation of motions can be decoupled completely (Humar, 2012) in this modal domain form, as defined:

$$\ddot{\mathbf{u}} + 2\xi\omega\dot{\mathbf{u}} + \omega^2\mathbf{u} = \mathbf{f}(\mathbf{t}), \tag{4.9}$$

where $\mathbf{C} = 2\xi\omega$, $\mathbf{u}$ is the normalised modal displacement vector, ξ is the damping ratio in an uncoupled mode, ω is the natural frequency of the system and $\mathbf{f}(\mathbf{t}) = \phi^T\mathbf{f_t}$ is the normalised force vector.

The above orthogonal transformation is only valid when the damping matrix is proportional to a linear function of the mass and stiffness matrices, $\mathbf{M}$ and $\mathbf{K}$. This proportionality relationship can be defined (Humar, 2012):

$$\mathbf{C} = \alpha\mathbf{M} + \beta\mathbf{K}. \tag{4.10}$$

The orthogonal transformation of the damping matrix, represented in Eq. 4.10, transforms the matrix $\mathbf{C}$ to the following form:

$$\phi^T\mathbf{C}\phi = \begin{pmatrix} \alpha + \beta\omega_1^2 & 0 & \cdots & 0 \\ 0 & \alpha + \beta\omega_2^2 & \cdots & 0 \\ \vdots & \vdots & \ddots & \vdots \\ 0 & 0 & \cdots & \alpha + \beta\omega_n^2 \end{pmatrix} \tag{4.11}$$

where by the symmetry of the terms it can be inferred that:

$$\begin{aligned} 2\xi_1\omega_1 &= \alpha + \beta\omega_1^2 \\ 2\xi_2\omega_2 &= \alpha + \beta\omega_2^2 \\ &\cdots\cdots\cdots\cdots \\ &\cdots\cdots\cdots\cdots \\ 2\xi_n\omega_2 &= \alpha + \beta\omega_n^2 \end{aligned} \tag{4.12}$$

Once the natural frequencies and mode shapes have been extracted, each of the decoupled equations can be analysed independently. Corresponding to the two parameter model, the damping ratio is thus defined, for a given mode:

$$\xi = \frac{1}{2}\left(\frac{\alpha}{\omega} + \beta\omega\right). \tag{4.13}$$

Eq. 4.13 indicates that the stiffness proportional term ($\beta\omega$) contributes damping linearly proportional to the response frequency and the mass proportional term (α/ω) contributes damping inversely proportional to the response frequency. From this two parameter damping model, the relationship between the damping ratio and the input frequency is schematically demonstrated in Fig. 4.2.

Fig. 4.2 shows that the mass proportional damping effect is dominant in the lower frequencies and the stiffness proportional damping is dominant at the higher frequencies. Therefore, the α and β coefficients govern the response to lower and higher input frequencies, ω, respectively. An iterative solution is also possible and can be applied by the best-fit values of α and β given more than two values of ω.

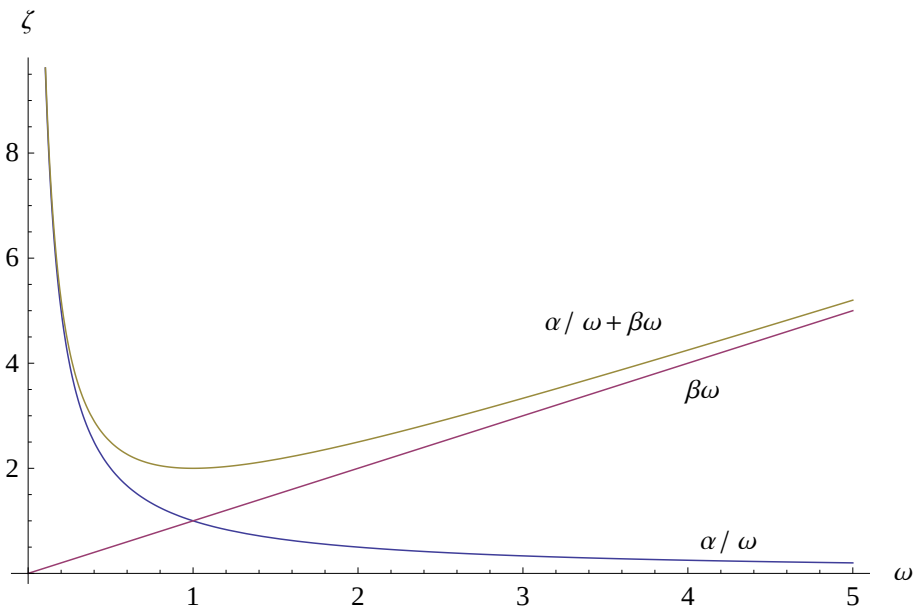

Figure 4.2 Schematic representation of a two-parameter RD model.

4.2 Equation of a linear elasticity

Based on Newton's second law, motion must satisfy the conditions of elastic equilibrium of forces defined (Slaughter, 2002) :

$$\nabla \cdot \boldsymbol{\sigma} + \mathbf{b} = \rho \ddot{\mathbf{u}}, \tag{4.14}$$

where $\boldsymbol{\sigma}$ is the stress tensor, $\mathbf{b}$ represents the internal body force, ρ is the density of a material and $\mathbf{u}$ is the displacement vector. For isotropic and homogeneous materials, Hooke's law in three dimension can be represented as:

$$\boldsymbol{\sigma} = 2\mu\boldsymbol{\epsilon} + \lambda \mathrm{tr}(\boldsymbol{\epsilon})\boldsymbol{I}, \tag{4.15}$$

where $\boldsymbol{\epsilon}$ is a volumetric strain tensor, $\mathrm{tr}(\boldsymbol{\epsilon})$ is a trace function of $\boldsymbol{\epsilon}$, and $\boldsymbol{I}$ is a second-order identity tensor. Substituting Eq. 4.15 into Eq. 4.14 results in:

$$\nabla \cdot (2\mu\boldsymbol{\epsilon} + \lambda \mathrm{tr}(\boldsymbol{\epsilon})\boldsymbol{I}) + \mathbf{b} = \rho \frac{\partial^2 \mathbf{u}}{\partial t^2}. \tag{4.16}$$

Here, the volumetric strain tensor, $\boldsymbol{\epsilon}$, is defined through displacement, $\mathbf{u}$:

$$\boldsymbol{\epsilon} = \frac{1}{2}\Big[\nabla \mathbf{u} + \nabla \mathbf{u}^T\Big]. \tag{4.17}$$

Substituting Eq. 4.17 into Eq. 4.16 leads to the equation of linear elasticity, represented in partial differential equation (PDE) form, commonly known as Navier's equation:

$$\nabla \cdot (\mu(\nabla \mathbf{u} + \nabla \mathbf{u}^T)) + \nabla(\lambda \nabla \cdot \mathbf{u}) = \rho \frac{\partial^2 \mathbf{u}}{\partial t^2}, \tag{4.18}$$

where $\mathbf{u}$ is the measured displacement data, μ and λ are material stiffness parameters known as Lamé's constants, and ρ is the density of the material. For the time-

harmonic motions, $\mathbf{u}$ could be represented as $\mathbf{u} = \hat{\mathbf{u}}e^{i\omega t}$, giving $\partial^2\mathbf{u}/\partial t^2 = -\omega^2\hat{\mathbf{u}}$.

In comparison to static elastography methods, where knowledge of boundary conditions is essential (Manduca, 2005), in dynamic methods absolute estimates of the material properties can be generated only with a local knowledge of displacement and density. Thus, measurement of a propagating shear wave in a small region is enough to determine the shear modulus of the tissue in that region.

4.3 Complex modulus from viscoelastic theory

Viscoelastic materials possess both viscous and elastic characteristics that can be modelled using an appropriate combination of springs and dashpots in series and parallel. This behaviour can be described using Hooke's law, but only for complex valued displacements that account for the phase changes generated due to the damping nature of the viscoelastic material. Complex moduli, Y, at frequency ω can be formulated as $Y = Y_R + iY_I$. Purely elastic materials have stress and strain in phase, so that the response of one caused by the other is immediate. The complex moduli of a purely elastic element is defined:

$Y_R = E$ and $Y_I = 0$.

In purely viscous materials, strain lags stress by 90 degrees of phase lag. The complex moduli of a purely viscous element is then defined:

$Y_R = 0$ and $Y_I = \eta$.

The complex moduli of elastic and viscoelastic elements, such as the Maxwell element, shown in Fig. 4.3 (a), in series is defined:

$$Y_R = \frac{\omega\eta^2 E}{E^2 + \omega^2\eta^2}, \qquad Y_I = \frac{\omega\eta E^2}{E^2 + \omega^2\eta^2}. \tag{4.19}$$

Equally, the complex moduli of elastic and viscoelastic elements in parallel, such as a Voigt element, shown in Fig. 4.3 (b), is defined:

$Y_R = E$ and $Y_I = \eta$,

Fig. 4.3 (c) represents a generalised viscoelastic element consisting of three components: a main elastic element, E, in parallel with two serialised elements, E and η. Such an element is capable of representing a variety of behaviours, from that of a linear elastic element to that of a viscous fluid, through manipulations of its various parameter values. The complex modulus of such an element can be written:

$$Y = E_0 + \frac{E\omega^2\eta^2 + iE^2\omega\eta}{E^2 + \omega^2\eta^2}. \tag{4.20}$$

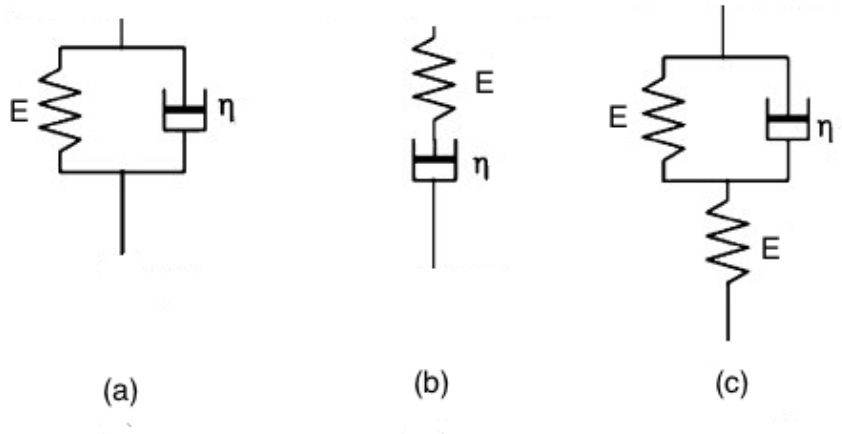

Figure 4.3 Schematic arrangements of (a) the Maxwell model, (b) the Kelvin-Voigt model, and (c) a three-element standard linear model for linear viscoelastic materials

The corresponding PDE description of motion in 3D becomes:

$$\nabla \cdot (\mu^*(\nabla \mathbf{u} + \nabla \mathbf{u}^T)) + \nabla(\lambda^* \nabla \cdot \mathbf{u}) = \rho \frac{\partial^2 \mathbf{u}}{\partial t^2}, \tag{4.21}$$

where $\lambda^* = \lambda_R + i\omega\lambda_I$ and $\mu^* = \mu_R + i\omega\mu_I$, with λ_R and λ_I are defined:

$$\begin{aligned} \lambda_R &= \frac{\nu}{(1+\nu)(1-2\nu)} \left[E_0 + \frac{E\omega^2\eta^2}{E^2 + \omega^2\eta^2} \right] \\ \lambda_I &= \frac{\nu}{(1+\nu)(1-2\nu)} \left[\frac{E^2\eta}{E^2 + \omega^2\eta^2} \right], \end{aligned} \tag{4.22}$$

while μ_R and μ_I are defined:

$$\mu_R = \frac{1}{2(1+\nu)}\left[E_0 + \frac{E\omega^2\eta^2}{E^2+\omega^2\eta^2}\right]$$
$$\mu_I = \frac{1}{2(1+\nu)}\left[\frac{E^2\eta}{E^2+\omega^2\eta^2}\right]. \tag{4.23}$$

4.4 The wave equation with damping

Navier's equation with damping force proportional to the velocity is defined:

$$\nabla\cdot(\mu(\nabla\mathbf{u}+\nabla\mathbf{u}^T))+\nabla(\lambda\nabla\cdot\mathbf{u}) = \rho\frac{\partial^2\mathbf{u}}{\partial t^2}+\bar{\alpha}\frac{\partial\mathbf{u}}{\partial t} \tag{4.24}$$

where $\bar{\alpha}$ is the real valued damping proportionality constant. Assuming time-harmonic motion of the form $\mathbf{u}(\mathbf{x},t)=\hat{\mathbf{u}}e^{iwt}$ gives:

$$\nabla\cdot(\mu(\nabla\hat{\mathbf{u}}+\nabla\hat{\mathbf{u}}^T))+\nabla(\lambda\nabla\cdot\hat{\mathbf{u}}) = i\bar{\alpha}\omega\hat{\mathbf{u}}-\rho\omega^2\hat{\mathbf{u}}; \tag{4.25}$$

Likewise substituting a complex density of the form $\rho=\rho_R+i\rho_I$ into Eq. 4.18 yields:

$$\nabla\cdot(\mu(\nabla\hat{\mathbf{u}}+\nabla\hat{\mathbf{u}}^T))+\nabla(\lambda\nabla\cdot\hat{\mathbf{u}}) = -\rho_R\omega^2\hat{\mathbf{u}}-i\rho_I\omega^2\hat{\mathbf{u}}. \tag{4.26}$$

Eq. 4.26 is equivalent to Eq. 4.25 when:

$$\rho_I = -\frac{\bar{\alpha}}{\omega} \tag{4.27}$$

4.5 Rayleigh damping model in time-harmonic MRE

A time-harmonic RD Finite Element (FE) model is implemented through the use of complex shear modulus and density together with incompressible elasticity equations (McGarry and Van Houten, 2008). In time-harmonic steady state elastography motion and forces can be written as $\mathbf{u}(\mathbf{x},t) = \hat{\mathbf{u}}e^{i\omega t}$ and $\mathbf{f}(\mathbf{x},t) = \hat{\mathbf{f}}e^{i\omega t}$, respectively. Thus, Eq. 4.6 can be written:

$$\Big[-\omega^2\mathbf{M} + i\omega\mathbf{C} + \mathbf{K}\Big]\hat{\mathbf{u}} = \hat{\mathbf{f}}. \tag{4.28}$$

Implementation of a RD assumption, described by Eq. 4.10, leads to the following transformation of Eq. 4.28:

$$\Big[-\omega^2\mathbf{M} + i\omega(\alpha\mathbf{M} + \beta\mathbf{K}) + \mathbf{K}\Big]\hat{\mathbf{u}} = \hat{\mathbf{f}}. \tag{4.29}$$

Further expansion, followed by collecting of similar terms, leads to:

$$\Big[(i\omega\alpha - \omega^2)\mathbf{M} + (1 + i\omega\beta)\mathbf{K}\Big]\hat{\mathbf{u}} = \hat{\mathbf{f}}, \tag{4.30}$$

$$\Big[-\omega^2\left(1 - \frac{i\alpha}{\omega}\right)\mathbf{M} + (1 + i\omega\beta)\,\mathbf{K}\Big]\hat{\mathbf{u}} = \hat{\mathbf{f}}, \tag{4.31}$$

where $\mathbf{K}$ and $\mathbf{M}$ are initial undamped stiffness and mass distributions, respectively. All terms in $\mathbf{M}$ contain the density, ρ, and all terms in $\mathbf{K}$ contain the shear modulus, μ. Thus, these parameters can be moved outside the matrices, giving:

$$\left[-\omega^2\left(\rho - \frac{i\alpha\rho}{\omega}\right)\hat{\mathbf{M}} + (\mu + i\omega\beta\mu)\,\hat{\mathbf{K}}\right]\hat{\mathbf{u}} = \hat{\mathbf{f}}, \tag{4.32}$$

where $\hat{\mathbf{M}}$ and $\hat{\mathbf{K}}$ are the normalised mass and stiffness matrices, respectively.

Eq. 4.32 shows that the RD model can be implemented using a complex density

$\rho = \rho_R + i\rho_I$ and complex shear modulus $\mu = \mu_R + i\mu_I$, where μ_R and ρ_R describe the original shear modulus and density in the undamped system, while μ_I and ρ_I can be expressed in terms of the Rayleigh damping parameters:

$$\rho_R = \rho, \; and \; \rho_I = \frac{-\alpha\rho}{\omega} \tag{4.33}$$

$$\mu_R = \mu, \; and \; \mu_I = \omega\beta\mu. \tag{4.34}$$

Eq. 4.33 is of the same form as Eq. 4.27, with $\bar{\alpha} = \rho\alpha$. Accepting that the terms $(1 - i\alpha/\omega)$ and $(1 + i\omega\beta)$ describe spatial distribution of RD parameters, Eq. 4.32 can be simplified:

$$\left[-\omega^2\rho\hat{\mathbf{M}} + \mu\hat{\mathbf{K}}\right]\hat{\mathbf{u}} = \hat{\mathbf{f}}, \tag{4.35}$$

The damping ratio, ξ_d, is then defined:

$$\xi_d = \frac{1}{2}\left(\frac{\alpha}{\omega} + \beta\omega\right), \tag{4.36}$$

and can be rewritten using Eq. 8.6 as:

$$\xi_d = \frac{1}{2}\left(\frac{\mu_I}{\mu_R} - \frac{\rho_I}{\rho_R}\right). \tag{4.37}$$

The damping ratio provides quantitative information about the attenuation within the medium. It is often multiplied by 100 and expressed as a percentage. In pure VE materials, for example, the density ratio will be zero as imaginary density equals zero by definition. To predict realistic behavior within the material, it is important to consider the signs of the terms in Eq. 4.37. Thus, the imaginary density must be negative and the imaginary shear modulus positive.

4.6 An inertial explanation of Rayleigh damping

4.6.1 Inertial force and Newton's 2^{nd} law

Based on Newton's 2^{nd} law of motion:

$$\mathbf{F} = \frac{\partial \mathbf{L}}{\partial t}, \tag{4.38}$$

where $\mathbf{L}$ is the *momentum* of the system, defined by $m\dot{\mathbf{u}}$ for mass m and velocity $\dot{\mathbf{u}}$. For a continuum, defined by volumetric quantities, the momentum of a unit volume is given by $\rho\dot{\mathbf{u}}$, where ρ is the mass density. The body force, $\mathbf{b}$, due to inertial forces is then, from Eq. 4.38, defined:

$$\mathbf{b} = \frac{\partial\left(\rho\dot{\mathbf{u}}\right)}{\partial t} = \frac{d\rho}{dt}\frac{\partial \mathbf{u}}{\partial t} + \rho\frac{\partial^2 \mathbf{u}}{\partial t^2} \tag{4.39}$$

for displacement $\mathbf{u}$. For a *time-harmonic* system, where the time-dependent behavior of $\mathbf{u}$ at angular frequency ω is given by $\mathbf{u}(\mathbf{x}, t) = \Re\Big\{\hat{\mathbf{u}}e^{i\omega t}\Big\}$, one obtains:

$$\begin{aligned}
\frac{\partial \mathbf{u}}{\partial t} &= \Re\Big\{i\omega\hat{\mathbf{u}}e^{i\omega t}\Big\} \\
&= \Re\Big\{i\omega(\mathbf{u}_R + i\mathbf{u}_I)(\cos\omega t + i\sin\omega t)\Big\} \\
&= \Re\Big\{i\omega\mathbf{u}_R\cos\omega t - \omega\mathbf{u}_R\sin\omega t - \omega\mathbf{u}_I\cos\omega t - i\omega\mathbf{u}_I\sin\omega t)\Big\} \\
&= -\omega\Big[\mathbf{u}_R\sin\omega t + \mathbf{u}_I\cos\omega t\Big]
\end{aligned} \tag{4.40}$$

for the complex valued $\mathbf{u} = \mathbf{u}_R + i\mathbf{u}_I$. Likewise:

$$\begin{aligned}\frac{\partial^2 \mathbf{u}}{\partial t^2} &= \Re\Big\{ -\omega^2 \hat{\mathbf{u}} e^{i\omega t} \Big\} \\ &= \Re\Big\{ -\omega^2 (\mathbf{u}_R + i\mathbf{u}_I)(\cos\omega t + i \sin\omega t) \Big\} \\ &= \Re\Big\{ -\omega^2 (\mathbf{u}_R \cos\omega t + i\mathbf{u}_I \sin\omega t + i\mathbf{u}_I \cos\omega t - u_I \sin\omega t) \Big\} \\ &= -\omega^2 \Big[\mathbf{u}_R \cos\omega t - \mathbf{u}_I \sin\omega t \Big]. \end{aligned} \tag{4.41}$$

Substituting Eq. 4.41 and Eq. 4.40 into Eq. 4.39, leads to the inertial force description"

$$\mathbf{b} = -\omega \frac{\partial \rho}{\partial t} (\mathbf{u}_R \sin\omega t + \mathbf{u}_I \cos\omega t) - \omega^2 \rho (\mathbf{u}_R \cos\omega t - \mathbf{u}_I \sin\omega t), \tag{4.42}$$

where the term $\partial\rho/\partial t$ describes changes in density occurring at angular frequency ω.

4.6.2 Time-harmonic Rayleigh damping

The time harmonic formulation of a RD elastic system results in a complex valued density, $\rho = \rho_R + i\rho_I$, which scales the acceleration term in the elastic equilibrium equation to give the inertial body forces for the system, defined

$$
\begin{aligned}
\mathbf{b} &= \rho\frac{\partial^2\mathbf{u}}{\partial t^2} \\
&= \Re\Big\{(\rho_R + i\rho_I)\frac{\partial^2\hat{\mathbf{u}}e^{i\omega t}}{\partial t^2}\Big\} \\
&= \Re\Big\{-\omega^2\left(\rho_R + i\rho_I\right)\hat{\mathbf{u}}e^{i\omega t}\Big\} \\
&= \Re\Big\{-\omega^2(\rho_R + i\rho_I)(\mathbf{u}_R + i\mathbf{u}_I)(\cos\omega t + i\sin\omega t)\Big\} \\
&= \Re\Big\{-\omega^2(\rho_R\mathbf{u}_R + i\rho_R\mathbf{u}_I + i\rho_I\mathbf{u}_R - \rho_I\mathbf{u}_I)(\cos\omega t + i\sin\omega t)\Big\} \\
&= \Re\Big\{-\omega^2(\rho_R\mathbf{u}_R\cos\omega t + i\rho_R\mathbf{u}_R\sin\omega t + i\rho_R\mathbf{u}_I\cos\omega t - \rho_R\mathbf{u}_I\sin\omega t + \\
&\qquad i\rho_I\mathbf{u}_R\cos\omega t - \rho_I\mathbf{u}_R\sin\omega t - \rho_I\mathbf{u}_I\cos\omega t - i\rho_I\mathbf{u}_I\sin\omega t)\Big\} \\
&= \Re\Big\{-\omega^2\Big[(\rho_R\mathbf{u}_R - \rho_I\mathbf{u}_I)\cos\omega t - (\rho_R\mathbf{u}_I + \rho_I\mathbf{u}_R)\sin\omega t + \\
&\qquad i\rho_R\mathbf{u}_I + i\rho_I\mathbf{u}_R)\cos\omega t + (i\rho_R\mathbf{u}_R - i\rho_I\mathbf{u}_I)\sin\omega t\Big]\Big\} \\
&= -\omega^2\Big[(\rho_R\mathbf{u}_R - \rho_I\mathbf{u}_I)\cos\omega t - (\rho_I\mathbf{u}_R + \rho_R\mathbf{u}_I)\sin\omega t\Big]. \qquad (4.43)
\end{aligned}
$$

4.6.3 Comparison of the two systems

Comparing the inertial body forces given by Eqs. 4.42 & 4.43, yields

$$
\begin{aligned}
&-\omega\frac{\partial\rho}{\partial t}(\mathbf{u}_R\sin\omega t + \mathbf{u}_I\cos\omega t) - \omega^2\rho(\mathbf{u}_R\cos\omega t - \mathbf{u}_I\sin\omega t)\cdots \\
&\cdots = -\omega^2((\rho_R\mathbf{u}_R - \rho_I\mathbf{u}_I)\cos\omega t - (\rho_I\mathbf{u}_R + \rho_R\mathbf{u}_I)\sin\omega t) \qquad (4.44)
\end{aligned}
$$

and simplifying and collecting similar terms leads to:

$$\begin{aligned}
&\frac{\partial \rho}{\partial t}\left[\mathbf{u}_R \sin\omega t + \mathbf{u}_I \cos\omega t\right] + \omega\rho\left[\mathbf{u}_R \cos\omega t - \mathbf{u}_I \sin\omega t\right] \cdots \\
&\cdots = \omega\Big[\left(\rho_R \mathbf{u}_R - \rho_I \mathbf{u}_I\right)\cos\omega t - \left(\rho_I \mathbf{u}_R + \rho_R \mathbf{u}_I\right)\sin\omega t\Big] \\
&\cdots = -\omega\rho_I(\mathbf{u}_R \sin\omega t + \mathbf{u}_I \cos\omega t) + \omega\rho_R(\mathbf{u}_R \cos\omega t - \mathbf{u}_I \sin\omega t)
\end{aligned} \tag{4.45}$$

where, from Eq. 4.45, there are equivalent terms, defined:

$$\frac{\partial \rho}{\partial t} = -\omega\rho_I \quad \Rightarrow \quad \rho_I = -\frac{1}{\omega}\frac{\partial \rho}{\partial t} \tag{4.46}$$

$$\omega\rho = \omega\rho_R \quad \Rightarrow \quad \rho = \rho_R. \tag{4.47}$$

According to Eq. 4.46, the imaginary density term in a RD continuum, ρ_I, describes the time rate of change in mass density scaled by the angular frequency, ω. For a compressible material, this would indicate some level of compression within the material, possibly indicated by the presence of divergence in the displacement field.

For an incompressible (or saturated) porous material, this change in density would represent the flow of fluid into and out of the solid elastic matrix. It is important to note that the term $\partial\rho/\partial t$ describes the *amplitude* of a time harmonic change at frequency ω, and thus $\partial\rho/\partial t > 0$, which is equivalent to the requirement that $\rho_I < 0$ to ensure that energy is lost from the system due to this mass transfer, rather than gained. Lastly, Eq. 4.47 shows that the real valued density term in a RD system, ρ_R, describes the actual mass density of the continuum, as expected.

4.6.4 Rheological interpretation of the imaginary density

The rheological interpretation of the imaginary density term can be approached by considering porous media. Porous media can be considered to consist of two compartments: solid and fluid. Thus, this poroelastic system will be characterized

by two pressure levels: a pressure level associated with the fluid compartment, P_f, and a pressure level associated with solid, P_s, compartments. When $P_f > P_s$, the fluid compartment will expand causing the solid compartment to shrink and vice versa. The total pressure level in the volume can be defined:

$$P_{tot} = \left(\frac{V_s}{V_{tot}}\right) P_s + \left(\frac{V_f}{V_{tot}}\right) P_f \tag{4.48}$$

In steady state time harmonic elastography, the compression rate is a function of time. Thus:

$$\frac{\partial P_{tot}}{\partial t} \neq 0 \tag{4.49}$$

Therefore, an imaginary density represents the rate of density change in the porous voxel due to the volume fraction between fluid and solid compartments. This effect is illustrated in Fig. 4.4

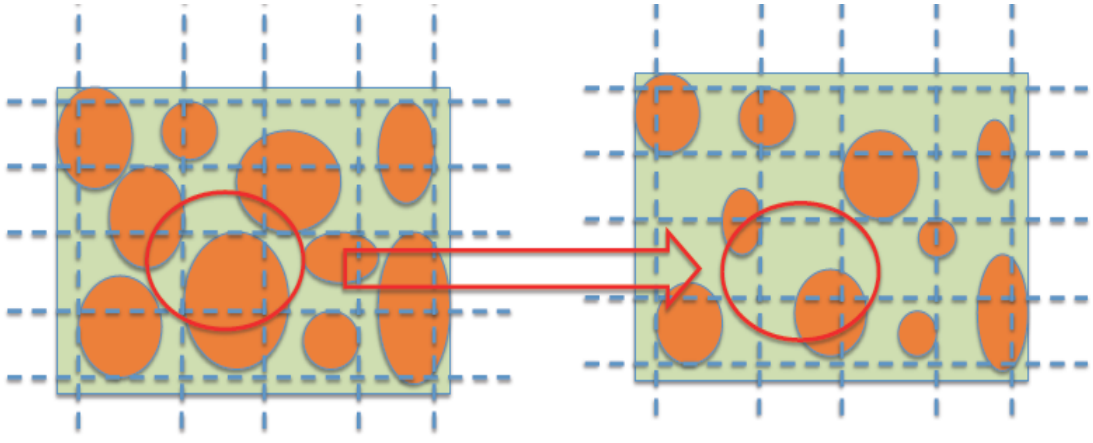

Figure 4.4 Schematic representation of the volume change in poroelastic media. Orange circles represent fluid compartments wiring the elastic solid, depicted in a green clolor

4.7 Summary

A time-harmonic RD FE model is implemented through the use of complex shear modulus and density together with the isotropic nearly incompressible and mildly compressible elasticity equations. Assumption of complex shear modulus and density allows incorporation of two damping mechanisms: the imaginary shear modulus, μ_I, represents damping effects proportional to the elastic forces within the media, and defined:

$$\mu_I = \omega\beta\mu. \tag{4.50}$$

while the imaginary density, ρ_I, describes damping related to the inertial forces, and defined:

$$\rho_I = \frac{-\alpha\rho}{\omega} \tag{4.51}$$

The real parts of the shear modulus and density, μ_R and ρ_R, represent actual stiffness and true density of the material, respectively. The combination of these two effects may allow better characterisation of the microscale interactions that cause motion attenuation, compared to the more commonly used viscoelastic model, which does not incorporate inertial damping effects.

Rheologically, the imaginary shear modulus represents the loss modulus of the material, and can be attributed to the viscosity measurement. On the other hand, rheological interpretation of imaginary density can be associated with the rate of density change in the porous voxel due to the volume fraction between fluid and solid compartments.

The damping ratio, ξ_d, provides quantitative information about the attenuation within the medium and can be defined:

$$\xi_d = \frac{1}{2}\left(\frac{\alpha}{\omega} + \beta\omega\right), \tag{4.52}$$

and can be rewritten using Eq. 8.6 as:

$$\xi_d = \frac{1}{2}\left(\frac{\mu_I}{\mu_R} - \frac{\rho_I}{\rho_R}\right). \tag{4.53}$$

The motion amplitude field, $\mathbf{u}$, is simulated from the Navier's equation:

$$\nabla \cdot (\mu(\nabla \mathbf{u} + \nabla \mathbf{u}^T)) + \nabla(\lambda \nabla \cdot \mathbf{u}) = \rho \frac{\partial^2 \mathbf{u}}{\partial t^2}, \tag{4.54}$$

where λ and μ are the first and second Lamé's parameters, ρ is the density of the material, and ω is the actuation frequency. Computed motion data is required to estimate three material properties: complex shear modulus and imaginary density term. Estimation of the material properties is performed through a constrained optimisation algorithm, where the difference between measured data and modelled simulation is minimised.

Chapter 5

Subzone-based image reconstruction algorithm

Mechanical property reconstruction is performed using a previously introduced 3D finite-element based nonlinear inversion technique that utilises MR captured motion data (Van Houten et al., 2001). The algorithm operates on small overlapping subzones that are processed in a hierarchical order determined by progressive error minimisation. The final output of the algorithm is reconstructed distributions of the specified material properties.

The research conducted in this thesis is based on the research code which has been developed over more than 10 years by the University of Canterbury and other collaborating institutes and universities. Since the detailed description of the algorithm is well documented elsewhere, only a summary of the main features is reported here. As the author did not have access to the source code, no contribution to the code development has been made within the scope of this research. Instead, significant efforts have been made towards optimising the output of the existing version of the algorithm to achieve the best performance of the elastographic based reconstruction output. For a more detailed treatment about initial development, implementation and testing of the algorithm refer to (Van Houten et al., 2005, 1999, 2003, 2001, 1999).

Image reconstruction in MR elastography is formulated as a constrained optimisation problem that involves two steps: the *forward problem solution* and the *parameter set update*. The solution of the forward computational problem produces a displacement field throughout the reconstruction domain by solving a system of linear partial differential equations (PDEs). The parameter update step then iteratively fits a set of mechanical properties, such that the FE model reproduces the MRI measured displacements as closely as possible.

5.1 The subzone concept

MRE typically produces very large data sets with the motion information encoded with relatively high MR pixel level resolution. The FE formulation for such a large data set would require many nodal points leading to long computations. In addition, the condition of the inverse problem decreases as the size of the problem increases.

To overcome these issues, a subzone concept was introduced to the FE based nonlinear reconstruction algorithm (Van Houten et al., 1999). The MR-detected motion dataset is refined into small data subsets, called *subzones*, where the Dirichlet boundary conditions, captured from the measured motion data, are applied. Results from the individual subsets can then be combined to encompass the whole geometry using an approach known as the *overlapping subzone method*. This method has been proven successful in reconstructing VE mechanical property distributions using MR-detected motion datasets from both tissue-simulating phantoms and *in-vivo* biological tissues (Van Houten et al., 2011, 2003, 1999). However, it has not been proven for RD model formulation.

A schematic diagram of the subzone concept is presented on Fig. 5.1. The total problem domain, Ω, is made up of multiple subdomains, or subzones, Ω_z. Displacement data is available throughout the Ω, leading to an appropriate formulation of the boundary conditions, Γ_z, at each subzone. Individual reconstructions that are performed on a set of subzones Ω_z can be combined to form a material property description $\boldsymbol{\theta}_z$ for the total problem domain Ω at MR pixel resolution. The technique effectively replaces the minimisation of a global objective function $\mathbf{F}_\Omega(\boldsymbol{\theta}_\Omega)$ with a sum of smaller minimizations $\mathbf{F}_z(\boldsymbol{\theta}_z)$, yielding a problem, defined:

$$\min \mathbf{F}_\Omega(\boldsymbol{\theta}_\Omega) = \min \left\{ \sum_{z=1}^{N_z} \mathbf{F}_z(\boldsymbol{\theta}_z) \right\} = \sum_{z=1}^{N_z} \min \mathbf{F}_z(\boldsymbol{\theta}_z), \tag{5.1}$$

where Ω represents the entire problem domain; and z represents the z'th subzone of a total of number of subzones N_z.

This approach offers a number of advantages. Primarily, the size of inversion problem and associated computational load is significantly reduced. In the earlier

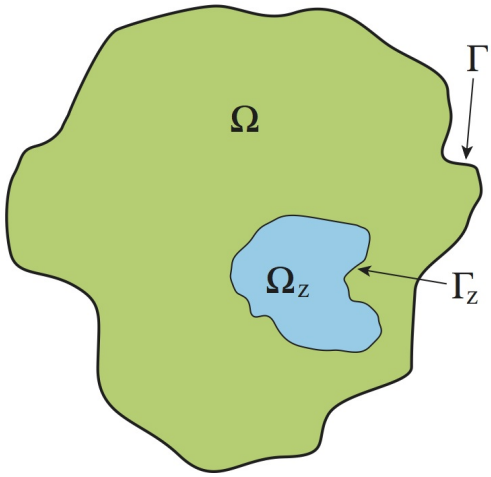

Figure 5.1 Schematic representation of the subzone concept. The global problem domain is represented by Ω with boundary Γ, and the domain of the subzone is represented by Ω_z with boundary Γ_z (McGarry, 2008).

versions of the algorithm (Van Houten et al., 2011, 2003, 1999), the size of the subzones was set to be an input variable to suit available computational resources. A new version of an algorithm allows automatic calculation of the subzone's size (McGarry et al., 2012). Secondly, the subzone concept enables a macro-parallelisation strategy that allows multiple subzones to be processed simultaneously on separate processors. Within an iteration, each subzone inversion is independent of the others. This approach thus enables efficient use of available computational resources by minimising inter-process communication.

Another advantage is improved reliability of the reconstruction results. The inverse optimisation methods are generally unreliable to some extent due to the nonlinear nature of the minimisation process (Glowinski, 2008). This lack of robustness is typically associated with a "local minima problem", where solutions converge to a local error minima rather than the global minima that correspond to the true parameter description. Another possible scenario is when the optimisation process fails to make any progress in reducing the error, but is not at a global optimal minimum. Because the subzone method encompasses a number of minimizations associated with different subzones, the occasional failure on one of the subzones will not lead to the failure of the entire reconstruction. The solution from the failed subzone can simply be ignored, and a different subzone or set of subzones can be defined that encompass the region of the failed subzone. Provided these subzones

are successful, the reconstructed material property description will still cover the full domain Ω. Again, it is important to note that these advantages have only been shown for VE reconstruction problem and remain to be verified in RD cases.

The subzone method is implemented using the Message Passing Interface (MPI). Each of these subzones can be assigned to a particular processor in the parallel computing environment. The geometry of subzones will dictate the number of nodes inside and thus the size of the optimisation problem each processor must solve. There are typically several thousands nodes in each subzone. The overall solution is iteratively refined, based on optimising the agreement between measured and calculated displacements.

The computational framework defines one of the processors as the *master* processor, which administrates tasks, such as dividing the problem into subzones, assigning each of them to the different processors (commonly called as *slave* processors), receiving the completed material property solutions, and combining these into an overall solution across entire domain. Once a subzone is sent to a *slave* processor, the inverse problem is undertaken for a particular subzone using the method outlined in section 5.3. When the master processor receives the solution for a particular zone, it inserts the solution into the correct location on a global solution array. Because the subzones overlap, multiple values for some material properties will be returned. These are dealt with by using an average value. The centre point for the grid of subzones is determined randomly, therefore a different set of subzones will be generated each time the geometry is subdivided, reducing the occurrence of boundary related artefacts in the final material property image.

5.2 The forward problem

The forward computational problem solves for the displacement $\mathbf{u}$ based on Navier's equation for isotropic linear elasticity. In the time-harmonic case, the discretised form of Navier's equation for VE material is formulated:

$$\nabla \cdot (\mu(\nabla \mathbf{u} + \nabla \mathbf{u}^T)) + \nabla(\lambda \nabla \cdot \mathbf{u}) = -\rho\omega^2 \mathbf{u}; \tag{5.2}$$

where $\mathbf{u}$ is the displacement within the medium; μ and λ are the shear stiffness and the first Lame's parameter, respectively; ρ is the density of the material. In the case of a nearly incompressible RD material, a PDE form of Navier's equation can be written:

$$\nabla \cdot (\mu(\nabla \mathbf{u} + \nabla \mathbf{u}^T)) - \nabla(\frac{1}{3}\nabla \cdot \mathbf{u}) - \nabla P = -\rho\omega^2 \mathbf{u}; \tag{5.3}$$

where the pressure term ∇P is related to volumetric changes through the bulk modulus, K :

$$\nabla P = K \nabla \cdot \mathbf{u} = K \left(\frac{\partial u_x}{\partial x} + \frac{\partial u_y}{\partial y} + \frac{\partial u_z}{\partial z} \right); \tag{5.4}$$

Eq. 5.3 effectively describes behaviour of a material with a Poisson's ratio of 0.499 and higher. The standard compressible elastic equations of Eq. 5.2 become highly sensitive for Poisson's ratios above about 0.495.

In 3D, Eq. 5.2 can be expanded in component form:

$$\begin{aligned}
\hat{\mathbf{x}} : 2\frac{\partial}{\partial x}\mu\frac{\partial u_x}{\partial x} + \frac{\partial}{\partial y}\mu\left(\frac{\partial u_x}{\partial y} + \frac{\partial u_y}{\partial x}\right) + \frac{\partial}{\partial z}\mu\left(\frac{\partial u_x}{\partial z} + \frac{\partial u_z}{\partial x}\right) + \\
+\frac{\partial}{\partial x}\left[\lambda\left(\frac{\partial u_x}{\partial x} + \frac{\partial u_y}{\partial y} + \frac{\partial u_z}{\partial z}\right)\right] = -\rho\omega^2 u_x; \\
\hat{\mathbf{y}} : \frac{\partial}{\partial x}\mu\left(\frac{\partial u_y}{\partial x} + \frac{\partial u_x}{\partial y}\right) + 2\frac{\partial}{\partial y}\mu\frac{\partial u_y}{\partial y} + \frac{\partial}{\partial z}\mu\left(\frac{\partial u_y}{\partial z} + \frac{\partial u_z}{\partial y}\right) + \\
+\frac{\partial}{\partial y}\left[\lambda\left(\frac{\partial u_x}{\partial x} + \frac{\partial u_y}{\partial y} + \frac{\partial u_z}{\partial z}\right)\right] = -\rho\omega^2 u_y; \\
\hat{\mathbf{z}} : \frac{\partial}{\partial x}\mu\left(\frac{\partial u_z}{\partial x} + \frac{\partial u_x}{\partial z}\right) + \frac{\partial}{\partial y}\mu\left(\frac{\partial u_z}{\partial y} + \frac{\partial u_y}{\partial z}\right) + 2\frac{\partial}{\partial z}\mu\frac{\partial u_z}{\partial z} + \\
+\frac{\partial}{\partial z}\left[\left(\lambda\left(\frac{\partial u_x}{\partial x} + \frac{\partial u_y}{\partial y} + \frac{\partial u_z}{\partial z}\right)\right] = -\rho\omega^2 u_z;
\end{aligned} \tag{5.5}$$

where u_x, u_y and u_z are the x, y and z components of the displacement vector $\mathbf{u}$, respectively. In the 3D FE formulation, solution of Eg. 5.5 is facilitated by

expending the approximate displacement solution onto the set of FE basis functions (ϕ_j) so that:

$$\begin{aligned} \hat{u}_x &= \sum_{j=1}^{N} u_{xj}\phi_j, \\ \hat{u}_y &= \sum_{j=1}^{N} u_{yj}\phi_j, \\ \hat{u}_z &= \sum_{j=1}^{N} u_{zj}\phi_j. \end{aligned} \tag{5.6}$$

Similarly, the unknown reconstructed parameters $\mu(x, y, z)$, $\lambda(x, y, z)$ and $\rho(x, y, z)$ can be expressed:

$$\begin{aligned} \mu(x, y, z) &= \sum_{k=1}^{N} \mu_k \phi_k(x, y, z), \\ \lambda(x, y, z) &= \sum_{k=1}^{N} \lambda_k \phi_k(x, y, z), \\ \rho(x, y, z) &= \sum_{k=1}^{N} \rho_k \phi_k(x, y, z). \end{aligned} \tag{5.7}$$

where $\phi_k(x, y, z)$ is a continuous FE basis function and μ_k, λ_k and ρ_k are the discrete parameter values at node k of the N total nodes within the FE mesh.

Substituting Eqs. 5.7 and 5.8 into Eq. 5.2 leads to the discrete algebraic system:

$$\mathbf{A}(\mu, \lambda, \rho)\{\mathbf{u}\} = \{\mathbf{b}\}, \tag{5.8}$$

where $\mathbf{A}$ is a matrix with elements linear in $\mu(x, y, z)_k$, $\lambda(x, y, z)_k$ and $\rho(x, y, z)_k$;

u is the approximate displacement vector; and **b** is the vector of forcing terms or boundary conditions. The displacement field **u** can be calculated by solving Eq. 5.8 across the entire domain with each new iteration with respect to the change in the unknown elasticity parameters. This solution is then passed to a Conjugate-Gradient (CG) inversion method to determine updates on the elasticity parameters.

The solution of Eq. 5.8 by FE techniques requires appropriate formulation of the boundary conditions throughout the domain. Fortunately, MRE provides measured displacements throughout the volume. Therefore, Dirichlet displacement boundary conditions are available for any conceivable boundary within the data.

The most recent version of the algorithm allows independent discretisation of each material property, so that each reconstructed property can be supported on a separate FE mesh. The resolution of each property mesh is independent of the data resolution, and can be chosen based on factors such as the expected scale of heterogeneity, parameter sensitivity and data SNR. An additional benefit of this multi-mesh approach is that the mesh resolution of the forward problem can also be chosen independent of the number of reconstructed properties (McGarry et al., 2012).

5.3 The inverse problem

The *inverse problem* can be defined as finding the material property distribution, $\boldsymbol{\theta}$, given the mechanical response **u** with respect to the applied boundary conditions. The inverse problem is implemented through the use of nonlinear optimisation-based techniques, which involves finding $\boldsymbol{\theta}$ that minimises an objective error function, $\boldsymbol{\Phi}$; given input measurements, yielding an optimization problem defined as:

$$\boldsymbol{\theta} = \arg\min_{\boldsymbol{\theta}}[\boldsymbol{\Phi}], \tag{5.9}$$

where $\mathbf{\Phi}$ is further minimised by the nonlinear iteration process defined:

$$\Phi(\boldsymbol{\theta}) = \sum_{i=1}^{N_m} (\mathbf{u}_i^m - \mathbf{u}_i^c(\boldsymbol{\theta}))(\mathbf{u}_i^m - \mathbf{u}_i^c(\boldsymbol{\theta}))^H, \tag{5.10}$$

where $\mathbf{u}_i^m$ represents the complex valued measured displacement data at i'th measurement point, $\mathbf{u}_i^c(\boldsymbol{\theta})$ is the analogous displacement calculated by a forward simulation of the model using a current estimate of the properties ($\boldsymbol{\theta}$). N_m is the number of measurements and the superscript H denotes the complex conjugate transpose.

In MRE, the number of measurements corresponds to the number of measured displacements. Minimisation is performed by updating $\boldsymbol{\theta}$ using the CG method. Regularisation methods, such as spatial filtering (SF) and total variation (TV) are usually necessary to stabilise the inverse problem. Due to the iterative nature of optimisation based techniques, multiple solutions of the forward problem are required to reach the minimum of Eq. 5.25. By comparing the measured displacement input data, $\mathbf{u}^m$, to displacements calculated using an estimate of the material property distribution $\mathbf{u}^c(\boldsymbol{\theta})$, the $\mathbf{\Phi}(\boldsymbol{\theta})$ function is minimised by finding where the derivatives of model agreement with respect to reconstructed material properties (μ_R, μ_I, ρ_I) approach zero:

$$\frac{\partial \mathbf{\Phi}(\boldsymbol{\theta})}{\partial \boldsymbol{\theta}} = \sum_{i=1}^{N_m} -\frac{1}{2} \frac{\partial \mathbf{u}_i^c(\boldsymbol{\theta})}{\partial \boldsymbol{\theta}} (\mathbf{u}_i^m - \boldsymbol{u}_i^c(\boldsymbol{\theta})) = 0 \tag{5.11}$$

Each parameter update iteration can be broken down into two steps. The first step involves selecting a material property *search direction*, $\mathbf{p}_k$, for each iteration, k, which is used to update the material property description, $\boldsymbol{\theta}$, so that the update for the k'th iteration is defined:

$$\boldsymbol{\theta}_k = \boldsymbol{\theta}_{k-1} + \alpha_{k-1}\mathbf{p}_{k-1}, \tag{5.12}$$

where α_k is some step size to be determined. Because these are minimisation techniques, restrictions are usually placed on the search direction to ensure some reduction in error is achieved with each iteration (Marquardt, 1963). Some reduction in

error is assured at small α_k values if the directional derivative of the error along $\mathbf{p}_k$ is negative:

$$\Re\Big\{\mathbf{p}_k^H \boldsymbol{g}_k\Big\} < 0, \tag{5.13}$$

where $\mathbf{g}_k$ is the current error gradient, $\partial\boldsymbol{\Phi}/\partial\boldsymbol{\theta}$.

The second step is called a *line search* and involves selection of α_k to minimise the error function $\boldsymbol{\Phi}$ along the search direction. This is achieved by taking directional derivatives along the search direction. The step size can be determined either exactly or inexactly. An exact line search is where an actual minima in the direction given by $\mathbf{p}_k$ is found, so that:

$$\Re\Big\{\boldsymbol{\Phi}(\boldsymbol{\theta}_k + \alpha_k \mathbf{p}_k)^H \boldsymbol{g}\Big\} = 0. \tag{5.14}$$

Exact searches are usually associated with high computational demand and general unreliability, thus, as a compromise, inexact line search methods are sometimes used (Burachik et al., 1995). These inexact line searches use simple and reliable methods to find a value for α_k that satisfies specified descent criteria, such as:

$$\boldsymbol{\Phi}(\boldsymbol{\theta}_k + \alpha_k \mathbf{p}_k) < \boldsymbol{\Phi}(\boldsymbol{\theta}_k). \tag{5.15}$$

The inexact line search benefits from low computational cost, allowing more optimisation iterations to be computed in a given time frame. However, the selected possible value for α_k is unlikely to be optimal, and may not lead to the greatest error reduction for that step.

5.3.1 Conjugate-gradient method

The *Conjugate-gradient (CG) method* is implemented in the inverse problem to allow optimisation based elastographic reconstruction. Details on the initial implementation of the CG method in the reconstruction algorithm used here are well

documented elsewhere (McGarry, 2008).

Briefly, the CG method (Oberai et al., 2003) is an iterative method for solving large system of linear or nonlinear system of equations. The CG can be considered as a modified *steepest descent (SD) method*, allowing more efficient choice of search directions. The SD method is based on selecting a search direction of steepest decrease of a function, which is the negative of the gradient (Curry, 1944):

$$\mathbf{p}_{sd} = -\frac{\partial \mathbf{\Phi}}{\partial \boldsymbol{\theta}}. \tag{5.16}$$

The gradient $\mathbf{p}_{sd}$ is a vector that, for any given point $\mathbf{x}$, points in the direction of the greatest decrease of $\mathbf{\Phi}(\mathbf{x})$. The main advantage of the CG method over the SD method is a faster convergence rate due to utilising a conjugate basis set of search directions build up from the gradient at each iteration. The CG methods are generally more computationally efficient and practically reliable, compared to the SD methods for non-linear inverse problems in elastography (Shewchuk, 1994).

In the current version of the CG method, the next search direction is selected based on a linear combination of the previous search direction, $\mathbf{p}_{k-1}$, and a current gradient, $\mathbf{g}_k$ (McGarry, 2008):

$$\mathbf{p}_k = -\mathbf{g}_k + \alpha_k \mathbf{p}_{k-1}, \tag{5.17}$$

where previous search directions $\mathbf{p}_k$ compose a conjugate basis set allowing selection of α_k based on the Polak-Ribére formula (Polak and Ribiere, 1969) , given by:

$$\alpha_k = \max\left[\frac{\Re\left\{\mathbf{g}_k^H(\mathbf{g}_k - \mathbf{g}_{k-1})\right\}}{\Re\left\{\mathbf{g}_{k-1}^H \mathbf{g}_{k-1}\right\}}, 0\right]. \tag{5.18}$$

Due to the non-linear nature of the elastographic inverse problem, the search directions would eventually loose their conjugacy after a certain number of iterations. To overcome this issue, periodic restart ($\alpha_k = 0$) is undertaken where a new set of conjugate directions is initiated (McGarry, 2008).

One of the significant benefits of the CG method compared to, for example, Newton's methods is that it is very memory efficient. The Newtons method in optimization requires storage of the Hessian matrix, consisting of the number of the parameters, whereas CG methods are based on simple algebraic vector-vector multiplication operations. Therefore, computational intensity of the CG is relatively low.

The selection of the CG next search direction is based on a linear combination of a conjugate set of all previous gradient values, $\partial\mathbf{\Phi}/\partial\boldsymbol{\theta_i}$. Finding the gradient is usually associated with a poor scaling between the values of the gradient terms. To alleviate this problem, the CG search direction terms are scaled in such a way that the contribution of each material property on the displacements is proportional to the relative change in μ (McGarry, 2008):

$$\mathbf{p}_t^s(k) = \delta_\mu \frac{\sum |\boldsymbol{\mu}|}{\sum |\mathbf{p}_\mu|} \cdot \frac{|J_g|_\mu}{|J_g|_t} \cdot \frac{|g|_t}{|g|_\mu} \mathbf{p}_q(k), \tag{5.19}$$

where δ_μ is a relative change in μ parameter, $\boldsymbol{\mu}$ is a vector containing set of μ terms, $\mathbf{p}_\mu$ is the vector of μ search direction terms, $|g|_\mu$ and $|g|_t$ are the sizes of the gradient terms for μ and the material property type being scaled, t, respectively; $|J_g|_\mu$ is the size of the Jacobian for μ and $|J_g|_t$ represent the sizes of the Jacobian for material property parameter, t, being scaled:

$$|J_g|_t = \sqrt{\frac{\partial \mathbf{u}}{\partial \boldsymbol{\theta}_t}^H \frac{\partial \mathbf{u}}{\partial \boldsymbol{\theta}_t}}. \tag{5.20}$$

The effect of each material property parameter, $\boldsymbol{\theta_t}$, on the final solution is calculated using change in the displacement, $\mathbf{u}$, due to the global change of that particular parameter.

Eq. 5.19 indicates how change in displacements from a specific material property influences an overall error reduction. This scaling factor is determined from the first iteration and held constant throughout an optimisation process to allow gradual reduction of the gradient terms as the algorithm approaches a global minima.

In addition, exact and inexact line search techniques are also implemented to

improve the performance and reliability the CG method. The CG method generally performs better with the exact line search methods (Gilbert and Nocedal, 1992). Therefore, a secant line search with the *Armijo* line search as a backup are used in the reconstruction algorithm. More detailed description on the line search techniques is well documented in (McGarry, 2008).

5.3.2 Regularisation methods

Optimisation based image reconstruction techniques do not place any restrictions on the material property values as long as the condition for minimisation of the error function $\mathbf{\Phi}$ is satisfied. This approach could lead to the physically unrealistic values of material properties. To alleviate this issue, some *a-priori* information of the expected material property solution can be declared throughout the reconstruction domain via an initial guess and parameter value bounds. Regularisation methods, which modify the error function $\mathbf{\Phi}$ in an attempt to help the reconstruction algorithm to select solutions that are close to the known *a-priori* information, are applied.

Several regularisation methods are included in the reconstruction code, such as Tikhonov regularisation (Golub et al., 1999), Marquardt regularisation (Marquardt, 1963), Joachimowicz regularisation (Joachimowicz et al., 1991), Constraint regularisation, Total variation minimisation (Chambolle, 2004), CG residual scaling (McGarry, 2008) and spatial filtering. To increase the flexibility of the inversion algorithm, the relative level of each type of regularisation is allowed to vary linearly as the iterations progress.

5.3.2.1 Tikhonov regularisation

Tikhonov regularisation ensures that values for material property solutions do not vary significantly from the values declared by the *initial guess* through modification of the error function $\mathbf{\Phi}$ to $\mathbf{\Phi}_{tk}$ (McGarry, 2008) :

$$\mathbf{\Phi}_{tk} = \frac{1}{2}(\mathbf{u}^c - \mathbf{u}^m)^H(\mathbf{u}^c - \mathbf{u}^m) + \alpha_{tk}(\boldsymbol{\theta} - \boldsymbol{\theta}_0)^H(\boldsymbol{\theta} - \boldsymbol{\theta}_0), \tag{5.21}$$

where $\boldsymbol{\theta}_0$ and $\boldsymbol{\theta}$ are the initial material property guess and the current material property estimate, respectively; and α_{tk} is the weighting factor applied to Tikhonov regularisation. Tikhonov regularisation effectively penalises solutions according to how far they deviate from the initial guess. Therefore, will preferentially select solutions that are closer to the initial guess. A modification to this method is where $\boldsymbol{\theta}_0$ is set to the previous material property estimate at each iteration ($\boldsymbol{\theta}_0 = \boldsymbol{\theta}_{k-1}$), limiting the change in material properties for each iteration, but not the total deviation from the initial guess.

5.3.2.2 Total variation minimisation

It is common for some biological tissue types to display a smooth distribution of material properties across specific areas. This phenomena suggested implementation of the total variation (TV) minimisation method (McGarry, 2008) that preferentially selects material property distributions with fairly homogeneous regions of constant material properties over distributions with a greater degree of spatial variation. The function for $\boldsymbol{\Phi}$ is thus modified to $\boldsymbol{\Phi}_{tv}$:

$$\boldsymbol{\Phi}_{tv} = \frac{1}{2}(\mathbf{u}^c - \mathbf{u}^m)^H(\mathbf{u}^c - \mathbf{u}^m) + \iiint_{\Omega} \left(\alpha_{tv}\sqrt{\nabla\boldsymbol{\theta}^H\nabla\boldsymbol{\theta}}\right)dV, \tag{5.22}$$

where $\nabla\boldsymbol{\theta}$ represents the spatial variation of the material property, multiplied by its complex conjugate transpose $\nabla\boldsymbol{\theta}^{\boldsymbol{H}}$, and α_{tv} is the weighting factor applied to TV. The integral means that the level of total variation is the area under the $\sqrt{\nabla\boldsymbol{\theta}^H\nabla\boldsymbol{\theta}}$ curve. Fig. 5.2 demonstrates examples of how spatial variation in material property distribution affects TV, represented as the area under the curve. Low variation in parameter distribution will result in low TV, whereas the desecrate areas with high variation of material properties will result in high TV. Therefore, implementation of TV to the objective function minimisation should help in promoting smoother, more cleaner solutions where the selection of areas with constant parameter distribution is preferential.

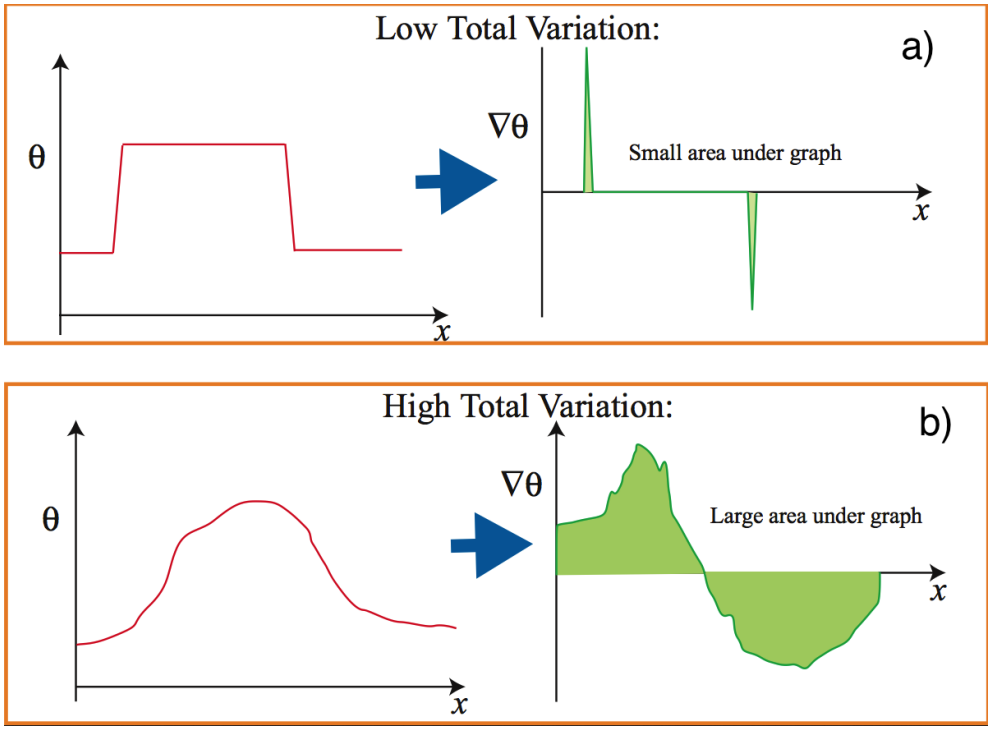

Figure 5.2 Schematic representation of the Total Variation (TV) in action: a) Material parameter with constant distribution of property values is illustrated as a red curve and a resulting TV, defined an an area under the curve $\nabla\boldsymbol{\theta}$, will produce small area under the graph: b) Material parameter with spatial variation in material properties distribution will produce larger area under the curve and thus, higher TV. Therefore low TV weighting promotes smoother solution of material property distributions. Image source: (McGarry, 2008)

5.3.2.3 Spatial filtering

Spatial filtering (SF) is a smoothing technique that penalises large variation in the material property distribution and is performed directly on the pixels of the reconstructed images. SF is implemented via replacing each value of material properties assigned to a specific pixel with a weighted average of of the material property values of its neighbouring pixels. Therefore, the new value of material property, $\boldsymbol{\theta_k}$, treated with SF is defined (McGarry, 2008):

$$\boldsymbol{\theta}_k = (1 - w_{sf})\boldsymbol{\theta}_k + \frac{w_{sf}}{N_{con}} \sum_{l=1}^{N_{con}} (\boldsymbol{\theta}_l), \tag{5.23}$$

where w_{sf} is a weighting applied to spatial filtering, l refers to the nodes in the neighbourhood of node k, and N_{con} is the number of these neighbourhood nodes.

SF preserves the idea that biological tissue types characterised by specific material properties should not have large variation in values of property distribution. However, the main drawback of this regularisation technique is a contribution towards the lost of the definition of boundaries between tissue types. Therefore, a gradual decrease of the SF weights is common as iterations progress.

5.3.2.4 Material property bounds

The optimisation-based reconstruction techniques often face difficulties related to the accurate identification of the true minima in the search space corresponding the correct material properties. Especially if several local minima are present. Unrealistically high values of the material property solutions might decrease the chance of the algorithm recovering a correct distinction between local optimal solutions and the global optimal solution, and will treat the former as actual solutions to the original problem.

Therefore, to minimise the risk of obtaining physically unrealistic solutions, material property bounds are applied as one of the constraints for optimisation processing (McGarry, 2008). There are two possibilities of when these bounds can be applied. The first and safest approach is to apply the bounds after material prop-

erties of each subzone have been computed. In this case, the bounds will have no effect on the actual processing of the material properties by the algorithm within each subzone. This method performs well in practice although modification of processed material property distributions returned from each subzone is considered disadvantageous as the update to the global property description is no longer one that is guaranteed to result in a reduction in the error.

Alternatively, the bounds can be directly applied each time the material properties are updated. This approach does not modify the returned solutions of material property distributions and, therefore, preserves any reduction in error. However, the method can sometimes cause the minimisation algorithm to fail completely for some subzones. This problem can be alleviated by applying constrained minimisation, where a penalty term is introduced to the error function for all reconstructed material properties which have physically unrealistic values. Another approach to overcome this issue is by forcing the search direction terms to the infeasible region of zero. A comparison study between the two approaches performed by McGarry (2008) suggested better convergence behaviour with the bounds applied every time the material properties are updated.

5.4 Summary

MR elastographic inversion is formulated as a constrained optimisation problem that involves two steps: the *forward problem solution* and the parameter update, commonly known as the *inverse problem*.

The solution of the forward computational problem produces a displacement field throughout the reconstruction domain. The constitutive model is a system of linear PDEs that incorporates a Rayleigh damped, isotropic, nearly incompressible, linearly elastic components of the Navier's equation, defined:

$$\nabla \cdot (\mu(\nabla \mathbf{u} + \nabla \mathbf{u}^T)) - \nabla(\frac{1}{3}\nabla \cdot \mathbf{u}) - \nabla P = -\rho\omega^2 \mathbf{u}; \tag{5.24}$$

where ∇P is the pressure term associated with volumetric changes of the material, $\mathbf{u}$ is the resulting calculated displacement field throughout the medium, μ is the

second Lamé's parameter associated with the shear stiffness of the material, λ is the first Lamé's parameter, ρ is the density of the material, and ω is the actuation frequency.

The parameter update step then iteratively fits a set of mechanical properties, μ_R, μ_I and ρ_I, such that the FE model reproduces the MRI measured displacements as closely as possible. This process is posed as a constrained optimisation problem where the objective error function, $\mathbf{\Phi}$, is minimised by iteratively updating the mechanical property distribution, $\boldsymbol{\theta}$:

$$\mathbf{\Phi}(\boldsymbol{\theta}) = \sum_{i=1}^{N_m} (\mathbf{u}_i^m - \mathbf{u}_i^c(\boldsymbol{\theta}))(\mathbf{u}_i^m - \mathbf{u}_i^c(\boldsymbol{\theta}))^H, \tag{5.25}$$

where $\mathbf{u}_i^m$ is measured displacement amplitude at location i, $\mathbf{u}_i^c$ is a computational model of the material behavior, and the H indicates the complex conjugate transpose. The minimisation is performed using the CG method with applied regularisation techniques to stabilise the solutions.

The RD model is integrated through the use of complex-valued shear modulus and density, and thus incorporates damping effects related to both elastic and inertial forces. Therefore, full three parameter identification is performed where μ_R, μ_I and ρ_I are estimated. Assuming that biological tissues are highly saturated, the real density term is usually set to 1000 kg/m^3 and λ is topically assumed to be large (10^8 Pa) to account for nearly incompressible behaviour expected in fluid saturated biological tissue, such as the brain.

RD model applied to MRE can provide additional diagnostic potential in application to *in vivo* brain imaging by mapping quantified damping properties. Although preliminary results of the RD MRE, performed on the phantoms, have been reported by Van Houten et al. (2011), the model still requires rigorous validation and thorough analysis of the identification of the reconstructed parameters. Therefore, this thesis focuses on examination of the performance, followed by identifiability analysis of the RD model on tissue simulating damping phantoms and *in vivo* healthy brain.

Chapter 6

Experimental methods, phantoms and actuation

In view of budget constraints and limited access to the MRI scanners in the Canterbury region of New Zealand due to the series of major earthquakes, the author worked in collaboration with various research institutes and was involved in initial discussion and decision making process regarding possible MRE imaging experiments and protocols. The collaborating research institutes were: Institute for biodiagnostics at National Research Council of Canada (CNRC); Department of Mechanical Science and Engineering at the University of Illinois at Urbana-Champaign (IL, USA), and Department of Mechanical Engineering at Dartmouth College (NH, USA). After the data was collected it was sent to the author for further conversion, reconstruction processing and analysis. The author gratefully acknowledges these institutions for their contribution.

The key aims of the full simultaneous three-parameter reconstruction of RD MRE phantom study data were:

- To assess the performance of the existing subzone based nonlinear image reconstruction algorithm on tissue-simulating phantoms by minimising the difference between the measured and calculated displacements.

- To assess the ability of the RD model to qualitatively map the viscoelastic and damping properties of various tissue-mimicking materials with reference to expected material behaviour of the phantoms.

- To investigate the behaviour of the reconstructed material properties in different material types with reference to their structure and composition.

- To validate the reconstructed material properties against their theoretically accepted rheological interpretations.
- To identify valuable diagnostic potential of reconstruction parameters with regards to differentiating and characterising of various material types.
- To collate and report the quantitative material property estimates of various material types across multiple frequencies.

The following studies use measured displacement data from variety of tissue-simulated phantoms. The goal is to test the viability a full simultaneous three-parameter reconstruction scheme to recover the distribution of complex shear modulus (storage and loss modulus), μ_R and μ_I, as well as imaginary density, ρ_I. Experimental data was collected from a variety of homogeneous and heterogeneous phantoms of varying material types, such as gelatine, water and porous tofu of various concentrations. These materials were chosen to mimic a range of material properties and situations that are expected when analysing brain MRI data.

6.1 Lightly damped gelatine phantom (ND2)

The ability of the RD model, applied to the subzone based nonlinear inversion algorithm, to produce reliable elastographic reconstructions was first tested using lightly damped tissue-mimicking gelatine phantoms. Gelatine is known as a good tissue simulating material which is commonly used in elastography experiments (Kruse et al., 2000; Madsen et al., 2003). Inclusions of higher stiffness were imbedded into the phantoms to specifically target the ability of the reconstruction algorithm:

- To ascertain and differentiate the same material of various concentrations;
- To accurately delineate the boundaries between background material and inclusions;
- To assess correlation between reconstructed material property distributions against physical homogeneity of the phantoms.
- To accurately map the geometry of viscoelastic and damping properties over both materials.

The lightly damped phantom (ND2 onwards) was initially developed and imaged by the Department of Mechanical Science and Engineering at the University of Illinois at Urbana-Champaign. ND2 was made of an agarose gel and had a rectangular parallelepiped shape. Three inclusions of different sizes (10, 15, and 20 mm) were embedded in the phantom. The inclusions had higher concentration of the agarose gel (2 %), compared to the phantom background material (1 %), and were thus stiffer.

A long rod, attached to the speaker membrane, was used to induce shear waves by vibrating the lower part of the phantom at mechanical frequency of 100 Hz. Motion encoding was performed using the multishot spiral MRE sequence with bipolar MEGs (TR/TE = 2000/35ms) (Johnson et al., 2012) where single period of vibration was sampled over eight equally spaced time harmonics. Twenty slices of 2 mm thickness were acquired corresponding to field of view (FOV) of 128 mm.

A 3D subzone based reconstruction algorithm using an isotropic, nearly incompressible linear RD material model (Van Houten et al., 2011) was applied to reconstruct both 2 parameter VE behaviour and the 3 parameter RD damping properties of the materials using following parameters: isotropic subzone size: $0.011 \times 0.011 \times 0.011$ m; subzone overlap $0.15 \times 0.15 \times 0.15$ (%/100); Initial and final total variation (TV) weighting was 10^{-15} and 10^{-14} with TV delta set to 10^{-19}. The initial and final spatial filtering (SF) weights were set to 0.25 % and 0.15 % respectively. Displacements were approximated on the mesh with $1.7 \times 1.7 \times 1.7$ mm voxel resolution, providing approximately 16 nodes per wavelength for the FE forward computational problem.

Initial *a-priori* information with regards to the globally defined parameters was: μ_R = 1800 Pa; μ_I = 180 Pa and ρ_I = -100 kg/m^3. The real density (ρ_R) and the bulk modulus (K) were constants: ρ_R = 1000 kg/m^3 and K = 1648900 Pa. Reconstructions were carried out on the *Blue Fern* HPC supercomputer facilities where a total of 32 processors were employed for reconstruction processing.

The reconstruction processing was performed on high performance computing (HPC) system *Blue Fern P575*. 32 processors were used to compute 100 iterations by CG method over an average time frame of 5 hours.

6.2 Poroelastic homogeneous tofu phantom

Most biological tissues are highly saturated. It has been hypothesised that fluid circulates within the tissue due to the underlying biological and physiological processes (Mow et al., 1984; Netti et al., 1997). These tissues may be modelled as a porous media generally consisting of a porous elastic solid and penetrating fluid (Gore et al., 2001). The mechanical behaviour of these tissue types has been described by various theories, such as classical consolidation theory (Terzaghi, 1943) or poroelasticity (Perriez et al., 2010). These theories postulate that poroelastic tissues are characterised by a continuous time-dependant interaction of two independent phases: a solid matrix phase and a fluid phase. This interaction is defined by permeability properties of the material as well its structural and mechanical properties.

Due to the high water content, incompressible or nearly incompressible assumptions are usually applied to model biological tissues (Righetti et al., 2004). These assumptions might only be valid on the global scale. However, although some tissue compartments might exhibit incompressible behaviour, according to the poroelasticity theory, the tissue must be compressible to support fluid transport within the tissue (Kyriacou et al., 2002). Therefore, some studies have shown that the Poisson's ratios of tendons, ligaments and cartilage are significantly lower than 0.5, indicating compressible nature (Kyriacou et al., 2002; Mow et al., 1984). Moreover, a network of fluid-filled cavities within the tissue might contribute to the changes of the local volume by allowing partial fluid movement (Kyriacou et al., 2002; Sarron et al., 2000). Therefore, while globally tissue might behave as a nearly-incompressible material, it can have local regions characterised by compressible material properties (Righetti et al., 2004; Sarron et al., 2000). Also, pathological tissues commonly display a change in effective mechanical property distribution which can thus affect the Poisson's ratio. Hence, reconstruction of these phantoms would provide insight into these behaviours and their existence.

In this study, the feasibility of using RD MRE to image the time-dependent mechanical behavior of poroelastic sample subjected to a time-harmonic actuation across multiple frequencies is investigated. The hypothesis at the basis of this work is that it is feasible to use time-harmonic RD MRE to distinguish among homogeneously poroelastic materials of different concentrations. It is further hypothesised that the use of RD based elastography will result in objectively more accurate elas-

tograms.

The studies reported in this work were performed using commercially available soft tofu slab. Tofu has been proposed recently as a sonographic and elastographic tissue-mimicking material with acoustic and mechanical properties similar to those of some soft tissues (Righetti et al., 2004; Wu, 2001). Tofu is known to possess a porous microstructure, which is composed of an organic solid matrix with pores of different sizes and shapes depending on the grade of the material.

A poroelastic phantom made of commercially available soft tofu was used in this study. A tofu slab was placed in the container and submerged in water. Piezo-electric actuation was utilized to introduce shear waves in the phantoms at consequent mechanical frequencies of 60 Hz, 80 Hz, 100 Hz and 125 Hz. The container was positioned onto the actuation plate attached to the actuator. Therefore, the base of the phantom, which was in contact with the actuation plate, exhibited more motion amplitude than top of the phantom. To hold the phantom submerged, another tofu slab was positioned on the top of the tofu slab being imaged. Thus, boundary conditions were applied to the top of the phantom. 3D motion data was recorded on 1.5 T Philips MRI scanner using SE based phase-contrast pulse sequence with added MEGs using following parameters: TR/TE = 480/10 ms; FOV = $150 \times 225 \times 40$ mm and 2 mm isotropic voxel. 20 coronal image slices were acquired.

6.3 Tofu-gelatine damping phantoms

This study further evaluates the time harmonic RD elastography reconstruction technique. The goal is to image the RD damping properties of various materials. A discussion of some of the uniqueness issues associated with the RD mechanical model is also presented, as well a summary of results and in-depth analysis from a study of tofu and gelatine phantoms.

The aim of this study is to investigate the capability of an isotropic, nearly-incompressible linear RD model to accurately reconstruct and characterise VE and damping properties of the tissue-mimicking damping phantoms, made of a combination of poroelastic and elastic materials, subjected to a time-harmonic actuation at multiple frequencies. The choice of the materials was made with a goal of achieving

a good damping contrast within the phantom. Since tofu has more attenuation than gelatine, significant contrast is expected in damping behaviour between these two materials. It is hypothesised that it is feasible to use time-harmonic RD MRE to distinguish between homogeneously poroelastic material (tofu) and homogeneously elastic material (gelatine) characterized by different mechanical properties.

The phantoms were constructed by the department of Mechanical Engineering at the Dartmouth College (NH, USA). The first damping phantom (P1 onwards) was made of soft tofu background with a single, stiff gelatine inclusion (10% Sigma Aldrich), as shown in Fig. 6.1. The second damping phantom (P2 onwards) was a reverse configuration of P1, with stiff 10% gelatine as the background and a soft tofu as the inclusion. Both phantoms had an external rectangular shape with a cylindrical inclusion located at the centre. For P1, the inclusion was generated by first removing a core from the soft tofu slab and then replacing it with a core extracted from a separate stiff gelatine slab. It was vice versa for P2.

Piezo-electric actuation was utilized to introduce shear waves into the phantoms at multiple mechanical frequencies of 50 Hz, 75 Hz, 100 Hz and 125 Hz. The phantoms were positioned on the actuation plate attached to the actuator. The orientation of the inclusions was perpendicular to the propagation of the shear strain waves. Therefore, the base of the phantom, which was in contact with the actuation plate, exhibited more motion amplitude than top of the phantom. No physical constrains were applied to the top of the phantom.

The MRE imaging experiments were performed on a 1.5 T Philips MRI scanner. 20 coronal slices of 3 mm thickness of 3D steady state displacement fields were acquired by an SE based phase-contrast sequence, extended with trigger timing and MEG modules, using the following parameters: TR/TE = 480/10 ms; FOV = $150 \times 225 \times 40$ mm and 2 mm isotropic voxel. A 3D quality-guided phase unwrapping method (Wang et al., 2011) was applied to the motion MRE data to suppress phase wrapping. The reconstruction results were then analysed to evaluate the presence of statistically significant differences among the two types of materials and for image quality analysis.

The set of experiments performed in this study is vital towards better understanding the advantages and limitations of RD reconstructions to distinguish damping in these types of materials. Preliminary RD MRE experiments on P1 phantom

configuration were performed by Van Houten et al. (2011) where RD reconstruction results were compared to VE reconstruction results. The investigated parameters were mainly real shear modulus (μ_R) and damping ratio (ξ_d). This study emphasises qualitative assessment of the RD parameters against their known rheological interpretation and quantitate behaviour of the parameters with regards to physical homogeneity of both materials within the phantoms across multiple frequencies.

Reconstruction processing using an isotropic, nearly-incompressible linear RD material model was perfumed to reconstruct VE behaviour and the RD damping properties of the materials using following parameters: subzone size: $0.016 \times 0.016 \times 0.016$ m; subzone overlap $0.15 \times 0.15 \times 0.15$ (%/100); Initial and final TV weighting was 10^{-15} and 10^{-14} with TV delta set to 10^{-19}. The initial and final SF weights were set to 0.25 % and 0.15 % respectively. The initial estimates for the material properties were: $\mu_R = 1800$ Pa; $\mu_I = 180$ Pa and $\rho_I =$ -100 kg/m^3. The real density (ρ_R) and the bulk modulus (K) were constants ($\rho_R = 1000$ kg/m^3 and $K = 1648900$ Pa) to account for a nearly incompressible behaviour of the tissue.

The reconstruction computations were carried out on the HPC system *Blue Fern P575*. A total of 32 processors were employed in parallel MPI environment to produce 100 iterations using CG optimisation method. The average runtime for the reconstruction processing was 5 hours. A single global iteration consisted of approximately 200 - 300 individual iterative subzone calculations containing an average of 550 - 600 nodes/subzone. Each parameter was interpolated at different resolution levels.

To provide comparable elastic property measurements for the gelatine and soft tofu phantom material, dynamic mechanical analysis (DMA) was performed using a TA instrument Q800 Device with measurements at 100 Hz computed using time temperature superposition (TTS). To quantifiably compare each reconstruction, regions of interest (ROIs) were selected from areas of each image representing particular material and the median and IQR of each property within these ROI were calculated. To provide an unbiased measurement of the relative difference between property values, a *mean difference* (MD) calculation was such that MD between measurements A and B is given by:

$$MD(A,B) = \left(\frac{||A - AB|| + ||B - AB||}{AB} \right) 100, \tag{6.1}$$

where $AB = \frac{A+B}{2}$.

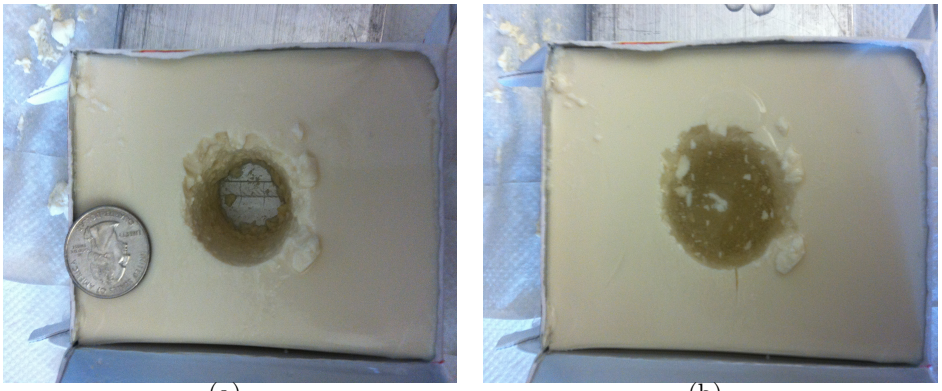

(a) (b)

Figure 6.1 P1 phantom configuration with tofu background and stiff gelatine inclusion. a) A hole is made in the tofu followed by b) insertion of a gelatine inclusion at the centre

6.4 Poroelastic double water inclusion phantom

A tissue-simulating damping phantom, made of a soft tofu material with water inclusions of different geometries, was considered for this study. The configuration and composition of the phantoms simulated a simplified representation of the brain, where water inclusions mimicked fluid-filled ventricles and porous tofu was an approximation for intracranial matter. The aim is to evaluate the ability of the isotropic, nearly-incompressible linear RD model:

- To locate the presence of the fluid-filled cavities within the porous media.
- To accurately delineate the geometry and boundaries between the fluid media and porous media
- To accurately characterise material properties of the fluid

The phantom was manufactured and imaged by the Department of Mechanical Engineering at the Dartmouth College (NH, USA). More specifically, the phantom (P5 onwards) was made of a soft tofu background with two water inclusions of different diameters located on the opposite site of the phantom. To prevent leaking

of tofu material and and maintain constant outside pressure level, P5 was fully submerged in water.

The phantom was placed onto the actuation plate attached to the piezo-electric actuator in such a way that inclusions were oriented perpendicular to the shear wave propagation. The phantom was actuated at multiple frequencies of 60 Hz, 80 Hz and 100 Hz. All MRE imaging experiments on 1.5 T Philips MRI scanner. 15 coronal slices of 3 mm thickness of 3D steady state displacement fields were acquired by a SE based phase-contrast sequence, extended with trigger timing and MEG modules, using the following parameters: TR/TE = 480/10 ms; FOV = 150 × 225 × 40 mm and 2 mm isotropic voxel.

Reconstruction of material properties using an isotropic linearly elastic nearly incompressible RD material model was performed using the following parameters: isotropic subzone size: 0.024 × 0.024 × 0.024 m; subzone overlap 0.15 × 0.15 × 0.15 %/100; Initial and final TV weighting was 10^{-15} and 10^{-14} with TV delta set to 10^{-19}. The initial and final SF weights were set to 0.25 % and 0.15 % respectively. Displacements were approximated on the mesh with 1.8 × 1.8 × 1.9 mm voxel resolution. Initial *a-priori* information with regards to the globally defined parameters was: μ_R = 3300 Pa; μ_I = 330 Pa and ρ_I = -100 kg/m^3. The real density (ρ_R) and the bulk modulus (K) were set to constants: $\rho_R = 1000\ kg/m^3$ and K = 1648900 Pa to account for the nearly incompressible behaviour expected in a highly saturated media.

The reconstruction computations were carried out on the HPC system *Blue Fern P575*. A total of 32 processors were employed in parallel MPI environment to produce 100 iterations using CG optimisation method. The average runtime for the reconstruction processing was 5 hours. Each parameter was interpolated at different resolution levels.

6.5 Summary

Experimental data was collected from a variety of homogeneous and heterogeneous phantoms of varying material types, such as gelatine, water and porous tofu of various concentrations. These materials are chosen to mimic a range of material

properties and situations that are expected when analysing *in vivo* brain MRE data. The goal is to test the viability a full simultaneous three-parameter reconstruction scheme to recover the distribution of complex shear modulus (storage and loss modulus), μ_R and μ_I, as well as imaginary density (ρ_I).

The key aims of the three-parameter reconstruction of RD MRE phantom study data were:

- To assess the performance of the existing subzone based nonlinear image reconstruction algorithm on tissue-simulating phantoms by minimising the difference between the measured and calculated displacements.
- To assess the ability of the RD model to qualitatively map the viscoelastic and damping properties of various tissue-mimicking materials with reference to expected material behaviour of the phantoms.
- To investigate the behaviour of the reconstructed material properties in different material types with reference to their structure and composition.
- To validate the reconstructed material properties against their theoretically accepted rheological interpretations.
- To identify valuable diagnostic potential of reconstruction parameters with regards to differentiating and characterising of various material types.
- To collate and report the quantitative material property estimates of various material types across multiple frequencies.

The summary of the simultaneous three parameter-based RD MRE reconstruction results is presented and discussed in the next chapter.

Chapter 7

Full three parameter-based RD MRE phantom results

This chapter summaries results at the 3 phantom types against the hypotheses developed in Chapter 6. The aim is to evaluate the overall results of RD three-parameter reconstruction. The expected results of the hypothesis is that RD model is able:

- To accurately recover VE and damping properties of various tissue-mimicking materials,
- To qualitatively distinguish different material types, and
- To accurately delineate boundaries between independent material zones.

It is further hypothesised that the RD parameters can characterise structure and composition of various material types based on different damping mechanisms, thus providing an added diagnostic potential. The ultimate goal is an accurate comprehensive qualitative as well as quantitative mapping of mechanical properties with potential to differentiate consistency between heathy and pathological biological tissues. It is also expected that the RD model is able to locate fluid-filled cavities within the highly saturated materials, such as tofu.

It is important to emphasise that full conditioning of the reconstructed parameters is a fundamental prerequisite for accurate recovery of mechanical properties. However, the inverse problem in elastography can be ill-conditioned due to its highly non-linear nature (Wall et al., 2011). Therefore, analysis examining identifiably of the inverse problem is also performed.

7.1 Lightly damped phantom (ND2)

An overall assessment of the RD model to produce accurate elastographic reconstructions was first performed using a lightly damped tissue-simulating phantom comprised of gelatine of different concentrations. The performance of the model was assessed based on these criteria:

- To ascertain and differentiate the same material of various concentrations;
- To accurately delineate the boundaries between the background material and inclusions;
- To map homogeneous distribution of the material properties based on physical homogeneity of the phantoms;
- To accurately map the presence, geometry and location as well as viscoelastic and damping properties of the background and inclusions.

Fig. 7.1 (a) shows a $T2^*$-weighted MR image of the ND2 with three inclusions clearly shown. The background and inclusions were segmented (Figs. 7.1 (b) and 7.1 (c)) to calculate the median and the interquartile range (IQR) of the material property values (Table 7.1). Fig. 7.2 shows the RD reconstruction for μ_R, μ_I, ρ_I and resulting ξ_d for the same ND2 at 100 Hz. It is clear that damping has not been clearly differentiated. Fig. 7.4 shows results for quantitative analysis and cumulative distribution functions (CDF) within selected region of interest (ROI) for different material properties. Each graph illustrates quantified behaviour of a particular parameter for multiple frequencies. Uncertainty bars represent the (5 25 50 75 95) percentiles. Fig. 7.4 supports Fig. 7.2 by showing a lot of overlap and lack of separation between materials for μ_I and ρ_I, whereas μ_R is more clear. This is also seen in Fig. 7.2.

Lastly, Fig. 7.3 shows the convergence plots of reconstructed material properties. The stabilisation of the statistical indicators of the parameter behaviour across all nodes as the number of iteration increases is used for evaluation of the convergence for a particular parameter. Therefore, Fig. 7.3 indicates that the convergence of all

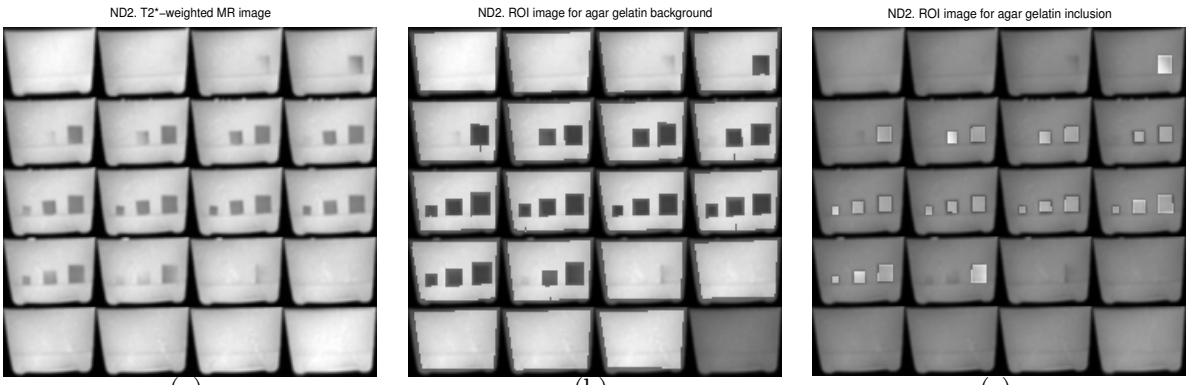

Figure 7.1 MRI image results of the ND2 with ROI selections indicated: (a) High resolution T2* weighted MR image; (b) MR image (background ROI indicated); (c) MR image (inclusion ROI indicated).

Table 7.1 Quantitative ROI analysis results of the ND2 phantom

Parameter Units	μ_R (Pa)	μ_I (Pa)	ρ_I (kg/m^3)	ξ_d (% / 100)
	Median [IQR]	Median [IQR]	Median [IQR]	Median [IQR]
Background (Agar gel 1 %)	3837 [3476 – 4213]	31[14 – 57]	–21 [-38 – -10]	0.016 [0.0097 – 0.026]
Inclusions (Agar gel 2 %)	11571 [9154 – 15180]	61 [30 – 86]	-7 [-26 – -3]	0.006 [0.003 – 0.017]

reconstructed parameters has been achieved. The convergence condition is carefully checked for every reconstruction output.

7.1.1 Discussion: ND2 (Lightly damped phantom)

μ_R results

Qualitatively, μ_R reconstruction was successful. The two large inclusions (15 and 20 mm) are distinct from the background while the small inclusion (10 mm) is visible, although with less clear margins. It has to be stressed that property resolution is a crucial factor for accurate characterisation of small scale objects. In this case, $2\times2\times2$ isotropic voxel resolution was sufficient to capture presence of a smaller inclusion. The average stiffness estimates for 1 % agar gel background and 2 % agar

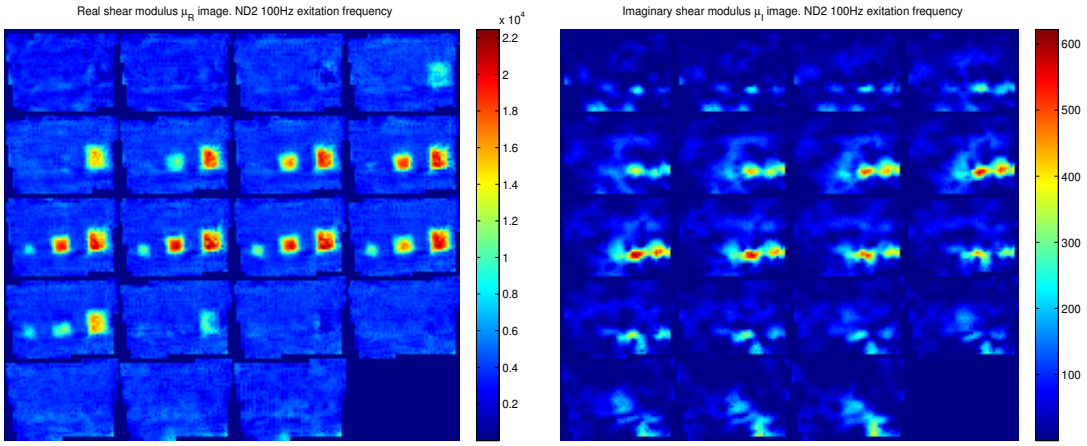

(a) μ_R (b) μ_I

(c) ρ_I (d) ξ_d

Figure 7.2 Image results for full 3 parameter-based RD reconstruction of the ND2 agar gel phantom using 100 Hz mechanical excitation: (a) storage modulus μ_R image (Pa); (b) loss modulus μ_I image (Pa); (c) imaginary density ρ_I image (kg/m^3) and (d) damping ratio (ξ_d) image (% / 100);

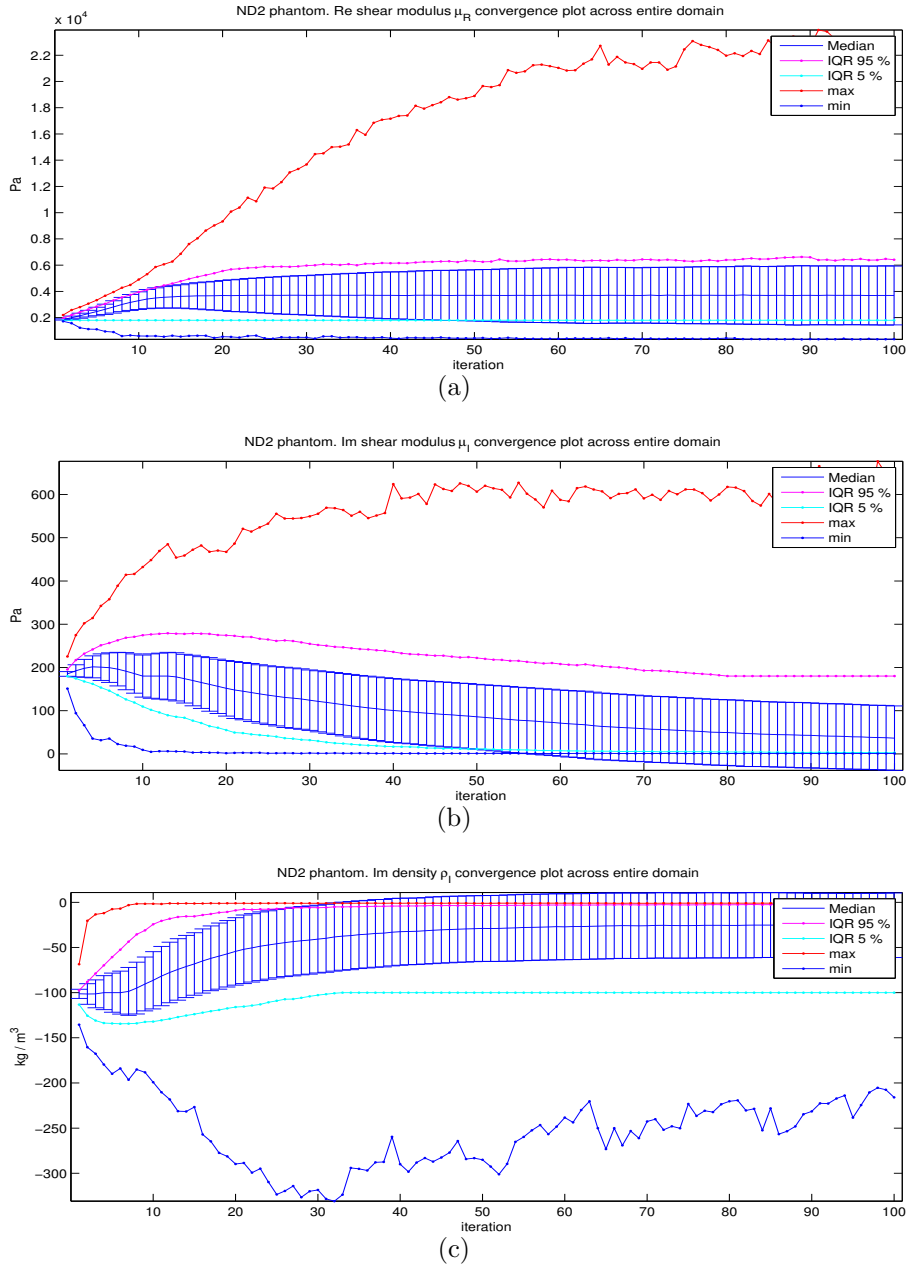

Figure 7.3 Convergence plots of the reconstructed parameters for the ND2 phantom at 100 Hz: (a) μ_R; (b) μ_I and (c) ρ_I. Different statistical indicators, such as median, IQR [5 75], max and min of the particular material property parameter across all nodes within the reconstructed domain are plotted across all iterations. The median of the material properties stabilises after approximately 50th iteration, indicating that convergence has been achieved.

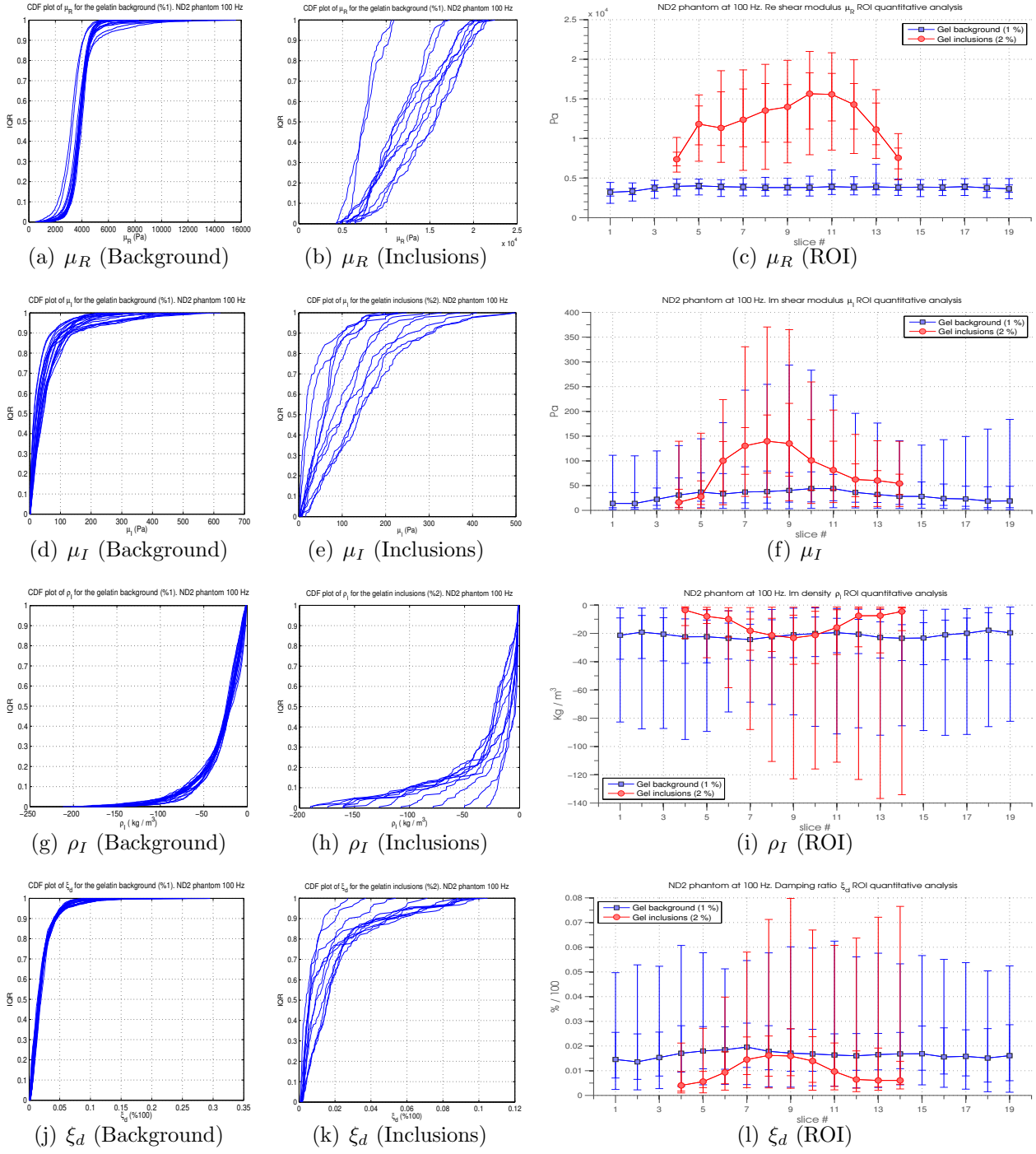

Figure 7.4 Quantitative ROI analysis of the ND2 agar gel phantom at 100 Hz for the gelatine background and stiffer gelatine inclusions for reconstructed material properties within the selected ROI and associated CDF plots for each material property: top row: μ_R, second row: μ_I, third row: ρ_I and bottom row: ξ_d. Uncertainty bars represent (5 25 50 75 95) percentiles.

gel inclusion are 3.8 kPa and 11.5 kPa, respectively (Table 7.1). Quantitative ROI analysis showed fairly homogeneous distribution of μ_R values within the background material, while μ_R behaviour within inclusions is not consistent across the phantom (refer to Fig. 7.4 (c)). The CDF plots show good agreement in property behaviour within background while small variation is seen in the inclusions (Figs. 7.4 (a) and 7.4 (b)).

μ_I results

Quantitatively, general trends, expressed by increased μ_I values, exist and indicate presence of the inclusions. However, accurate characterisation regarding the spatial location and geometry failed. Two larger inclusions of 20 mm and 15 mm are picked up in the μ_I image with increased values, however the location and geometry does not correlate well with the T2*-weighted MR image. The smaller inclusion was not effectively identified. Average μ_I estimates for the background material and inclusions are 31 Pa and 61 Pa, respectively in Table 7.1.

ρ_I results

A very similar situation is observed in the ND2 phantom for ρ_I and μ_I. Qualitatively, small contrast is seen between the background (-21 kg/m^3) material and three inclusions ($-7kg/m^3$) although some slices show promise in capturing the presence of the inclusions. The location and geometry of the inclusions on the ρ_I image does not correlate with the location and geometry in the MR image. Fig. 7.4 (c) shows relatively uniform distribution of the ρ_I values across the phantom. High variation in material properties across the slices is observed, as confirmed by the uncertainty bars in Fig. 7.4 (i) and shape of the CDF functions in Fig. 7.4 (g) and (h).

There are two possible explanations of the lack in contrast in the ρ_I image. The first one is related to the rheological interpretation of the imaginary density term. In the RD model, ρ_I term corresponds to the rate of density change in the bi-phasic system. Since gelatine is mainly made of densely packed cells, it does not have a porous nature. Therefore, it is expected that there should be no contrast in ρ_I image. Another possible explanation is related to the meaning of the ρ_I term in the RD model. The ρ_I term contributes to the damping that is inversely proportional to the input frequency, thus ρ_I term is dominant in the lower frequencies. Since

the phantom was actuated at a relatively high excitation frequency of 100 Hz, the influence of the ρ_I term on the resultant displacement may not be distinguished.

ξ_d results

Qualitatively, ξ_d reconstruction had a poor success as expected from the μ_R, μ_I and ρ_I results. The presence of inclusions in the ξ_d image can not be distinguished. Significant variations are present in areas of supposedly constant material properties as can be qualitatively seen in Fig. 7.2 (d). A relatively uniform distribution is observed in ξ_d within the gelatine background material, characterisation of the inclusions is poor and inconsistent, as confirmed by Fig. 7.4 (l) and associated CDF plots in Figs. 7.4 (j) and 7.4 (k).

7.1.2 Summary: ND2 (Lightly damped phantom)

The aim of the experiment was to test the abilities and limitations of the RD model to accurately characterise RD properties of the lightly damped gelatine phantom. This was done by performing MRE experiments followed by reconstruction processing.

The best success was achieved in reconstructing μ_R properties of the phantoms. Unfortunately, independently measured values of static shear modulus are not available for comparison analysis. However, the algorithm failed in accurate characterisation of stiffer inclusions in the μ_I image. The algorithm also struggled in correct mapping of the ρ_I properties of the gelatine, which may be due to non porous structure of the gelatin and also high actuation frequency.

7.2 Poroelastic homogeneous tofu phantom

A homogeneous isotropic poroelastic phantom, made of highly saturated soft tofu material, was chosen to specifically investigate the ability of the RD model to map homogeneous distribution of the material properties corresponding to the physical homogeneity of the phantom. Thus, small variations in the reconstructed property distributions are expected. The reconstructions were performed across multiple

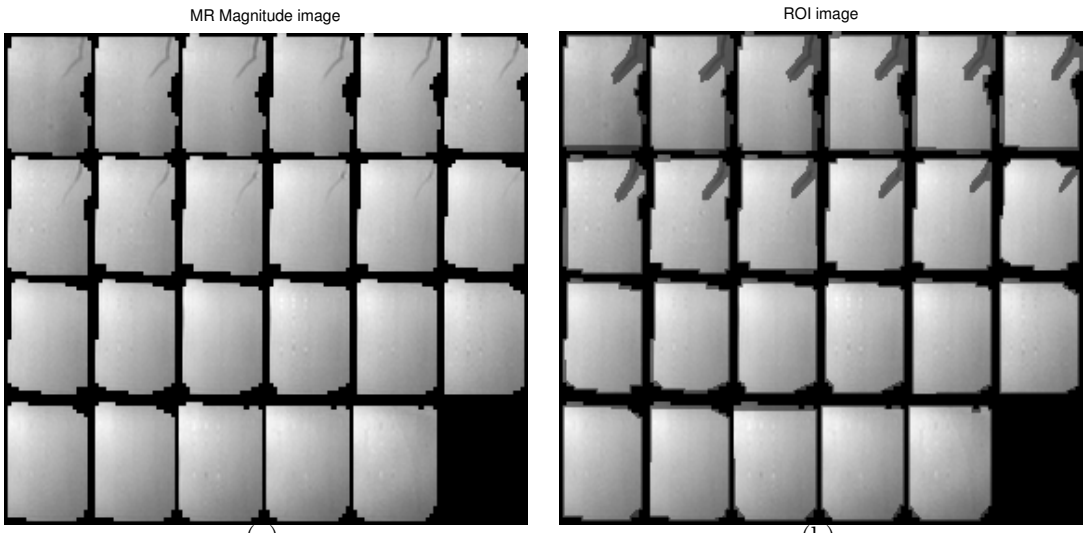

Figure 7.5 MRI image results of the poroelastic homogeneous tofu phantom with ROI selections indicated: (a) High resolution $T2^*$-weighted MR image; (b) MR image (background).

frequencies.

Fig. 7.5 (a) shows a T2*-weighted MR image of the poroelastic homogeneous tofu phantom while Fig. 7.5 (b) shows superimposed ROI used for quantitative analysis. Fig. 7.6 shows the 3-parameter RD reconstruction results. Fig. 7.7 shows quantitative analysis for the behaviour of the reconstructed parameters, including motion amplitude (MA) across multiple frequencies, and Fig. 7.8 shows corresponding CDF plots across multiple frequencies. Summary of this results is presented in Table 7.2. Again, it is clear, as in ND2 in the prior section, that μ_I and ρ_I reconstruction have not provided the relatively isotropic results expected for this homogeneous phantom.

7.2.1 Discussion

It is important to emphasise that since the phantom is isotropic and homogeneous, homogeneous distributions of all parameters are expected across the phantom. How-

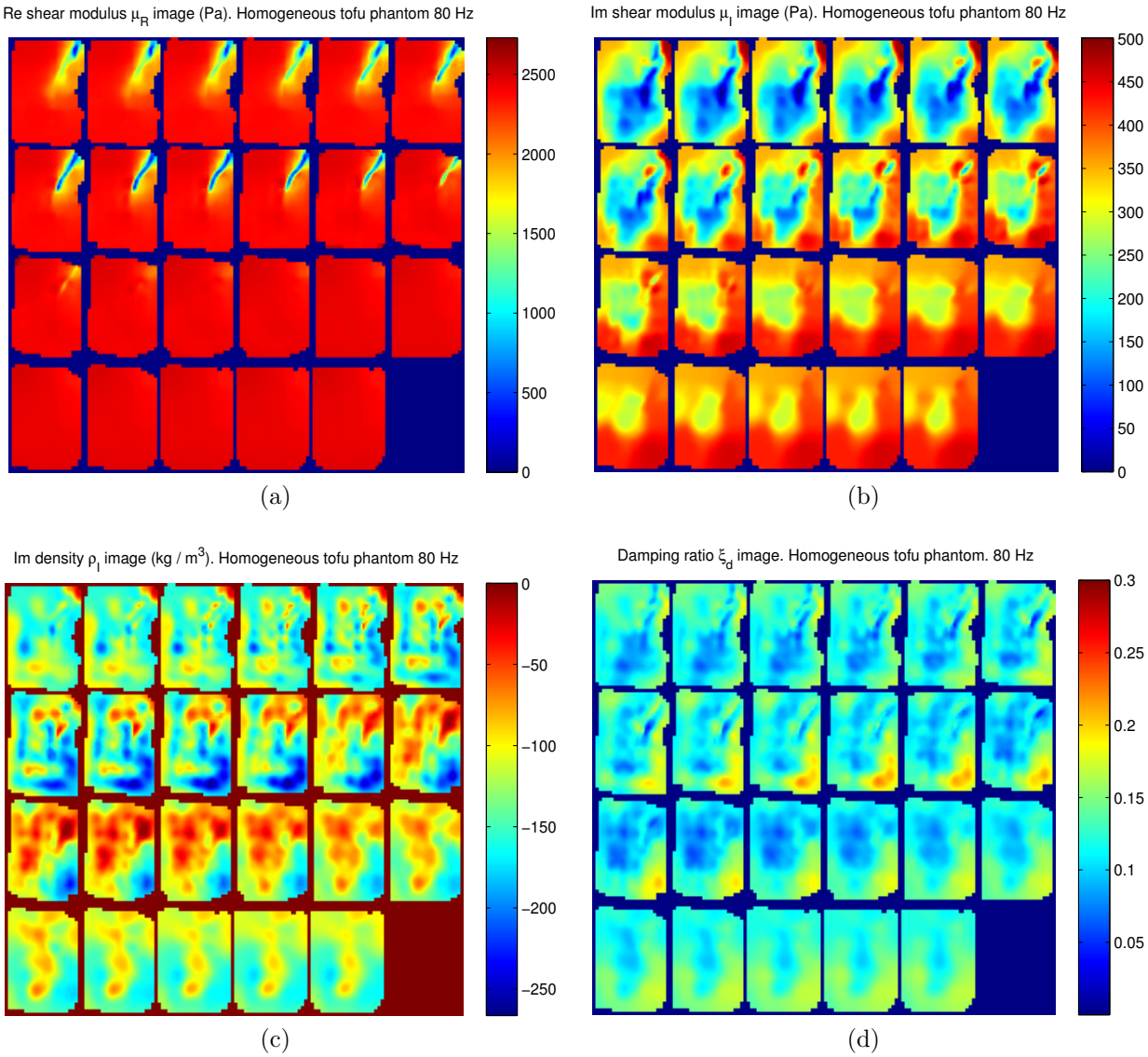

Figure 7.6 Image results for the full 3 parameter-based RD reconstruction of the poroelastic homogeneous tofu phantom using 80 Hz mechanical excitation: (a) Storage modulus (μ_R) image (Pa); (b) Loss modulus (μ_I) image (Pa); (c) Imaginary density (ρ_I) image (kg/m^3); (d) Damping ratio (ξ_d) image (% / 100);

Table 7.2 ROI analysis results of the poroelastic homogeneous tofu phantom

Parameter Units	MA (μm)	μ_R (Pa)	μ_I (Pa)	ρ_I (kg/m^3)	ξ_d (% / 100)
	Median [IQR]	Median [IQR]	Median [IQR]	Median [IQR]	Median [IQR]
Soft tofu (60 Hz)	2.2 [1.9 – 2.5]	2396 [2376 – 2415]	293 [270 – 327]	-112 [-124 – -97]	0.12 [0.1 – 0.13]
Soft tofu (80 Hz)	3.3 [2.9 – 3.6]	2606 [2539 – 2675]	335 [271 – 403]	-127 [-150 – -109]	0.12 [0.1 – 0.14]
Soft tofu (100 Hz)	1.2 [1 – 1.5]	2650 [2554 – 2713]	462 [350 – 529]	-112 [-144 – -88]	0.14 [0.11 – 0.16]

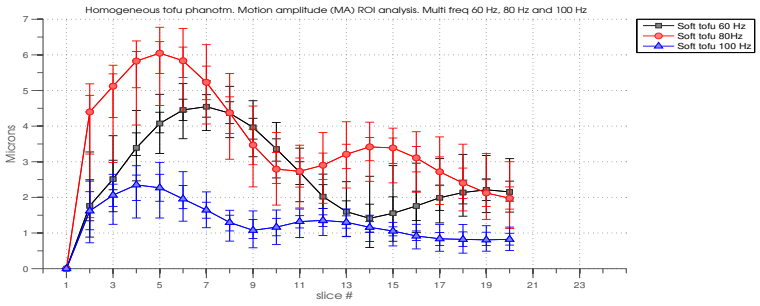

(a) Motion aplitude

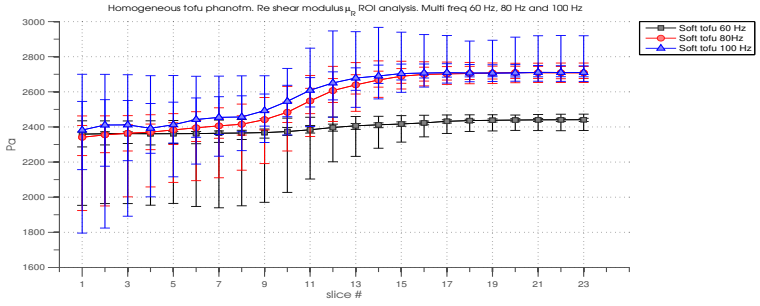

(b) μ_R

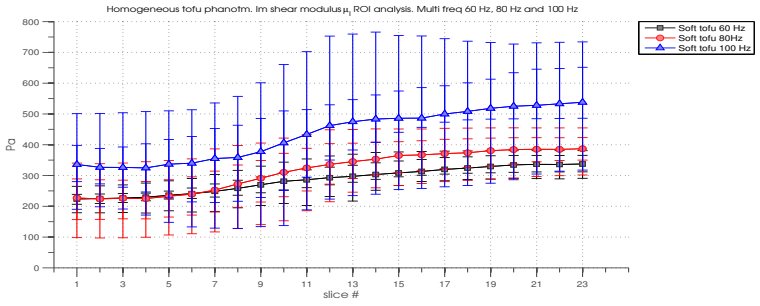

(c) μ_I

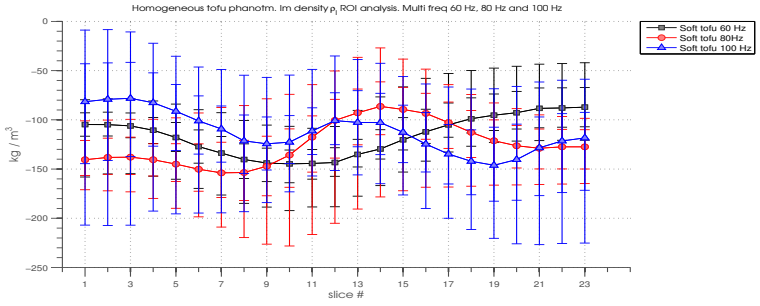

(d) ρ_I

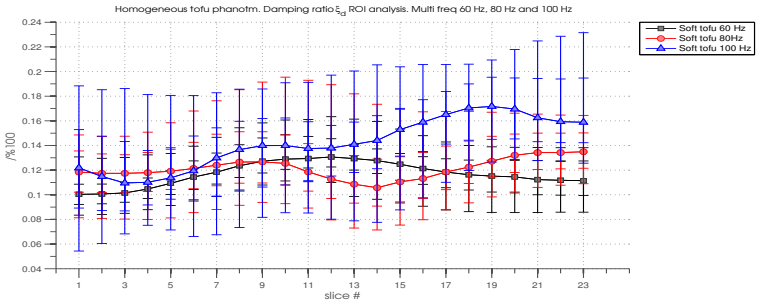

(e) ξ_d

Figure 7.7 Quantitative ROI and CDF slice by slice analysis of the poroelastic homogeneous tofu phantom for the behaviour of the reconstructed material properties: (a) motion amplitude; (b) μ_R; (c) μ_I; (d) ρ_I and (e) ξ_d. Uncertainties are represented as error bars, indicating the (5 25 75 95) percentiles.

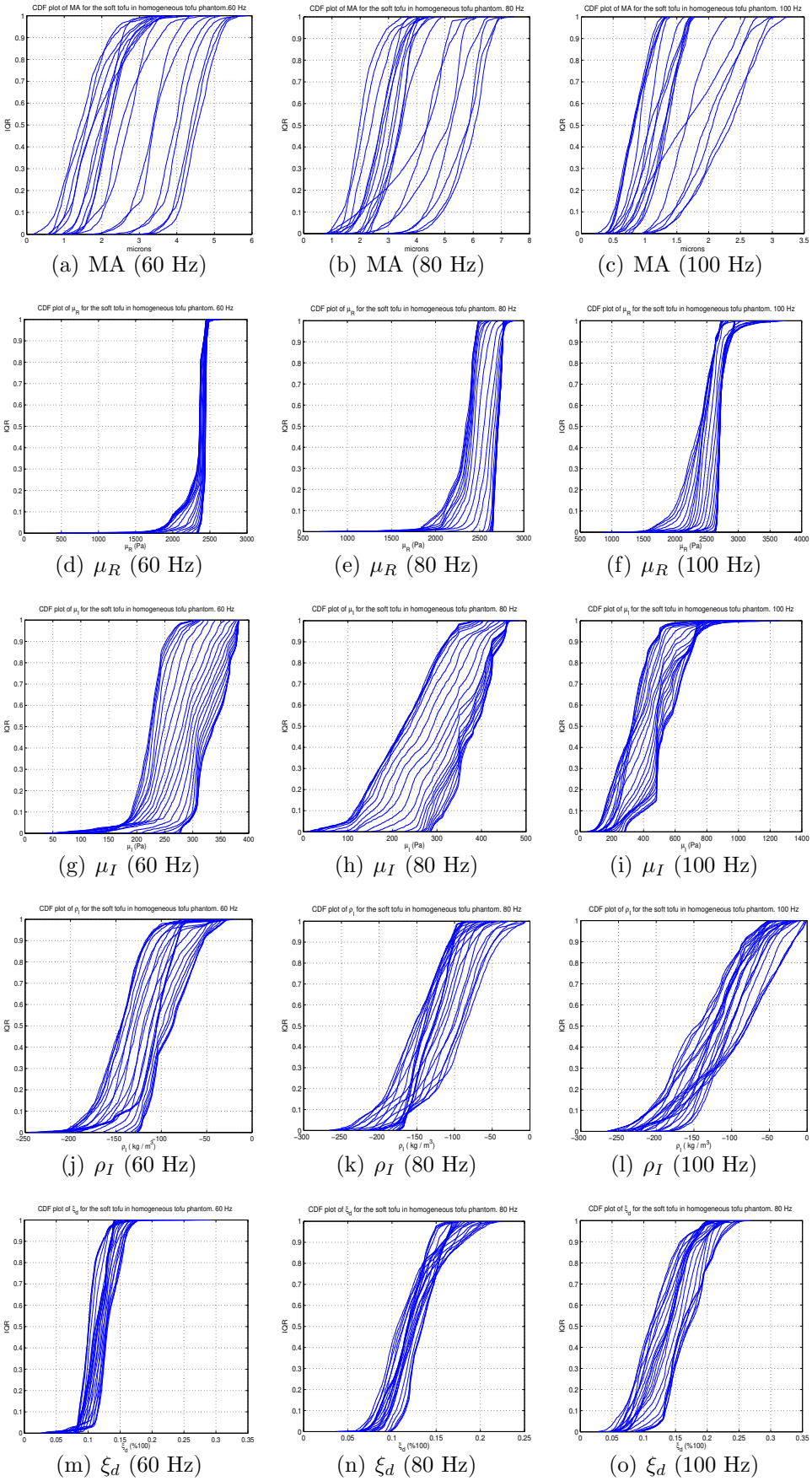

(a) MA (60 Hz) (b) MA (80 Hz) (c) MA (100 Hz)

(d) μ_R (60 Hz) (e) μ_R (80 Hz) (f) μ_R (100 Hz)

(g) μ_I (60 Hz) (h) μ_I (80 Hz) (i) μ_I (100 Hz)

(j) ρ_I (60 Hz) (k) ρ_I (80 Hz) (l) ρ_I (100 Hz)

(m) ξ_d (60 Hz) (n) ξ_d (80 Hz) (o) ξ_d (100 Hz)

Figure 7.8 CDF plots for the soft tofu material of the isotropic homogeneous poroelastic tofu phantom across multiple frequencies of 60 Hz, 80 Hz and 100 Hz: (a), (b) and (c) MA; (d), (e) and (f) μ_R; (g), (h) and (i) μ_I; (j), (k) and (l) ρ_I; (m), (n) and (o) ξ_d

ever, in the nonlinear inverse optimisation problem the accuracy of reconstruction of even straightforward parameters has its limitations and error, thus some variation is not unexpected.

Motion amplitude (MA) results

Fig. 7.7 (a) shows MA behaviour across consequent frequencies of 60, 80 and 100 Hz. MA behaviour across multiple frequencies does follow normal pattern of attenuation. MA is higher near the bottom of the phantom and dissipates in a shape of Bessel functions. This observed drop in MA towards the top of the phantom can be attributed to actuation methodology where the bottom slices are located near the actuation. Relatively small variations are present in MA across the slice across multiple frequencies indicated by the size of error bars on 7.7 (a) and further confirmed by the spread of the CDF function 7.8 (a), (b) and (c). Median values of MA for 60, 80 and 100 Hz are 2.2 μm, 3.3 μm and 1.2 μm, respectively. ROI analysis were performed on original data set containing 20 slices. Hence for a given slice, relatively uniform actuation was received so any variations in results is not due to the uneven actuation.

μ_R results

Qualitatively, the images obtained for the μ_R reconstructions show good recovery of the expected spatial variation in shear modulus across multiple frequencies as can be seen in Fig. 7.6 (a). The soft tofu background was found to be relatively uniform, reflecting the expected homogeneity of the material. During positioning the phantom in the container, a fracture appeared due to the fragile nature of the soft tofu material. The observed drop in shear modulus at the vicinity of the fracture can be attributed to excess fluid that accumulated in the fracture during phantom submersion. The fracture was considered to be an artefact and was excluded from further analysis. All three reconstructions produced similar estimates of the shear modulus for the soft tofu background, yielding a maximum variation in the median of less than 6.5 %.

μ_I results

Fig. 7.6 (b) shows image results of the imaginary shear modulus (μ_I) reconstruction at 80 Hz. Quantitative ROI analysis plots indicate similar μ_I behaviour

throughout the phantom across multiple frequencies with increase towards the top of the phantom (Fig. 7.7 (c)). μ_I seems to have frequency dependant behaviour as confirmed by the median values with maximum variation less than 25.5 % (Table 7.2). Moderate variations in μ_I values distributions across the slices are seen as confirmed by the error bars in Fig. 7.7 (c) and corresponding CDF plots in Figs. 7.8 (g), (h) and (i). μ_I behaviour does not seem to correlate with the MA behaviour.

ρ_I results

Fig. 7.6 (c) presents reconstruction results of imaginary density (ρ_I) at 80 Hz. Variations in parameter behaviour across the slices is clearly visible. Based on quantitate ROI analysis, ρ_I behaviour appears to correlate with the MA behaviour, although some discrepancy between the trends exists. These trends seem to make sense as ρ_I represents rate of the density change and is dependant on the compression level and associated motion (e.g. MA). Variations to different extent in ρ_I parameter values across different slices can be seen on Fig. 7.7 (d) and CDF plots on Figs. 7.8 (j), (k) and (l).

ξ_d results

Qualitatively, the damping ratio (ξ_d) reconstructions again show similar results for multiple frequencies as can be seen on Fig. 7.6 (d). Reconstructed damping distribution looks relatively smooth throughout the phantom, save for some variations across the slices. Based on visual inspection, ξ_d behaviour is inversely proportional to ρ_I behaviour and obviously influenced by μ_I which tends to have relatively constant behaviour throughout the phantom. Quantitative ROI analysis show similar average ξ_d value for multiple frequencies as can be seen in Fig. 7.7 (e).

7.2.2 Summary: isotropic homogeneous poroelastic tofu phantom

The aim of the experiment was to test the ability of the isotropic RD model to accurately characterise viscoelastic properties and damping behaviour of the isotropic homogeneous poroelastic medium. Reconstructed μ_R images were generally of a highest quality compared to the reconstructed RD based parameters for μ_I and ρ_I,

that showed significant variations in a supposedly homogeneous material.

7.3 Tofu-gelatine phantoms

The goal of this study is to investigate the capability of RD MRE to accurately reconstruct and characterise VE and damping properties of the tissue-mimicking damping phantoms. The phantoms were made of a combination of poroelastic and elastic materials, subjected to a time-harmonic actuation at multiple frequencies. The choice of the materials was made with a goal of achieving a good damping contrast within the phantoms. Since tofu has more attenuation than gelatine, significant contrast is expected in damping behaviour between these two materials. It is hypothesised that it is feasible to use time-harmonic RD MRE to distinguish between homogeneously poroelastic material (tofu) and homogeneously elastic material (gelatine) characterized by different mechanical properties. A discussion of some of the uniqueness issues associated with the RD mechanical model is also presented, as well a summary of results and in-depth analysis from a study of tofu-gelatine phantoms.

Tables 7.4 and 7.5 summarise the results across multiple frequencies. Figs. 7.9 and 7.12 show the T2*- weighted MR images for P1 and P2 phantoms with selected ROIs for the background and inclusions. Fig. 7.10 shows the 3 parameter-based RD MRE reconstruction results, which, as in prior cases, shows significant failure to differentiate materials clearly in μ_I and ρ_I results. Fig. 7.13 shows the same results for the inverted P2 phantom configuration with similar qualitative outcomes. Table 7.3 shows comparison between computed by MRE results to DMA measured results. Lastly, Table 7.6. summarises MD differences between MRE, DMA and other published results.

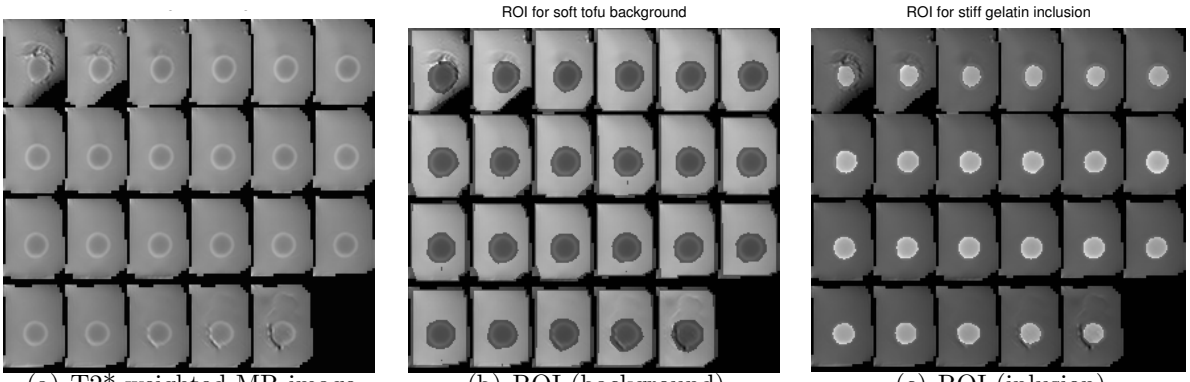

(a) T2*-weighted MR image (b) ROI (background) (c) ROI (inlusion)

Figure 7.9 MRI image results of the P1 phantom with ROI selections indicated: (a) High resolution $T2^*$ weighted MR image; (b) MR image (background ROI indicated); (c) MR image (inclusion ROI indicated).

Table 7.3 Comparison between DMA and MRE results for the gelatine & soft tofu at 100Hz

Material	Gelatine		Tofu	
Parameter	MRE	DMA	MRE	DMA
μ_R (Pa)				
P1	11636 [10068 – 12355]	8800 ± 900	3590 [3327 – 4113]	6368 ± 390
P2	14506 [14287 – 15911]		7200 [5378 – 9151]	
μ_I (Pa)				
P1	31 [18 – 50]	294 ± 131	109 [59 – 211]	NA
P2	510 [394 – 551]		137 [80– 230]	

Table 7.4 Quantitative ROI analysis of the P1 phantom for multiple frequencies

Parameter Units	MA (μm)	μ_R (Pa)	μ_I (Pa)	ρ_I (kg/m^3)	ξ_d (% / 100)
	Median [IQR]	Median [IQR]	Median [IQR]	Median [IQR]	Median [IQR]
Gelatine (50 Hz)	1.42 [1.37 – 1.56]	4926 [4763 – 5052]	3.6 [2.8 – 6.6]	-4 [-13 – -2]	0.0038 [0.0013 – 0.0125]
Gelatine (75 Hz)	1.64 [1.56 – 1.80]	8372 [8053 – 8635]	80 [63 – 98]	-13[-20 – -5]	0.014 [0.001 – 0.020]
Gelatine (100 Hz)	2.33 [2.29 – 2.39]	11638 [10680 – 12355]	31 [18 – 50]	-19 [-58 – -5]	0.012 [0.0037 – 0.0395]
Gelatine (125 Hz)	2.32 [2.10 – 2.49]	14790 [13838 – 15860]	51 [19 – 194]	-73[-108 – -39]	0.037 [0.020 0.054]
Soft tofu (50 Hz)	2 [1.56 – 2.54]	3288 [3034 – 3601]	85 [33 – 353]	-46 [-114 – -9]	0.066 [0.030 – 0.124]
Soft tofu (75 Hz)	1.92 [1.52 2.46]	3341 [3105 – 3624]	256 [123 – 393]	-85 [-192 – -32]	0.10 [0.07 – 0.14]
Soft tofu (100 Hz)	1.94 [1.65 – 2.33]	3590 [3327 – 4113]	109 [59 – 211]	-157 [-260 – -92]	0.11 [0.072 – 0.156]
Soft tofu (125 Hz)	1.79 [1.42 – 2.31]	4902 [4181 – 6128]	102 [30 – 325]	-401 [-658 – -130]	0.22 [0.11 – 0.34]

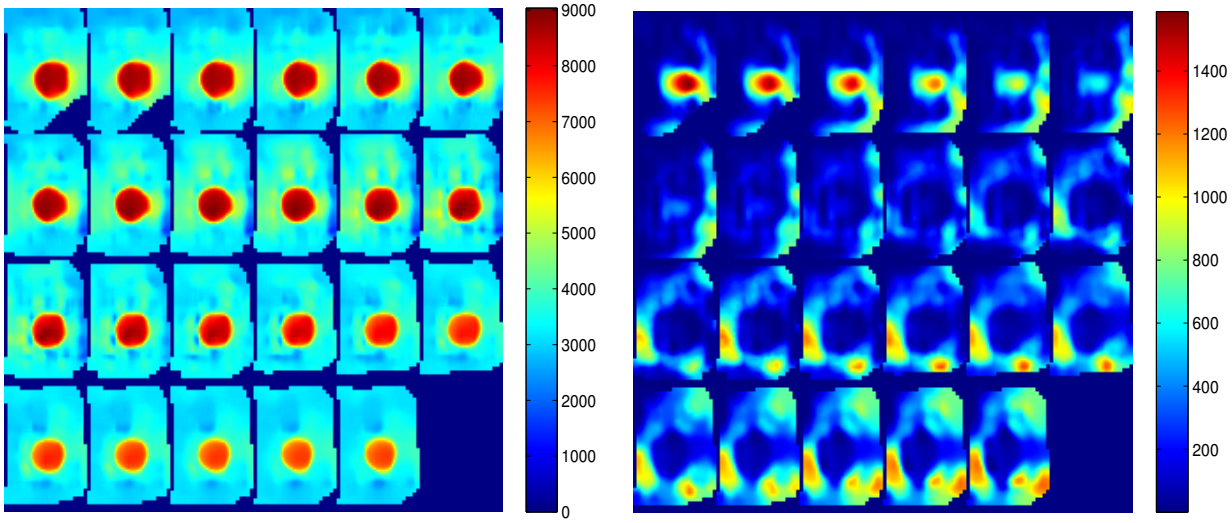

(a) μ_R (b) μ_I

(c) ρ_I (d) ξ_d

Figure 7.10 Image results for the full 3 parameter-based RD reconstruction of the P1 phantom (soft tofu background with a single stiff gelatine inclusion) using 75 Hz mechanical excitation: (a) storage modulus μ_R image (Pa); (b) loss modulus μ_I image (Pa); (c) imaginary density ρ_I image (kg/m^3) and (d) damping ratio ξ_d image (% / 100)

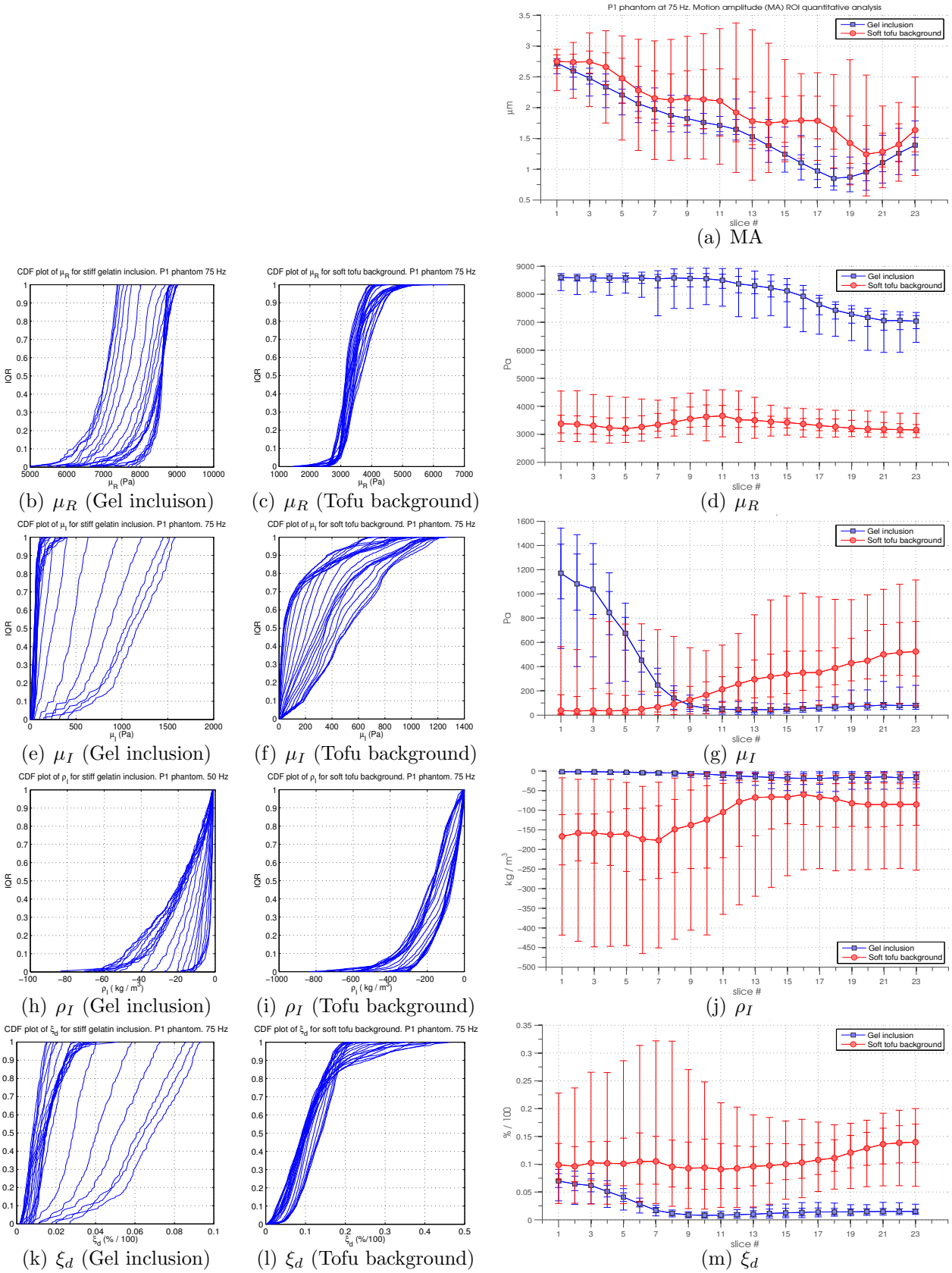

(a) MA (b) μ_R (Gel incluison) (c) μ_R (Tofu background) (d) μ_R (e) μ_I (Gel inclusion) (f) μ_I (Tofu background) (g) μ_I (h) ρ_I (Gel inclusion) (i) ρ_I (Tofu background) (j) ρ_I (k) ξ_d (Gel inclusion) (l) ξ_d (Tofu background) (m) ξ_d

Figure 7.11 Quantitative analysis of P1 phantom at 75 Hz for the soft tofu background material and the stiffer gelatine inclusion for the reconstructed material properties within the selected ROIs, and associated CDF plots for each material property: top row: motion amplitude, second row: μ_R, third row: μ_I, forth row: ρ_I and bottom row: ξ_d

Table 7.5 Quantitative ROI analysis of the P2 phantom for multiple frequencies

Parameter Units	MA (μm) Median [IQR]	μ_R (Pa) Median [IQR]	μ_I (Pa) Median [IQR]	ρ_I (kg/m^3) Median [IQR]	ξ_d (% /100) Median [IQR]
Gelatine (50 Hz)	1.6 [1.34 – 1.86]	8920 [8435 – 9278]	276 [241 – 312]	-15 [-27 – -8]	0.024 [0.0193 – 0.032]
Gelatine (75 Hz)	1.75 [1.45 – 2]	10930 [10733 – 11202]	445 [324 – 537]	-58 [-78 – -28]	0.05 [0.03 – 0.062]
Gelatine (100 Hz)	1.77 [1.31 – 1.98]	14506 [14287 – 15911]	510 [394 – 551]	-47 [-81 – -23]	0.04 [0.028 – 0.054]
Gelatine (125 Hz)	1.72 [1.47 – 2.14]	16048 [15763 – 16714]	732 [474 – 866]	-63 [-117 – -25]	0.054 [0.036 – 0.082]
Soft tofu (50 Hz)	2.6 [2 – 3]	6688 [5661 – 7508]	161 [110 – 186]	-154 [-257 – -70]	0.088 [0.045 – 0.14]
Soft tofu (75 Hz)	2 [1.66 – 2.6]	5189 [4034 – 7679]	267 [59 – 472]	-50 [-132 – -6]	0.06 [0.03 – 0.098]
Soft tofu (100 Hz)	2.23 [1.8 – 2.64]	7200 [5378 – 9151]	137 [80 – 230]	-228 [-356 – -140]	0.12 [0.091 0.186]
Soft tofu (125 Hz)	1.85 [1.57 – 2.18]	8995 [6325 – 11550]	97 [42 – 210]	-262 [-500 – -83]	0.13 [0.05 – 0.25]

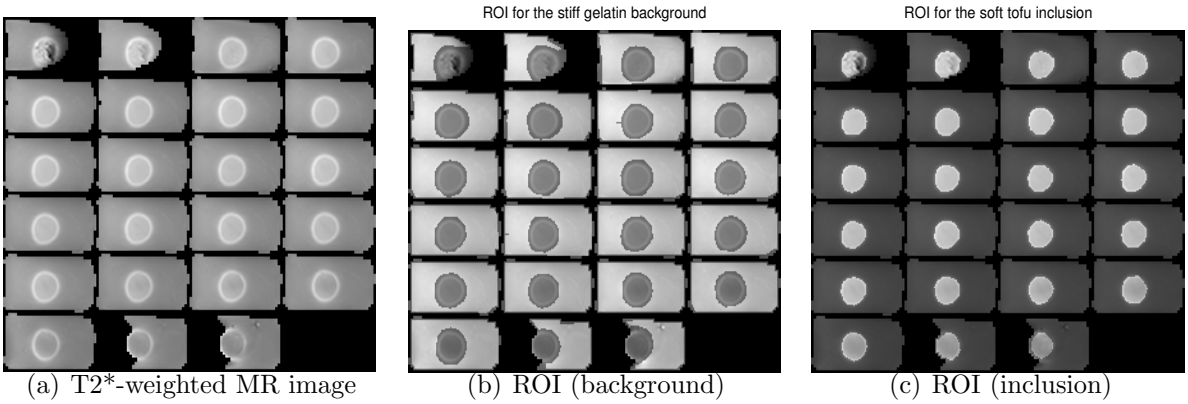

(a) T2*-weighted MR image (b) ROI (background) (c) ROI (inclusion)

Figure 7.12 MRI image results of the P2 with ROI selections indicated: (a) High resolution $T2^*$ weighted MR image; (b) MR image (background ROI indicated); (c) MR image (inclusion ROI indicated).

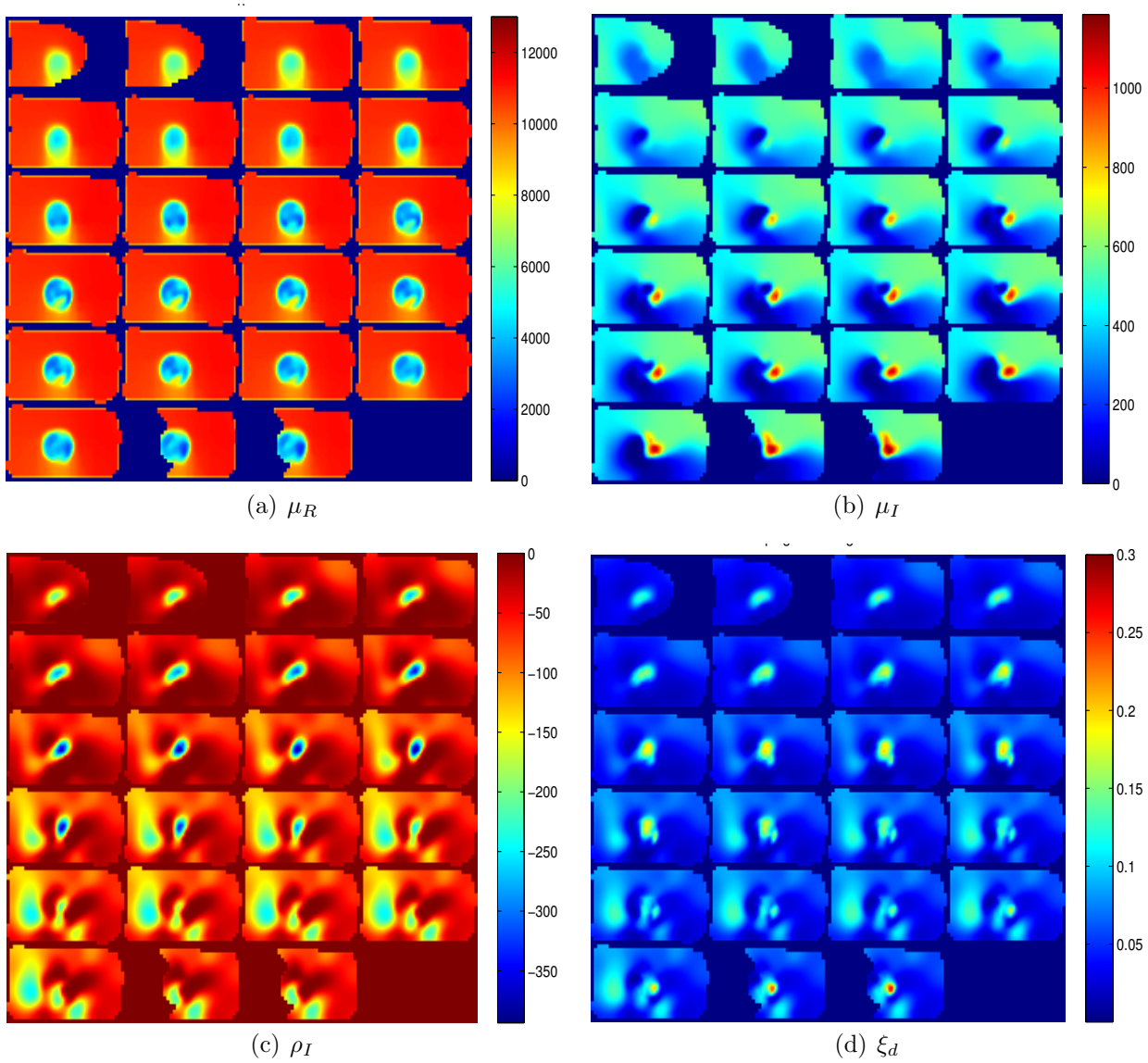

(a) μ_R (b) μ_I

(c) ρ_I (d) ξ_d

Figure 7.13 Image results for the full 3 parameter-based RD reconstruction of the P2 phantom (stiff gelatine background with a single soft tofu inclusion) using 75 Hz mechanical excitation: (a) storage modulus μ_R image (Pa); (b) loss modulus μ_I image (Pa); (c) imaginary density ρ_I image (kg/m^3) and (d) damping ratio ξ_d image (% / 100)

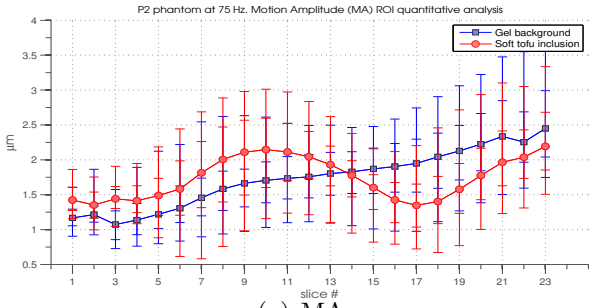

(a) MA

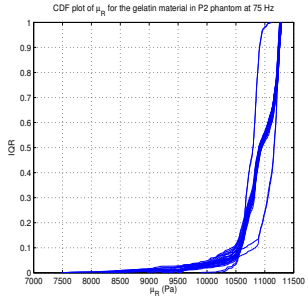

(b) μ_R (Gel Background)

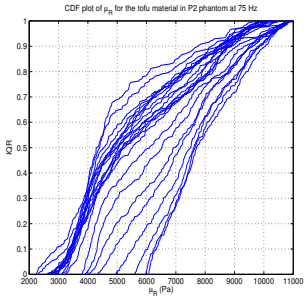

(c) μ_R (Tofu inclusion)

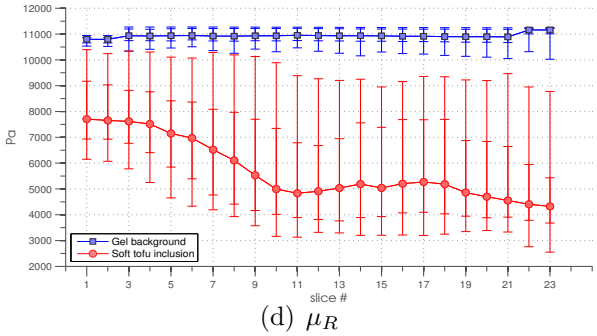

(d) μ_R

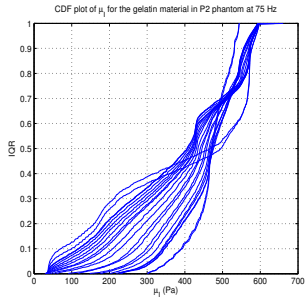

(e) μ_I (Gel Background)

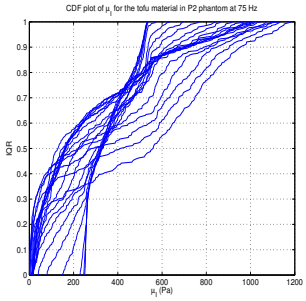

(f) μ_I (Tofu inclusion)

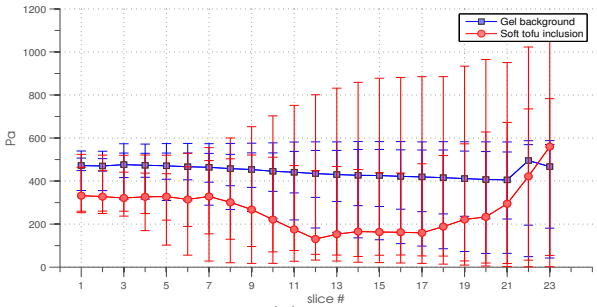

(g) μ_I

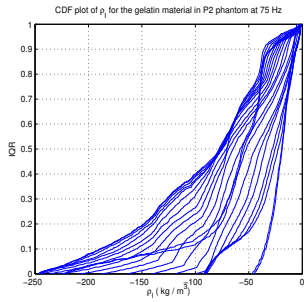

(h) ρ_I (Gel Background)

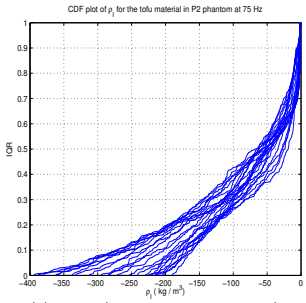

(i) ρ_I (Tofu inclusion)

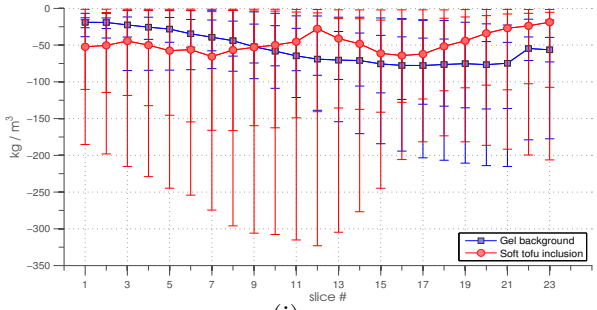

(j) ρ_I

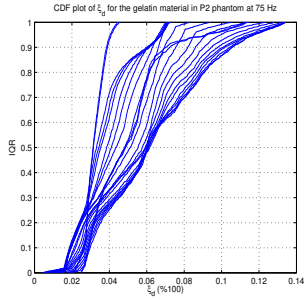

(k) ξ_d (Gel Background)

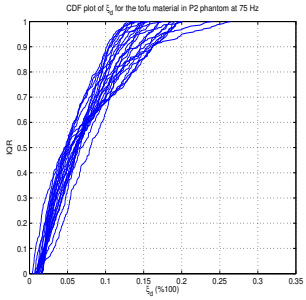

(l) ξ_d (Tofu inclusion)

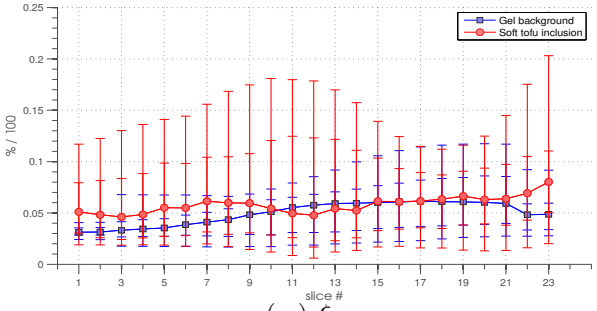

(m) ξ_d

Figure 7.14 Quantitative analysis of P2 phantom for the gelatine background material and soft tofu inclusion for reconstructed material properties within the selected ROI and associated CDF plots for each material property: top row: motion amplitude, second row: μ_R, third row: μ_I, forth row: ρ_I and bottom row: ξ_d

Table 7.6 MD comparison of parameters measured by MRE and DMA for P1 and P2 and Hmg tofu phantom

Soft Tofu	μ_R (%)	μ_I (%)	ρ_I (%)	ξ_d (%)
P1 vs P2 (50 Hz)	68	61	108	28
P1 vs P2 (75 Hz)	43	4	51	50
P1 vs P2 (100 Hz)	66	23	36	8
P1 vs P2 (125 Hz)	59	5	41	51
P1 (50 Hz) vs Hmg (60 Hz)	31	110	83	58
P1 (75 Hz) vs Hmg (80 Hz)	25	112	40	18
P1 (100 Hz) vs Hmg (100 Hz)	30	123	33	24
P1 (100 Hz) vs Van Houten et al. (2011)	30	81	Na	Na
P2 (50 Hz) vs Hmg (60 Hz)	94	58	31	30
P2 (75 Hz) vs Hmg (80 Hz)	66	22	87	66
P2 (100 Hz) vs Hmg (100 Hz)	92	109	68	15
P1 (100 Hz) vs DMA	55	Na	Na	Na
P2 (100 Hz) vs DMA	12	Na	Na	Na
10 % Gelatine	μ_R (%)	μ_I (%)	ρ_I (%)	ξ_d (%)
P1 vs P2 (50 Hz)	57	194	115	145
P1 vs P2 (75 Hz)	26	139	126	112
P1 vs P2 (100 Hz)	22	177	84	107
P1 vs P2 (125 Hz)	31	173	14	37
P1 (100 Hz) vs DMA	28	161	Na	Na
P2 (100 Hz) vs DMA	48	53	Na	Na
P1 (100 Hz) vs Van Houten et al. (2011)	25	68	Na	Na
P2 (100 Hz) vs Hmg (100 Hz)	57	Na	Na	61

7.3.1 Discussion: tofu-gelatine phantoms

Motion amplitude (MA) results

Generally, in the P1 phantom MA gradually decreases towards the top of the phantom. This is an expected behaviour as the bulk of the phantom is made of porous tofu material, which has higher rate of attenuation compared to the gelatine. Generally, MA is slightly higher in the tofu than in gelatin. High variation in MA is seen in the tofu background across the slices and low variation in MA distribution is seen in the stiff gelatin inclusion within each slice. In P2, the opposite tends in MA behaviour are noted.

It is important to emphasise that since both phantoms were homogenous, all reconstruction parameters should have consistent behavior across the slices. Previously introduced analysis showed that reconstructed parameters (μ_R, μ_I, ρ_I and resulting ξ_d) did not behave uniformly throughout the phantoms despite materials homogeneity and are dependant on MA. Thus, some of the observed trends in parameter behaviour was due to unmodelled non-linear responses to MA.

μ_R results

Qualitatively, the μ_R reconstruction of both materials in the P1 phantom at 75 Hz was successful in confirming the higher stiffness of the gelatine inclusion compared to the soft tofu background (refer to Fig. 7.10 (a)). Boundaries between the two materials were accurately delineated with no significant artefacts present. Generally, the μ_R behaviour within both materials is consistent throughout the phantom as confirmed by plotted median values in Fig. 7.11 (d). The variation in the distribution of the μ_R values within both materials was found to be relatively low, as confirmed by the IQR values given in Table 7.4. These trends were further supported by the CDF plots, indicating similar behaviour and normal distribution of the μ_R values within the soft tofu material as noted in Fig. 7.11 (c). The difference in μ_R median values within the gelatine inclusion is depicted by CDF offsets as shown in Fig. 7.11 (b).

Agreement in the μ_R reconstruction results within the soft tofu material between P1 at 75 Hz and a homogeneous tofu phantom at 80 Hz was 25%; while agreement within the soft tofu between both phantoms at 100 Hz was 30%. Agreement between

the 3 parameter-based RD reconstruction results and the DMA measurements for the μ_R within the soft tofu material was poor, with a difference of 55%; and within the stiff gelatine was reasonable, with the a difference of 28%. Finally, MD comparison revealed that agreement between μ_R values observed for both materials in P1 at 100 Hz and those observed by Van Houten et al. (2011) in a similar phantom configuration (single stiff gelatine inclusion within soft tofu background) at 100 Hz was relatively moderate, with differences ranging from 30% to 25% for the tofu background and 10% gelatine inclusion, respectively. For more detailed treatment of MD comparison between different materials refer to Table 7.6.

The opposite qualitative trends were observed in the P2 phantom across multiple frequencies where the tofu inclusion was reconstructed with lower stiffness values compared to the stiff gelatine background. Qualitatively, the μ_R reconstruction at 75 Hz showed good success as shown in Fig. 7.13 (a). Both materials were accurately characterised, with relatively low shear modulus for the soft tofu inclusion compared to higher stiffness values within the stiff gelatine background. Smooth distribution of property values is seen in both materials. Boundaries between the two materials were also accurately delineated except for the lower slices.

The trends in μ_R behaviour within porous medias, such as tofu, are not fully understood. Agreement in μ_R medians within the soft tofu background in P1 at 75 Hz and the soft tofu inclusion in P2 at 75 Hz was relatively poor, with difference of 43%; and for the gelatine inclusion in P1 compared to the gelatine background in P2 the agreement was better, differing by 26%.

Overall, quantitate ROI analysis indicates stable parameter behaviour of either material being a background of the phantom. In contrast, the parameter behaviour within the inclusions generally show variations throughout the phantom. Furthermore, the identified values of μ_R in both materials consistently increased in both phantoms with higher frequencies (refer to Table 7.4 and Table 7.5), which correlates well with the *power law* (Newman, 2005). Agreement in μ_R medians for the soft tofu material between P1 and P2 was relatively poor, ranging from 68% at 50 Hz to 59 % at 125 Hz (refer to Table 7.6). For the 10 % gelatine material, the difference in μ_R median values between P1 and P2 was slightly better, ranging from 57% at 50 Hz to 31% at 125 Hz.

Independent measurements of the shear modulus of the materials are not avail-

able to compare numerical values. Therefore, assessment of quantitate accuracy of the RD MRE is not possible. Comparison of the quantified stiffness estimates of both tofu and gelatine materials by RD MRE with DMA measurements at 100 Hz generally showed a poor agreement, with differences ranging from 55% to 12% as shown in Table 7.6.

μ_I results

In P1 phantom, the μ_I behaviour generally followed similar quantitate trends across multiple frequencies. More specifically, μ_I values in the soft tofu background increased towards the top of the phantom and were lower in the stiffer gelatine inclusion. The inclusion appears in relatively high μ_I values in the bottom slices of the phantom (located near the actuation source) and gradually decreases towards the top of the phantom. In contrast, the μ_I behaviour within the soft tofu background tends to gradually increase towards the top of the phantom.

In P2 phantom, μ_I behaviour also displayed similar trends across multiple frequencies. However, these trends were different to those observed in P1. Generally, the μ_I within the stiff gelatine background did not drop towards the top of the phantom, as was seen within the gelatine inclusion in P1 across multiple frequencies. Similarly, the μ_I within the soft tofu inclusion did not increase towards the top of the phantom, as was seen in P1 within the soft tofu background across multiple frequencies.

Qualitatively, μ_I reconstruction in P1 phantom at 75 Hz was not successful (refer Fig. 7.10 (b)). Large variations were observed in μ_I within the soft tofu background while small variations were seen within the soft tofu inclusion as confirmed by IQR values and associated error bars in Fig. 7.11 (g). CDF plots indicate uniform distribution of property values within the gelatine inclusion and a relatively normal distribution within the tofu background as shown in Figs. 7.11 (e) and 7.11 (f).

Qualitatively, μ_I reconstruction of P2 at 75 Hz showed smooth distribution of property values within the stiff gelatine background material (refer to Fig. 7.13 (b)). The appearance of the artefact, depicted with high μ_I values, on the RHS of the inclusion could easily be traced with visual inspection of the image. No change in parameter behaviour was seen throughout the phantom within the stiff gelatine background with relatively small variations present, as confirmed by the medians

and corresponding IQR values (refer to Fig. 7.14 (g)). In case of the soft tofu inclusion, changes in the parameter behaviour with accompanying large variations were seen throughout the phantom. CDF plots indicate variations in parameter distributions across each slice for both materials (Fig. 7.14 (e) and Fig. 7.14 (f)).

In the RD model formulation, the μ_I represent a stiffness proportional term ($\beta\omega$) that contributes damping linearly proportional to the input frequency. Therefore, increase of μ_I values with the frequency increase is expected. Based on quantitate ROI analysis overall increase of the μ_I property values proportional to the increase of the input frequency was observed in P1 except μ_I quantitative estimates at 75 Hz. In P2, increase of μ_I values with the input frequency was seen in the gelatine background material. The μ_I parameter behaviour within the soft tofu inclusion did not display consistent increase, but rather decrease in property values. These observations suggest a potential identifiably problem of the RD model at a single frequency.

ρ_I results

In P1, the overall ρ_I behaviour had similar trends across multiple frequencies. More specifically, ρ_I estimates within the soft tofu background material were relatively high compared to the low ρ_I values found in the stiff gelatine inclusion. These trends seem to support rheological interpretation of the ρ_I and associated density change in bi-phasic porous media. The gelatine is made of densely packed collagen fibers, therefore no increase in the ρ_I values is expected.

Qualitatively, the ρ_I reconstruction in P1 at 75 Hz had a moderate success (refer to Fig. 7.10 (c)). Especially good qualitative success was achieved in the lower half of the phantom where the location of the inclusion was clearly distinguished within the background material. Reasonably good delineation of the inclusion boundaries was also observed. Less success was seen in the upper half of the phantom, where the location of the inclusion was not clearly distinguished with a poor delineation of boundaries between the two independent material regions.

In P2, the ρ_I reconstruction results at 75 Hz were qualitatively poor. Here, the presence of the inclusion was partially captured in the ρ_I image. However, the geometry and location of the inclusion did not correspond to the one seen in the T2* MR image. The transition between two independent material zones was

evident, however accurate delineation of the inclusion boundaries failed (refer to Fig. 7.13 (c)). Quantitative ROI plots indicate relatively consistent ρ_I behaviour with large image variations within the stiff gelatine background; while increase in property values within the soft tofu inclusion was observed towards the top of the phantom (refer to Fig. 7.14 (j)). The difference in ρ_I median values between the gelatine inclusion in P1 and the gelatin background in P2 at 75 Hz was 126 %; while variation in ρ_I median values between the tofu background in P1 and the tofu inclusion in P2 at 75 Hz was moderate, with difference of 51 %.

ξ_d results

It is important to recapitulate that RD MRE is able to quantify the amount of damping present in the medium by expressing the damping matrix as a sum of two terms. One is proportional to the mass matrix (ρ_I) and the other to the stiffness matrix (μ_I). Therefore, an optimisation based fitting of those two independent parameters enables quantification of damping distribution throughout the medium. Furthermore, the RD model postulates an increase in the damping ratio (ξ_d) to be linearly proportional to the increase of the input frequency.

Generally, qualitative ξ_d reconstruction in P1 was successful across multiple frequencies, correctly indicating higher damping level in the more attenuating tofu material compared to the gelatine. A contrast between damping profiles of both materials could be clearly distinguished, although only in the bottom slices and not matching the ROI size. Moderate variations were seen within the both materials as confirmed by IQR values in quantitative ROI analysis plots. In case of lower frequencies, ξ_d distribution is relatively uniform across the phantoms with slight variations.

Qualitatively, ξ_d reconstruction in P1 at 75 Hz (refer to Fig. 7.10 (d)) had a moderate success. Here, the geometry and location of these artefacts correlated well with those seen in the ρ_I image (refer to Fig. 7.10 (c)). CDF plots indicate generally good agreement in property distributions within the tofu background material throughout the phantom (Fig. 7.11 (l))). Agreement in ξ_d values for the soft tofu background in P1 at 75 Hz and homogeneous tofu phantom at 80 Hz was reasonable, with a difference of 18 %.

In P2, ξ_d images generally identified presence of the tofu inclusion, correctly

confirming higher loss of mechanical energy in the more attenuating tofu material compared to the stiffer gelatine background across multiple frequencies. However, accurate characterisation of both materials as well as delineation of the boundaries failed. The difference in ξ_d values between the tofu background in P1 at 75 Hz and the tofu inclusion in P2 at 75 Hz was moderate with difference of 50 %; and with regards to the gelatin inclusion in P1 and the gelatin background in P2 was relatively large, with difference of 112 %.

7.3.2 Summary: tofu-gelatine phantoms

Overall, good success was achieved in reconstruction of real shear modulus in both phantom configurations across multiple frequencies. Generally, μ_R images showed reasonable characterisation of both material types with acceptable delineation of the boundaries. Reconstruction of the RD based properties displayed a consistent effect of poor reconstruction accuracy in both phantoms across multiple frequencies. Rheological interpretation of the μ_I and ρ_I images remains inconclusive. The trends in the parameter behaviour are not fully understood and certainly warrant further investigation of the identifiability of the model. Generally, reconstructed ξ_d provided acceptable differentiation of a the tofu material compared to the gelatine which is in agreement with the expected damping behaviour of both materials. Generally, the location of the inclusion was distinguished in ξ_d image in both phantoms across multiple frequencies.

7.4 Tofu-water damping phantom (P5)

This study evaluates the viability of the full 3 parameter-based RD MRE to reconstruct VE properties and damping behaviour of the fluid filled cavities within the porous media. It is important to investigate whether RD model is able to accurately reconstruct the mechanical properties of the fluids. The tofu-water phantoms are a reasonable approximation of the brain, where the soft tofu mimics the porous structure of the brain matter and fluid filled inclusions mimic the CSF filled ventricles.

Fig. 7.15 (a) show a T2*-weighted high resolution MR magnitude image of the P5 phantom. Both water inclusion of different diameters are clearly depicted. Figs.

7.15 (b) and 7.15 (c) show MR images with indicated ROIs for the soft tofu background and water inclusions, respectively. Figs. 7.16 -7.17 show RD reconstruction results. Summary of the quantitative ROI analysis is presented in Table 7.7. Again, in Figs. 7.16 - 7.17 it is clear that μ_I and ρ_I are not easily identified to expected differences or values across materials, regardless of frequency.

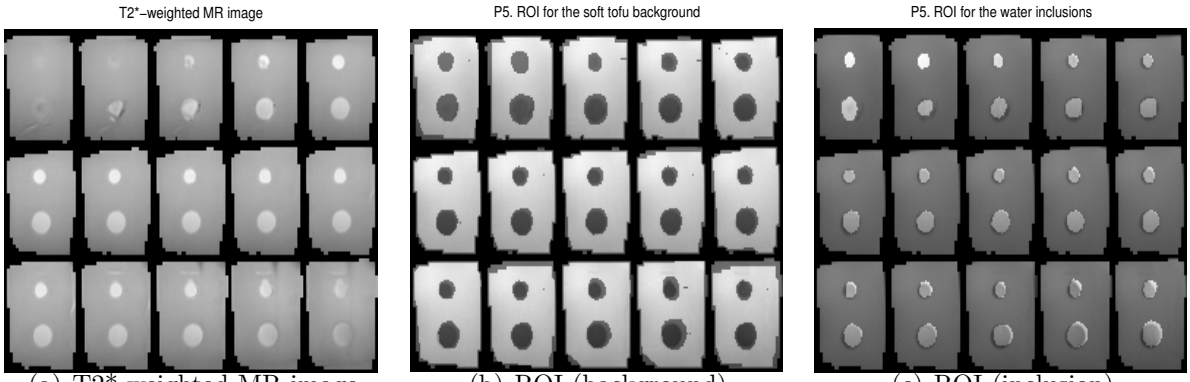

(a) T2*-weighted MR image (b) ROI (background) (c) ROI (inclusion)

Figure 7.15 MRI image results of the P5 phantom with ROI selections indicated: (a) High resolution $T2^*$-weighted MR image of P5 phantom; (b) MR image (background ROI indicated) and (c) MR image (inclusion ROI indicated)

Table 7.7 ROI analysis results of the poroelastic tofu phantom with a double water inclusion (P5)

Parameter Units	MA (μm)	μ_R (Pa)	μ_I (Pa)	ρ_I (kg/m^3)	ξ_d (% / 100)
	Median [IQR]	Median [IQR]	Median [IQR]	Median [IQR]	Median [IQR]
Soft tofu (60 Hz)	1.47 [1.26 – 1.85]	2065 [1996 – 2165]	276 [225 – 323]	-100 [-127 – -72]	0.11 [0.095 – 0.13]
Soft tofu (80 Hz)	1.7 [1.4 – 1.95]	2183 [2086 – 2260]	360 [293 – 481]	-90 [-118 – -69]	0.13 [0.11 – 0.15]
Soft tofu (100 Hz)	1.78 [1.49 – 2]	2286 [2169 – 2336]	414 [306 – 545]	-96 [-134 – -58]	0.13 [0.11 – 0.16]
Water (60 Hz)	1.44 [1.30 – 1.66]	1514 [931 – 1805]	130 [90 – 184]	-80 [-105 – -37]	0.09 [0.07 – 0.14]
Water (80 Hz)	1.9 [1.62 – 2]	1291 [874 – 1746]	384 [225 – 602]	-76 [-104 – -45]	0.19 [0.11 – 0.29]
Water (100 Hz)	1.6 [1.48 – 1.71]	1356 [991 – 1531]	450 [272 – 681]	-79 [-107 -56]	0.2 [0.14 – 0.29]

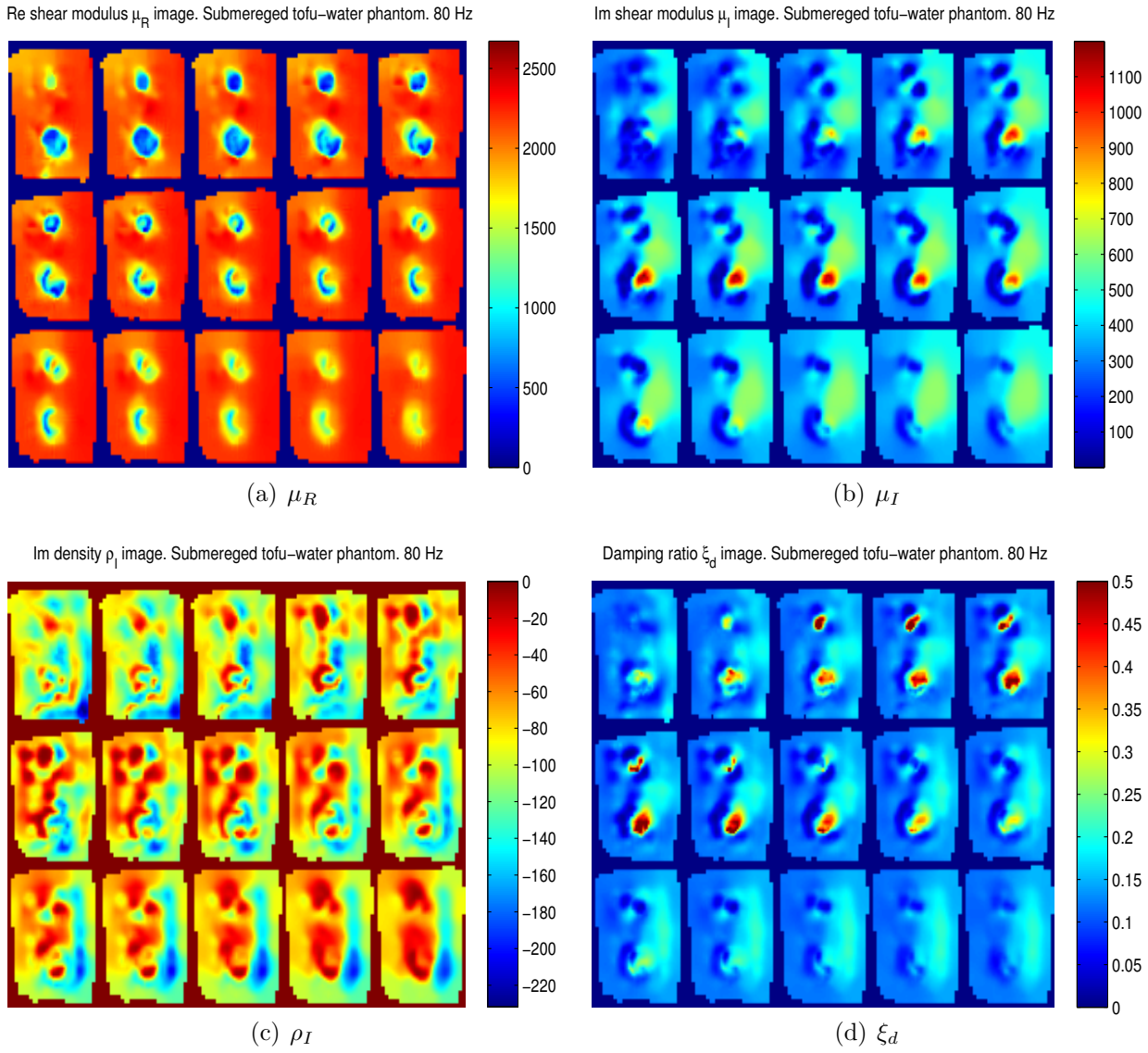

(a) μ_R (b) μ_I

(c) ρ_I (d) ξ_d

Figure 7.16 Image results for the full 3 parameter-based RD reconstruction of the P5 phantom (soft tofu background with a double water inclusion) using 80 Hz mechanical excitation: (a) storage modulus μ_R image (Pa); (b) loss modulus μ_I image (Pa); (c) imaginary density ρ_I image (kg/m^3); and (d) damping ratio ξ_d image (% / 100)

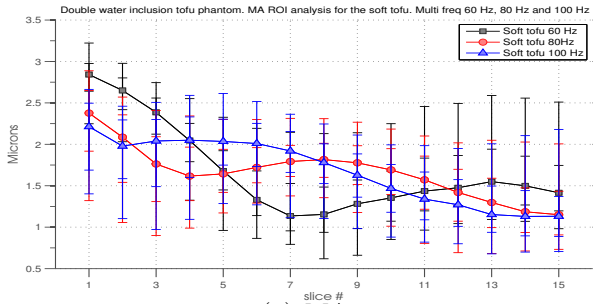

(a) MA

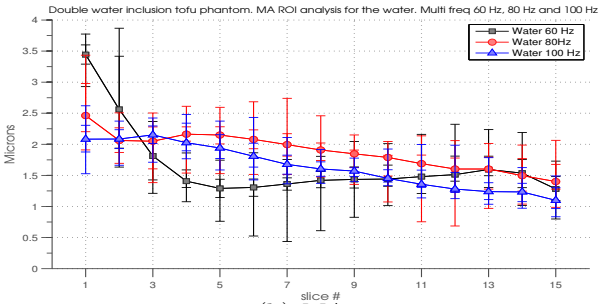

(b) MA

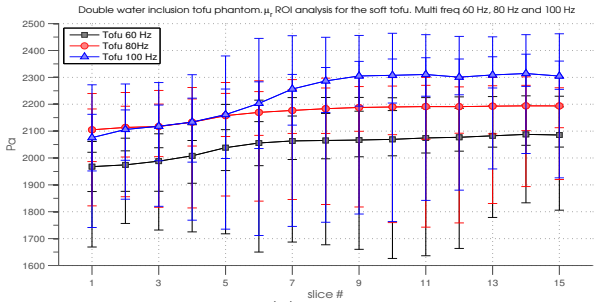

(c) μ_R

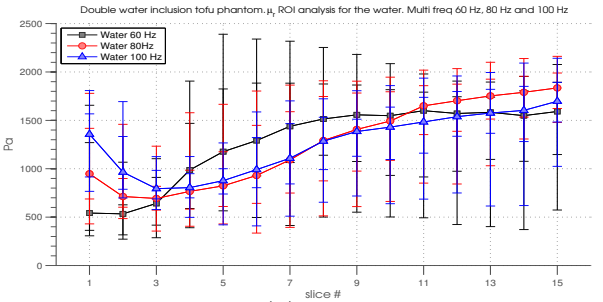

(d) μ_R

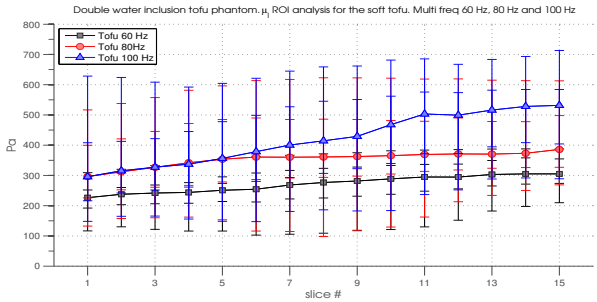

(e) μ_I

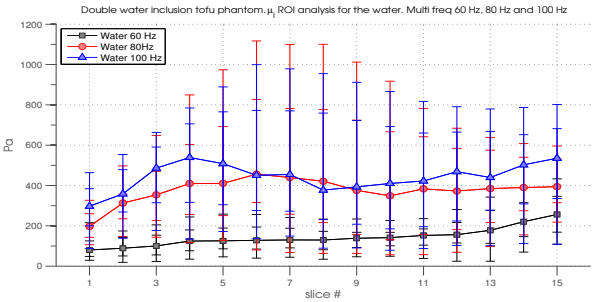

(f) μ_I

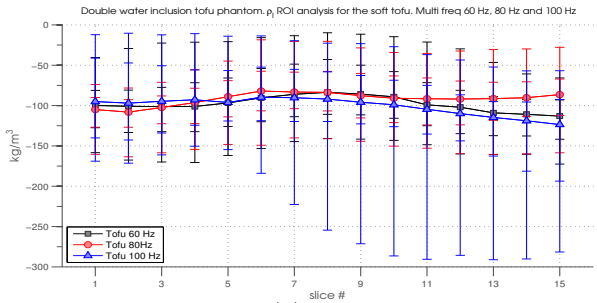

(g) ρ_I

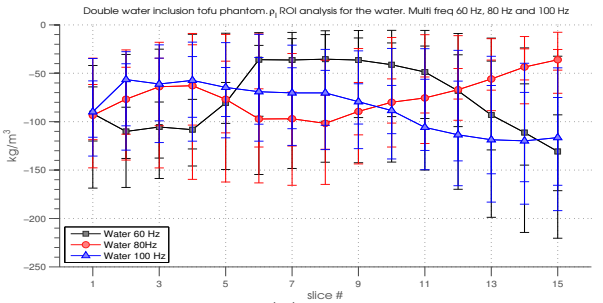

(h) ρ_I

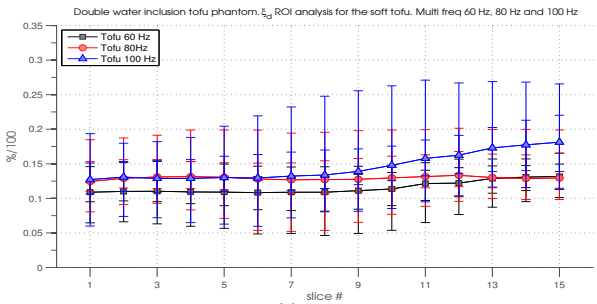

(i) ξ_d

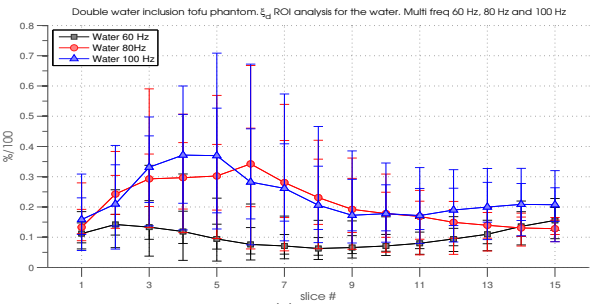

(j) ξ_d

Figure 7.17 Quantitative ROI slice by slice analysis of the soft tofu background (left column) and a double water inclusion (right column) of the P5 for different material properties across multiple frequencies of 60 Hz, 80 Hz and 100 Hz: (a) and (b) MA; (c) and (d) μ_R; (e) and (f) μ_I; (g) and (h) ρ_I and (e) ξ_d

7.4.1 Discussion: P5 phantom

μ_R results

In the RD model the fluid is modelled as an elastic solid, therefore accurate characterisation of the fluid properties is not anticipated due to the fundamental data-model mismatch. Based on the Navier-Stokes equation for the the fluid, near zero shear modulus are expected within the fluid as there is no resistance to the shear displacement.

Qualitatively, the images obtained for the μ_R reconstructions of the double water inclusion tofu phantom (P5) across multiple frequencies had a mixed success. In general, the variation in the μ_R values within the soft tofu background material across multiple frequencies was seen to be relatively low, as confirmed by the median and IQR values, given in Table 7.7. Stable μ_R parameter behavior was generally observed within the soft tofu background with slight increase towards the top of the phantom in all three frequencies (refer to Fig. 7.17 (c)).

For the μ_R reconstruction, high variations were seen within the region of the inclusions, where incompressible fluid assumptions in the RD model would be inaccurate. The presence of the fluid filled inclusions was evident, however only partial success in accurate characterisation of the properties of the fluid was achieved. More specifically, relatively low shear modulus were seen in the exterior of the fluid inclusion compared to the high shear modulus observed in the interior of the inclusions. The boundaries of the inclusion were accurately delineated.

Interestingly, relatively low μ_R values were seen across the entire region of both inclusions in the lower half of the phantom across multiple frequencies. Based on quantitative ROI analysis of the accurately reconstructed fluid inclusions near the base of the phantom, the μ_R medians were 500 Pa, 700 Pa and 800 Pa for 60 Hz, 80 Hz, and 100 Hz, respectively. These values are still high compared to expected near zero shear modulus. Relatively accurate delineation of the fluid filled inclusions seems to correlate well with the high MA near the base of the phantom (refer to Fig. 7.17 (b)). An artefact (stiff spot in the middle of the water inclusion) started to appear in the upper half of the phantom for all three frequencies. The limitation of the RD model to correctly interpret stiffness estimates of the fluid inclusions in the upper half of the phantom may be attributed to the significant motion attenuation

within the water inclusions towards the top of the phantom (refer to Fig. 7.17 (b)).

There are two possible explanations for the appearance of the artefact (area with the high shear modulus) in the middle of the water inclusion. The first one might be related to the fundamental data-model mismatch and a limitation of the RD model to correctly estimate mechanical properties of the fluid. The second one might be related to the experimental set up, actuation methodology and, most importantly, the symmetry of the inclusion with regards to the phantom configuration. The latter might caused the reflected acoustic waves to interfere in the middle of the water inclusion in such a way that caused appearance of the artefact.

μ_I results

Overall, the μ_I showed poor reconstruction accuracy across multiple frequencies. Generally, poor qualitative characterisation of both medias was observed in the μ_I image across multiple frequencies. Since the water is a nearly inviscid fluid, near zero μ_I values were expected. Again, high variations were seen within both tofu and water regions throughout the phantom as confirmed by IQR values in Figs. 7.17 (e) and 7.17 (f). Quantitatively, good agreement between the μ_I and μ_R parameters behaviour was observed with the soft tofu background material (refer to Figs. 7.17 (c) and 7.17 (f)).

ρ_I results

The reconstructed ρ_I image was generally of a poor quality across multiple frequencies. The presence of the water inclusions was not outlined on the in the ρ_I images across multiple (refer to Fig. 7.16 (c)). No significant contrast was seen between two independent material zones. Interestingly, the RHS of the phantom was reconstructed with comparatively high ρ_I values. Quantitative ROI analysis indicated good agreement in parameter behaviour within the soft tofu background material across multiple frequencies (refer to Fig. 7.17 (g)). However, large variations and different trends in ρ_I parameter behaviour were observed within the water inclusions across multiple frequencies (refer to Fig. 7.17 (h)).

The imaginary density does not appear in the Navier-Stokes equations, therefore in the RD model the ρ_I term can be interpreted to model the heavy attenuation within the fluid. Since the water is inviscid fluid, near zero μ_I values are expected.

Thus, to match correct damping high ρ_I values are expected in the water. Due to fundamental data-model mismatch and possible model non-identifiability issue, optimisation process trades off between μ_I and ρ_I values, thus ρ_I image is not accurate and does not reflect realistic behaviour of two materials.

ξ_d results

ξ_d reconstruction had a mixed success across multiple frequencies. More specifically, at 60 Hz the water inclusions were generally reconstructed with lower damping levels compared to the soft tofu background. ξ_d reconstruction at 80 Hz and 100 Hz was more successful compared to 60 Hz. Here, high damping levels were seen within the both inclusions mainly in the lower half of the phantom. However, the algorithm struggled to accurately estimate the damping levels of the water inclusions in the upper half of the phantom (refer to Fig. 7.16 (d)). Again, this effect is probably due to significant attenuation of the MA. Consistent parameter behaviour with high variations was seen within the soft tofu background across multiple frequencies (Fig. 7.17 (i)) and different ξ_d trends were observed for the water inclusions across multiple frequencies (Fig. 7.17 (j)).

7.4.2 Summary: tofu-water phantom

RD MRE studies were performed on tissue-simulating damping phantoms comprised of poroelastic and fluid components with objective to further investigate the limitations of current-elasticity-based methods in accurately characterising viscoelastic and damping properties. The results indicated that elastographic reconstructions based in isotropic linear elastic RD model of both fluid-saturated porous media and fluid could yield misleading effective property distributions resulting from fundamental data-model mismatch and model non-identifiability.

7.5 Summary

The full three parameter reconstructions of RD based elastic properties were performed on the damping phantoms, combining elastic and poroelastic medias, to investigate the viability of the time-harmonic 3 parameter-based RD MRE in pro-

ducing accurate recovery of VE properties as well as describing realistic damping behaviour. Assessment of the quantitative accuracy of the MRE was outside the scope of these studies. It was mainly the ability of the algorithm to accurately reconstruct differences in mechanical properties between materials that was assessed from qualitative perspective.

The differences between the quality of reconstruction for the different parameters is evident, with the real shear modulus (μ_R) having the highest quality image and the images of RD based parameters (μ_I and ρ_I) being significantly poorer. Generally, reconstruction quality of μ_I was relatively poor around material boundaries and within homogeneous material regions. Weak characterisation of both material types was usually observed. High variations were also seen within the homogeneous material regions. Similar problems were seen in ρ_I reconstructions.

A possible explanation for the poor quality of reconstruction of the RD parameters might be due to the ill-posed nature of the optimisation problem at a single frequency. Given that in the RD formulation shear modulus and density are complex quantities, elastographic reconstruction of the RD properties, represented as unknown imaginary components (μ_I and ρ_I), becomes non-trivial and possibly non-identifiable.

The obtained results indicated that accurate delineation of the RD based properties at a single frequency was very difficult even with number of regularisation techniques applied to the optimisation algorithm. The results also suggested addressing a non-identifiability of the RD based properties that might be poorly conditioned in the RD formulation. Therefore, reconstructed RD based properties might simply be meaningless and random. Based on these observations, more thorough analysis of the RD identifiability is needed. Also, a broad range of frequencies may be required to correctly identify RD coefficients based on captured damping.

Next chapter describes the structured identifiability analysis of the time-harmonic 3 parameter based RD model applied to MRE.

Chapter 8

Structural identifiability analysis of the RD model

Chapter 7 showed that 3 parameter-based RD model yields impractical material property estimates. In particular, the parameter values do not accurately assess expected outcomes for ρ_I and μ_I. Thus, a structural analysis will be performed to investigate the identifiability of the model.

8.1 Theoretical background of parameter identification

A number of mathematical models have been developed for numerical approximation of a variety of physiological and biological phenomena. Most such models are systems of first order linear or nonlinear ordinary differential equations that contain a number of parameters that are optimised to fit the measured data. Accurate delineation of the model parameters is crucial for successful recovery of the true observed behaviour of the phenomena (Ritt, 1950). Typically, the parameter values that produce the closest match between the model simulations and measured behaviour are used to distinguish and quantitatively characterise the observed phenomena. However, due to the complexity of some models, certain parameters can be poorly defined due to the ill-posed nature of the model and thus cannot be uniquely defined. To prevent such an identification failure, *a-priori* global identifiability analysis is a necessary procedure for any biological or physiological phenomena.

The feasibility of the model to uniquely recover unknown parameters is a fundamental prerequisite in the model development. Although a variety of methods have been proposed to test identifiability of nonlinear models (Audoly et al., 2001; Bellu et al., 2007; Pia Saccomani et al., 2003), it can still be a challenging mathematical

problem. Audoly et al. (2001) presented a new algorithm for testing global identifiability of nonlinear dynamic models, based on differential algebra. The algorithms were reported to be capable of handling many features arising in biological models, including zero initial conditions and time-varying parameters. (Pia Saccomani et al., 2003) showed that the identifiability test procedures based on differential algebra may fail for systems which are started at specific initial conditions and that this problem is strictly related to the accessibility of the system from the given initial conditions. Bellu et al. (2007) proposed a differential algebra algorithm to perform parameter identifiability analysis (DAISY) for both linear and nonlinear dynamic models described by polynomial or rational equations.

However, the derivative-based identifiability methods are typically limited to ideal conditions of noise-free observations and error-free model structure. Therefore, these *a-priori* derivative-based identifiability methods can produce false assurances of identifiability of the model parameters. In particular, real input / output measurements that include noisy data can limit practical identifiably. Without a guarantee of *a-priori* identifiability, the parameter estimates, that have even been obtained by numerical optimisation methods, might be unreliable or random.

Due to limitations of the derivative-based identifiability methods, a new demand has arisen for practical identifiability methods that account for imperfections in measured data and its associated error on discrete measurements (Raue et al., 2009) which often causes parameter trade-off. The new methods suggest not only compulsory *a-priori* identifiability check of the model, but also testing tendency of the parameters for mutually interference. In this context, Docherty et al. (2011) presented a novel graphical method for identifiability analysis that accounts for both measurement noise and data-model based error.

The method of Docherty et al. (2011) is based on distinctive measurement of the integral formulations of the parameter coefficients with adjustable sampling rate and can thus estimate the susceptibility of the parameters to the effects of measurement error. Furthermore, the integral-based approach can identify ways to improve practical identifiability by indicating potential model improvements and required sampling rates that make the model more identifiable. The method proved successful in capturing analogous nature of identifiability in Monte Carlo simulations in a number of different scenarios, including protocol alterations, parameter changes and differences in participant behaviour. Due to the development stage of this

algorithm, it is currently limited to the first-order, two-parameter nonlinear models. However, it still offers insight into the practical identifiability of the RD model.

Many researches neglect identifiability analyses despite its crucial role in accurate parameter identification. Use of a non-uniquely identifiable model in a clinical setting may result in parameter values that are not due to the true observed behaviour. The resulting error in parameter estimation might lead to faulty estimation of current physiological conditions or unjustified conclusions. Even a small error can have critical impact in some medical applications when used for diagnosis or to guide treatment.

Identifiability analysis can also contribute towards appropriate design of the experimental protocol to provide an optimal baseline between input and output parameter configurations to ensure unique or (more) robust identifiability. This aspect is particularly useful in the modelling of physiological systems that are often associated with limited input / output parameters. Identifiability analysis can also be helpful to provide guidelines to deal with non-identifiability issues, either providing hints on how to simplify the model structure or indicating when more information (measured data) are needed for the specific experiment.

8.2 Application to the time-harmonic RD model

Navier's equation with damping can be simply represented as:

$$\mathbf{M}\ddot{\mathbf{u}} + \mathbf{C}\dot{\mathbf{u}} + \mathbf{K}\mathbf{u} = \mathbf{f} \tag{8.1}$$

where discretised formulation of mass, damping and stiffness are $\mathbf{M}$, $\mathbf{C}$ and $\mathbf{K}$, respectively; $\mathbf{u}$ is the displacement vector ($\dot{\mathbf{u}}$ and $\ddot{\mathbf{u}}$ correspond to the first and second oder time derivatives, respectively) and $\mathbf{f}$ is the discrete representation of external & body forces acting on the system. In time harmonic steady state elastography, motion and forces can be written as $\mathbf{u}(\mathbf{x}, t) = \hat{\mathbf{u}}e^{i\omega t}$ and $\mathbf{f}(\mathbf{x}, t) = \hat{\mathbf{f}}e^{i\omega t}$, respectively,

thus giving:

$$-\omega^2\mathbf{M}\hat{\mathbf{u}} + i\omega\mathbf{C}\hat{\mathbf{u}} + \mathbf{K}\hat{\mathbf{u}} = \mathbf{f}, \tag{8.2}$$

$$\Big[-\omega^2\mathbf{M} + i\omega\mathbf{C} + \mathbf{K}\Big]\hat{\mathbf{u}} = \hat{\mathbf{f}}. \tag{8.3}$$

Implementation of a RD assumption, $\mathbf{C} = \alpha\mathbf{M} + \beta\mathbf{K}$, leads to the following transformation of Eq. 8.3:

$$\Big[-\omega^2\mathbf{M} + i\omega(\alpha\mathbf{M} + \beta\mathbf{K}) + \mathbf{K}\Big]\hat{\mathbf{u}} = \hat{\mathbf{f}}. \tag{8.4}$$

Using complex density $\rho = \rho_R + i\rho_I$ and complex shear modulus $\mu = \mu_R + i\mu_I$, where μ_R and ρ_R describe the original shear modulus and density in the undamped system, while μ_I and ρ_I can be expressed in terms of the RD parameters:

$$\rho_R = \rho, \qquad \rho_I = \frac{-\alpha\rho}{\omega}. \tag{8.5}$$

$$\mu_R = \mu, \qquad \mu_I = \omega\beta\mu. \tag{8.6}$$

Therefore, the RD parameters α and β can be formulated from Eqs. 8.5 and 8.6:

$$\alpha = \frac{-\omega\rho_I}{\rho_R}, \qquad \beta = \frac{\mu_I}{\omega\mu_R}. \tag{8.7}$$

Considering that all terms in $\mathbf{M}$ contain the density (ρ_R) and all terms in $\mathbf{K}$ contain the shear modulus (μ_R), then for a single degree of freedom system by substituting Eq. 8.7 into Eq. 8.4 results:

$$\Big[-\omega^2\rho_R + i\omega\Big(\frac{-\omega\rho_I}{\rho_R}\rho_R + \frac{\mu_I}{\omega\mu_R}\mu_R\Big) + \mu_R\Big]\hat{\mathbf{u}} = \hat{\mathbf{f}}, \tag{8.8}$$

$$\Big[-\omega^2\rho_R + i\omega\Big(\frac{\mu_I}{\omega} - \omega\rho_I\Big) + \mu_R\Big]\hat{\mathbf{u}} = \hat{\mathbf{f}}. \tag{8.9}$$

Collecting the coefficients of the $\Re$ and $\Im$ terms yields:

$$\Big[-\omega^2\rho_R + \mu_R\Big]\mathbf{u}_R + \Big[\mu_I - \omega^2\rho_I\Big]\mathbf{u}_I = \hat{\mathbf{f}}. \tag{8.10}$$

Eq. 8.10 indicates that $\mathbf{u}_R$ is described by $\rho_R + \mu_R$. In RD reconstruction, the real density (ρ_R) of a material is assumed to be the density of water, e.g. $\rho_R = 1000$ kg/m^3. Therefore, μ_R becomes a direct function of the real displacements: $\mu_R = f(\mathbf{u}_R)$. Hence, thus it is easily and uniquely identifiable.

On the other hand, variance in $\mathbf{u}_I$ is described in Eq. 8.10 by mutual changes ρ_I or μ_I. Both parameters can have a model role, but the relative contribution cannot be uniquely defined at a single frequency. Hence, the RD model will not produce unique identification of voxel behaviour in term of ρ_I and μ_I from single frequency data, as supported by the poor ρ_I and μ_I results of Chapter 7. Fig. 8.1 shows how the observed behaviour at a single frequency can be explained by different combinations of RD curves.

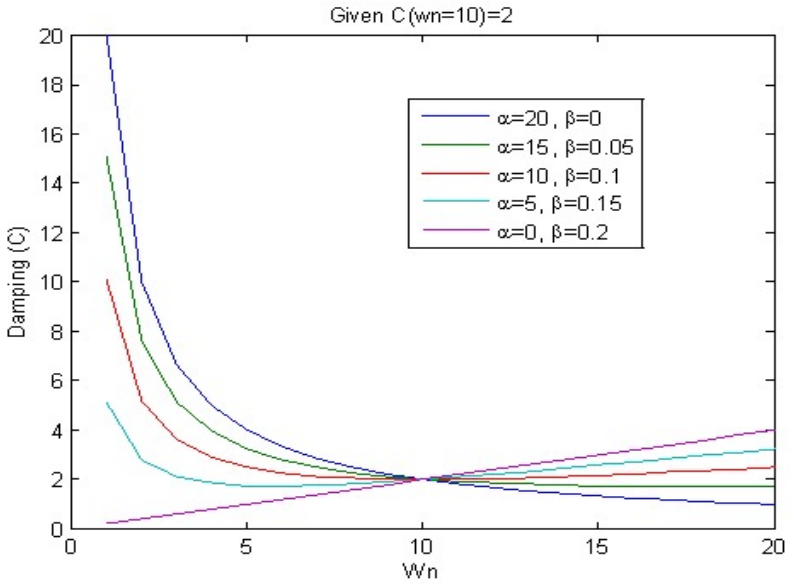

Figure 8.1 Schematic representation of possible Rayleigh damping curves on given response to one frequency (10 Hz).

Using ρ_I and μ_I, ξ_d plots can be obtained that show that damping can be measured well, but the RD values ρ_I and μ_I are not individually identifiable or accurate. Fig. 8.2 shows RD and VE reconstruction results of the P1 phantom at 125 Hz. Despite using two different models, no change in ξ_d was observed. Thus, the ρ_I parameter in RD model was not accurately identified to the high input frequency and non-identifiability of the RD model. Hence, in the RD model, the μ_I parameter does not reflect realistic loss modulus behaviour and therefore is misleading due to this lack of identifiability.

Fig. 8.3 shows error minimisation in the VE reconstruction. It can be seen that model minima are achieved quickly, while the rest of the iterations are just parameter smoothing. Therefore, it is a post inverse function problem.

To make the RD model structurally identifiable, there are two fundamental approaches that can be used:

1. **Multifrequency**, where identification is run simultaneously on motion data

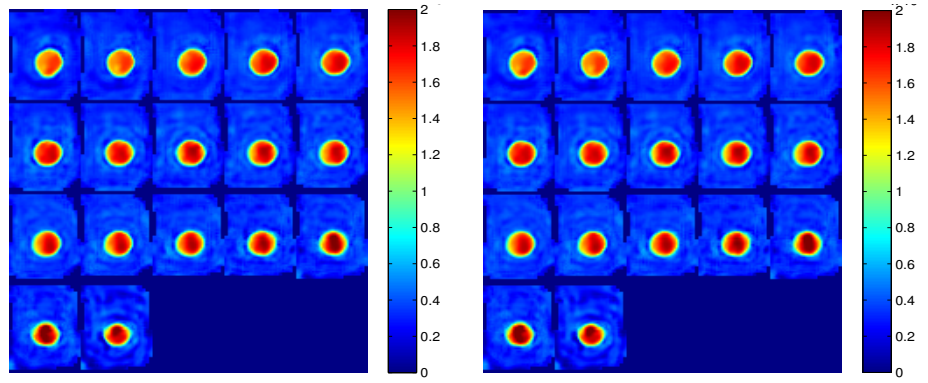

(a) μ_R (RD) (b) μ_R (VE)

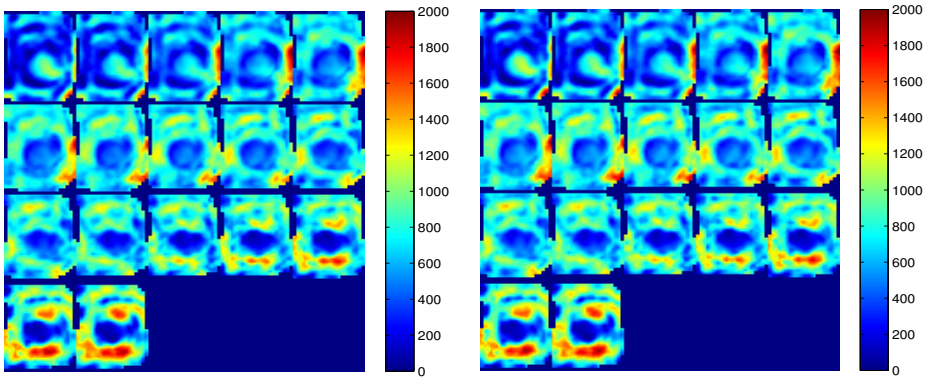

(c) μ_I (RD) (d) μ_I (VE)

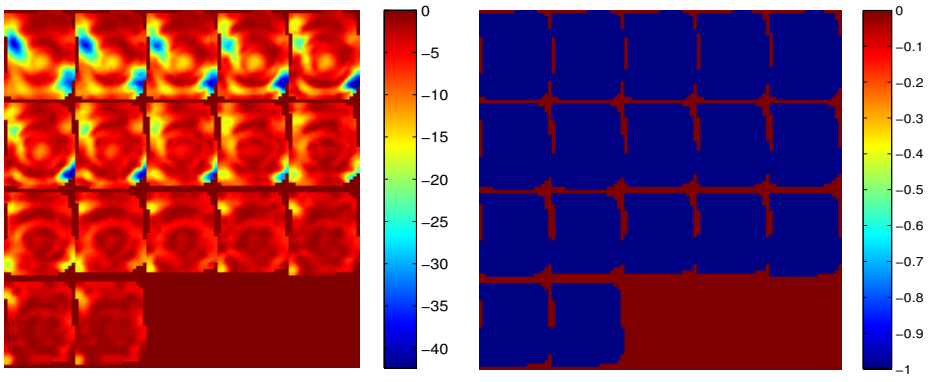

(e) ρ_I (RD) (f) ρ_I (VE)

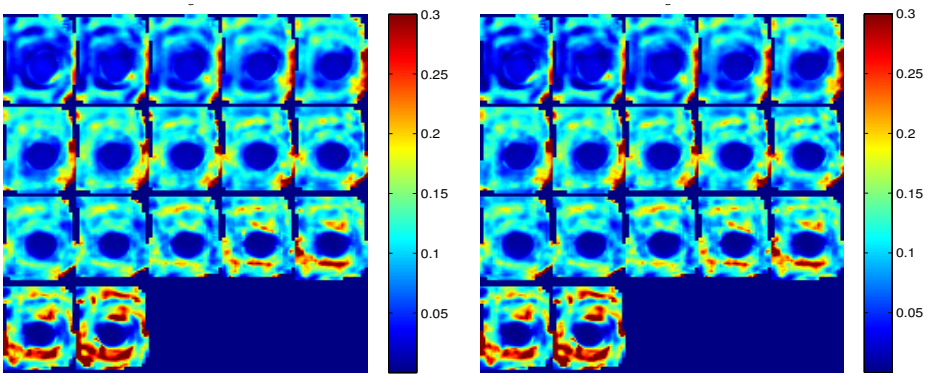

(g) ξ_d (RD) (h) ξ_d (VE)

Figure 8.2 Image results for the RD (left column) and VE (right column) reconstruction with CG optimisation method of the P1 phantom configuration at 125 Hz using same experimental protocol.

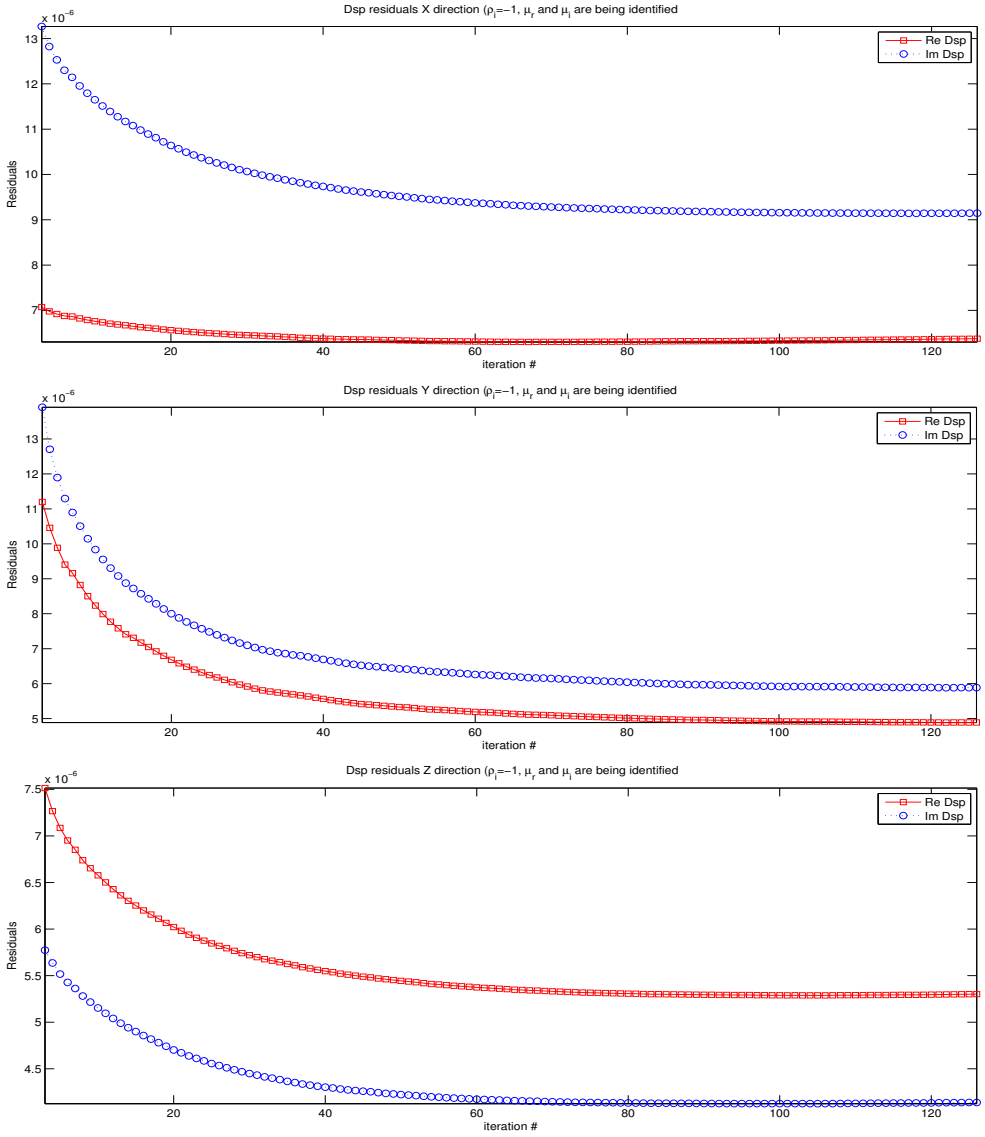

Figure 8.3 Calculated residuals between measured displacement and model simulated displacement, representing error reduction with CG optimisation method in P1 phantom configuration at 125 Hz (VE reconstruction): μ_R and μ_I being identified) : a) x motion direction b) y motion direction C) z motion direction

from two frequencies of input.

$$\Big[-\omega^2 \rho_I + \mu_I \Big] \mathbf{u}_I = \hat{\mathbf{f}}_I \tag{8.11}$$

Here, two parameters are both frequency dependant.

$$\begin{pmatrix} -\omega^2 \mathbf{u}_I & \mathbf{u}_I \\ -\omega^2 \mathbf{u}_I & \mathbf{u}_I \\ \vdots & \vdots \\ -\omega^2 \mathbf{u}_I & \mathbf{u}_I \end{pmatrix} \begin{pmatrix} \rho_I \\ \mu_I \end{pmatrix} = \begin{pmatrix} \hat{\mathbf{f}}_I \\ \hat{\mathbf{f}}_I \\ \vdots \\ \hat{\mathbf{f}}_I \end{pmatrix} \tag{8.12}$$

In Eq. 8.12, row [1] $\propto$ [2], and [1] = [2] and [1] = [2$-N$]. Thus, we have one equation with two unknowns which is impossible to resolve without specifying either ρ_I or μ_I in some fashion. Thus, the solution is a multifrequency approach $\omega = [\omega_1, \omega_2]$:

$$\begin{pmatrix} -\omega_1^2 \mathbf{u}_{I1} & \mathbf{u}_{I1} \\ \vdots & \vdots \\ -\omega_2^2 \mathbf{u}_{I2} & \mathbf{u}_{I2} \\ \vdots & \vdots \end{pmatrix} \begin{pmatrix} \rho_I \\ \mu_I \end{pmatrix} = \begin{matrix} [1] \\ \\ [5] \\ \\ \end{matrix} \begin{pmatrix} \hat{\mathbf{f}}_{I1} \\ \vdots \\ \hat{\mathbf{f}}_{I2} \\ \vdots \end{pmatrix} \tag{8.13}$$

where row [1] $\propto$ [2]. However, row [1] $\not\propto$ [5]. By dividing row [1] $\div \mathbf{u}_{I1}$ and row [5] $\div \mathbf{u}_{I2}$ results in the system of decoupled equations:

$$\begin{pmatrix} \text{-}\omega_1^2 & 1 \\ \vdots & \vdots \\ -\omega_2^2 & 1 \\ \vdots & \vdots \end{pmatrix} \begin{pmatrix} \rho_I \\ \mu_I \end{pmatrix} = \begin{matrix} [1] \\ \\ [5] \\ \\ \end{matrix} \begin{pmatrix} \hat{\mathbf{f}}_{I1}/\mathbf{u}_{I1} \\ \vdots \\ \hat{\mathbf{f}}_{I1}/\mathbf{u}_{I2} \\ \vdots \end{pmatrix} \tag{8.14}$$

In Eq. 8.14 is a system of two equations with two unknowns where $-\omega_1^2 + 1 \neq$

$-\omega_2^2+1$ as $\omega_1 \neq \omega_2$. Eq. 8.14 indicates that at least two frequencies are required for identification of the RD parameters. However, practical identifiability is not assured if both frequencies are within similar range, i.e. $\omega_1 \approx \omega_2$ as $-\omega_1^2+1 \approx -\omega_2^2+1$. Another condition to assure strong practical identifiability is that both frequencies shall be in the wide range, i.e. $\omega_1 \gg \omega_2$ or $\omega_1 \ll \omega_2$.

2. **Parametrisation**, where either ρ_I or μ_I is set to a constant or dependant functions, thus, specifying its value. This approach yields a system effectively composing one equation with one unknown in Eq. 8.10 which is uniquely identifiable.

$$\begin{pmatrix} \mathbf{u}_I \\ \mathbf{u}_I \\ \vdots \\ \mathbf{u}_I \end{pmatrix} \Big(\mu_I\Big) = \begin{pmatrix} \hat{\mathbf{f}}_I + \omega^2 \rho_I \mathbf{u}_I \\ \hat{\mathbf{f}}_I + \omega^2 \rho_I \mathbf{u}_I \\ \vdots \\ \mathbf{f}_I + \omega^2 \rho_I \mathbf{u}_I \end{pmatrix} \tag{8.15}$$

$$\begin{pmatrix} -\omega^2 \mathbf{u}_I \\ -\omega^2 \mathbf{u}_I \\ \vdots \\ -\omega^2 \mathbf{u}_I \end{pmatrix} \Big(\rho_I\Big) = \begin{pmatrix} \hat{\mathbf{f}}_I - \mu_I \mathbf{u}_I \\ \hat{\mathbf{f}}_I - \mu_I \mathbf{u}_I \\ \vdots \\ \mathbf{f}_I + \mu_I \mathbf{u}_I \end{pmatrix} \tag{8.16}$$

8.3 Summary

Full simultaneous three parameter-based RD reconstruction at a single frequency has bee shown to be non-trivial due to the ill-posed nature of the imaginary components. By definition, the RD model describes the rate of change in damping with different modes over frequency. Therefore, the relative contribution of the RD parameters to overall damping can not be uniquely identified at a single frequency. It thus must be defined at at least two frequencies, by selecting ξ_a and ξ_b to obtain a specific RD curve, thus a unique α and β. Furthermore, the structural analysis confirmed that multiple frequencies are required for the RD model to accurately delineate the RD model parameters μ_I and ρ_I and the resulting damping behaviour, expressed as a damping ratio ξ_d. An alternative approach of establishing practical identifiably of the RD model is parametrisation where on the RD model parameters is set to a constant.

Next chapter will explore multi-frequency-based and parametric-based RD MRE studies to investigate whether they can produce more accurate elastographic reconstructions compared to the single frequency-based RD elastographic reconstructions.

Chapter 9

Multi-frequency / parametric RD MRE studies

This chapter summarises results of the simultaneous multi-frequency (MF) based RD MRE studies on tissue simulating damping phantoms. The goal is to assess the ability of the RD model to accurately recover both VE and damping properties of various materials based on simultaneous MF inverse problem solution. The hypothesis behind this work is that MF-based RD MRE contributes towards structural identifiability of the RD elastography. Therefore, more accurate reconstruction of the viscoelastic and damping properties is expected, as well as accurate delineation of the RD properties compared to a single frequency (SF) based optimisation.

Furthermore, parametric based RD MRE studies are reported to demonstrate an alternative way to establish structural identifiability of the RD model applied to MRE. Thus, these analyses should provide alternative solution and highlight any differences in performance.

9.1 Multi-frequency RD MRE studies

9.1.1 Materials and methods

Multiple excitation frequencies were applied to a variety of previously introduced tissue-simulating damping phantoms: poroelastic homogeneous tofu phantom, tofu-gelatine phantoms and tofu-water phantom. Detailed description of the actuation methodology is presented in chapter 6. Due to the inability of the piezo-electric actuator to produce frequencies lower than 50 Hz, only a relatively higher frequency

range above 50 Hz was explored. It has been demonstrated previously that a broad range of frequencies is required for accurate delineation of the RD based parameters. In particular, the effect of imaginary density ρ_I which is inversely proportional to the input frequency. Thus, the results of this analysis will delineate any negative effects due to having only higher frequencies. In particular, where multiple frequencies make the system theoretically identifiable, it may not be practically identifiable (Docherty et al., 2011).

In the MF mode of the reconstruction processing, the objective function is computed as a sum across all input frequencies:

$$\mathbf{\Phi} = \sum_{freq_i} ||\mathbf{u}^m(\omega_i) - \mathbf{u}^c(\omega_i, \boldsymbol{\theta})||^2. \tag{9.1}$$

Importantly, no particular scaling is available to be applied to the different frequency data sets in the software used, so that they are all weighted equally in the objective function. This lack of scaling could lead to a situation where larger displacements lead to larger contributions to the objective function, skewing the results. Meanwhile, the material properties $\boldsymbol{\theta}$ across frequencies are computed using two available models:

- Zero order model, where there is no variation of material property value as a function of frequency.
- Power-law model, where the values of material properties are function dependant.

The power-law model for μ_R and μ_I parameters is defined:

$$\mu_R(\omega) = \mu_{R0} \cdot \omega^{\alpha}, \qquad \mu_I(\omega) = \mu_{R0} \cdot \omega^{\alpha} \tag{9.2}$$

where both parameters μ_{R0} and μ_{I0} and α are reconstructed for each node within the imaging volume. Alternatively, power-law relationship for the imaginary density

ρ_I is defined:

$$\rho_I(\omega) = \rho_{I0} \cdot \left(\frac{1}{\omega}\right)^{\alpha} \tag{9.3}$$

It should be noted that a power-law model allows calculation of property values at a particular frequency ($\omega = 2\pi f$) through the relationships formulated by Eqs. 9.3 and 9.2. Two models were applied to reconstruct material properties based on MF-based RD MRE.

9.1.2 Results

9.1.2.1 Poroelastic homogeneous tofu phantom

Fig. 9.1 shows zero order model simultaneous MF-based RD reconstruction results at 60, 80 and 100 Hz for μ_R, μ_I, ρ_I and resulting ξ_d for the homogeneous poroelastic tofu phantom. Reconstructed μ_R image shows relatively smooth property value distributions throughout the phantom. μ_I reconstruction has also been relatively successful with small variations within the slices. Reconstructed ρ_I image shows some variations of the parameter in the lower part of the phantom. Finally, the reconstructed ξ_d image shows good recovery of the overall damping profile of phantom. Overall, MF reconstruction improved accuracy of the reconstructed parameters compared to a SF RD results.

9.1.2.2 Tofu-gelatine phantoms

Fig. 9.2 shows the zero order model MF-based RD results at 50 Hz, 75 Hz, 100 Hz and 125 Hz compared to SF-based RD results at 125 Hz of the P1 phantom. Obvious similarity between reconstruction results clearly demonstrates limitations of the MF optimisation, where the objective function at 125 Hz appears to dominate contributions of the other objective functions of 50, 75 and 100 Hz frequency range. Appropriate weighting of the objective functions at each frequency, so that overall optimisation process is mutually normalised, would potentially solve this issue.

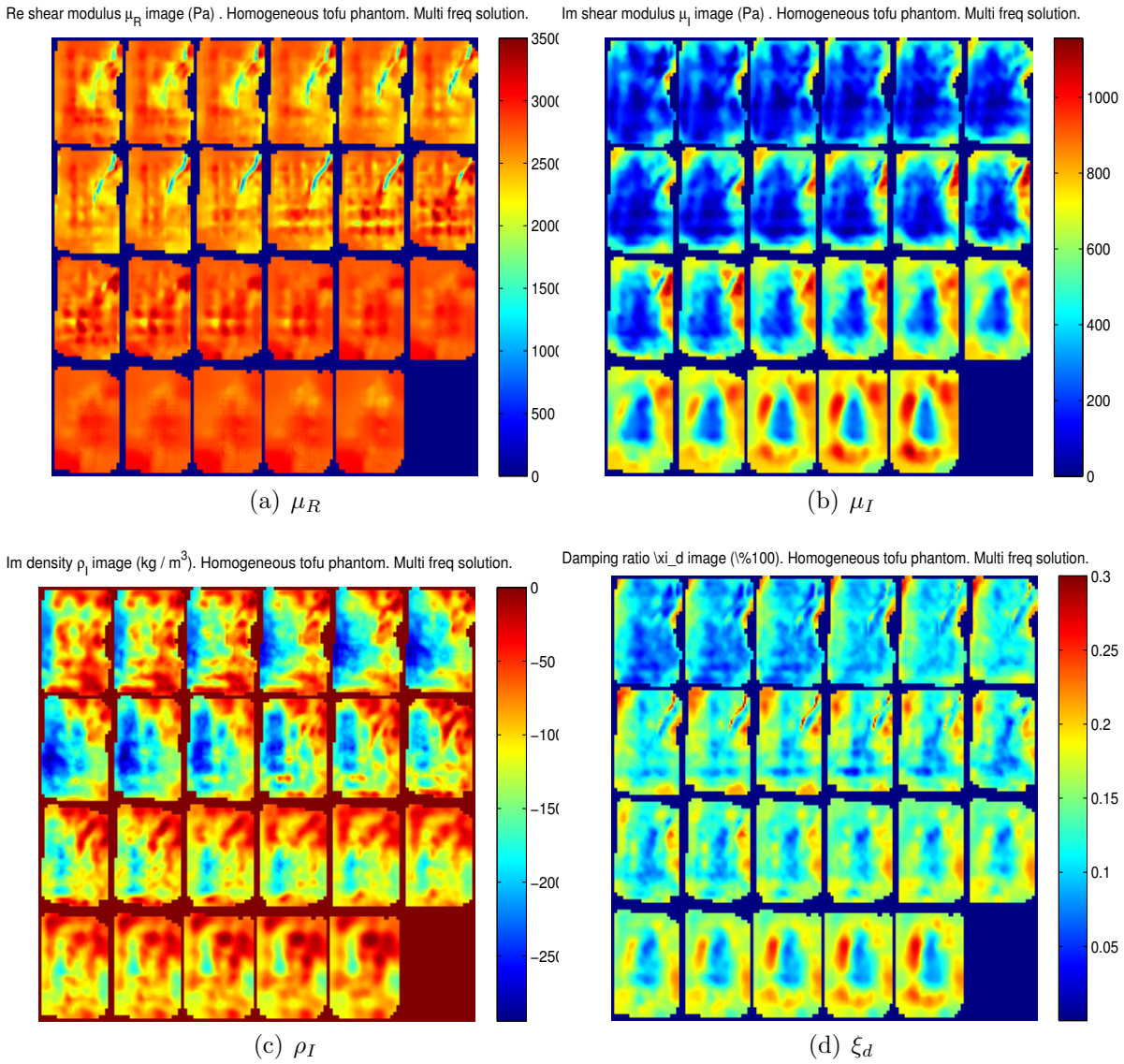

(a) μ_R (b) μ_I

(c) ρ_I (d) ξ_d

Figure 9.1 Image results for the zero order MF-based RD reconstruction of the poroelastic homogeneous tofu phantom at 60 Hz, 80 Hz and 100 Hz: (a) storage modulus μ_R image (Pa); (b) loss modulus μ_I image (Pa); (c) imaginary density ρ_I image (kg/m^3); and (d) damping ratio ξ_d image (% / 100)

However, due to the limited access to the numerical source code such modifications were not possible and, therefore, remain to be explored as a future work.

Qualitatively, the reconstructed μ_R image shows good differentiation of the stiffer gelatine inclusion within the soft tofu background (refer to Fig. 9.2 (a)). Although variation in μ_R values are present within both materials, the boundaries of the inclusion were still clearly delineated. The stiffness estimates of the gelatine inclusion are unrealistically high at approximately 18 kPa and not consistent throughout the phantom.

MF-based reconstruction of the RD parameters looks very similar to SF-based RD results. μ_I reconstruction demonstrated poor success in accurate characterisation of the loss modulus of both materials. While the bottom half of the phantom did not display any contrast in μ_I image, the top half of the phantom showed a clear increase in μ_I values within the tofu background material as shown in Fig. 9.2 (c). Qualitatively, reconstructed ρ_I image showed similar trends to the RD reconstruction at a SF. Overall trends tend to distinguish two independent material zones, although high variation of ρ_I values was seen. Finally, the ξ_d reconstruction was able to characterise damping levels of both materials, correctly confirming higher damping levels in the more attenuating tofu material compared to the gelatine.

Alternatively, Fig. 9.3 shows the power-law model MF-based RD reconstruction results of the P1 phantom at 100 Hz. Although, obvious correlation in qualitative trends is observed between zero order model and power-law based MF results, some differences are still visible. This difference in results is especially pronounced in RD parameters μ_I and ρ_I and concomitant ξ_d. However, due to the close correlation of the reconstruction result, no obvious advantages of the power-law model was noted. These results suggest that power-law model might not be appropriate model to account for MF-based MRE.

Fig. 9.4 shows zero order model MF-based RD reconstruction results at 50 Hz, 75 Hz, 100 Hz and 125 Hz in comparison to RD results at 125 Hz for P2 phantom. Again, clear correlation between qualitative and quantitate trends is observed, suggesting the previously discussed issue with normalisation of the objective functions is also playing a role.

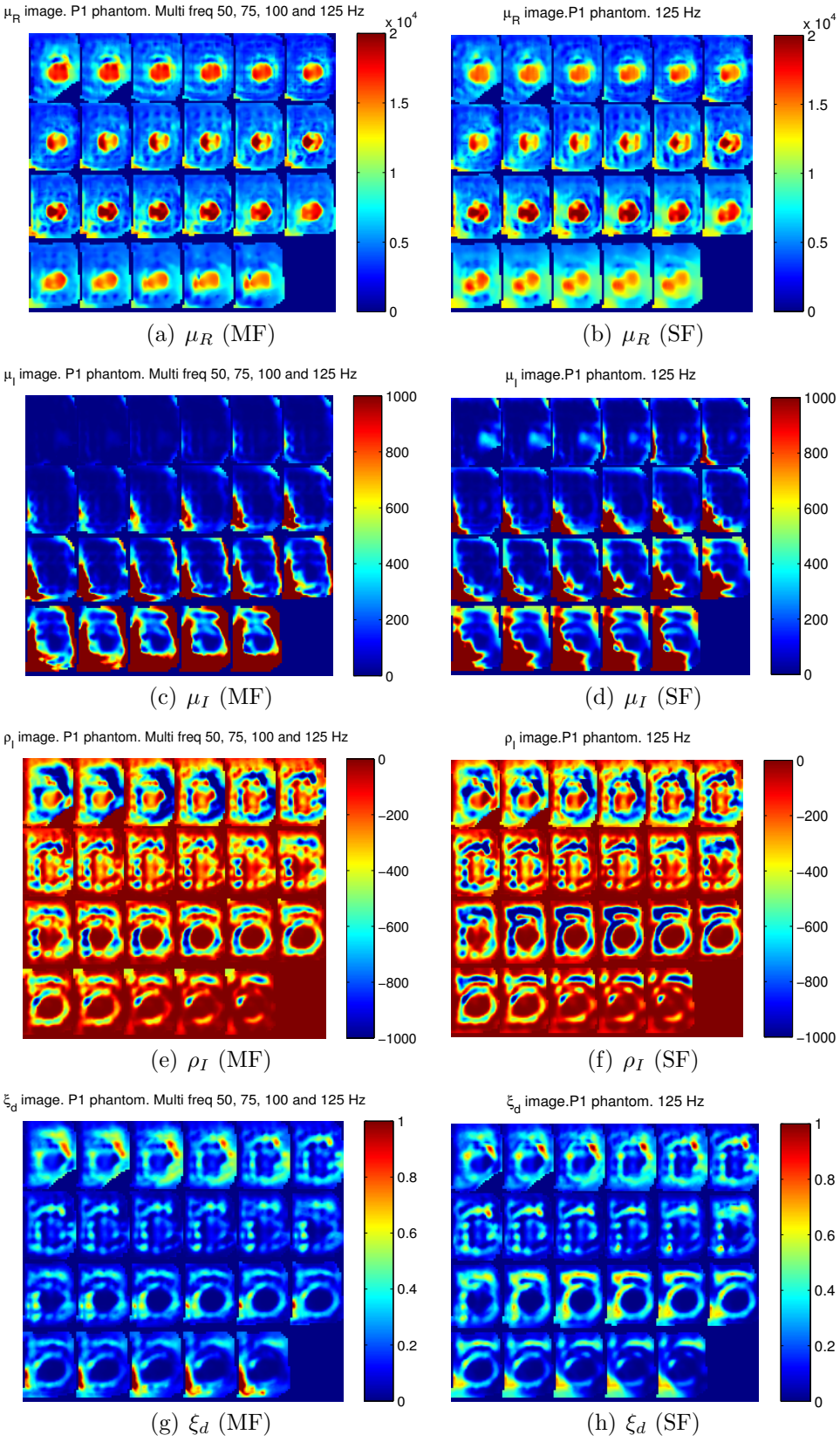

(a) μ_R (MF) (b) μ_R (SF)

(c) μ_I (MF) (d) μ_I (SF)

(e) ρ_I (MF) (f) ρ_I (SF)

(g) ξ_d (MF) (h) ξ_d (SF)

Figure 9.2 Image results for the zero order model MF-based RD reconstruction at 50 Hz, 75 Hz, 100 Hz and 125 Hz compared to SF-based RD reconstruction at 125 Hz of the P1 phantom (soft tofu background with a stiff gelatine inclusion): (a) and (b) storage modulus μ_R image (Pa); (b) and (c) loss modulus μ_I image (Pa); (d) and (e) imaginary density ρ_I image (kg/m^3); and (g) and (h) damping ratio ξ_d image (% / 100)

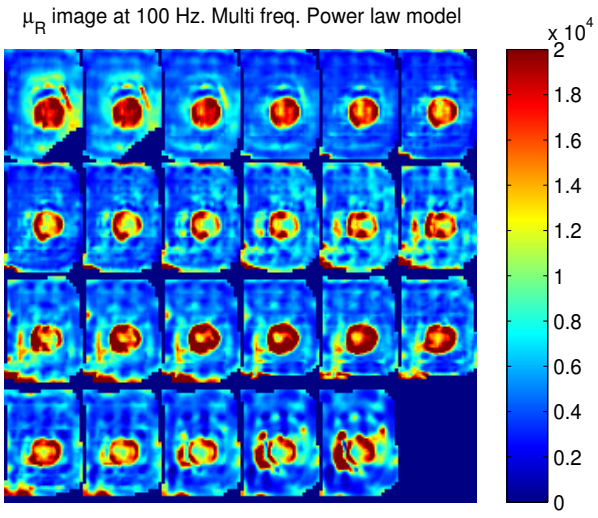

(a) μ_R

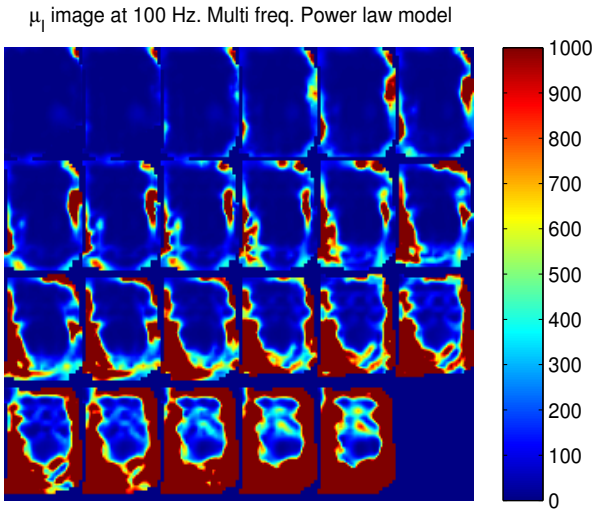

(b) μ_I

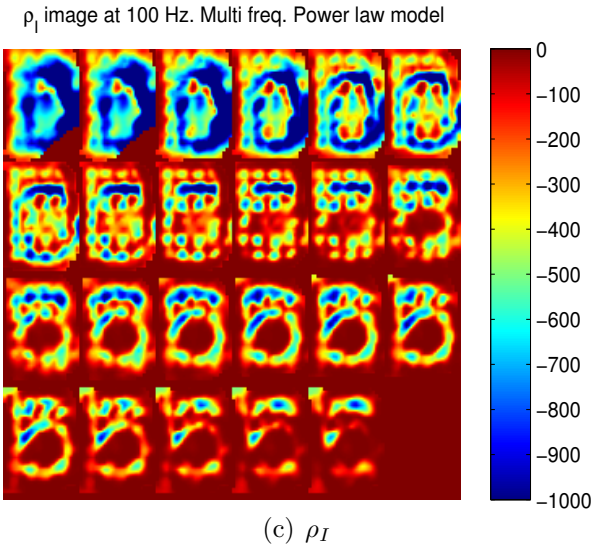

(c) ρ_I

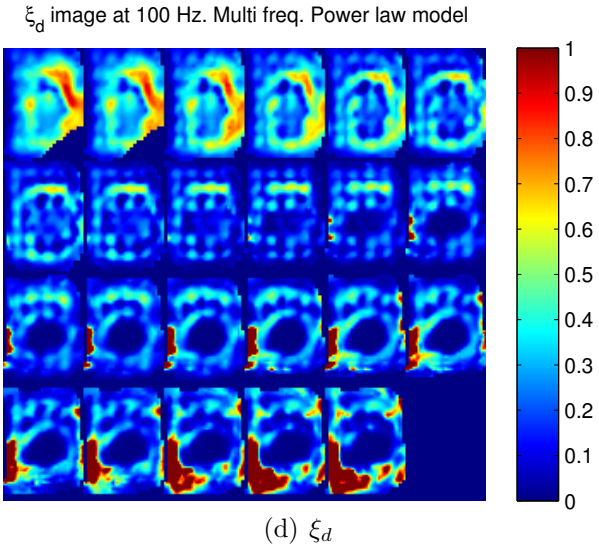

(d) ξ_d

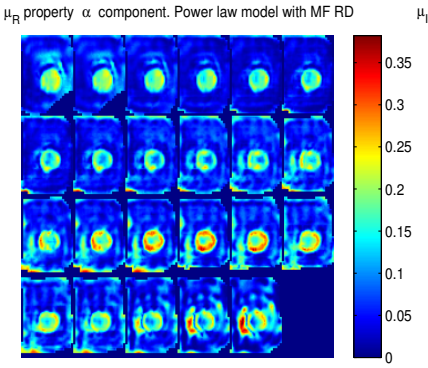

(e) α (μ_R)

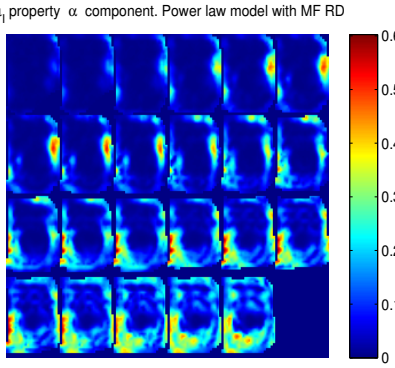

(f) α (μ_I)

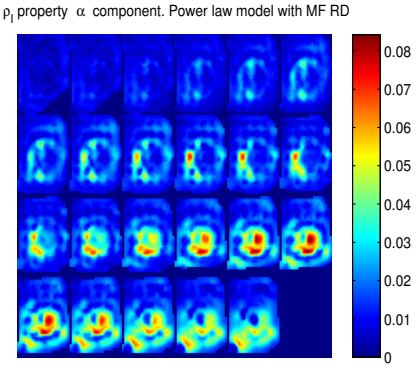

(g) α (ρ_I)

Figure 9.3 Image results for the power-law model MF-based RD reconstruction of the P1 phantom at 100 Hz: (a) storage modulus μ_R image (Pa); (b) loss modulus μ_I image (Pa); (c) imaginary density ρ_I image (kg/m^3); and (d) damping ratio ξ_d image (% / 100). (e) calculated α component of the μ_R; (f) calculated α component of the μ_I, and (g) calculated α component of the ρ_I

The reconstructed μ_R image clearly distinguished the soft tofu inclusion within the stiff gelatine background. MF based RD reconstruction of μ_R showed better delineation of the inclusion boundaries compared to a SF RD results. Reconstructed μ_I images showed some trends towards distinguishing two independent material zones. Interestingly, the tofu inclusion was reconstructed with low μ_I values, while gelatine background material with high μ_I values, which is opposite from expectations. ρ_I reconstruction had partial success in capturing the presence of the inclusion. However, the location and geometry of the inclusion did not correlate with the one seen on the MRI image. Finally, the ξ_d image was able to detect a higher damping level in the more attenuating tofu inclusion, however accurate delineation of geometry and location of the inclusion failed.

Another possible explanation of the poor reconstruction accuracy of RD based parameters might be related to the high frequency range. It is possible that all four input frequencies are located above the natural frequency of the system. Therefore, all frequencies provide very similar phase and motion amplitude information, which make is very difficult. Hence, where it is theoretically identifiable, it may not be practically identifiable (Docherty et al., 2011). Therefore, for the RD model to work multiple frequencies across a broad range around the the natural frequency would deliver the most informative data.

Summary: Tofu-gelatine phantoms (P1 & P2)

Simultaneous MF RD did not produce much better results due to the high range of the actuation frequencies. The RD model by definition thus appear to require a wide frequency range to delineate frequency dependant RD based parameters. The zero order model lead no better, so it is not necessarily the frequency dependency at issue, but the practical identifiability.

9.1.2.3 Tofu-water phantom (P5)

Fig. 9.5 shows simultaneous zero order model MF-based RD reconstruction results at 50 Hz, 80 Hz and 100 Hz compared to the SF-based RD reconstruction at 80 Hz of the submerged poroelastic tofu phantom with double fluid-filled inclusions of different diameters. The definition of the fluid-filled inclusions becomes unclear in

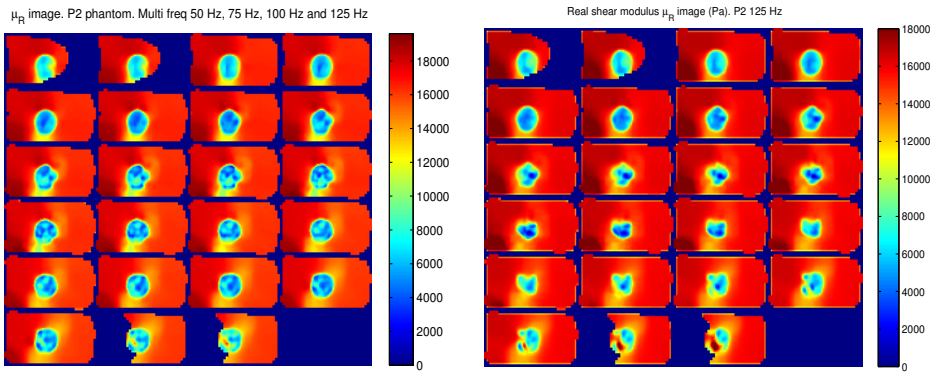

(a) μ_R (MF)

(b) μ_R (SF)

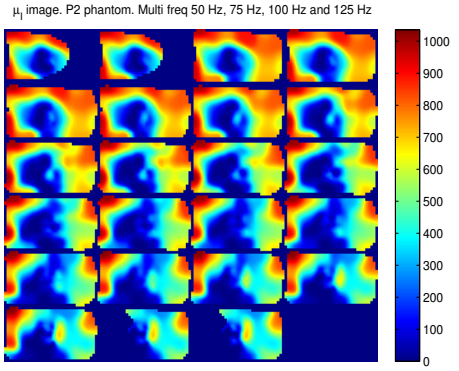

(c) μ_I (MF)

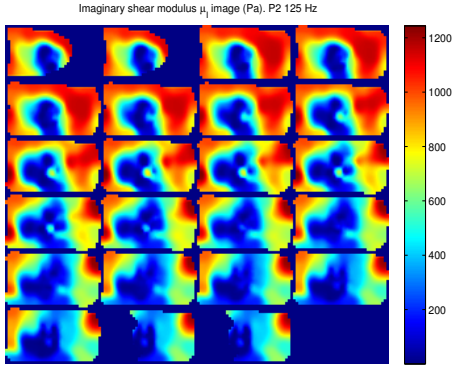

(d) μ_I (SF)

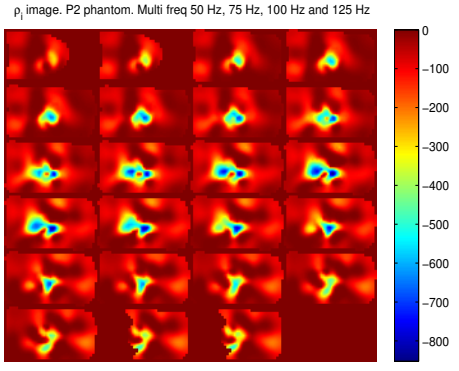

(e) ρ_I (MF)

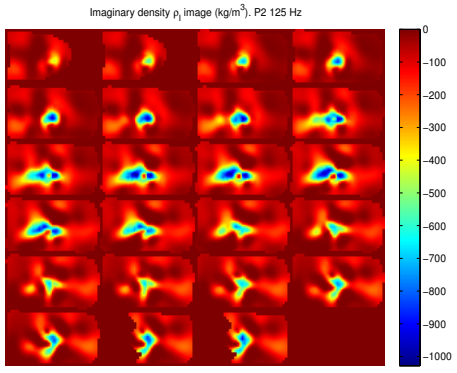

(f) ρ_I (SF)

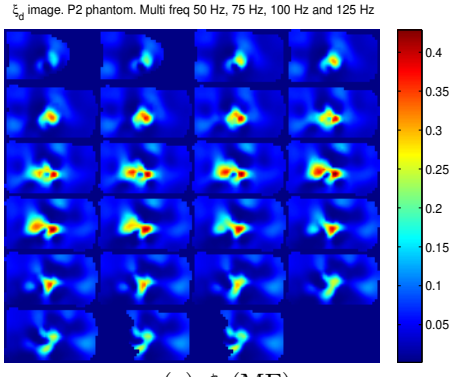

(g) ξ_d(MF)

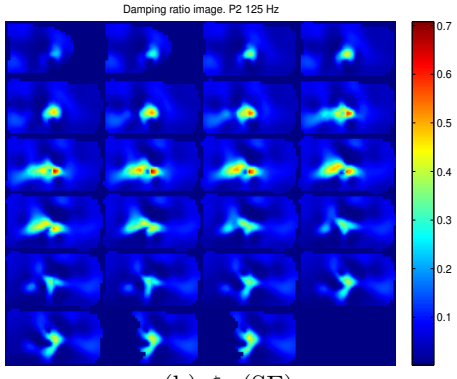

(h) ξ_d (SF)

Figure 9.4 Image results for the zero order model MF-based RD reconstruction at 50 Hz, 75 Hz, 100 Hz and 125 Hz compared to a SF-based RD reconstruction at 125 Hz of the P2 phantom (stiff gelatine background with soft tofu inclusion): (a) and (b) storage modulus μ_R image (Pa); (c) and (d) loss modulus μ_I image (Pa); (e) and (f) imaginary density ρ_I image (kg/m^3); and (g) and (h) damping ratio ξ_d image (% / 100)

the upper part of the phantom in the μ_R image computed by SF-based RD model as shown in Fig. 9.5 (b). However, significant improvement in differentiation of fluid-filled inclusions is observed in μ_R image computed by MF-based zero order RD model, where the geometry and location of the inclusions can be easily traced throughout the phantom (refer to Fig. 9.5 (a)). Accurate characterisation of the fluid properties failed, although some promising potential is still evident in the lower part of the phantom.

Again, accurate identification of the RD based parameters, μ_I and ρ_I, was poor. While some trends can be extracted from the μ_I image, the ρ_I image was rather random. A much higher quality of the reconstructed ξ_d image, computed by a zero order MF RD model (refer to Fig. 9.5 (g)), was observed compared to the ξ_d image, computed by a SF-based RD model (refer to Fig. 9.5 (h)). Here, a clear definition of the increased damping levels in the vicinity of both inclusions can be observed which correlates well with the expected high attention within the water filled cavity. Therefore, qualitatively, MF-based RD model improved accuracy of elastographic reconstruction compared to a SF-based RD model. This experimental outcomes confirming the hypothesis outlined generated in chapter 8.

Summary: Tofu-water phantom (P5)

Overall, a zero-order MF-based RD model significantly improved accuracy of elastographic reconstruction compared to a SF-based RD MRE. Higher quality results were mainly observed in reconstructed μ_R and ξ_d images. Similar to the MF results from tofu-gel phantoms, these MF RD results further confirm that although RD model was able to locate fluid filled cavities as well as capture damping behaviour of both materials, accurate delineation of the RD based parameters μ_I and ρ_I failed.

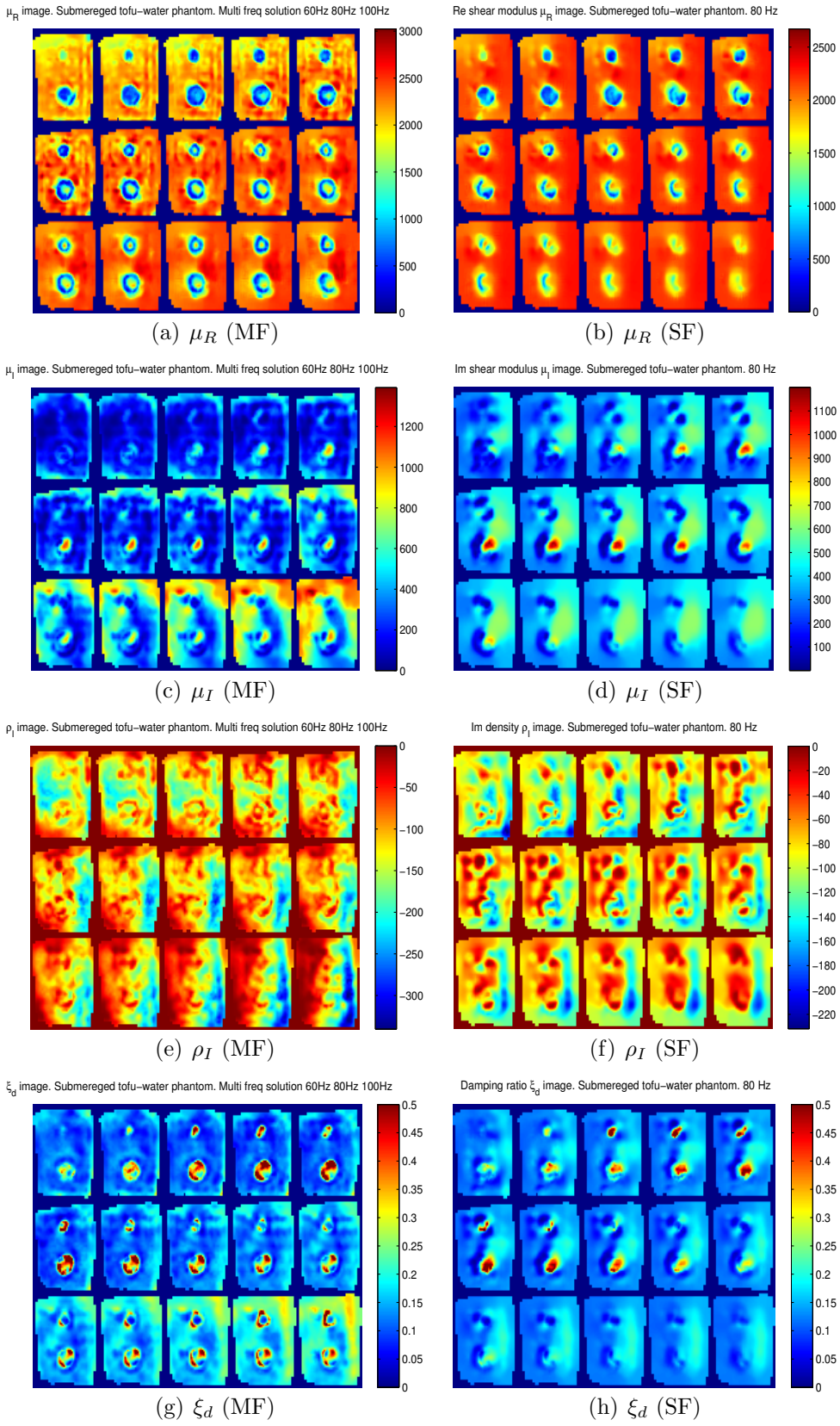

Figure 9.5 Image results for the zero order MF-based RD reconstruction at 60 Hz, 80 Hz and 100 Hz, compared to a SF-based RD results at 80 Hz of the P5 phantom (soft tofu background with a double fluid-filled inclusion): (a) and (b) storage modulus μ_R image (Pa); (c) and (d) loss modulus μ_I image (Pa); (e) and (f) imaginary density ρ_I image (kg/m^3); and (g) and (h) damping ratio ξ_d image (% / 100)

9.2 Parametric-based RD MRE studies

9.2.1 Materials and methods

Another, direct means to eliminate identifiability problems with three parameter RD elastography is *parametric optimisation*, where one of the RD based parameters, μ_I or ρ_I, is specified. It is important to stress that specifying μ_R does not solve the identifiability problem, as the imaginary components of the complex valued parameters are independent from their real components. Therefore, parametric reconstruction was carried out on all the phantoms where one of the RD based parameters, μ_I or ρ_I, was specified.

To demonstrate main advantages and limitations of parametric RD optimisation, as well as to evaluate difference in trends compared to MF-based RD reconstructions, only results computed on tofu-gelatine phantoms are presented. The goal of the parametric RD MRE studies was to evaluate parametric-based RD MRE:

- To differentiate various material types,
- To accurately reconstruct material property values against expected estimates

The reconstruction code only allows a single value of a particular parameter to be globally declared throughout the reconstruction domain, thus automatically leading to a limitation of the RD model to accurately reconstruct two independent material regions characterized by different mechanical properties. However, trends and differences should be captured. Another obvious limitation is the global definition of the Bulk modulus, K, that correspond to nearly incompressible isotropic model. Highly saturated porous tofu material will have a different Poisson's ratio compared to gelatine, leading to a second clear limitation.

9.2.2 Results

Fig. 9.6 shows parametric RD reconstruction results of the P1 phantom at 125 Hz with globally defined μ_I= 1 Pa, μ_I= 220 Pa and μ_I= 550 Pa, respectively.

For all three parametric RD reconstructions, qualitative μ_R reconstruction was successful with clear differentiation of the stiff gelatine inclusion within the soft tofu background. Again, quantitative stiffness estimates for the gelatine were very high. Overall, ρ_I reconstruction showed reasonable characterisation of two independent material regions in all three cases. Reconstructed ρ_I images for RD reconstruction with specified μ_I= 1 Pa and μ_I= 220 Pa showed relatively similar qualitative trends. However, different trends were observed in the ρ_I image with specified μ_I= 550 Pa. ξ_d reconstruction was the most successful in μ_I= 220 Pa and μ_I= 550 Pa cases, where clear damping behaviour of the more attenuating tofu material was observed. However, all three cases showed reasonably good differentiation.

Fig. 9.7 shows parametric based RD reconstruction results of the P1 at 125 Hz with globally defined ρ_I= -1 (kg/m^3) and ρ_I= -100 kg/m^3, respectively. Again, qualitative μ_R reconstruction was successful in both cases with clear differentiation of the stiff gelatine inclusion within the soft tofu background. Quantitative estimates of the gelatine inclusion were again unrealistically high.

Depending on different values for defined ρ_I, μ_I images also displayed different quantitative, as well as qualitative trends. However, qualitative reconstruction of μ_I images was accurate, correctly mapping higher loss modulus in the tofu material which has higher attenuation profile compared to the gelatine. Based on correct qualitative trends in μ_I images, ξ_d images were generally of a good quality, correctly depicting higher damping levels in the tofu martial compared to the gelatine.

9.2.3 Summary: parametric-based RD MRE studies

Parametric-based RD MRE studies, where one of the RD parameters, ρ_I or μ_I was globally defined, were performed on tofu-gelatine phantoms to overcome structural identifiably issue. The results showed a clear improvement of the reconstruction accuracy of the RD parameters being identified as well as mapping damping profile of the phantoms. Reconstructed μ_I image with fixed ρ_I parameter does show relatively higher loss modulus in the more attenuating tofu material compared to the gelatine. Alternatively, reconstructed ρ_I image with fixed μ_I does show higher values in the tofu material which correlates well with the expected rheological interpretation of

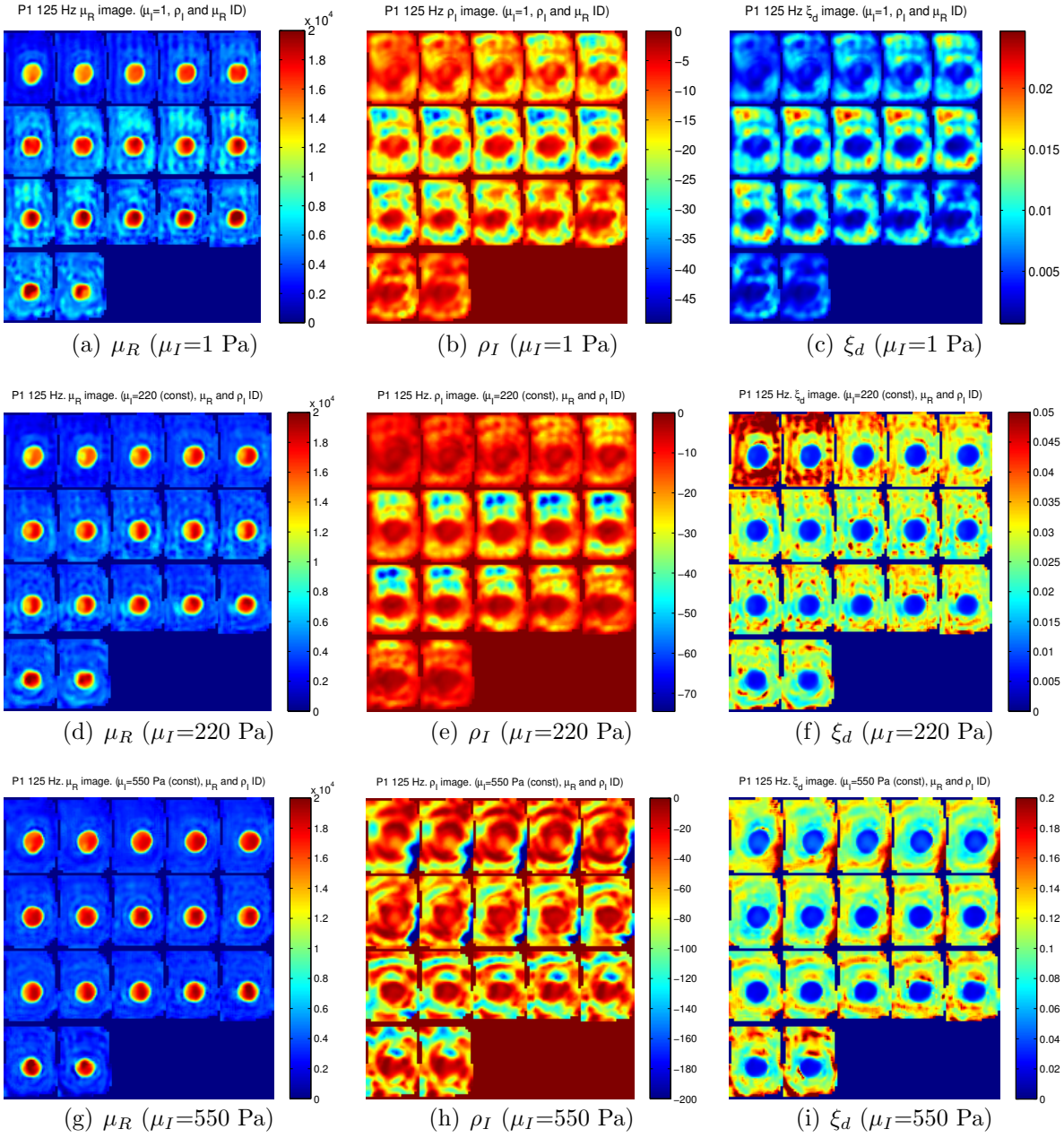

(a) μ_R (μ_I=1 Pa) (b) ρ_I (μ_I=1 Pa) (c) ξ_d (μ_I=1 Pa)

(d) μ_R (μ_I=220 Pa) (e) ρ_I (μ_I=220 Pa) (f) ξ_d (μ_I=220 Pa)

(g) μ_R (μ_I=550 Pa) (h) ρ_I (μ_I=550 Pa) (i) ξ_d (μ_I=550 Pa)

Figure 9.6 Image results for the parametric-based RD reconstruction of P1 phantom at 125 Hz using following parameters: top row: μ_I= 1 Pa (const), middle row: μ_I= 220 Pa (const), bottom row: μ_I= 550 Pa (const); initial *a-priori* conditions for all three cases were: ρ_I= -1 (kg/m^3) and μ_R= 3300 (Pa). ρ_I= 1000(kg/m^3) (const). (a), (d) and (g): storage modulus μ_R image (Pa); (b), (e) and (h) imaginary density ρ_I image (kg/m^3); and (c), (f) and (i): damping ratio ξ_d image (% / 100)

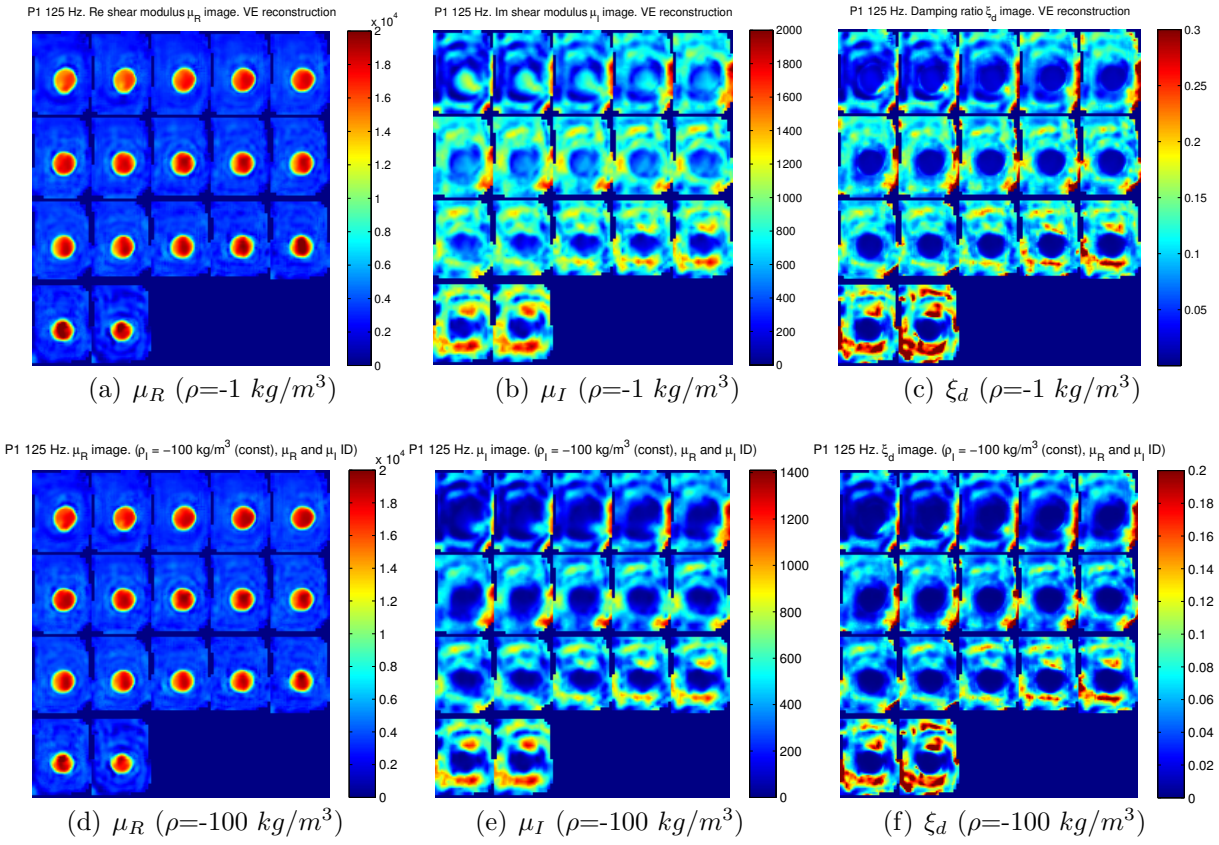

(a) μ_R (ρ=-1 kg/m^3) (b) μ_I (ρ=-1 kg/m^3) (c) ξ_d (ρ=-1 kg/m^3)

(d) μ_R (ρ=-100 kg/m^3) (e) μ_I (ρ=-100 kg/m^3) (f) ξ_d (ρ=-100 kg/m^3)

Figure 9.7 Image results for the parametric RD reconstruction of P1 phantom at 125 Hz using following parameters: top row: ρ_I=-1 kg/m^3 (const); bottom row: ρ_I= -100 kg/m^3 (const). Initial *a-priori* conditions: ρ_R= 1000 kg/m^3 (const), μ_R= 3300 Pa and μ_I= 330 Pa. (a) and (d) storage modulus μ_R image (Pa); (b) and (e) loss modulus μ_I image (Pa); (c) and (f) damping ratio ξ_d image (% / 100)

the imaginary density term.

Reconstruction results produced by parametric RD model were compared to the MF-based RD model results with regards to the following criteria:

- Differentiation - ability of the RD model to differentiate various materials characterised by different material properties as well as clear delineation of the boundaries between two material zones
- Qualitative accuracy - ability of the RD model to accurately distinguish stiffness profiles of the materials
- Quantitative accuracy - ability of the RD model to produce accurate quantitative estimates of the stiffness and damping

Table 9.1 Comparison between parametric and MF RD MRE results

Criteria	MF RD MRE		Parametric RD MRE	
	μ_R	ξ_d	μ_R	ξ_d
Differentiation	✓	✓✗	✓✓	✓✓
Qualitative Accuracy	✓	✓✗	✓✓	✓
Quantitative Accuracy	✗✗	✗	✗	✗

9.3 Summary of MF / parametric RD MRE studies

Simultaneous MF-based RD elastography was performed to investigate the ability of the RD model to accurately identify both VE and RD based parameters in a variety of tissue simulating damping phantoms. Furthermore, parametric RD MRE studies were carried out to overcome fundamental identifiability limitation of the RD model.

Overall, MF-based RD reconstruction results demonstrated poor success in accurate delineation of the RD based properties. Although slight improvement in

reconstruction accuracy was observed, the difference between SF and MF based RD results was minimal. These results were likely due to effect of the small input frequency range on practical identifiability.

Similar to SF RD results, μ_R reconstruction was again of the highest quality in all phantom configurations. Reconstruction of the RD parameters was generally associated with poor characterisation of different material types and relatively high variations within supposedly homogenous material regions and materials boundaries. No distinguished trends were observed in μ_I or ρ_I, although ρ_I reconstruction somewhat displayed better accuracy in capturing presence of two materials.

A possible explanation for the poor quality of the MF based RD reconstruction might be due to the high range of the actuation frequencies that are above the natural frequency of the system. Much more distinct input frequencies far apart might make RD model practically identifiable, whereas 3 frequencies of a broad range might make it possible to tell if RD is an appropriate model for the particular damped system. Another explanations is related to the absence of the scaling between individual terms in the objective function that contribute to the overall error minimisation.

Parametric RD reconstructions generally produced better results compared to MF-based RD results. A clear differentiation of the materials was seen. Moreover, moderately accurate reconstruction of ξ_d was observed when one of the fixed RD parameters was adjusted appropriately. Therefore, parametric RD MRE was considered to be an optimal method for accurate elastographic RD reconstruction.

Chapter 10

Healthy *in-vivo* brain RD MRE experiments

This chapter summarises results from RD MRE studies on *in-vivo* healthy brain. The goal is to examine the RD model to accurately image VE and concomitant damping properties of the *in-vivo* healthy brain. The hypothesis behind this study is that if RD model provides a better description for the overall damping behaviour of a biological tissue than a viscoelastic model, it may allow better reconstructions of other material properties, such as real shear modulus, due to reduced data-model discrepancy. Thus, RD model may still be of value even if the RD based properties are not fully identifiable.

The results shown in Chapters 7 and 8 indicated nonidentifiabilty of the RD model at a single frequency. However, modifying the algorithm to fix one damping value throughout the reconstruction domain and to identify the other two RD parameters showed promising potential to differentiate the materials characterised by different mechanical properties. The combination of these two aspects suggests that initial investigation of the RD model in a clinical setting might have diagnostic potential. The aim of the *in-vivo* brain RD MRE was to assess the ability of the RD model:

- To perform qualitative differentiation between different brain tissue types, such as white matter and gray matter;
- To accurately delineate the location of the fluid filled ventricles and any areas of markedly different damping;
- To evaluate weather variation in RD parameters μ_I and ρ_I provide a mechanism for differentiating tissue structure based on different attenuation effects

in addition to measuring elastic stiffness;

- To provide overall assessment of the RD elastography as a valuable diagnostic imaging tool in a clinical setting.

10.1 Materials and Methods

The motion brain data sets were obtained from two different sources: National Research Council of Canada (CNRC) and University of Illinois at Urbana-Champaign (Urbana, Illinois, USA). The author would like to greatly acknowledge Dr Peter Latta, Dr Marco Gruwell at CNRC and Curtis Johnson from University of Illinois at Urbana-Champaign for their contribution into the project.

10.1.1 CNRC data

In-vivo brain MRE studies were performed on healthy volunteers under the the CNRC GHI protocol. Informed consent was obtained prior to subject testing. Ethics approval was obtained from the National Research Council Ethics Board (NRCEB). Subjects gave written informed consent and were free of exclusion criteria for MRI.

MRE examinations were performed on a 3T MRI scanner (Tim Trio, Siemens Medical Solutions, Erlangen, Germany) using a standard single channel head coil. 3D steady state displacement fields were acquired by a single shot, SE EPI sequence, extended with trigger timing and MEGs modules, using following parameters: TR/TE = 3000/120 ms; FOV = 220×220 mm; matrix resolution of 128×128 pixels; and 10 slices of 3 mm thickness. Prior to each excitation of the MR signal, a mechanical vibration was applied for a time interval of 400 ms. The isochromatic displacements were encoded with 1 cycle of sinusoidal-shaped MEGs of 32 mT/m magnitude in 8 equally spaced time increments. Each time increment was acquired two times using opposing MEG signals (Latta et al., 2010).

To suppress a linear phase shift caused by a rotation component of the rigid body motion (head movement of the subject), zero and first order phase correction in the k-space domain (Latta et al., 1998) were applied prior to FFT. The raw data

was then analysed with MATLAB in which a two dimensional FFT was performed for each slice. Slices acquired with opposite MEG were subtracted to eliminate phase errors. To further suppress phase wrapping, a 3D quality-guided phase unwrapping method (Wang et al., 2011) was also applied. OSS-SNR (McGarry et al., 2011) was calculated to estimate the quality of the MRE motion data.

Acoustic actuation was utilized to introduce shear waves into the head at 50 Hz. Two active subwoofers, modified with airtight acrylic lids (refer to Fig. 10.2(a)), were used to generate acoustic waves delivered through long tubing to pressure actuated drivers (PADs), located in the MRI head coil (refer to Fig. 10.2(b)) and placed under the subject's head (refer to Fig. 10.2(d)). A function generator (Tektronix AFG3022B), triggered from the MRE pulse sequence, was used to generate the desired acoustic waveforms. To induce side-to-side, cradle-like head motion the PADs were inflated with air pressure waveforms with a 180° mutual phase difference (Latta et al., 2010).

Several MF-based MRE examinations were also performed on the *in vivo* brain at the mechanical frequencies of 50, 60, 70 and 80 Hz. However, due to the strong attenuation of the shear strain waves at the higher frequencies, the motion data was of a poor quality leading to inaccurate elastographic reconstructions. Fig. 10.1 shows an example of a poor data quality of the displacement measured by MRE at 80 Hz compared to the data of a moderate quality at 50 Hz. Therefore, reconstruction results from MF-based MRE are not presented in this chapter. Producing accurate and reliable estimates of the mechanical properties of the *in vivo* brain tissue is critically dependent on the quality of the acquired MRE motion data set. OSS-SNR (McGarry et al., 2011) was used to estimate the quality of the data.

10.1.2 University of Illinois at Urbana-Champaign data

The ability of the RD elastography to reconstruct accurate and reproducible elastograms was tested by performing a repeatability MRE study. Six repetitive MRE examinationons were undertaken on a healthy volunteer following the approval of the Institutional Review Board and after obtaining written informed consent. The studies were carried out by the Department of Mechanical Science and Engineering,

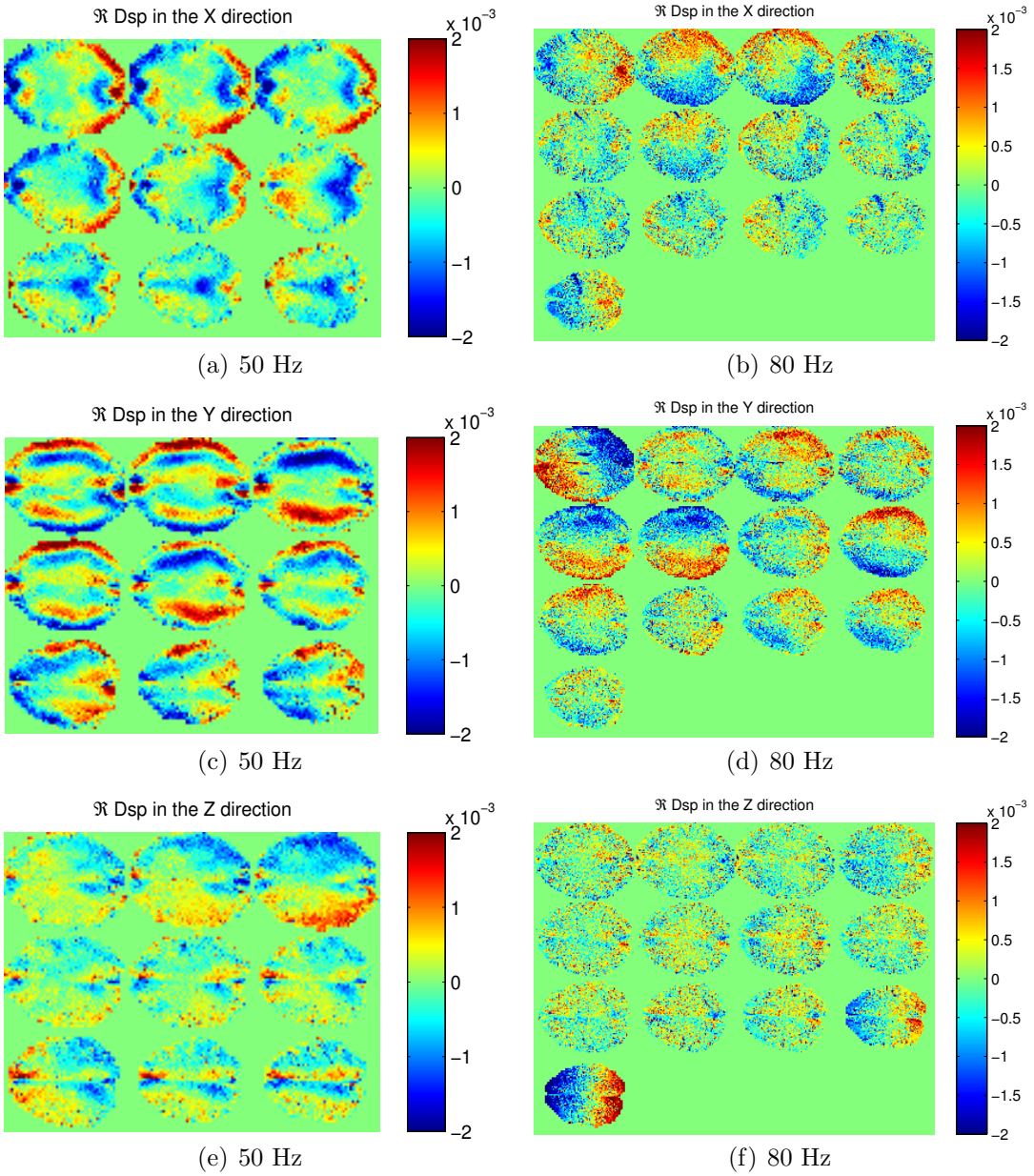

Figure 10.1 Comparison of MRE data acquired at 50 Hz (left column) and 80 Hz (right column) excitation frequencies by pneumatic-based actuation methodology. The difference in displacement data quality can be clearly observed with 50 Hz data being of a highest quality. Similar trends of a poor data quality (due to the strong attenuation of the shear stain waves inside the brain) were also seen in the higher frequencies of 70 Hz and 90 Hz. (a) and (b) $\Re$ component of the measured displacement in the x-direction; (c) and (d) $\Re$ component of the measured displacement in the y-direction; (e) and (g) $\Re$ component of the measured displacement in the z-direction

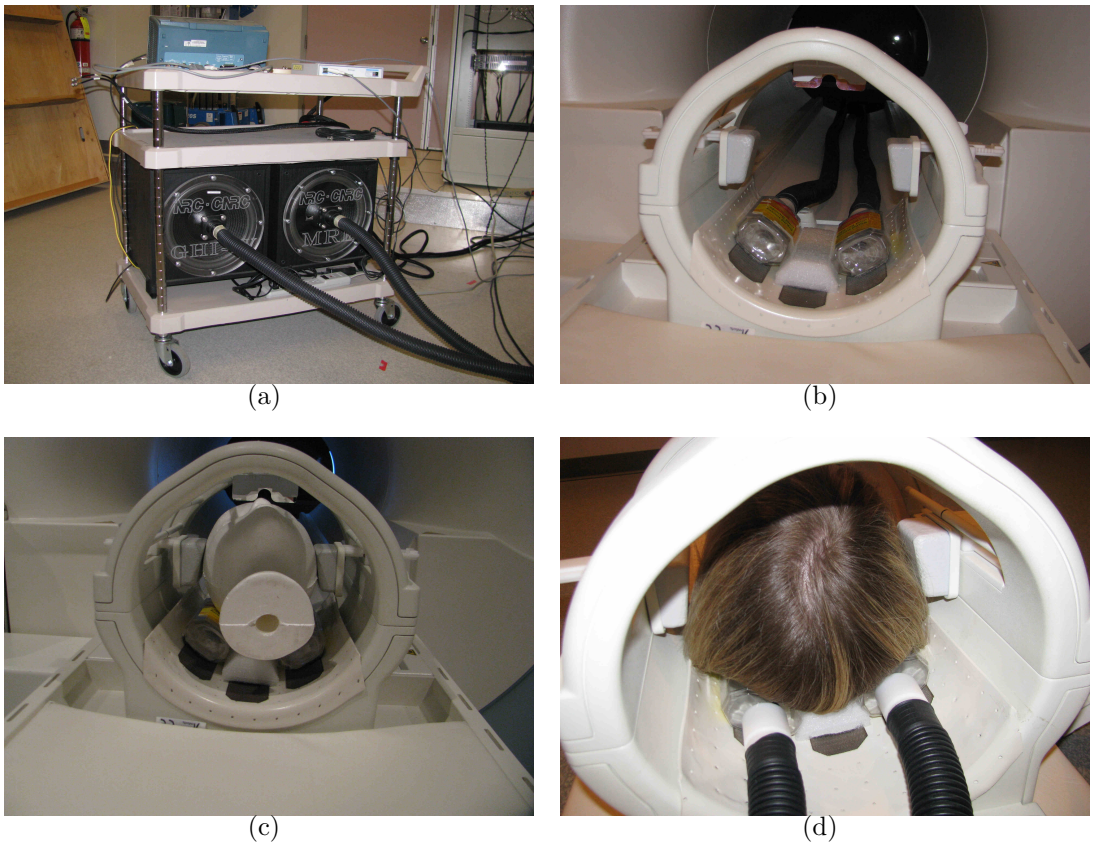

Figure 10.2 MRE experimental set up for performing *in vivo* brain human studies: two modified active subwoofers (a) are used to deliver acoustic pressure waves into the PADs, located in the MR head coil (b). The subject lies supine and the PADs are positioned underneath the head (c and d). The PADs are driven with the mutual phase shift of 180° which cause the head to undergo rotation.

University of Illinois at Urbana-Champaign (Urbana, Illinois, USA).

MRE examinations were performed using a 3T Allegra head-only scanner (Siemens Medical Solutions, Erlangen, Germany). 3D motion encoding was achieved by an innovative multi-shot spiral MRE sequence with bi-polar MEGs (Johnson et al., 2012) using following parameters: 6 k-space intervals, TR/TE= 2000/55 ms, FOV= 256 mm, 128×128 matrix. 20 coronal axial slices of 2 mm thick were acquired resulting in an isotropic voxel resolution of $2 \times 2 \times 2$ mm. Wave acquisition was performed by 8 equally spaced time harmonics over a single period. The area of brain imaging was in the region of the *corpus callosum* (refer to Fig.) Total MRE acquisition time was less than 10 minutes. A T1-weighted MPRAGE images were also acquired for each subject using following parameters: TR/TI/TE=2000/900/2.2 ms; $1 \times 1 \times 1$ mm isotropic voxel resolution . The actuation methodology was similar to MRE studies reported by Sack et al. (2009). The system comprised a long rod that was mutually attached to a speaker membrane at one end and a custom-made cradle on which the head was positioned on the other end. 50 Hz excitation frequency was applied.

Wave images were acquired by subtracting positive and negative obtained images followed by further phase unwrapping method (Wang et al., 2011) . FFT was applied to extract motion at a first harmonic which resulted in 3D complex values displacements (refer to Fig. 10.8). No further filtering was applied to the data prior to reconstruction processing. Quality of each MRE data set was evaluated by calculating OSS-SNR (McGarry et al., 2011). OSS-SNR revealed that high quality data was obtained with high OSS-SNR value even in the middle of the brain where motion undergoes significant attenuation. Therefore, the noise in the displacements fields is not expected to influence accuracy of the elastographic results. The summary of the quantified OSS-SNR values across different brain tissue regions is summarised in Table 10.1.

Image registration between the high-resolution T1-weighted MPRAGE and MRE images was performed using the Brain Extraction Tool (BET) and the FMRIB Linear Image Registration Tool (FLIRT) (Jenkinson et al., 2002) in the FMRIB Software Library (FSL) (Smith et al., 2004). Furthermore, segmentation of the intracranial matter (white & gray matter) and CSF was performed (refer to Fig. 10.3) using the FMRIB Automated Segmentation Tool (FAST) (Zhang et al., 2001) to calculate statistic distribution of the material property values (Table 10.1.) Finally,

to evaluate ability of the RD MRE to reproduce the results, data from 6 repetitive MRE scans was co-registered using FLIRT to calculate the mean, standard deviation (STD) and coefficient of variation (CV) of the reconstructed property values (refer to Fig. 10.10).

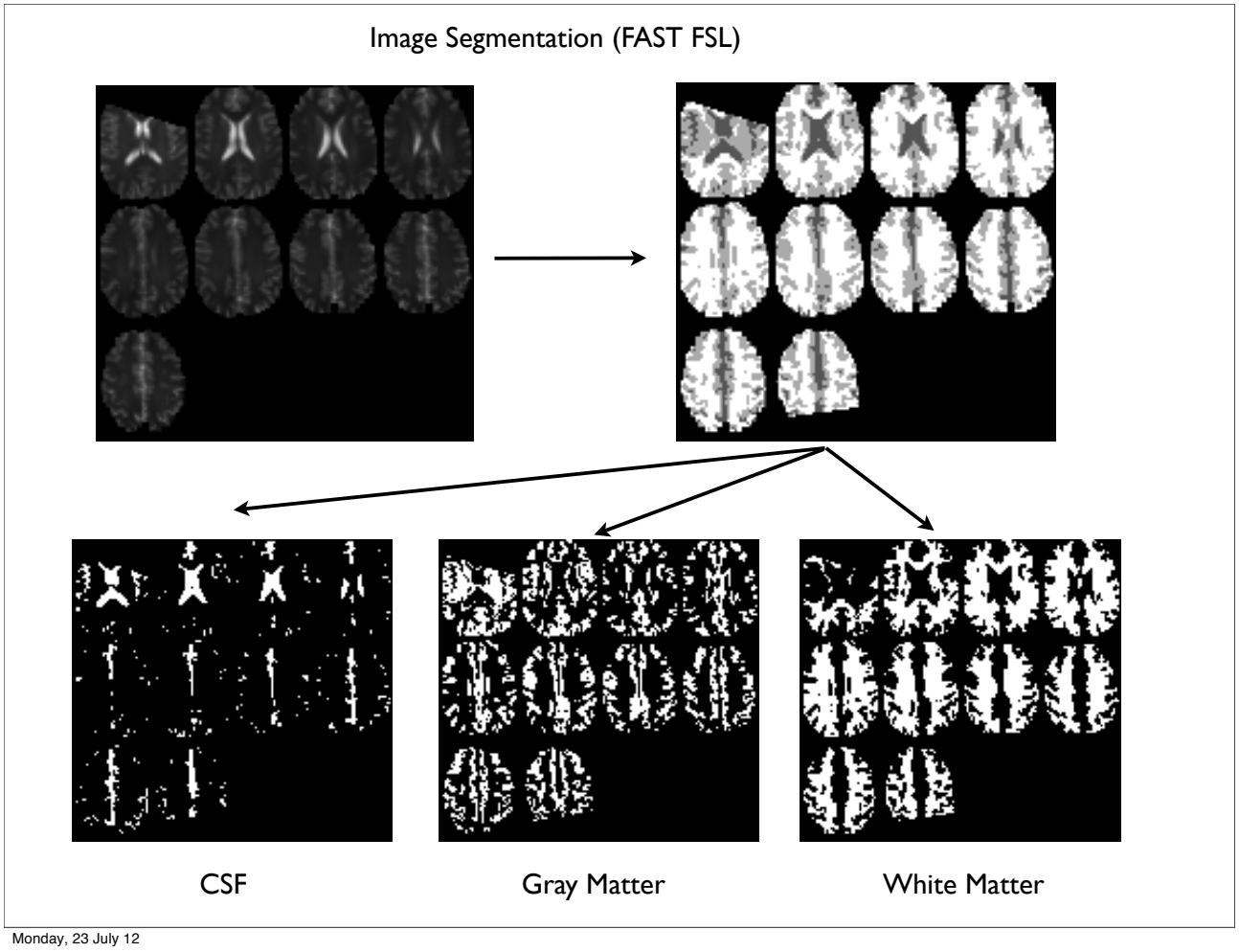

Figure 10.3 Segmentation of the white matter, gray matter and cerebrospinal fluid (CSF) of the 6 co-registered repetitive MRE examinations of the *in vivo* healthy brain using the FMRIB Automated Tissue-Type Segmentation Tool (FAST) in the FMRIB Software Library (FSL).

10.1.3 RD elastographic reconstructions

Reconstruction computations of both data sets were performed on HPC *Blue Fern P575*. A total of 32 processors under an MPI protocol were utilized. An isotropic, nearly incompressible RD model, applied to a subzone based nonlinear inversion algorithm, was used to identify complex valued shear modulus (μ_R and μ_I) and

imaginary part of the density (ρ_I). Damping ratio (ξ_d) was then calculated as a sum of ratios between imaginary and real components of the shear modulus and density. The reconstruction parameters were: subzone edge factor was $6 \times 8 \times 1$ resulting in subzone size of $0.02 \times 0.02 \times 0.02$ m. Each subzone contained approximately 1400 nodes. Total number of nodes and elements were 45247 and 4819, respectively. The initial *a-priori* conditions were: μ_R= 1000 Pa, μ_I= 100 Pa, ρ_I= -100 kg/m^3. ρ_R was set to 1000 kg/m^3 and was defined as a constant; λ was assumed to be large (10^8 Pa) to model the nearly incompressible behavior expected for fluid saturated tissues such as the brain. Total reconstruction time was approximately 4 hours. Nodal based support of the material properties was used.

Error minimisation was performed by the CG optimisation method over 100 iterations with residual scaling factor of 0.02. Regularisation techniques used were TV, SF and constraints. Initial and finally TV weights: μ_R: 10^{-17} - 10^{-17}, μ_I: 10^{-17} - 10^{-17} and ρ_I: 10^{-16} - 10^{-16}. TV delta values were set to 10^{-19}. Finally, initial and final SF weights for all reconstruction parameters were: 25 and 15 (%). Tikhonov regularisation, Joachimowicz regularisation and Marquardt regularisation techniques were not used for brain elastographic reconstructions.

10.2 Results

10.2.1 CNRC data

Fig. 10.4 shows a T2*-weighted MR images for different regions of *in-vivo* healthy brains (subject V1 and subject V2) for anatomical reference. The anatomical structure of the ventricles can be clearly seen. Fig. 10.5 shows 3 parameter RD reconstruction results for μ_R, μ_I, ρ_I and concomitant ξ_d of the two *in-vivo* healthy brains at 50 Hz.

Figs. 10.5 (a) and 10.5 (b) show the estimated μ_R image. The latter revealed that the central region of the brain about the ventricles exhibits much lower elasticity than the surrounding intracranial matter regions. Figs. 10.5 (c) and 10.5 (d) show reconstructed μ_I image. No obvious qualitative trends correlating with the anatomical structures were noted. Figs. 10.5 (e) and 10.5 (f) show reconstructed ρ_I image. The location of the fluid-filled ventricles was captured in the first data set

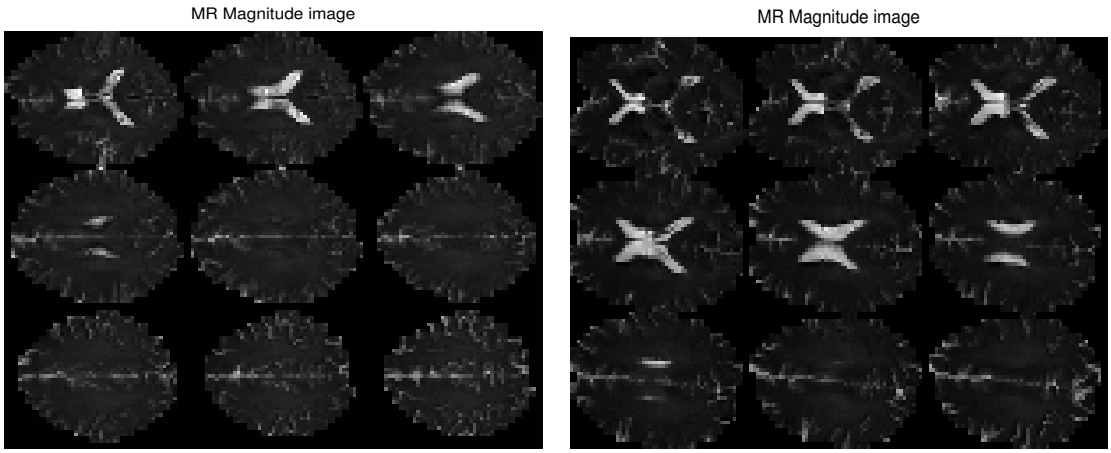

(a) T2*-weighted MR image (V1) (b) T2*-weighted MR image (V2)

Figure 10.4 T2*-weighted MR images of the *in-vivo* healthy brains: (a) first volunteer (b) second volunteer

(refer to Fig. 10.5 (e)), however failed in the other data set (refer to Fig. 10.5 (f)). Finally, Figs. 10.5 (g) and 10.5 (h) show estimated ξ_d image. High damping levels detected in the middle of the brain are plausible due to the strong attenuation of the shear strain waves. Fig. 10.5 (h) shows clearly distinguished increased damping levels within the ventricles, indicating high loss of mechanical energy within the inviscid CSF.

Fig. 10.6 shows parametric based RD reconstruction results with globally defined μ_I= 333 Pa of the *in vivo* healthy brain at 50 Hz. Similar qualitative trends were observed in all reconstructed parameters between parametric-based RD reconstruction and 3 parameter-based RD reconstruction. Although no significant improvement was noted in the reconstructed ρ_I image of both data sets, reconstructed μ_R and ξ_d images, computed by parametric RD model (refer to Figs. 10.6 (a), (b), (g) and (h)), appeared to be of a higher quality compared to corresponding μ_R and ξ_d images, computed by full 3 parameter-based RD model (refer to Figs. 10.5 (a), (b), (g) and (h)). For example, no boundary artefacts were seen in the reconstructed V2 ξ_d image (refer to Fig. 10.6 (h)), which was presumably triggered by inaccurate reconstruction of μ_I image in the full RD reconstruction, as shown in Fig. 10.5 (d).

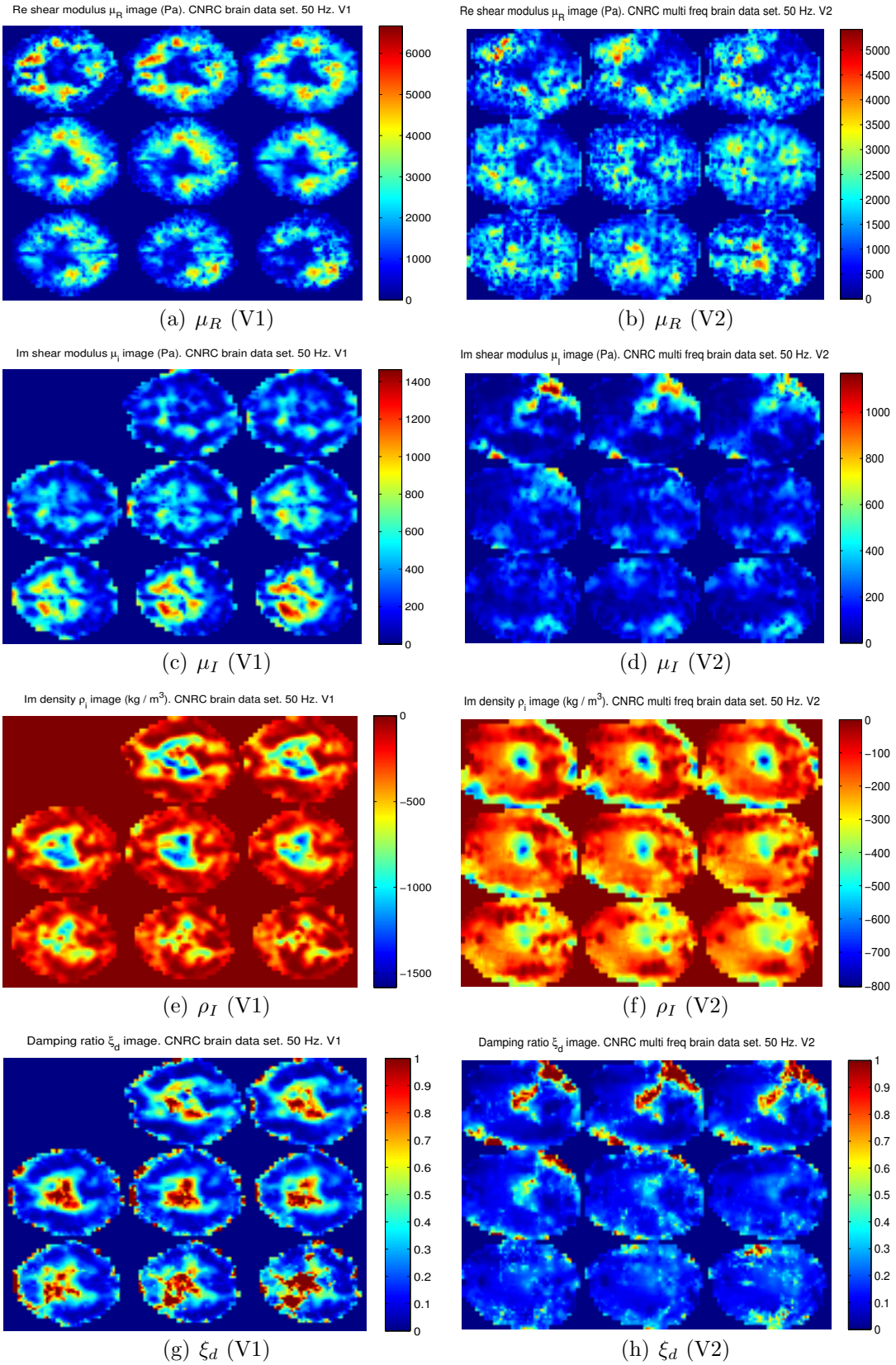

(a) μ_R (V1) (b) μ_R (V2)

(c) μ_I (V1) (d) μ_I (V2)

(e) ρ_I (V1) (f) ρ_I (V2)

(g) ξ_d (V1) (h) ξ_d (V2)

Figure 10.5 Image results of the 3 parameter-based RD reconstruction of the *in-vivo* healthy brains (Subject V1 and Subject V2) at 50 Hz (CNRC data set) : (a) and (b) storage modulus μ_R image (Pa); (c) and (d) loss modulus μ_I image (Pa); (e) and (f) imaginary density ρ_I image (kg/m^3); and (g) and (h) damping ratio ξ_d image (% / 100)

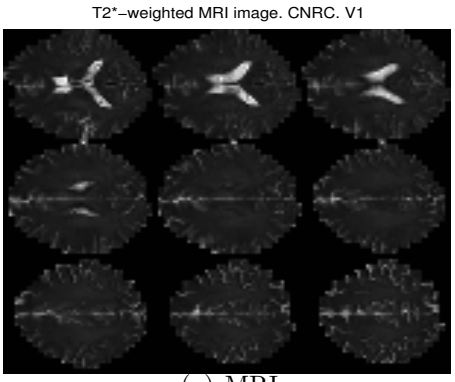

(a) MRI

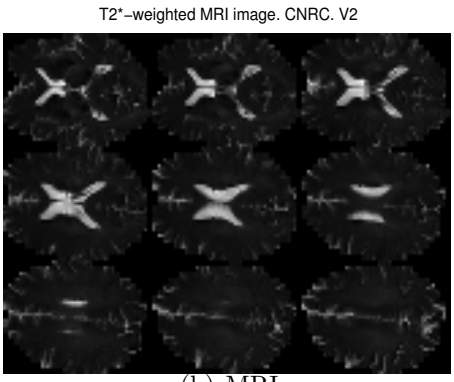

(b) MRI

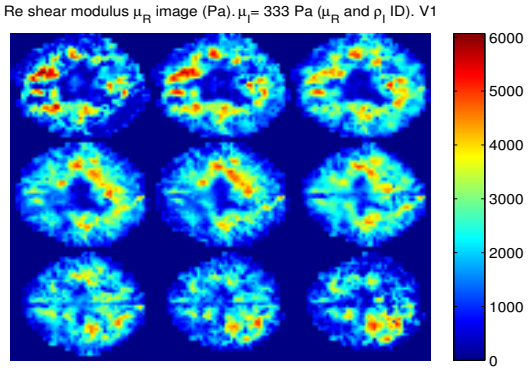

(c) μ_R

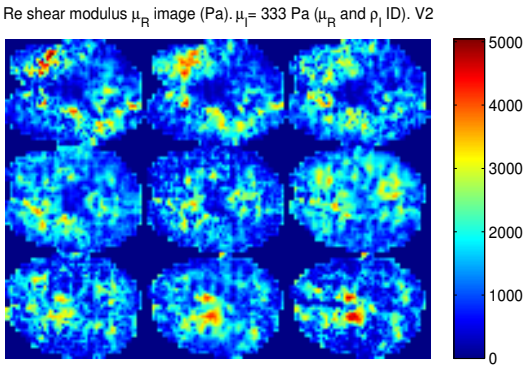

(d) μ_R

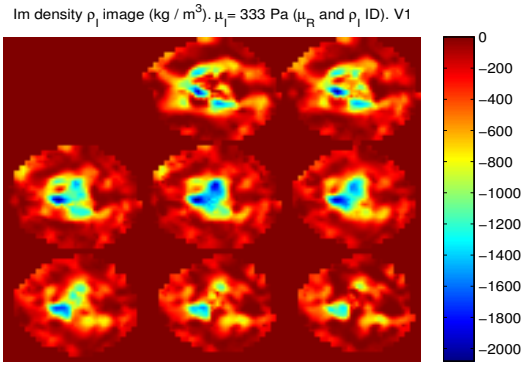

(e) ρ_I

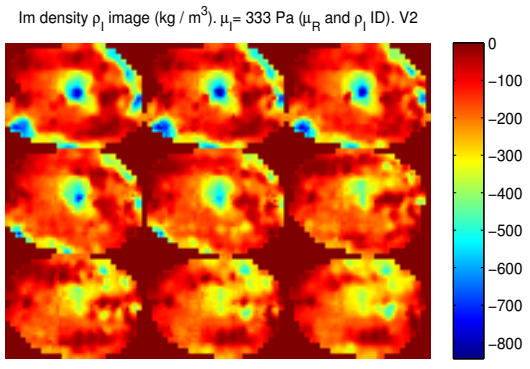

(f) ρ_I

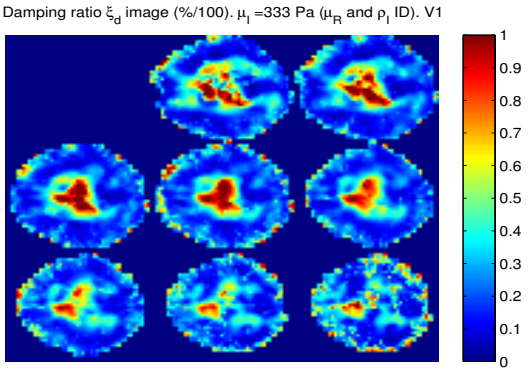

(g) ξ_d

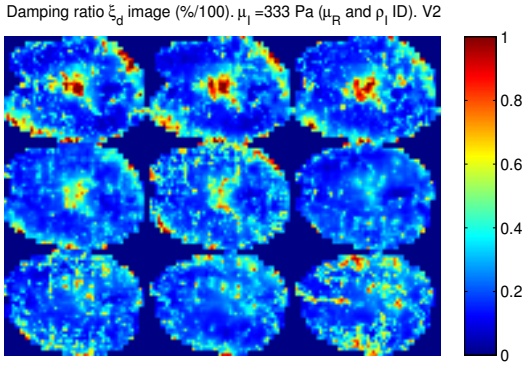

(h) ξ_d

Figure 10.6 Image results of the parametric-based RD reconstruction with globally defined μ_I = 333 Pa of the *in-vivo* healthy brains (subject V1 and subject V2) from Fig. 10.5 at 50 Hz (CNRC data set): (a) and (b) T2*-weighted MRI images, (c) and (d) storage modulus μ_R image (Pa); (e) and (f) imaginary density ρ_I image (kg/m^3); and (g) and (h) damping ratio ξ_d image (% / 100)

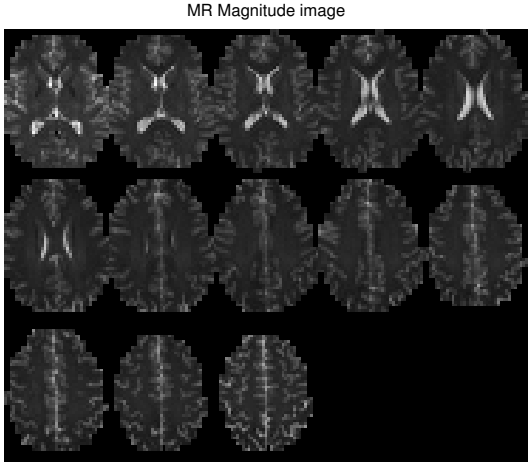

Figure 10.7 T1-weighted MPRAGE MRI image of the brain for anatomical reference.

10.2.2 University of Illinois at Urbana-Champaign data

Fig. 10.7 shows high-resolution T1-weighted MPRAGE MR image of the brain. Fig. 10.8 shows the $\Re$ and $\Im$ components of the measured displacement fields in three orthogonal directions from one of the repetitive MRE examinations. Particular actuation methodology as well as correction for rigid body motion (RBM) induced phase-errors resulted in high quality motion data with average OSS-SNR value of ~ 4.5 which is above previously established threshold value of ~ 3.0 for accurate inversion.

Fig. 10.9 shows 3 parameter-based RD reconstruction results of two repetitive MRE examinations from a healthy *in-vivo* brain. The structure of the ventricles, depicted by relatively low μ_R values compared to the white / gray matter regions, can be distinguished in the μ_R image (refer to Figs. 10.9 (a) and 10.9 (b)). Reconstructed μ_I images (Figs. 10.9 (c) and 10.9 (d)) systematically revealed area with low μ_I values through the middle of the brain, correlating with the location of the *falx cerebri*. The appearance of the area with increased μ_I values in the middle of the brain does not communicate with any rheological interpretations nor anatomical structures. Therefore, it may be an artefact of the experimental design or alternatively arise due to the nonidentifiabilty of the model. An estimated ρ_I images were able to detect fluid-filled ventricles within intracranial matter by increased ρ_I values even at a single frequency. The location and geometry of the the ventricles on the ρ_I images partially correlates with the location and geometry of the ventricles on the

Table 10.1 Quantitative analysis for the mean, standard deviation (STD) and coefficient of variation (CV) of the mechanical properties of the *in vivo* healthy brain measured by the RD model over six repetitive MRE examinations

Parameter Units	OSS-SNR	μ_R (kPa)	μ_I (kPa)	ρ_I (kg/m^3)	ξ_d (%)
Brain matter (white and gray)					
Examination 1	5.761	2.586	0.453	-294.662	0.274
Examination 2	4.962	2.741	0.390	-312.526	0.254
Examination 3	4.465	2.412	0.346	-279.152	0.240
Examination 4	4.554	2.623	0.450	-280.503	0.257
Examination 5	2.840	2.647	0.286	-266.737	0.230
Examination 6	4.502	2.524	0.377	-275.537	0.246
Mean	**4.514**	**2.589**	**0.466**	**-284.853**	**0.242**
STD	0.955	0.112	0.08	16.300	0.020
CV	0.211	0.043	0.171	-0.057	0.083
White matter					
Examination 1	5.136	3.099	0.546	-344.242	0.274
Examination 2	4.428	3.118	0.466	-334.345	0.254
Examination 3	3.877	2.843	0.408	-316.671	0.240
Examination 4	3.938	3.087	0.565	-304.483	0.257
Examination 5	2.593	3.028	0.354	-318.314	0.230
Examination 6	3.954	2.892	0.459	-305.591	0.246
Mean	**3.988**	**3.011**	**0.466**	**-320.608**	**0.250**
STD	0.833	0.116	0.080	15.834	0.015
CV	0.209	0.038	0.171	-0.0494	0.061
Gray matter					
Examination 1	6.279	2.101	0.369	-248.376	0.259
Examination 2	5.436	2.350	0.311	-283.931	0.235
Examination 3	4.986	2.027	0.285	-241.363	0.230
Examination 4	5.087	2.197	0.345	-252.858	0.251
Examination 5	3.040	2.286	0.222	-213.406	0.182
Examination 6	4.973	2.197	0.305	-240.092	0.230
Mean	**4.967**	**2.193**	**0.305**	**-246.671**	**0.231**
STD	1.064	0.117	0.051	22.836	0.026
CV	0.214	0.053	0.167	-0.0926	0.011

MR image. Lastly, calculated ξ_d images indicated higher damping levels within the ventricles and generally in the deeper brain regions. Regions of increased ξ_d values generally correlate with the regions of increased ρ_I values.

Fig. 10.10 shows the mean, STD and CV of the estimated parameter values within the co-registered slices between 6 repetitive MRE examinations. Quantified values of parameter values for white matter, gray matter and intracranial matter

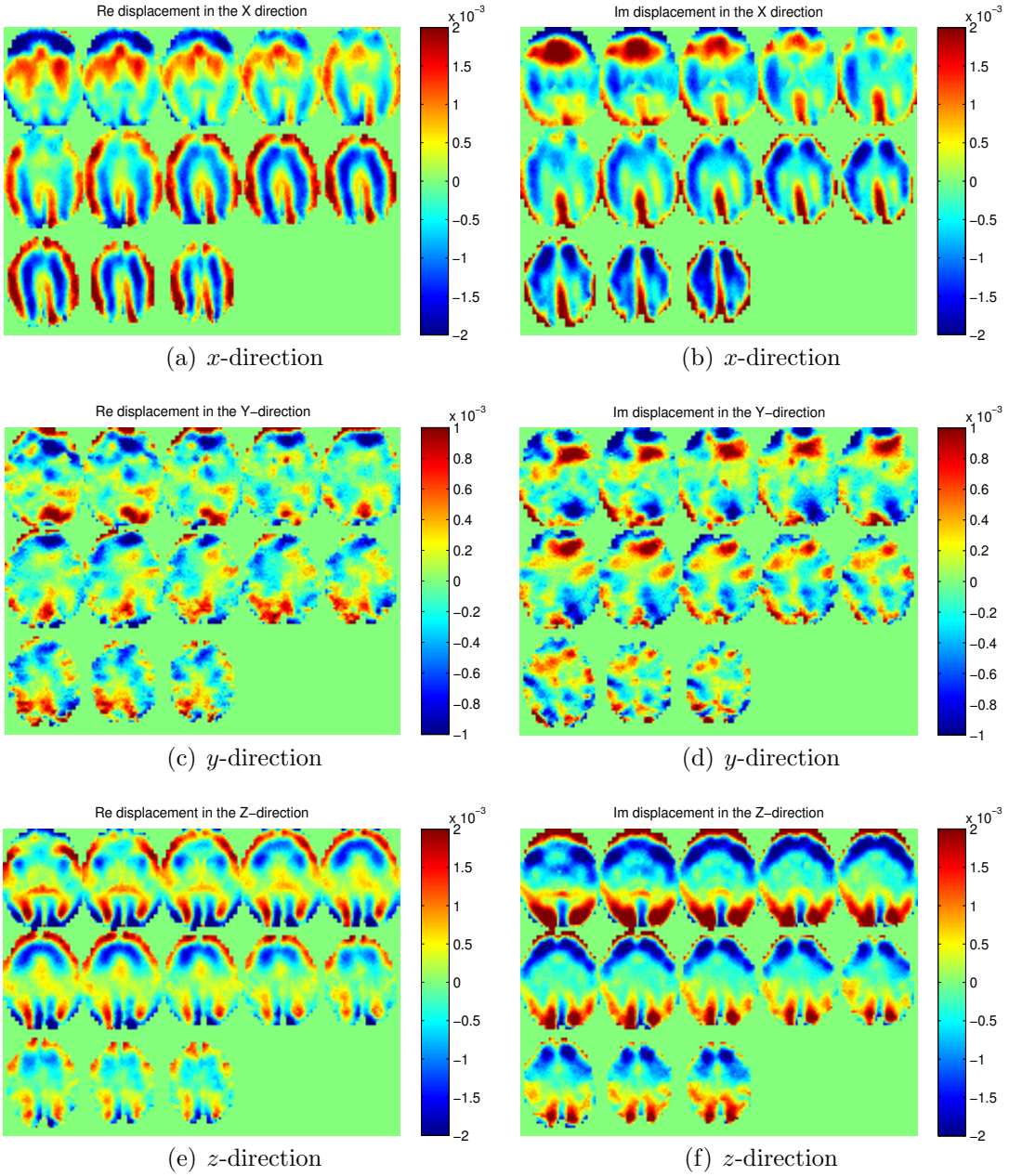

(a) x-direction (b) x-direction

(c) y-direction (d) y-direction

(e) z-direction (f) z-direction

Figure 10.8 Image results for the $\Re$ and $\Im$ components of the complex valued displacements from a healthy *in vivo* brain during one of the repeatability MRE studies. University of Illinois brain data set. (a) and (b) x-direction; (c) and (d) y-direction; (e) and (f) z-direction.

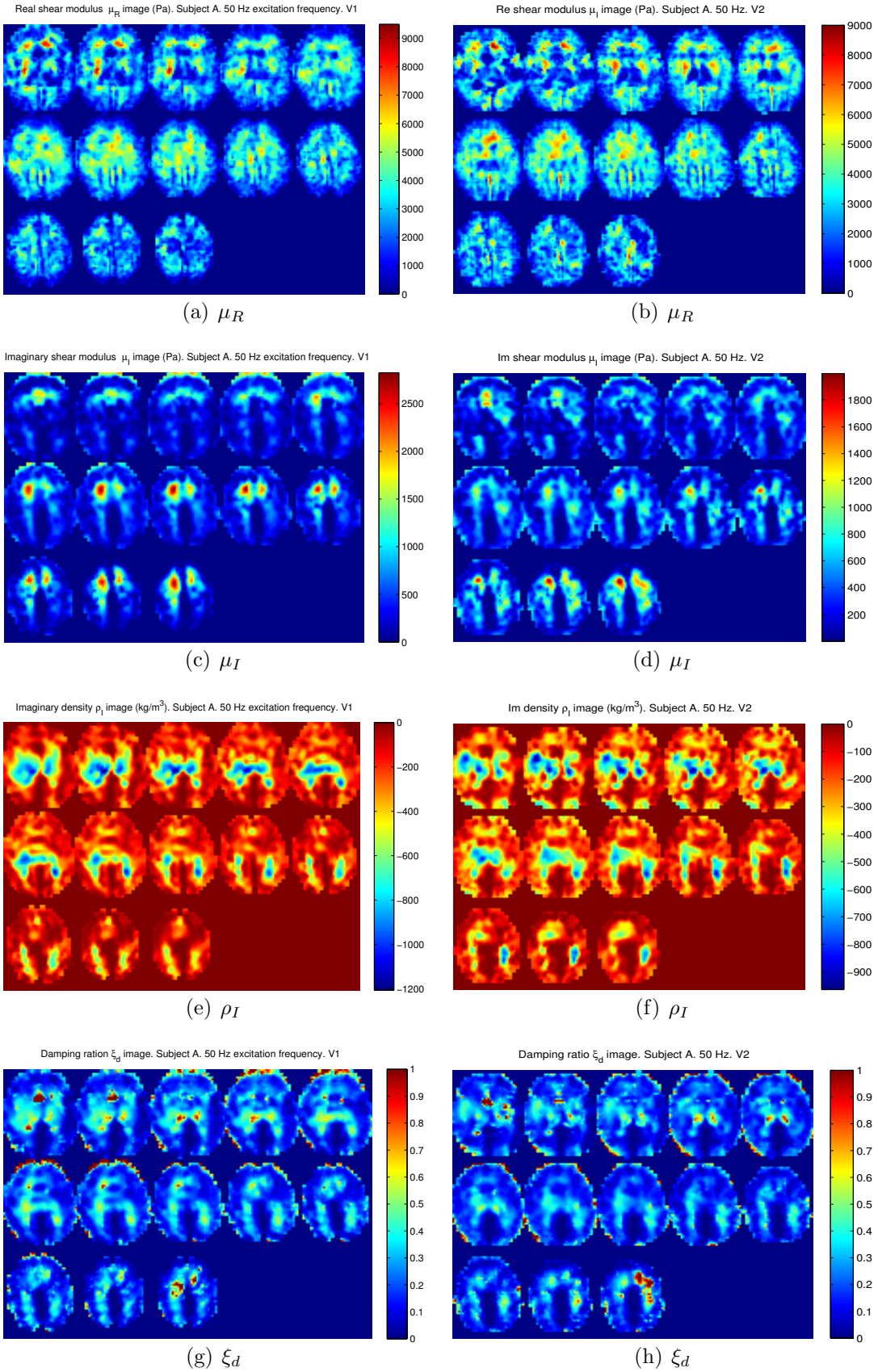

Figure 10.9 Image results for the full 3 parameter-based RD reconstruction of the two repetitive MRE examinations of the *in-vivo* healthy brain at 50 Hz: (a) and (b) storage modulus μ_R image (Pa); (c) and (d) loss modulus μ_I image (Pa); (e) and (f) imaginary density ρ_I image (kg/m^3); and (g) and (h) damping ratio ξ_d image (% / 100)

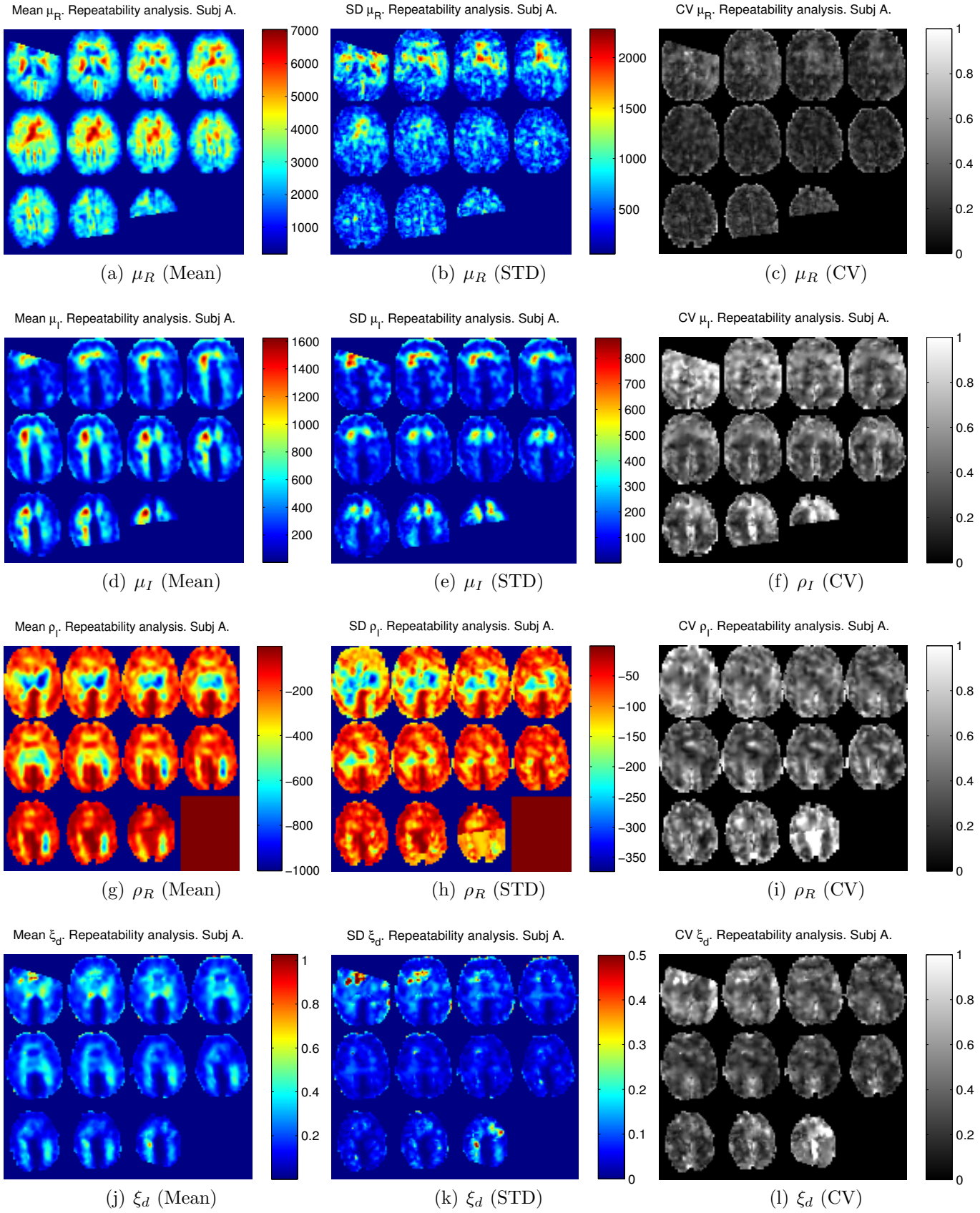

(a) μ_R (Mean) (b) μ_R (STD) (c) μ_R (CV)

(d) μ_I (Mean) (e) μ_I (STD) (f) ρ_I (CV)

(g) ρ_R (Mean) (h) ρ_R (STD) (i) ρ_R (CV)

(j) ξ_d (Mean) (k) ξ_d (STD) (l) ξ_d (CV)

Figure 10.10 Image results for the mean, STD and CV within the co-registered slices between 6 repetitive full 3 parameter-based RD reconstruction of the *in-vivo* healthy brain at 50 Hz: (a), (b) and (c) μ_R; (d), (e) and (f) μ_I; (g), (h) and (i) ρ_I; and (j), (k) and (l) ξ_d

are summarised in Table 10.1.

Although similar qualitative trends are observed in parameters among repetitive RD reconstructions, the non-identifiability of the model reconstructed RD based parameters μ_I and ρ_I limit any physical meaning. Therefore, to overcome identifiability issue parametric-based RD reconstructions were performed where μ_I was globally declared and excluded from identification. Fig. 10.11 shows parametric-based RD reconstruction results of the *in vivo* healthy brain with μ_I=333 Pa and μ_I=1000 Pa. Reconstruction results indicated that selecting reasonable value for μ_I distribution has major effect on the reconstructed ρ_I image and concomitant calculated ξ_d image. More specifically, reconstructed ρ_I image with a more realistic μ_I=333 Pa value representative of a greater portion of the brain tissue showed more accurate differentiation of the ventricles within the intracranial matter compared to the estimated ρ_I image with μ_I=1000 Pa. Consequently, the ξ_d reconstruction with μ_I= 330 Pa accurately captured relatively higher damping levels within the vicinity of the ventricles.

10.2.3 Discussion

This investigation assessed the efficacy of the RD model to accurately estimate VE and damping characteristics of the *in-vivo* healthy brain. The results present qualitative evidence that RD model applied to MRE is able to resolve local variations in tissue stiffness as well as damping profile that correlate with brain anatomical structures.

More specifically, the estimated μ_R distribution showed correlation with the white & gray matter and ventricles located in the centre of the brain, confirming rapid attenuation of the shear strain waves within the CSF. The latter could be described as Newtonian viscous fluid, with viscosity 0.7 - 1 mPa.s (Bloomfield et al., 1998), which leads to a nearly zero elasticity μ_R as well as μ_I values that are much lower than the surrounding brain tissue. The shear stiffness, μ_R, decreases in the area of the ventricles, while the magnitude of the ξ_d increases. The quantified values of the viscoelastic parameters for different regions agree well with *in vitro* and *in vivo* data published elsewhere (Green et al., 2006, 2008; Klatt et al., 2007; Sack et al.,

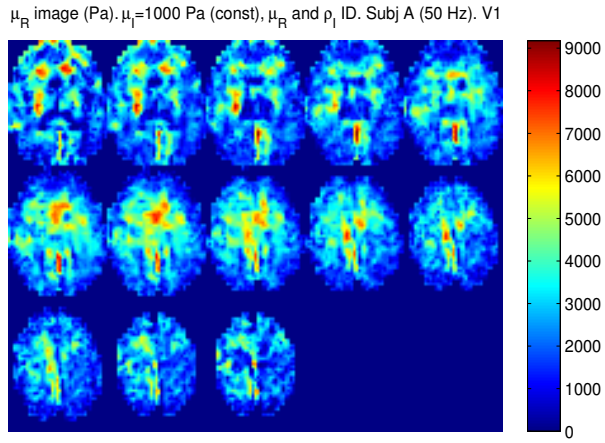

(a) μ_R (μ_I=1000 Pa)

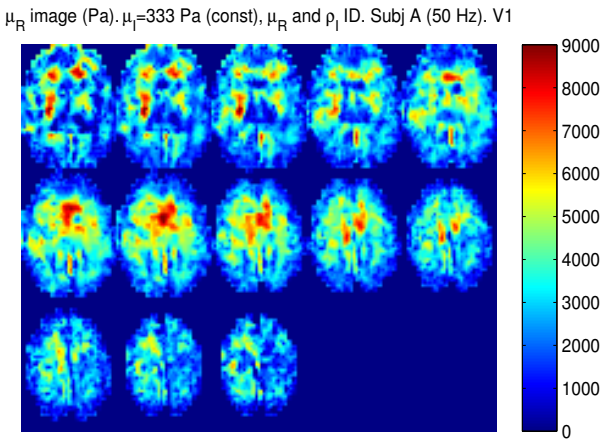

(b) μ_R (μ_I=333 Pa)

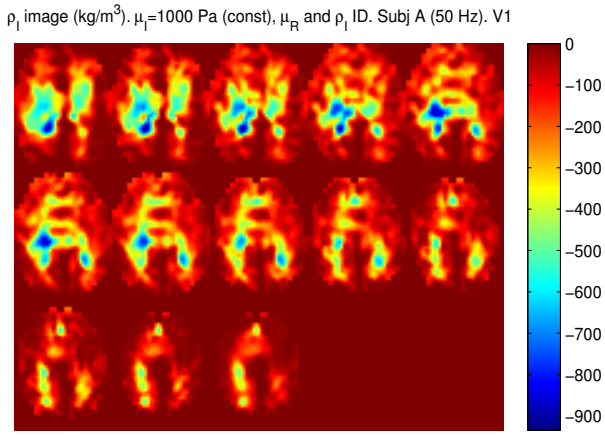

(c) ρ_I (μ_I=1000 Pa)

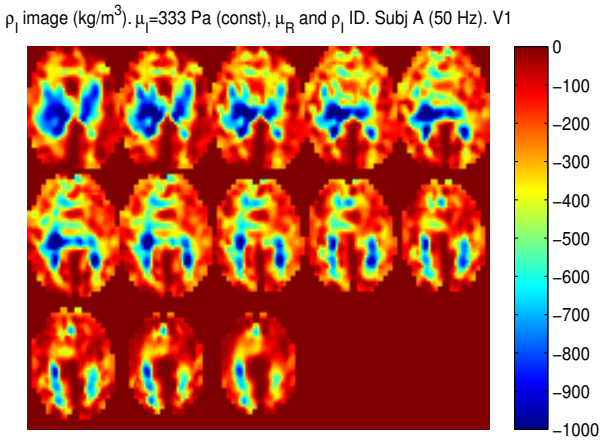

(d) ρ_I (μ_I=333 Pa)

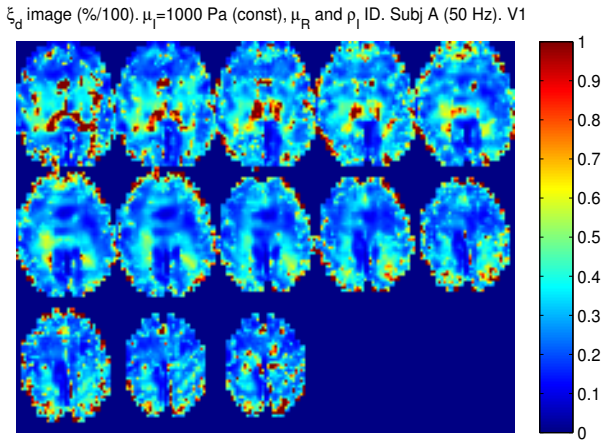

(e) ξ_d (μ_I=1000 Pa)

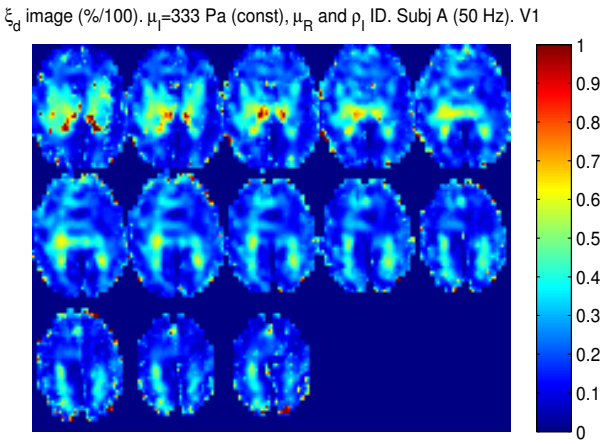

(f) ξ_d (μ_I=333 Pa)

Figure 10.11 Image results for parametric-based RD reconstruction of the *in-vivo* healthy brains at 50 Hz with globally defined μ_I=1000 Pa (left column) and μ_I=333 Pa (right column): (a) and (b) storage modulus μ_R image (Pa); (c) and (d) loss modulus μ_I image (Pa); (e) and (f) imaginary density ρ_I image (kg/m^3); and (g) and (h) damping ratio ξ_d image (% / 100).

Table 10.2 Current mechanical property estimates of brain tissue by MRE using nonlinear inversion (NLI) algorithm, direct inversion (DI) approach and local frequency estimation (LFE) algorithm.

RD	Actuation	Inversion	ω (Hz)	μ_R (kPa)	μ_I (kPa)
RD model	Head rocker	NLI			
White matter			50	3	0.46
Gray matter			50	2.1	0.3
Wuerfel *et al* (2009)	Head rocker	DI			
White / Gray Matter			50	1.6	0.65
Green *et al* (2008)	Bite bar	DI			
White Matter			60	2.7	2.5
Gray Matter			60	3.1	2.5
Kruse *et al* (2008)	Bite bar	LFE			
White Matter			100	13.6	NA
Gray Matter			100	5.22	NA
Sack *et al* (2009)	Head rocker	PWI			
White / Gray Matter			50	1.5	0.6
White / Gray Matter			62.5	2	0.8
Sack *et al* (2008)	Head rocker	PWI			
White / Gray Matter			25	1.17	3.1 Pa
White / Gray Matter			50	1.5	3.4 Pa
Vappou *et al* (2007)	Electromagnetic	PWI			
White / Gray Matter			80	1.15	0.91
White / Gray Matter			100	1.13	0.93
White / Gray Matter			120	1.19	1.01
White / Gray Matter			140	1.22	1.07
McCracken *et al* (2006)					
White Matter			TP	12	NA
Gray Matter			TP	8	NA
Uffman *et al* (2004)	Bite bar	DI			
White Matter			80	15.2	NA
Gray Matter			80	12.9	NA

2007; Vappou et al., 2007). Table 10.2 provides comparison between previously reported mechanical properties of the *in vivo* brain estimated by MRE and current estimates obtained by MRE based on RD material model.

Due to the ill-posed nature of the RD parameters μ_I and ρ_I at a single frequency, no conclusion can be drawn as to whether they provide a mechanism for differentiating tissue structure in addition to measuring elastic stiffness and attenuation. Based on a single frequency based RD reconstructions, the connection between the ρ_I and anatomical structure is less obvious, but some correlation is evident. For example, the region in the vicinity of the ventricle structures has relatively high ρ_I values and thus is indicated as fluidic in nature, while the white/ gray matter shows a more viscoelastic nature with lower ρ_I. Some correlation was also found between reconstructed μ_I image and brain anatomy. For instance, the area in the middle of the brain was systematically estimated with the lower μ_I values and correlates well with the location of the *falx cerebri*. No variation in ρ_I or μ_I correlating with differentiation between white and gray matter was noted, however higher μ_I values in the white matter were generally observed. Hence, further studies using brain phantoms and multifrequency RD elastography are required.

The damping in biological tissues occurs due to the complex, multiscale interactions between microstructural tissue elements. Any biomechanical model approximates a material as a continuum and therefore struggles to correctly assess underlying multiple-scattering tissue behavior. Since the RD model is able to differentiate between two classes of attenuation originating from different structural effects, it may be able to provide a more accurate description for the brain tissue mechanics If the non-identifiability can be overcome; thus improving the accuracy and performance of optimisation based elastographic reconstruction.

The RD material model represents a simplified model of the damping behavior in complex materials such as soft tissue and that, in general, damping forces can be expected to have components proportional to both elastic and inertial forces as well as additional components that are not proportional to either forcing component. Thus, the RD model will be expected to produce artefacts when used as the basis for elastographic property reconstruction in real tissue, although RD offers the capability to account for one additional component of the overall damping effect.

Also, it is important to emphasise that accuracy of the elastographic reconstruc-

tion results produced by such indirect imaging algorithms can only be as good as the fundamental assumptions that underlie the reconstruction approach. The reconstruction code models tissue as a nearly incompressible, RD viscoelastic continuum. However, the brain is known to be a highly heterogeneous, orthotropic, fluid saturated medium. Therefore reconstruction results may not be accurate due to the data-model discrepancy.

10.3 Summary

This research presents first results for RD based brain MRE. The values obtained for brain viscoelastic properties agree well with previously published *in vitro* and *in vivo* data. Parametric RD reconstruction show promise for potential *in vivo* determination of different brain tissue types, and the possibility of providing additional diagnostic tools. Further multi-frequency RD brain elastography experiments as well as studies of a variety brain simulating damping phantoms are needed to investigate attenuation mechanisms across different intracranial tissue types, including tissue in diseased states such as multiple sclerosis, Alzhiemer's, hydrocephalus and cancer.

Chapter 11

Conclusions and future work

The ability of the MRE to provide non-invasive assessment of the mechanical properties of biological tissues would significantly complement and enhance conventional diagnostic imaging techniques that are incapable of direct evaluation of the mechanical consistency of tissue. Qualitative mapping of tissues characterised by different mechanical properties would help in tissue characterisation, early detection of pathological changes in the tissue and, for example, pre-operative planning of the most appropriate approach for a tumor resection. Furthermore, accurate quantitative estimates of tissue mechanical properties deduced by MRE in combination with anatomical, functional and molecular imaging modalities would definitely augment important information on pre-operative and intra-operative data for the best surgical planning.

However, current MRE methodologies have been unsuccessful in performing accurate and reproducible measurements of the mechanical properties of *in vivo* brain tissue. Fundamental limitations of the constitutive models used in the inverse problem techniques, as well as inability to efficiently generate shear waves inside the brain due to its natural shielding might have also prevented accurate characterisation of intracranial tissue *in vivo*. Therefore, the purpose of this research was to non-invasively obtain quantitative estimates of the mechanical properties of the *in vivo* brain tissue, as well as to measure damping behaviour via MRE using the RD material model.

In addition, available brain actuation methods are generally not well suited for clinical applications due to the technology complexity, device non-portability, MRI non-compatibility and poor patient comfort. Therefore, a novel pneumatic actuator design, as an alternative to electromechanical actuators used in previous MRE brain

studies, was developed. The actuator comprises a pair of passive subwoofers used to generate acoustic pressure waves that are transmitted via wave-guides to the pneumatically actuated drivers positioned under the subject's head. The actuator allows an easy and fast set up, as well as a flexible configuration for different experimental settings, and can be used for both phantoms and human studies. Assessment of the actuator performance showed sufficient motion generation within the frequency range of 60-80 Hz which is suitable for brain MRE experiments. Due to the limited access to MRI in Canterbury after the earthquake, the actuator has yet to be tested in a clinical setting. However a very similar actuator design was used by a collaborating institute CNRC, which provided data used in this thesis.

A thorough assessment of the RD model was performed using various tissue-simulating phantoms under different experimental protocols. Experimental data was collected from homogeneous and heterogeneous phantoms of varying material types, such as gelatine, water and porous tofu of various concentrations. The choice of materials was based on a reasonable approximation of the range and constitution of mechanical properties expected in the brain. Initially, full simultaneous three parameter RD reconstructions were performed where the identified parameters were a complex shear modulus, μ_R and μ_I, and the imaginary density component, ρ_I. Rheologically, μ_R and μ_I can be interpreted as a storage modulus and loss modulus, respectively, while the imaginary density ρ_I was mathematically interpreted to represent the rate of the density change in a poroelastic medium.

Overall, success was achieved in reconstruction of real shear modulus μ_R in all phantom configurations across multiple frequencies. Generally, μ_R images showed reasonable characterisation of various material types, compared to expectations, with acceptable delineation of the different material boundaries. The reconstructed damping ratio, ξ_d, provided acceptable differentiation of various material types correctly confirming expected damping profiles of the materials. However, reconstruction of the RD based properties μ_I and ρ_I displayed a consistent effect of poor reconstruction accuracy in all phantom configurations. The trends in the RD parameter behaviours were not fully understood and warranted further investigation of the structural identifiability of the model.

Since RD parameter values did not accurately identify expected outcomes for ρ_I and μ_I either quantitatively and qualitatively, a detailed analysis was performed to investigate the identifiability of the RD model. The analysis revealed that the full

simultaneous 3 parameter-based RD reconstruction of the imaginary components of the complex shear modulus and density is non-identifiable at a single frequency which is a commonly used approach in a range of elastographic inverse problems used in biomedical applications of this model.

Two approaches were developed to overcome this fundamental identifiability issue of the model. One involves an application of multiple input frequencies over a broad range. The second is a parametric RD reconstruction, where one of the RD parameters (μ_I or ρ_I) is globally defined allowing accurate identification of the remaining two RD parameters.

Simultaneous multi-frequency-based (MF-based) RD elastography was performed to investigate an improvement in elastographic reconstruction accuracy of viscoelastic and RD parameters over a single-frequency-based (SF-based) RD reconstruction in tissue-simulating damping phantoms. Both zero order model and power-law MF model were assessed with regards to accurate mechanical property reconstruction. Furthermore, parametric RD MRE studies were carried out and compared to the MF-based results.

Overall, MF-based RD reconstruction results demonstrated limited success in accurate delineation of the RD material properties. Although a slight improvement in reconstruction accuracy was observed, the difference between SF and MF based RD results was minimal. These results were likely due to the lack of practical identifiability. Another possible reason was the limited range of actuation frequencies. Similar to a SF RD results, μ_R reconstruction was again of the highest quality in all phantom configurations. Reconstruction of the RD parameters is generally associated with poor characterisation of different material types and relatively high variations within supposedly homogenous material regions and materials boundaries. No distinguished trends are observed in μ_I or ρ_I parameters, although ρ_I image displays better characterisation of different materials.

Parametric-based RD reconstructions generally produced better results compared to MF-based RD results. A better material differentiation was observed in the μ_R image, as well as in the identified RD parameters. Moreover, moderately accurate reconstruction of ξ was observed when one of the fixed RD parameters was adjusted appropriately. Therefore, parametric RD MRE was considered to be an optimal method for accurate elastographic RD reconstruction, although with the

stated limitations to drive future work in this area.

Finally, partial success in reconstructing material property distributions within the phantoms, as well as the development of the MR compatible brain actuator, suggested preliminary assessment of the RD MRE in application to *in vivo* brain imaging. Here, parametric RD reconstructions showed apparent success in mapping stiffness distribution of the brain which correlated well with brain anatomical structures. Additionally, it provided quantitative measures of the elasticity of the white and gray matter that compared well with values reported in the literature.

In conclusion, RD MRE showed some initial promise in qualitative characterisation of the material property distributions as well as some significant issues related to accurate identification of the RD parameters at a single frequency. To establish full identifiability of the model, multiple frequencies over a broad range are required. Parametrisation can be also performed as an alternative solution. An achieved success in elastic property reconstruction indicates the method is a potentially valuable approach to medical imaging.

Future work for parametric-based RD model would include specification of the multiple ROIs where individual material properties can be defined for each individual region. Here, segmentation of different tissues will allow more accurate local definition of the material properties and thus would improve parametric based RD elastographic reconstruction. For MF-based RD MRE, a broad range of the actuation frequencies will deliver the most informative data for accurate inversion. Furthermore, further research is to be done into investigation of the appropriate MF model that would best describe frequency dependant behaviour of brain mechanics.

Lastly, current RD material models approximate the tissue as an isotropic, nearly incompressible linear continuum. However, brain is known to be a heterogeneous, orthotropic, non-linear media. Therefore, current reconstruction modality can not fully account for the complexity of the inner brain environment due to the fundamental limitations of the model and a data-model mismatch. Hence, the breakthrough would be to apply a newly developed orthotropic viscoelastic RD material model to reconstruct mechanical properties of the brain. Realistically, this will require a more sophisticated actuation strategy and inverse problem architecture. More specifically, the brain should be separately actuated from three different directions so that good motions are generated throughout. We believe that with the proper

actuation methodology and orthotropic reconstruction model, we will be able to achieve accurate brain reconstruction results.

References

Ali-Osman, F. (2005). *Brain Tumors*. Contemporary Cancer Research. Humana Press.

Anvekar, B. (2011). Dr balaji anvekar's neuroradiology cases. `http://www.neuroradiologycases.com/2011/10/meningioma-mr-spectroscopy.html`.

Anvekar, B. (2012). Dr balaji anvekar's neuroradiology cases. `http://www.neuroradiologycases.com/2012/03/thalamic-glioma-anaplastic-astrocytoma.html`.

Arbogast, K. B. and S. S. Margulies (1998). Material characterization of the brainstem from oscillatory shear tests. *Journal of Biomechanics 31*(9), 801–807.

Aronen, H., I. Gazit, D. Louis, B. Buchbinder, F. Pardo, R. Weisskoff, G. Harsh, G. Cosgrove, E. Halpern, and F. Hochberg (1994). Cerebral blood volume maps of gliomas: comparison with tumor grade and histologic findings. *Radiology 191*(1), 41–51.

Asbach, P., D. Klatt, U. Hamhaber, J. Braun, R. Somasundaram, B. Hamm, and I. Sack (2008). Assessment of liver viscoelasticity using multifrequency mr elastography. *Magnetic Resonance in Medicine 60*(2), 373–379.

Audoly, S., G. Bellu, L. D'Angio, M. Saccomani, and C. Cobelli (2001). Global identifiability of nonlinear models of biological systems. *Biomedical Engineering, IEEE Transactions on 48*(1), 55–65.

Bancroft, L., M. Kransdorf, J. Peterson, and M. OíConnor (2006). Benign fatty tumors: classification, clinical course, imaging appearance, and treatment. *Skeletal radiology 35*(10), 719–733.

Bandak, F., M. VORST, L. Stuhmiller, P. Mlakar, W. Chilton, and J. Stuhmiller (1995). An imaging-based computational and experimental study of skull fracture: finite element model development. *Journal of neurotrauma 12*(4), 679–688.

Basser, P. (1992). Interstitial pressure, volume, and flow during infusion into brain tissue. *Microvascular research 44*(2), 143–165.

Bayly, P. V., E. E. Black, R. C. Pedersen, E. P. Leister, and G. M. Genin (2006). In vivo imaging of rapid deformation and strain in an animal model of traumatic brain injury. *Journal of Biomechanics 39*(6), 1086–1095.

Bellu, G., M. Saccomani, S. Audoly, and L. DíAngiò (2007). Daisy: A new software tool to test global identifiability of biological and physiological systems. *Computer methods and programs in biomedicine 88*(1), 52.

Bensamoun, S., S. Ringleb, L. Littrell, Q. Chen, M. Brennan, R. Ehman, and K. An (2005). Determination of thigh muscle stiffness using magnetic resonance elastography. *Journal of Magnetic Resonance Imaging 23*(2), 242–247.

Biersack, H., F. Grünwald, and J. Kropp (1991). Single photon emission computed tomography imaging of brain tumors. In *Seminars in nuclear medicine*, Volume 21, pp. 2–10. Elsevier.

Bilston, L. E., Z. Liu, and N. Phan-Thien (1997). Linear viscoelastic properties of bovine brain tissue in shear. *Biorheology 34*(6), 377.

Bloomfield, I., I. Johnston, and L. Bilston (1998). Effects of proteins, blood cells and glucose on the viscosity of cerebrospinal fluid. *Pediatric neurosurgery 28*(5), 246–251.

Bradley Jr, W. G., A. R. Whittemore, A. S. Watanabe, S. J. Davis, L. M. Teresi, and M. Homyak (1991). Association of deep white matter infarction with chronic communicating hydrocephalus: implications regarding the possible origin of normal-pressure hydrocephalus. *American Journal of Neuroradiology 12*(1), 31.

Brands, D. W. A., G. W. M. Peters, and P. H. M. Bovendeerd (2004). Design and numerical implementation of a 3-d non-linear viscoelastic constitutive model for brain tissue during impact. *Journal of Biomechanics 37*(1), 127–134.

Braun, J., J. Bernarding, T. Tolxdorff, and I. Sack (2002). In vivo magnetic resonance elastography of the human brain using ultrafast acquisition techniques. In *ISMRM*. Proceedings of the 10th Conference of the International Society of Magnetic Resonance in Medicine.

Burachik, R., L. G. Drummond, A. N. Iusem, and B. Svaiter (1995). Full convergence of the steepest descent method with inexact line searches. *Optimization 32*(2), 137–146.

Chambolle, A. (2004). An algorithm for total variation minimization and applications. *Journal of Mathematical imaging and vision 20*(1), 89–97.

Chen, Q., J. Basford, and K. An (2008). Ability of magnetic resonance elastography to assess taut bands. *Clinical Biomechanics 23*(5), 623–629.

Chopra, R., A. Arani, Y. Huang, M. Musquera, J. Wachsmuth, M. Bronskill, and D. Plewes (2009). In vivo mr elastography of the prostate gland using a transurethral actuator. *Magnetic Resonance in Medicine 62*(3), 665–671.

Claussen, C., M. Laniado, E. Kazner, W. Schörner, and R. Felix (1985). Application of contrast agents in ct and mri (nmr): their potential in imaging of brain tumors. *Neuroradiology 27*(2), 164–171.

Curry, H. B. (1944). The method of steepest descent for nonlinear minimization problems. *Quart. Appl. Math 2*(3), 250–261.

Di Ieva, A., F. Grizzi, E. Rognone, Z. Tse, T. Parittotokkaporn, F. Rodriguez y Baena, M. Tschabitscher, C. Matula, S. Trattnig, and R. Rodriguez y Baena (2010). Magnetic resonance elastography: a general overview of its current and future applications in brain imaging. *Neurosurgical review 33*(2), 137–145.

Docherty, P., J. Chase, T. Lotz, T. Desaive, et al. (2011). A graphical method for practical and informative identifiability analyses of physiological models: A case study of insulin kinetics and sensitivity. *Biomedical engineering online 10*(1), 1–20.

Dommelen, J., M. Hrapko, and G. Peters (2009). Mechanical properties of brain tissue: characterisation and constitutive modelling. *Mechanosensitivity of the Nervous System*, 249–279.

Donnelly, B. R. and J. Medige (1997). Shear properties of human brain tissue. *Journal of biomechanical engineering 119*, 423.

Drevelegas, A. (2011). *Imaging of Brain Tumors with Histological Correlations*. Springer.

Duck, F. (2012). *Physical Properties of Tissue: A Comprehensive Reference Book*. Institution of Physics & Engineering in Medicine & Biology.

Elgeti, T., J. Rump, U. Hamhaber, S. Papazoglou, B. Hamm, J. Braun, and I. Sack (2008). Cardiac magnetic resonance elastography: initial results. *Investigative radiology 43*(11), 762–772.

Encyclopedia, T. N. W. (2013). Neuron. `http://www.newworldencyclopedia.org/entry/File:Neuron.svg`.

Engelhard, H. (2001). Progress in the diagnosis and treatment of patients with meningiomas-part i: diagnostic imaging, preoperative embolization. *Surgical neurology 55*(2), 89–101.

Engelhard, H., A. Stelea, and A. Mundt (2003). Oligodendroglioma and anaplastic oligodendroglioma:: Clinical features, treatment, and prognosis. *Surgical neurology 60*(5), 443–456.

Engin, A. (1969). The axisymmetric response of a fluid-filled spherical shell to a local radial impulse—a model for head injury. *Journal of Biomechanics 2*(3), 325–341.

Estes, M. S. and J. H. McElhaney (1970). Response of brain tissue to compressive loading. *American Society of Mechanical Engineers 70*, 1–4.

Fallenstein, G. T., V. D. Hulce, and J. W. Melvin (1969). Dynamic mechanical properties of human brain tissue. *Journal of Biomechanics 2*(3), 217–226.

Ferrant, M., S. Warfield, A. Nabavi, F. Jolesz, and R. Kikinis (2000). Registration of 3d intraoperative mr images of the brain using a finite element biomechanical model. In *Medical Image Computing and Computer-Assisted Intervention–MICCAI 2000*, pp. 249–258. Springer.

Galford, J. and J. McElhaney (1969). Some viscoelastic properties of scalp, brain, and dura. ASME.

Galford, J. E. and J. H. McElhaney (1970). A viscoelastic study of scalp, brain, and dura. *Journal of Biomechanics 3*(2), 211.

Gennisson, J., C. Cornu, S. Catheline, M. Fink, and P. Portero (2005). Human muscle hardness assessment during incremental isometric contraction using transient elastography. *Journal of biomechanics 38*(7), 1543–1550.

Gilbert, J. C. and J. Nocedal (1992). Global convergence properties of conjugate gradient methods for optimization. *SIAM Journal on Optimization 2*(1), 21–42.

Glowinski, R. (2008). *Lectures on Numerical Methods for Non-Linear Variational Problems*. Scientific Computation. Springer.

Goldsmith, B., W. Wara, C. Wilson, and D. Larson (1994). Postoperative irradiation for subtotally resected meningiomas. *Journal of neurosurgery 80*(2), 195–201.

Golub, G. H., P. C. Hansen, and D. P. O'Leary (1999). Tikhonov regularization and total least squares. *SIAM Journal on Matrix Analysis and Applications 21*(1), 185–194.

Gore, J., A. Anderson, M. Does, D. Gochberg, J. Joers, R. Kennan, E. Parsons, and M. Schachter (2001). The relationship of problems in biomedical mri to the study of porous media. *Magnetic resonance imaging 19*(3), 295–300.

Goss, B., K. McGee, E. Ehman, A. Manduca, and R. Ehman (2006a). Magnetic resonance elastography of the lung: technical feasibility. *Magnetic resonance in medicine 56*(5), 1060–1066.

Goss, B. C., K. P. McGee, E. C. Ehman, A. Manduca, and R. L. Ehman (2006b). Magnetic resonance elastography of the lung: technical feasibility. *Magnetic Resonance in Medicine 56*(5), 1060–1066.

Green, M., R. Sinkus, and L. E. Bilston (2006). High resolution 3d brain mr-elastography. In *ISMRM*, pp. 2021.

Green, M. A., L. E. Bilston, and R. Sinkus (2008). In vivo brain viscoelastic properties measured by magnetic resonance elastography. *NMR in Biomedicine 21*(7), 755–764.

Greenleaf, J., M. Fatemi, and M. Insana (2003). Selected methods for imaging elastic properties of biological tissues. *Annual review of biomedical engineering 5*(1), 57–78.

Guillaume, A., D. Osmont, D. Gaffie, J. Sarron, and P. Quandieu (1997). Effects of perfusion on the mechanical behavior of the brain exposed to hypergravity. *Journal of biomechanics 30*(4), 383–389.

Hamhaber, U., I. Sack, S. Papazoglou, J. Rump, D. Klatt, and J. Braun (2006). Three-dimensional analysis of shear wave propagation observed by in vivo magnetic resonance elastography of the brain. *Acta Biomaterialia 3*(1), 127–137.

Hirakawa, K., K. Hashizume, and T. Hayashi (1981). Viscoelastic property of human brain-for the analysis of impact injury (author's transl). *Brain and nerve 33*(10), 1057.

Humar, J. (2012). *Dynamics of Structures*. Taylor & Francis Group.

Hutchings, R. (2013). Transverse section of the human brain showing the interior of the cerebral hemispheres. `http://www.allposters.com/-sp/Transverse-Section-of-the-Human-Brain-Showing-the-Interior-of-the-Cerebral-Hemisphe i8999680_.htm`.

Institute, N. C. (2013). Meninges of the brain. `http://training.seer.cancer.gov/brain/tumors/anatomy/meninges.html`.

Jenkinson, M., P. Bannister, M. Brady, S. Smith, et al. (2002). Improved optimization for the robust and accurate linear registration and motion correction of brain images. *Neuroimage 17*(2), 825–841.

Joachimowicz, N., C. Pichot, and J.-P. Hugonin (1991). Inverse scattering: An iterative numerical method for electromagnetic imaging. *Antennas and Propagation, IEEE Transactions on 39*(12), 1742–1753.

Johnson, C., M. McGarry, E. Van Houten, J. Weaver, K. Paulsen, B. Sutton, and J. Georgiadis (2012). Magnetic resonance elastography of the brain using multishot spiral readouts with self-navigated motion correction. *Magnetic Resonance in Medicine*.

Jurgen, B., G. Buntkowsky, J. Bernarding, T. Tolxdorff, and I. Sack (2001). Simulation and analysis of magnetic resonance elastography wave images using coupled harmonic oscillators and gaussian local frequency estimation. *Magnetic Resonance Imaging 19*, 10.

Kaczmarek, M., R. Subramaniam, and S. Neff (1997). The hydromechanics of hydrocephalus: steady-state solutions for cylindrical geometry. *Bulletin of mathematical biology 59*(2), 295–323.

Kemper, J., R. Sinkus, J. Lorenzen, C. Nolte-Ernsting, A. Stork, G. Adam, et al. (2004). Mr elastography of the prostate: initial in-vivo application. *RoFo: Fortschritte auf dem Gebiete der Rontgenstrahlen und der Nuklearmedizin 176*(8), 1094.

Klatt, D., P. Asbach, J. Rump, S. Papazoglou, R. Somasundaram, J. Modrow, J. Braun, and I. Sack (2006). In vivo determination of hepatic stiffness using steady-state free precession magnetic resonance elastography. *Investigative radiology 41*(12), 841.

Klatt, D., U. Hamhaber, P. Asbach, J. Braun, and I. Sack (2007). Noninvasive assessment of the rheological behavior of human organs using multifrequency mr elastography: a study of brain and liver viscoelasticity. *Physics in Medicine and Biology 52*(24), 7281–7294.

Kono, K., Y. Inoue, K. Nakayama, M. Shakudo, M. Morino, K. Ohata, K. Wakasa, and R. Yamada (2001). The role of diffusion-weighted imaging in patients with brain tumors. *American journal of neuroradiology 22*(6), 1081–1088.

Kruse, S., R. Grimm, D. Lake, A. Manduca, and R. Ehman (2006). Fast EPI Based 3D MR Elastography of the Brain. In *Proc. Intl. Soc. Mag. Reson. Med*, Volume 14, pp. 3385.

Kruse, S., J. Smith, A. Lawrence, M. Dresner, A. Manduca, J. Greenleaf, and R. Ehman (2000). Tissue characterization using magnetic resonance elastography: preliminary results. *Physics in medicine and biology 45*(6), 1579.

Kruse, S. A., M. A. Dresner, P. J. Rossman, J. P. Felmlee, C. R. Jack, and R. L. Ehman (1999). "palpation of the brain" using magnetic resonance elastography. In *ISMRM*, pp. 258. MR Research Laboratory, Mayo Clinic.

Kruse, S. A., G. H. Rose, K. J. Glaser, A. Manduca, J. P. Felmlee, C. R. Jack, and R. L. Ehman (2007). Magnetic resonance elastography of the brain. *Neuroimage 39*(1), 231–237.

Kyriacou, S., A. Mohamed, K. Miller, and S. Neff (2002). Brain mechanics for neurosurgery: modeling issues. *Biomechanics and Modeling in Mechanobiology 1*(2), 151–164.

Latta, P., M. Gruwel, P. Debergue, B. Matwiy, U. Sboto-Frankenstein, and B. Tomanek (2010). Convertible pneumatic actuator for magnetic resonance elastography of the brain. *Magnetic Resonance Imaging*.

Latta, P., V. Jellúš, L. Budinskỳ, V. Mlynárik, I. Tkáč, and R. Luypaert (1998). Motion artifacts reduction in dwi using navigator echoes: A robust and simple correction scheme. *Magnetic Resonance Materials in Physics, Biology and Medicine 7*(1), 21–27.

Law, M., S. Oh, G. Johnson, J. Babb, D. Zagzag, J. Golfinos, and P. Kelly (2006). Perfusion magnetic resonance imaging predicts patient outcome as an adjunct to histopathology: a second reference standard in the surgical and nonsurgical treatment of low-grade gliomas. *Neurosurgery 58*(6), 1099–1107.

Lee, J. (2008). *Meningiomas*. SpringerLink : Bücher. Springer.

Lewa, C. J. (1991). Magnetic resonance imaging in the presence of mechanical waves: Nmr frequency modulation, mechanical waves as nmr factor, local temperatur variations. *Spectroscopy letters 24*(1), 55–67.

Lewa, C. J. and J. D. Certaines (1995). Mr imaging of viscoelastic properties. *Journal of Magnetic Resonance Imaging 5*(2), 242–244.

Ljung, C. (1975). A model for brain deformation due to rotation of the skull. *Journal of Biomechanics 8*(5), 263.

llmari Karonen (2005). Mass-spring-damper system. `http://vyznev.net/misc/Mass-Spring-Damper.svg`.

Lopez, O., K. Amrami, A. Manduca, and R. Ehman (2008). Characterization of the dynamic shear properties of hyaline cartilage using high-frequency dynamic mr elastography. *Magnetic Resonance in Medicine 59*(2), 356–364.

Lorenzen, J., R. Sinkus, M. Lorenzen, M. Dargatz, C. Leussler, P. Röschmann, G. Adam, et al. (2002). Mr elastography of the breast: preliminary clinical results. *RoFo: Fortschritte auf dem Gebiete der Rontgenstrahlen und der Nuklearmedizin 174*(7), 830.

Madsen, E., G. Frank, T. Krouskop, T. Varghese, F. Kallel, and J. Ophir (2003). Tissue-mimicking oil-in-gelatin dispersions for use in heterogeneous elastography phantoms. *Ultrasonic imaging 25*(1), 17–38.

Maia, A., S. Malheiros, A. da Rocha, C. da Silva, A. Gabbai, F. Ferraz, and J. Stávale (2005). Mr cerebral blood volume maps correlated with vascular endothelial growth factor expression and tumor grade in nonenhancing gliomas. *American journal of neuroradiology 26*(4), 777–783.

Majós, C., M. Julià-Sapé, J. Alonso, M. Serrallonga, C. Aguilera, J. Acebes, C. Arús, and J. Gili (2004). Brain tumor classification by proton mr spectroscopy: comparison of diagnostic accuracy at short and long te. *American Journal of Neuroradiology 25*(10), 1696–1704.

Manduca, A. (2005). *Analysis of dynamic magnetic resonance elastography data* (Advanced image processing in magnetic resonance imaging ed.). Taylor & Francis, Boca Raton.

Manduca, A., T. E. Oliphant, M. A. Dresner, J. L. Mahowald, S. A. Kruse, E. Amromin, J. P. Felmlee, J. F. Greenleaf, and R. L. Ehman (2001). Magnetic resonance elastography: non-invasive mapping of tissue elasticity. *Medical Image Analysis 5*(4), 237–254.

Margulies, S. and M. Prange (2002). Regional, directional, and age-dependent properties of the brain undergoing large deformation. *J Biomech Eng 124*, 244–252.

Mariappan, Y., K. Glaser, and R. Ehman (2010). Magnetic resonance elastography: a review. *Clinical Anatomy 23*(5), 497–511.

Marquardt, D. W. (1963). An algorithm for least-squares estimation of nonlinear parameters. *Journal of the Society for Industrial & Applied Mathematics 11*(2), 431–441.

Matthies, C. and M. Samii (1997). Management of 1000 vestibular schwannomas (acoustic neuromas): clinical presentation. *Neurosurgery 40*(1), 1.

McCracken, P. J., A. Manduca, and R. L. Ehman (2003). Mr elastography for studying the biomechanics of traumatic brain injury. In *ISMRM*, Volume 799. Proceedings of the 11th Annual Meeting of ISMRM. Toronto.

McCracken, P. J., A. Manduca, J. Felmlee, and R. L. Ehman (2005). Mechanical transient-based magnetic resonance elastography. *Magnetic resonance in medicine 53*(3), 628.

McCracken, P. J., A. Manduca, J. P. Felmlee, and R. L. Ehman (2004). Transient-based mr elastography of the brain. In *ISMRM*. Proceedings of the 12th Annual Meeting of ISMRM, Kyoto, Japan.

McGarry, M., H. Berger, and E. Van Houten (2007). Damping models in elastography. In *Medical Imaging*, pp. 65111W–65111W. International Society for Optics and Photonics.

McGarry, M. and E. Van Houten (2008). Use of a rayleigh damping model in elastography. *Medical and Biological Engineering and Computing 46*(8), 759–766.

McGarry, M., E. Van Houten, C. Johnson, J. Georgiadis, B. Sutton, J. Weaver, and K. Paulsen (2012). Multiresolution mr elastography using nonlinear inversion. *Medical Physics 39*, 6388.

McGarry, M., E. Van Houten, P. Perrinez, A. Pattison, J. Weaver, and K. Paulsen (2011). An octahedral shear strain-based measure of snr for 3d mr elastography. *Physics in Medicine and Biology 56*, N153.

McGarry, M. D. J. (2008). Rayleigh damped magnetic resonance elastography. Master's thesis, University of Canterbury.

McGee, K., R. Hubmayr, and R. Ehman (2007). Mr elastography of the lung with hyperpolarized 3he. *Magnetic Resonance in Medicine 59*(1), 14–18.

McKnight, A., J. Kugel, P. Rossman, A. Manduca, L. Hartmann, and R. Ehman (2002). Mr elastography of breast cancer: preliminary results. *American Journal of Roentgenology 178*(6), 1411–1417.

Metz, H., J. McElhaney, and A. K. Ommaya (1970). A comparison of the elasticity of live, dead, and fixed brain tissue. *Journal of Biomechanics 3*(4), 453.

Miga, M., K. Paulsen, P. Hoopes, F. Kennedy Jr, A. Hartov, and D. Roberts (2000). In vivo quantification of a homogeneous brain deformation model for updating preoperative images during surgery. *Biomedical Engineering, IEEE Transactions on 47*(2), 266–273.

Miga, M., K. Paulsen, F. Kennedy, J. Hoopes, A. Hartov, and D. Roberts (1998a). Initial in-vivo analysis of 3d heterogeneous brain computations for model-updated image-guided neurosurgery. *Medical Image Computing and Computer-Assisted InterventationóMICCAIí98*, 743–752.

Miga, M., K. Paulsen, F. Kennedy, P. Hoopes, A. Hartov, and D. Roberts (1998b). Modeling surgical loads to account for subsurface tissue deformation during stereotactic neurosurgery. In *BiOS'98 International Biomedical Optics Symposium*, pp. 501–511. International Society for Optics and Photonics.

Miller, K. (2005). Method of testing very soft biological tissues in compression. *Journal of Biomechanics 38*(1), 153–158.

Miller, K. and K. Chinzei (1997). Constitutive modelling of brain tissue: experiment and theory. *Journal of Biomechanics 30*(11), 1115–1121.

Miller, K. and K. Chinzei (2002). Mechanical properties of brain tissue in tension. *Journal of Biomechanics 35*(4), 483–490.

Miller, K., K. Chinzei, G. Orssengo, and P. Bednarz (2000). Mechanical properties of brain tissue in-vivo: experiment and computer simulation. *Journal of Biomechanics 33*(11), 1369–1376.

Moonen, C. and P. Bandettini (2000). *Functional Mri*. Medical Radiology / Diagnostic Imaging Series. Springer-Verlag GmbH.

Moore, D. F., R. Pursley, E. Dimitriadis, and S. L. Talagala (2003). Magnetic resonance imaging of brain transverse acoustic waves. In *ISMRM*, pp. 2298.

Mow, V. C., M. H. Holmes, and W. Michael Lai (1984). Fluid transport and mechanical properties of articular cartilage: a review. *Journal of biomechanics 17*(5), 377–394.

Murphy, M. C., J. Huston, C. R. Jack, K. J. Glaser, A. Manduca, J. P. Felmlee, and R. L. Ehman (2011). Decreased brain stiffness in alzheimer's disease determined by magnetic resonance elastography. *Journal of Magnetic Resonance Imaging 34*(3), 494–498.

Muthupillai, R., D. J. Lomas, P. J. Rossman, J. F. Greenleaf, A. Manduca, and R. L. Ehman (1995). Magnetic resonance elastography by direct visualization of propagating acoustic strain waves. *Science 269*(5232), 1854.

Muthupillai, R., P. Rossman, D. Lomas, J. Greenleaf, S. Riederer, and R. Ehman (1996). Magnetic resonance imaging of transverse acoustic strain waves. *Magnetic Resonance in Medicine 42*(4), 779–86.

Nagashima, T., T. Shirakuni, S. Rapoport, et al. (1990). A two-dimensional, finite element analysis of vasogenic brain edema. *Neurologia medico-chirurgica 30*(1), 1.

Nagashima, T., Y. Tada, S. Hamano, M. Skakakura, K. Masaoka, N. Tamaki, S. Matsumoto, et al. (1990). The finite element analysis of brain oedema associated with intracranial meningiomas. *Acta neurochirurgica. Supplementum 51*, 155.

Netti, P. A., L. T. Baxter, Y. Boucher, R. Skalak, and R. K. Jain (1997). Macro-and microscopic fluid transport in living tissues: Application to solid tumors. *AIChE journal 43*(3), 818–834.

Neville H. Fletcher, T. D. R. (1991). *The Physics of Musical Instruments*. Springer-Verlag.

Newman, M. E. (2005). Power laws, pareto distributions and zipf's law. *Contemporary physics 46*(5), 323–351.

Noguchi, K., N. Watanabe, T. Nagayoshi, T. Kanazawa, S. Toyoshima, M. Shimizu, and H. Seto (1999). Role of diffusion-weighted echo-planar mri in distinguishing between brain abscess and tumour: a preliminary report. *Neuroradiology 41*(3), 171–174.

Nolte, J. (2009). *The human brain: an introduction to its functional anatomy*. Human Brain: An Introduction to Its Functional Anatomy. Mosby/Elsevier.

Oberai, A. A., N. H. Gokhale, and G. R. Feijóo (2003). Solution of inverse problems in elasticity imaging using the adjoint method. *Inverse Problems 19*(2), 297.

Ohgaki, H. and P. Kleihues (2005). Population-based studies on incidence, survival rates, and genetic alterations in astrocytic and oligodendroglial gliomas. *Journal of Neuropathology & Experimental Neurology 64*(6), 479–489.

Okamoto, K., J. Ito, K. Ishikawa, K. Sakai, and S. Tokiguchi (2000). Diffusion-weighted echo-planar mr imaging in differential diagnosis of brain tumors and tumor-like conditions. *European radiology 10*(8), 1342–1350.

Oliphant, T. E., A. Manduca, R. L. Ehman, and J. F. Greenleaf (2001). Complex-valued stiffness reconstruction for magnetic resonance elastography by algebraic inversion of the differential equation. *Magnetic resonance in Medicine 45*(2), 299–310.

Ophir, J., S. Alam, B. Garra, F. Kallel, E. Konofagou, T. Krouskop, and T. Varghese (1999). Elastography: ultrasonic estimation and imaging of the elastic properties of tissues. *Proceedings of the Institution of Mechanical Engineers, Part H: Journal of Engineering in Medicine 213*(3), 203–233.

Othman, S., H. Xu, T. Royston, and R. Magin (2005). Microscopic magnetic resonance elastography (μmre). *Magnetic resonance in medicine 54*(3), 605–615.

OXCFMRI (2013). Mri image of human head. `http://www.fmrib.ox.ac.uk`.

Ozan, C. (2008). *Mechanical modeling of brain and breast tissue*. Ph. D. thesis, Georgia Institute of Technology.

Pamidi, M. and S. Advani (1978). Nonlinear constitutive relations for human brain tissue. *Journal of Biomechanical Engineering 100*, 44.

Papazoglou, S., J. Rump, J. Braun, and I. Sack (2006). Shear wave group velocity inversion in mr elastography of human skeletal muscle. *Magnetic resonance in medicine 56*(3), 489–497.

Patin, D. J., E. C. Eckstein, K. Harum, and V. S. Pallares (1993). Anatomic and biomechanical properties of human lumbar dura mater. *Anesthesia & Analgesia 76*(3), 535–540.

Pattison, A., P. Perrinez, M. McGarry, J. Weaver, and K. Paulsen (2011). Estimating hydraulic conductivity in vivo using magnetic resonance elastography. *Mechanics of Biological Systems and Materials, Volume 2*, 41–48.

Paulsen, K., M. Miga, F. Kennedy, P. Hoopens, A. Hartov, and D. Roberts (1999). A computational model for tracking subsurface tissue deformation during stereotactic neurosurgery. *Biomedical Engineering, IEEE Transactions on 46*(2), 213–225.

Pena, A., M. Bolton, H. Whitehouse, and J. Pickard (1999). Effects of brain ventricular shape on periventricular biomechanics: a finite-element analysis. *Neurosurgery 45*(1), 107.

Pena, A., J. D. Pickard, D. Stiller, N. G. Harris, and M. U. Schuhmann (2005). Brain tissue biomechanics in cortical contusion injury: a finite element analysis. *Acta Neurochirurgica 95*, 333.

Perriez, P., F. Kennedy, E. Van Houten, J. Weaver, and K. Paulsen (2010). Magnetic resonance poroelastography: an algorithm for estimating the mechanical properties of fluid-saturated soft tissues. *Medical Imaging, IEEE Transactions on 29*(3), 746–755.

Peters, A., A. Milsant, J. Rouzé, L. Ray, J. Chase, and E. Houten (2004). Digital image-based elasto-tomography: proof of concept studies for surface based mechanical property reconstruction. *JSME International Journal Series C 47*(4), 1117–1123.

Pia Saccomani, M., S. Audoly, and L. D'Angiò (2003). Parameter identifiability of nonlinear systems: the role of initial conditions. *Automatica 39*(4), 619–632.

Plewes, D., J. Bishop, A. Samani, and J. Sciarretta (2000). Visualization and quantification of breast cancer biomechanical properties with magnetic resonance elastography. *Physics in Medicine and Biology 45*(6), 1591.

Polak, E. and G. Ribiere (1969). Note on the convergence of conjugate direction methods.

Pollack, I., P. Gerszten, A. Martinez, K. Lo, B. Shultz, A. Albright, J. Janosky, and M. Deutsch (1995). Intracranial ependymomas of childhood: long-term outcome and prognostic factors. *Neurosurgery 37*(4), 655–667.

Prange, M., D. Meaney, S. Margulies, et al. (2000). Defining brain mechanical properties: effects of region, direction, and species. *Stapp car crash journal 44*, 205.

Purves, D. (2012). *Neuroscience*. Sinauer Associates.

Raksin, P. (2003). Imaging of meningiomas. In *Seminars in Neurosurgery*, Volume 14, pp. 193–202. THIEME.

Raue, A., C. Kreutz, T. Maiwald, J. Bachmann, M. Schilling, U. Klingmüller, and J. Timmer (2009). Structural and practical identifiability analysis of partially observed dynamical models by exploiting the profile likelihood. *Bioinformatics 25*(15), 1923–1929.

Reimann, P. (2013). Falx cerebri and tentorium cerebelli of the human brain. `http://www.neurofeedback-arnhem.nl/brein.htm`.

Righetti, R., J. Ophir, S. Srinivasan, T. Krouskop, et al. (2004). The feasibility of using elastography for imaging the poisson's ratio in porous media. *Ultrasound in medicine & biology 30*(2), 215–228.

Rimsten, A., B. Stenkvist, H. Johanson, and A. Lindgren (1975). The diagnostic accuracy of palpation and fine-needle biopsy and an evaluation of their combined use in the diagnosis of breast lesions: report on a prospective study in 1244 women with symptoms. *Annals of surgery 182*(1), 1.

Ritt, J. (1950). *Differential algebra*, Volume 33. Amer Mathematical Society.

Roberts, H., T. Roberts, T. Lee, and W. Dillon (2002). Dynamic, contrast-enhanced ct of human brain tumors: quantitative assessment of blood volume, blood flow, and microvascular permeability: report of two cases. *American journal of neuroradiology 23*(5), 828–832.

Rossman, P. J., S. A. Kruse, T. Hulshizer, and R. L. Ehman (2006). Pneumatically actuated driver for use in mre of the brain. In *ISMRM (fLow and motion study group workshop)*. ISMRMóFlow and Motion Study Group Workshop, New York, NY.

Rouvière, O., M. Yin, M. Dresner, P. Rossman, L. Burgart, J. Fidler, and R. Ehman (2006). Mr elastography of the liver: Preliminary results1. *Radiology 240*(2), 440–448.

Sack, I., B. Beierbach, U. Hamhaber, D. Klatt, and J. Braun (2007). Non-invasive measurement of brain viscoelasticity using magnetic resonance elastography. *NMR in Biomedicine 21*(3), 265–271.

Sack, I., B. Beierbach, J. Wuerfel, D. Klatt, U. Hamhaber, S. Papazoglou, P. Martus, and J. Braun (2009). The impact of aging and gender on brain viscoelasticity. *Neuroimage 46*(3), 652–657.

Sack, I., J. Rump, T. Elgeti, A. Samani, and J. Braun (2008). Mr elastography of the human heart: noninvasive assessment of myocardial elasticity changes by shear wave amplitude variations. *Magnetic Resonance in Medicine 61*(3), 668–677.

Sahay, K., R. Mehrotra, U. Sachdeva, and A. Banerji (1992). Elastomechanical characterization of brain tissues. *Journal of biomechanics 25*(3), 319–326.

Samani, A., J. Zubovits, and D. Plewes (2007). Elastic moduli of normal and pathological human breast tissues: an inversion-technique-based investigation of 169 samples. *Physics in medicine and biology 52*(6), 1565.

Sarron, J., C. Blondeau, A. Guillaume, and D. Osmont (2000). Identification of linear viscoelastic constitutive models. *Journal of Biomechanics 33*(6), 685–693.

Sarvazyan, A. (1993). Shear acoustic properties of soft biological tissues in medical diagnostics. *The Journal of the Acoustical Society of America 93*, 2329.

Schellinger, P., H. Meinck, and A. Thron (1999). Diagnostic accuracy of mri compared to cct in patients with brain metastases. *Journal of neuro-oncology 44*(3), 275–281.

Scholz, M., V. Noack, I. Pechlivanis, M. Engelhardt, B. Fricke, U. Linstedt, B. Brendel, K. Schmieder, H. Ermert, and A. Harders (2005). Vibrography during tumor neurosurgery. *Journal of ultrasound in medicine 24*(7), 985–992.

Shah, N., S. Kruse, D. Lager, G. Farell-Baril, J. Lieske, B. King, and R. Ehman (2004). Evaluation of renal parenchymal disease in a rat model with magnetic resonance elastography. *Magnetic resonance in medicine 52*(1), 56–64.

Shewchuk, J. R. (1994). An introduction to the conjugate gradient method without the agonizing pain.

Shuck, L. Z. and S. H. Advani (1972). Rheological response of human brain tissue in shear. *Journal of basic engineering 94*, 905–911.

Siegmann, K. C., T. Xydeas, R. Sinkus, B. Kraemer, U. Vogel, and C. D. Claussen (2010). Diagnostic value of mr elastography in addition to contrast-enhanced mr imaging of the breastóinitial clinical results. *European radiology 20*(2), 318–325.

Sinha, S. and U. Sinha (2009). Recent advances in breast mri and mrs. *NMR in biomedicine 22*(1), 3–16.

Sinkus, R., K. Siegmann, T. Xydeas, M. Tanter, C. Claussen, and M. Fink (2007). Mr elastography of breast lesions: Understanding the solid/liquid duality can improve the specificity of contrast-enhanced mr mammography. *Magnetic Resonance in Medicine 58*(6), 1135–1144.

Sinkus, R., M. Tanter, S. Catheline, J. Lorenzen, C. Kuhl, E. Sondermann, and M. Fink (2005). Imaging anisotropic and viscous properties of breast tissue by

magnetic resonance-elastography. *Magnetic resonance in medicine 53*(2), 372–387.

Sinkus, R., M. Tanter, T. Xydeas, S. Catheline, J. Bercoff, and M. Fink (2005). Viscoelastic shear properties of in vivo breast lesions measured by mr elastography. *Magnetic resonance imaging 23*(2), 159–165.

Skovoroda, A., S. Emelianov, and M. O'Donnell (1995). Tissue elasticity reconstruction based on ultrasonic displacement and strain images. *Ultrasonics, Ferroelectrics and Frequency Control, IEEE Transactions on 42*(4), 747–765.

Škrinjar, O., C. Studholme, A. Nabavi, and J. Duncan (2001). Steps toward a stereo-camera-guided biomechanical model for brain shift compensation. In *Information Processing in Medical Imaging*, pp. 183–189. Springer.

Slaughter, W. (2002). *The Linearized Theory of Elasticity*. Birkhäuser.

Smith, S. M., M. Jenkinson, M. W. Woolrich, C. F. Beckmann, T. Behrens, H. Johansen-Berg, P. R. Bannister, M. De Luca, I. Drobnjak, D. E. Flitney, et al. (2004). Advances in functional and structural mr image analysis and implementation as fsl. *Neuroimage 23*, S208.

Sordillo, P. P., L. Helson, S. I. Hajdu, G. B. Magill, C. Kosloff, R. B. Golbey, and E. J. Beattie (2006). Malignant schwannomaóclinical characteristics, survival, and response to therapy. *Cancer 47*(10), 2503–2509.

Srinivasan, S., T. Krouskop, and J. Ophir (2004). A quantitative comparison of modulus images obtained using nanoindentation with strain elastograms. *Ultrasound in medicine & biology 30*(7), 899–918.

Streitberger, K.-J., E. Wiener, J. Hoffmann, F. B. Freimann, D. Klatt, J. Braun, K. Lin, J. McLaughlin, C. Sprung, R. Klingebiel, et al. (2011). In vivo viscoelastic properties of the brain in normal pressure hydrocephalus. *NMR in Biomedicine 24*(4), 385–392.

Sze, G., E. Milano, C. Johnson, and L. Heier (1990). Detection of brain metastases: comparison of contrast-enhanced mr with unenhanced mr and enhanced ct. *American Journal of Neuroradiology 11*(4), 785–791.

Taylor, Z. and K. Miller (2004). Reassessment of brain elasticity for analysis of biomechanisms of hydrocephalus. *Journal of biomechanics 37*(8), 1263–1269.

Tenti, G., S. Sivaloganathan, and J. Drake (1999). Brain biomechanics: steady-state consolidation theory of hydrocephalus. *Can. Appl. Math. Q 7*, 111–125.

Terzaghi, K. (1943). Theoretical soil mechanics.

UCLA (2013). Oligodendoglioma of the brain. `http://radonc.ucla.edu/body.cfm?id=155`.

Uffmann, K., C. J. Galban, S. Maderwald, T. Paul, M. U. Schlamann, A. de Greiff, and M. E. Ladd (2005). Mr elastography of the human brain: Case study involving a patient with a temporal glioma. In *ISMRM*, Volume 13, pp. 757.

Uffmann, K., S. Maderwald, W. Ajaj, C. Galban, S. Mateiescu, H. Quick, and M. Ladd (2004). In vivo elasticity measurements of extremity skeletal muscle with mr elastography. *NMR in Biomedicine 17*(4), 181–190.

Uffmann, K., S. Maderwald, A. de Greiff, and M. E. Ladd (2004). Determination of gray and white matter elasticity with mr elastography. In *ISMRM*. Proceedings of the 12th Annual Meeting of ISMRM. Kyoto.

Unger, F., C. Walch, O. Schrottner, S. Eustacchio, B. Sutter, and G. Pendl (2002). Cranial nerve preservation after radiosurgery of vestibular schwannomas. *ACTA NEUROCHIRURGICA SUPPLEMENTUM-WIEN- 84*, 77–84.

Van Houten, E., M. Doyley, F. Kennedy, K. Paulsen, and J. Weaver (2005). A three-parameter mechanical property reconstruction method for mr-based elastic property imaging. *Medical Imaging, IEEE Transactions on 24*(3), 311–324.

Van Houten, E., M. Doyley, F. Kennedy, J. Weaver, and K. Paulsen (2002). Initial in vivo experience with steady-state subzone-based mr elastography of the human breast. *Journal of Magnetic Resonance Imaging 17*(1), 72–85.

Van Houten, E., M. McGarry, P. Perrinez, I. Perreard, J. Weaver, and K. Paulsen (2011). Subzone based magnetic resonance elastography using a rayleigh damped material model. *Medical Physics 38*, 1993.

Van Houten, E., K. Paulsen, M. Miga, F. Kennedy, J. Weaver, et al. (1999). An overlapping subzone technique for mr-based elastic property reconstruction. *Magnetic resonance in medicine 42*(4), 779–786.

Van Houten, E. E., M. Doyley, F. E. Kennedy, J. B. Weaver, and K. D. Paulsen (2003). Initial in vivo experience with steady-state subzone-based mr initial in

vivo experience with steady-state subzone-based mr elastography of the human breast. *Journal of Magnetic Resonance Imaging 17*, 72–85.

Van Houten, E. E. W., M. I. Miga, J. B. Weaver, F. E. Kennedy, and K. D. Paulsen (2001). Three-dimensional subzone-based reconstruction algorithm for mr elastography. *Magnetic Resonance in Medicine 45*(5), 827–837.

Van Houten, E. E. W., J. B. Weaver, M. I. Miga, F. E. Kennedy, and K. D. Paulsen (1999). Elasticity reconstruction from experimental mr displacement data: initial experience with an overlapping subzone finite element inversion process. *Medical Physics 27*, 101.

Vandenabeele, F., J. Creemers, and I. Lambrichts (1996). Ultrastructure of the human spinal arachnoid mater and dura mater. *Journal of anatomy 189*(Pt 2), 417.

Vappou, J., E. Breton, P. Choquet, C. Goetz, R. Willinger, and A. Constantinesco (2007). Magnetic resonance elastogrpahy compared with rotational rheometry for in vitro brain tissue viscoelasticity measurements. *Magnetic Resonance Materials in Physics, Biology and Medicine 20*, 273–278.

Vaquero, J., R. Martı nez, and M. Manrique (2000). Stereotactic biopsy for brain tumors: is it always necessary? *Surgical neurology 53*(5), 432–438.

Venkatesh, S., M. Yin, J. Glockner, N. Takahashi, P. Araoz, J. Talwalkar, and R. Ehman (2008). Mr elastography of liver tumors: preliminary results. *American Journal of Roentgenology 190*(6), 1534–1540.

Wall, D. J., P. Olsson, and E. E. Van Houten (2011). On an inverse problem from magnetic resonance elastic imaging. *SIAM Journal on Applied Mathematics 71*(5), 1578–1605.

Walsh, E. and A. Schettini (1984). Calculation of brain elastic parameters in vivo. *American Journal of Physiology-Regulatory, Integrative and Comparative Physiology 247*(4), R693–R700.

Walsh, E. K. and A. Schettini (1976). Elastic behavior of brain tissue in vivo. *American Journal of Physiology 230*(4), 1058.

Wang, H., J. Weaver, I. Perreard, M. Doyley, and K. Paulsen (2011). A three-dimensional quality-guided phase unwrapping method for mr elastography. *Physics in Medicine and Biology 56*, 3935.

Wang, H. C. and A. S. Wineman (1972). A mathematical model for the determination of viscoelastic behavior of brain in vivo–i oscillatory response. *Journal of Biomechanics 5*(5), 431–446.

Weaver, B. J., E. W. E. Van Houten, I. M. Miga, and E. F. Kennedy (2001). Magnetic resonance elastofaphy using 3d gradient echo measuremnts of steady-state motion. *Medical Physics 28*(8), 28.

Weber, M., S. Zoubaa, M. Schlieter, E. Jüttler, H. Huttner, K. Geletneky, C. Ittrich, M. Lichy, A. Kroll, J. Debus, et al. (2006). Diagnostic performance of spectroscopic and perfusion mri for distinction of brain tumors. *Neurology 66*(12), 1899–1906.

Weller, R. (2008). Microscopic morphology and histology of the human meninges.

Welsh, D. (1997). *Alcohol's Effect on Organ Function*. Diane Publishing Company.

White, W., M. H. Shiu, M. K. Rosenblum, R. A. Erlandson, and J. M. Woodruff (2006). Cellular schwannoma. a clinicopathologic study of 57 patients and 58 tumors. *Cancer 66*(6), 1266–1275.

Wilcox, R. K., L. E. Bilston, D. C. Barton, and R. M. Hall (2003). Mathematical model for the viscoelastic properties of dura mater. *Journal of orthopaedic science 8*(3), 432–434.

Wong, T., G. van der Westhuizen, R. Coleman, et al. (2002). Positron emission tomography imaging of brain tumors. *Neuroimaging Clinics of North America 12*(4), 615.

Wu, J. (2001). Tofu as a tissue-mimicking material. *Ultrasound in medicine & biology 27*(9), 1297–1300.

Wuerfel, J., F. Paul, B. Beierbach, U. Hamhaber, D. Klatt, S. Papazoglou, F. Zipp, P. Martus, J. Braun, and I. Sack (2010, Feb). Mr-elastography reveals degradation of tissue integrity in multiple sclerosis. *Neuroimage 49*(3), 2520–5.

Xu, L., Y. Lin, J. C. Han, Z. N. Xi, H. Shen, and P. Y. Gao (2006). Magnetic resonance elastography of brain tumors: preliminary results. *Acta Radiologica 48*(3), 327–330.

Xu, L., Y. Lin, Z. N. Xi, H. Shen, and P. Y. Gao (2007). Magnetic resonance elastography of the human brain: a preliminary study. *Acta Radiologica 48*(1), 112–115.

Zhang, Y., M. Brady, and S. Smith (2001). Segmentation of brain mr images through a hidden markov random field model and the expectation-maximization algorithm. *Medical Imaging, IEEE Transactions on 20*(1), 45–57.

Zheng, Y., Q. Chan, G. Li, E. Lam, and E. Yang (2007). A study of femoral artery by twin drivers in magnetic resonance interference elastography. In *Engineering in Medicine and Biology Society, 2007. EMBS 2007. 29th Annual International Conference of the IEEE*, pp. 2034–2037. IEEE.

Zheng, Y., G. Li, M. Chen, Q. C. C. Chan, S. G. Hu, X. N. Zhao, R. L. Ehman, E. Y. Lam, and E. S. Yang (2007). Magnetic resonance elastography with twin pneumatic drivers for wave compensation. In *IEEE EMBS*, pp. 2611–2613. Engineering in Medicine and Biology Society, 2007. EMBS 2007. 29th Annual International Conference of the IEEE.